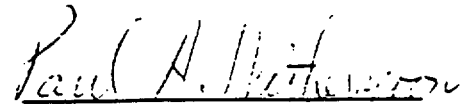


MECHANICAL TRANSPORT IN TWO-DIMENSIONAL NETWORKS OF FRACTURES

Howard K. Endo

Ph.D.

Material Science
and
Mineral Engineering



Paul A. Witherspoon
Chairman of Committee

Abstract

The objectives of this research are to evaluate directional mechanical transport parameters for anisotropic fracture systems, and to determine if fracture systems behave like equivalent porous media. The tracer experiments used to measure directional tortuosity, longitudinal geometric dispersivity, and hydraulic effective porosity are conducted with a uniform flow field and measurements are made from the fluid flowing within a test section where linear length of travel is constant. Since fluid flow and mechanical transport are coupled processes, the directional variations of specific discharge and hydraulic effective porosity are measured in regions with constant hydraulic gradients to evaluate porous medium equivalence for the two processes, respectively. If the fracture region behaves like an equivalent porous medium, the system has the following stable properties: 1) specific discharge is uniform in any direction and can be predicted from a permeability tensor and, 2) hydraulic effective porosity is directionally stable. Fracture systems with two parallel sets of continuous fractures satisfy criterion 1. However, in these systems hydraulic effective porosity is directionally dependent, and thus, criterion 2 is violated. Thus, for some fracture systems, fluid flow can be predicted using porous media assumptions, but it may not be possible to predict transport using porous media assumptions.

Two discontinuous fracture systems were studied which satisfied both criteria. Hydraulic

effective porosity for both systems has a value between rock effective porosity and total porosity. A length-density analysis (LDS) of Canadian fracture data shows that porous media equivalence for fluid flow and transport is likely when systems have narrow aperture distributions. Hydraulic effective porosities are equal to and greater than rock effective porosity for the continuous and the discontinuous systems exhibiting porous media equivalence in the LDS, respectively. All fracture systems studied showed different polar plots of longitudinal geometric dispersivity. In most porous media transport studies, anisotropic media is treated as equivalent isotropic media such that longitudinal geometric dispersivity is directionally stable. The use of directionally-stable longitudinal geometric dispersivities for these fracture systems could lead to serious errors in transport prediction.

Table of Contents

Table of Contents	i
List of Figures	iv
List of Tables	ix
Notation	x
Acknowledgments	xv
CHAPTER 1 INTRODUCTION	1
CHAPTER 2 LITERATURE REVIEW	
2.1 INTRODUCTION	3
2.2 DISPERSION IN POROUS MEDIA	3
2.2.1 The Advective Transport Process	4
2.2.2 The Dispersive Transport Process	5
2.2.3 Stochastic Models for Porous Media Dispersion	10
2.3 DISCRETE MECHANICAL TRANSPORT MODELS FOR FRACTURE ROCK MASSES	15
CHAPTER 3 THEORETICAL DEVELOPMENT	
3.1 INTRODUCTION	21
3.2 MICROSCOPIC LEVEL TRANSPORT	22
3.3 PORE TRANSPORT MODELS	24
3.4 POROUS MEDIA TRANSPORT MODEL	27
3.5 PROPER FLOW FIELD AND APPROPRIATE TEST SECTION USED IN A TRACER EXPERIMENT	33
3.6 EXECUTING THE SET OF TRACER EXPERIMENTS TO MEASURE DIRECTIONAL MECHANICAL TRANSPORT	35
3.7 MEASURING MECHANICAL TRANSPORT WITH THE BREAKTHROUGH CURVE	38
3.7.1 Mean of the Breakthrough Curve	38
3.7.2 Variance of the Breakthrough Curve	41
3.8 EQUIVALENT POROUS MEDIUM BEHAVIOR	47

CHAPTER 4 THE DISCRETE NUMERICAL MODEL

4.1 INTRODUCTION	55
4.2 FRACTURE SYSTEM GENERATION STAGE	55
4.3 HYDRAULIC HEAD CALCULATION	58
4.4 MECHANICAL TRANSPORT SIMULATION	60

CHAPTER 5 INVESTIGATION OF CONTINUOUS FRACTURE SYSTEMS

5.1 INTRODUCTION	69
5.2 CONTINUOUS SYSTEM WITH TWO SETS OF CONSTANT-APERTURE FRACTURES	69
5.3 SYSTEM WITH TWO ORTHOGONAL SETS OF CONTINUOUS FRACTURES	79

CHAPTER 6 INVESTIGATION OF DISCONTINUOUS FRACTURE SYSTEMS

6.1 INTRODUCTION	88
6.2 DISCONTINUOUS FRACTURE SYSTEM OF TWO SETS ORIENTED AT 0° AND 30°	88
6.3 DISCONTINUOUS FRACTURE SYSTEM OF TWO SETS ORIENTED AT 0° AND 60°	102
6.4 SENSITIVITY ANALYSIS	116
6.4.1 Sensitivity of Mean Geometric Parameters and Set Areal Density	118
6.4.2 Sensitivity of Distributed Geometric Parameters	130

CHAPTER 7 INVESTIGATION OF MECHANICAL TRANSPORT AT RESEARCH SITE IN MANITOBA, CANADA

7.1 INTRODUCTION	134
7.2 CONSTANT APERTURE LENGTH-DENSITY SERIES	137
7.3 DISTRIBUTED APERTURE LENGTH-DENSITY SERIES	153
7.3.1 Distributed Aperture Length-Density Study with Standard Deviation Equal to Mean Aperture	153
7.3.2 Distributed Aperture Length-Density Study with Standard Deviation Equal to 0.3 of Mean Aperture	175

7.4 SUMMARY OF LENGTH-DENSITY ANALYSIS	185
CHAPTER 8 CONCLUSIONS AND RECOMMENDATIONS	
8.1 CONCLUSION	191
8.2 RECOMMENDATIONS	197
REFERENCES	201

List of Figures

- Figure 2-1 Three Microscopic Mechanisms in Mechanical Transport.
- Figure 2-2 Graphical Representation of Mixing Conditions at a Node.
- Figure 2-3 Modeling Conditions Used in Earlier Mechanical Transport Models for Fracture Networks.
- Figure 3-1 Modeling of Transport Within a Control Volume at the Microscopic Level.
- Figure 3-2 Early Stages of Transport When a Uniform Pulse is Injected Between Two Parallel Plates Under Laminar Flow Conditions.
- Figure 3-3 Tortuosity for a Single Pore.
- Figure 3-4 Determination of the Flow Field for an Anisotropic Porous Medium With a Constant Hydraulic Gradient Using Flow Net Theory.
- Figure 3-5 Example of Groundwater Flow in an Anisotropic Porous Medium Showing a Cross-Hatched Zone Where Travel Length is Constant.
- Figure 3-6 Procedure Used in Conducting a Set of Tracer Experiments to Measure Directional Mechanical Transport for an Anisotropic Porous Medium.
- Figure 3-7 Divergence of Flow Paths in Flow Regions Within an Inhomogeneous Regional Flow System.
- Figure 3-8 Semilog Plot of Peclet Number Versus the Ratio of the Variance of the Breakthrough Curve to the Squared Mean Travel Time.
- Figure 3-9 Three Breakthrough Curves for a) Pe of 0.5, b) Pe of 0.2, and c) Pe of 0.025.
- Figure 3-10 Square Root of Permeability in Direction of Flow for the Anisotropic Porous Medium Shown in Figure 3-4.
- Figure 4-1 Stochastic Generation of a Fracture System Consisting of Two Sets of Fractures.
- Figure 4-2 A Typical Line Element of Aperture b With Labeled Nodes.
- Figure 4-3 Redistribution of Streamtubes at a Node.
- Figure 4-4 Creation of New Streamtubes at a Node.
- Figure 4-5 Fracture Network With Inflow Streamtubes Initiated in Elements 1, 2, and 5.
- Figure 5-1 Fracture System With Two Sets of Parallel, Continuous, and Constant Aperture Fractures.
- Figure 5-2 Convergence of Specific Discharge and Porosity to Their Theoretical Values as Size of Flow Region Increases (Ratio is q/q_T or ϕ/ϕ_T).
- Figure 5-3 Polar Plots of a) Specific Discharge and b) Average Linear Velocity Factor Versus Direction of Flow for System of Two Set of Parallel, Continuous, and Constant Aperture Fractures.
- Figure 5-4 Polar Plot of Hydraulic Effective Porosity Versus Direction of Flow for System of Two Sets of Parallel, Continuous, and Constant Aperture Fractures.

- Figure 5-5 Tortuosity Versus Direction of Flow for Fracture System of Two Sets of Parallel, Continuous, and Constant Aperture Fractures.
- Figure 5-6 Actual Mean Pore Velocity, Calculated Mean Pore Velocity, and Calculated Mean Pore Velocity With Tortuosity of $\sqrt{2}$ for Fracture System of Two Sets of Continuous, Parallel, and Constant Aperture Fractures.
- Figure 5-7 Polar Plot of Longitudinal Geometric Dispersivity for Fracture System of Two Sets of Continuous, Parallel, and Constant Aperture Fractures.
- Figure 5-8 Fracture System With Two Orthogonal Sets of Continuous Fractures.
- Figure 5-9 Polar Plots of a) Specific Discharge and b) Average Linear Factors Versus Direction of Flow for System With Two Orthogonal Sets of Continuous Fractures.
- Figure 5-10 Polar Plot of Hydraulic Effective Porosity for System of Two Orthogonal Sets of Continuous Fractures.
- Figure 5-11 Polar Plot of Tortuosity for Fracture System With Two Orthogonal Sets of Continuous Fractures.
- Figure 5-12 Polar Plot of Longitudinal Geometric Dispersivity for System With Two Orthogonal Sets of Continuous Fractures.
- Figure 6-1 Fracture Network in the Generation Region for Discontinuous Fracture System of Two Sets of Fractures Oriented at 0° and 30° With Constant Aperture and Length.
- Figure 6-2 Networks of a) Fractures and b) Connected Fracture Segments in Flow Region Oriented at 130° for Discontinuous Fracture System of Two Sets Oriented at 0° and 30° .
- Figure 6-3 Polar Plot of Square Root of Permeability in Direction of Flow for Discontinuous Fracture System of Two Sets Oriented at 0° and 30° .
- Figure 6-4 Mean DEVF and Mean DEVA Versus Direction of Flow for Discontinuous Fracture System of Two Sets Oriented at 0° and 30° .
- Figure 6-5 Polar Plot of Tortuosity for Discontinuous Fracture System of Two Sets Oriented at 0° and 30° .
- Figure 6-6 Actual Mean Pore Velocity and Calculated Mean Pore Velocity for First Realization of Discontinuous Fracture System of Two Sets Oriented at 0° and 30° .
- Figure 6-7 Polar Plots of Total Porosity, Hydraulic Effective Porosity, and Rock Effective Porosity for Discontinuous Fracture System of Two Sets Oriented at 0° and 30° .
- Figure 6-8 Three Breakthrough Curves for Directions of Flow Which Increase From the Direction of Maximum Permeability to the Direction of Minimum as One Proceeds Down the Figure.
- Figure 6-9 Polar Plot of Longitudinal Geometric Dispersivity Versus Direction of Flow for Discontinuous System of Two Sets Oriented at 0° and 30° .
- Figure 6-10 Fracture Network in the Generation Region for Discontinuous System of Two Sets Oriented at 0° and 60° .
- Figure 6-11 Networks of a) Fractures and b) Connected Fracture Segments in the Flow

Region Oriented at 30° for Discontinuous System of Two Sets Oriented at 0° and 60°.

- Figure 6-12 Mean Hydraulic Effective Porosity for Orientations 30°, 75°, and 120° Versus the Number of Realizations.
- Figure 6-13 Polar Plot of Square Root of Permeability in Direction of Flow for Discontinuous System of Two Sets Oriented at 0° and 60°.
- Figure 6-14 Mean DEVF and Mean DEVA Versus Direction of Flow for Discontinuous System of Two Sets Oriented at 0° and 60°.
- Figure 6-15 Polar Plot of Tortuosity for Discontinuous System of Two Sets Oriented at 0° and 60°.
- Figure 6-16 Polar Plots of Rock Effective Porosity, Hydraulic Effective Porosity, and Total Porosity for Discontinuous System of Two Sets Oriented at 0° and 60°.
- Figure 6-17 Polar Plot of Longitudinal Geometric Dispersivity for Discontinuous System of Two Sets Oriented at 0° and 60°.
- Figure 6-18 Longitudinal Geometric Dispersivity Versus Width of Flow Region for Discontinuous System of Two Sets Oriented at 0° and 60°.
- Figure 6-19 Three General Types of Sensitivity Relationships.
- Figure 6-20 Total Porosity, Rock Effective Porosity, and Hydraulic Effective Porosity Versus Number of Fractures in Set, Mean Fracture Length, and Orientation of Set 2.
- Figure 6-21 Specific Discharge Versus Number of Fractures in Set, Mean Fracture Length, and Orientation of Set 2.
- Figure 6-22 Rock Effective Porosity and Specific Discharge Versus Connectivity.
- Figure 6-23 Mean Travel Time Versus Number of Fractures in Set, Mean Fracture Length, and Orientation of Set 2.
- Figure 6-24 Variance of the Breakthrough Curve Versus Number of Fractures in Set, Mean Fracture Length, and Orientation of Set 2.
- Figure 7-1 Map of Hydrogeological Research Site in Manitoba, Canada.
- Figure 7-2 Fracture Network in the Generation Region for Discontinuous System With Mean Fracture Length of 10 m.
- Figure 7-3 Network of a) Fractures and b) Connected Fracture Segments in the Flow Region Oriented at 0° for Discontinuous System With Mean Fracture Length of 10 m.
- Figure 7-4 Fracture Network in the Generation Region for Discontinuous System With Mean Fracture Length of 35 m.
- Figure 7-5 Network of a) Fractures and b) Connected Fracture Segments in the Flow Region Oriented at 0° for Discontinuous System With Mean Fracture Length of 35 m.
- Figure 7-6 Polar Plots of Tortuosity for a) Systems With Mean Fracture Lengths of 30 and 35 m and b) System With Mean Fracture Length of 50 m and the Continuous

Fracture System.

- Figure 7-7 Polar Plots of Hydraulic Effective Porosity for a) Systems With Mean Fracture Lengths of 30 and 35 m and b) System With Mean Fracture Length of 50 m and the Continuous Fracture System.
- Figure 7-8 Polar Plots of Longitudinal Geometric Dispersivity for Systems With Mean Fracture Lengths of a) 30 m and b) 35 m.
- Figure 7-9 Polar Plots of Longitudinal Geometric Dispersivity for a) System With Mean Fracture Length of 50 m and b) the Continuous Fracture System.
- Figure 7-10 Polar Plot of Mean Longitudinal Geometric Dispersivity for Five Realizations of the System With Mean Fracture Length of 50 m.
- Figure 7-11 Polar Plot of Hydraulic Effective Porosity for System With Mean Fracture Length of 50 m Using Square Flow Region of Width 330 m.
- Figure 7-12 Polar Plot of Hydraulic Effective Porosity for System With Mean Fracture Length of 50 m Using Square Flow Region of Width 175 m.
- Figure 7-13 Polar Plot of Hydraulic Effective Porosity for System With Mean Fracture Length of 50 m Using Square Flow Region of Width 60 m.
- Figure 7-14 Fracture Network in the Generation Region for Continuous System in the First Distributed Aperture Study.
- Figure 7-15 Mean Hydraulic Effective Porosity in All Directions Versus the Number of Realizations.
- Figure 7-16 Standard Error in Mean Hydraulic Effective Porosity Versus the Number of Realizations.
- Figure 7-17 Fracture Network in a) Generation Region and b) Flow Region Oriented at 60° for Realization 12 of the Continuous System in the First Distributed Aperture Study.
- Figure 7-18 Breakthrough Curve for Direction of Flow 120° for Continuous System in the First Distributed Aperture Study.
- Figure 7-19 Polar Plots of Mean Hydraulic Effective Porosity After Five Realizations and Ten Realizations.
- Figure 7-20 Polar Plots of Mean Hydraulic Effective Porosity After Fifteen Realizations and Twenty-Five Realizations.
- Figure 7-21 Mean DEVF and Mean DEVA Versus Direction of Flow for Continuous System in the First Distributed Aperture Study.
- Figure 7-22 Polar Plot of Mean Tortuosity for Continuous System in the First Distributed Aperture Study.
- Figure 7-23 Polar Plots of Total Porosity, Hydraulic Effective Porosity, and Rock Effective Porosity for Discontinuous System With Mean Fracture Length of 50 m and Linearly Correlated Apertures.
- Figure 7-24 Breakthrough Curve in a Direction in Which Hydraulic Effective Porosity is Three Times Larger Than Rock Effective Porosity.

- Figure 7-25 Mean DEVF and Mean DEVA Versus Direction of Flow for System With Mean Fracture Length of 50 m and Linearly Correlated Apertures.
- Figure 7-26 Polar Plot of Mean Tortuosity for System With Mean Fracture Length of 50 m and Linearly Correlated Apertures.
- Figure 7-27 Polar Plot of Mean Hydraulic Effective Porosity for System With Mean Fracture Length of 50 m in the First Distributed Aperture Study.
- Figure 7-28 Mean DEVF and Mean DEVA Versus Direction of Flow for System With Mean Fracture Length of 50 m in the First Distributed Aperture Study.
- Figure 7-29 Polar Plots of Total Porosity and Hydraulic Effective Porosity for Continuous System With σ_b/μ_b of 0.3.
- Figure 7-30 Mean DEVF and Mean DEVA Versus Direction of Flow for Continuous System With σ_b/μ_b of 0.3.
- Figure 7-31 Polar Plot of Tortuosity for Continuous System With σ_b/μ_b of 0.3.
- Figure 7-32 Polar Plot of Longitudinal Geometric Dispersivity for Continuous System With σ_b/μ_b of 0.3.
- Figure 7-33 Polar Plots of Total Porosity, Rock Effective Porosity, and Hydraulic Effective Porosity for Discontinuous System With μ_1 of 50 m and σ_b/μ_b of 0.3.
- Figure 7-34 Mean DEVF and Mean DEVA Versus Direction of Flow for Discontinuous System With μ_1 of 50 m and σ_b/μ_b of 0.3.
- Figure 7-35 Polar Plot of Longitudinal Geometric Dispersivity for Discontinuous System with μ_1 of 50 m and σ_b/μ_b of 0.3.
- Figure 7-36 Polar Plot of Tortuosity for Discontinuous System With μ_1 of 50 m and σ_b/μ_b of 0.3.

List of Tables

- Table 4-1 Macroscopic Parameters Calculated in Mechanical Transport Simulation Stage.
- Table 5-1 Specific Discharge Results for Fracture System With Two Sets of Parallel, Continuous, and Constant-Aperture Fractures.
- Table 5-2 Specific Discharge Results for Fracture System With Two Orthogonal Sets of Fractures.
- Table 6-1 Orientations, Estimated Directions of Flow, and Flow Region Sizes Used in Monte Carlo Simulation of Discontinuous System Consisting of Two Sets of Fractures Oriented at 0° and 30°.
- Table 6-2 Orientations, and Estimated Directions of Flow Used in Monte Carlo Simulation of the Discontinuous System Consisting of Two Sets of Fractures Oriented at 0° and 60°.
- Table 6-3 Orientations and Directions of Flow Calculated for Monte Carlo Study of the Discontinuous System of Two Sets Oriented at 0° and 60°.
- Table 6-4 Mean Sensitivity and Maximum Magnitude of Relative Sensitivity for Mean Orientation, Set Areal Density, and Mean Fracture Length Sensitivity Studies.

Notation

A	area of flow, L^2
ANFC	angle of flow based on uniformity of flow, degrees
ANFD	angle of flow based on components of specific discharge, degrees
b	fracture aperture, L
c	concentration, M/L^3
[C]	conductance matrix, L/T
c_o	concentration in an outflow fracture, M/L^3
\bar{d}	diffusive mass flux, M/TL^2
d_c	diameter of capillary tube, L
D	free solution molecular diffusion coefficient, L^2/T
DEVA	deviation in angle of flow, degrees
DEVF	deviation in flow
[D_F]	dispersed plug flow dispersion tensor, L^2/T
D_L	axial dispersed plug flow longitudinal dispersion coefficient, L^2/T
D_o	effective molecular diffusion coefficient L^2/T
E	normalized concentration, 1/T
E'	dimensionless concentration
E_S	dimensionless concentration for zone of slow movement
E_F	dimensionless concentration for zone of fast movement
g	acceleration of gravity, L/T^2
h	half width of parallel plate conduit, L

\bar{j}	hydraulic gradient
$[k]$	intrinsic permeability tensor, L^2
$[K]$	permeability tensor, L/T
K_f	permeability in direction of flow, L/T
K_x	maximum principal permeability, L/T
K_y	minimum principal permeability, L/T
l	fracture length, L
L	linear length of travel, L
L_a	mean travel length of flow between sides 2 and 4, L
L_C	width on side 2 of zone of continuous flow from side 2 to 4, L
L_e	length of element, L
L_{NC}	width on side 2 of zone of non-continuous flow from side 2 to 4, L
L_{ST}	total travel length of streamtube, L
L_x	width of flow region, L
L_y	height of flow region, L
\bar{m}	mechanical dispersive flux, M/TL^2
$[M]$	mechanical dispersion tensor, L^2/T
M_L	longitudinal mechanical dispersion coefficient, L^2/T
MPV	mean pore velocity, L/T
NC	number of streamtubes flowing between sides 2 and 4
θ	fracture orientation, degrees
p	pressure, M/LT^2
Pe	Peclet number

\bar{q}	specific discharge, L/T
q_T	theoretical magnitude of specific discharge, L/T
Q	flow rate in direction of flow, L^2/T (2-D) or L^3/T (3-D)
Q_C	flow rate for fluid that flows from side 2 to 4, L^2/T
Q_e	flow rate in element, L^2/T
Q_N	total flow rate into node, L^2/T
Q_{NC}	flow rate for fluid flowing into side 2 that does not exit on side 4, L^2/T
Q_{ST}	flow rate in streamtube, L^2/T
Q_x	flow rate in the x direction, L^2/T (2-D) or L^3/T (3-D)
Q_{S1}	flow rate into side 1, L^2/T
Q_{S2}	flow rate into side 2, L^2/T
Q_{S3}	flow rate out of side 3, L^2/T
Q_{S4}	flow rate out of side 4, L^2/T
r	coordinate perpendicular to direction of flow, L
r_h	hydraulic radius, L
s	coordinate in direction of flow, L
s_f	shape factor
S	relative sensitivity
SD	standard deviation of normalized breakthrough curve, T
S_m	mean sensitivity
S_s	specific surface, 1/L
t	time, T
\bar{T}	mean flow travel time, T

t_{ST}	travel time of streamtube in element, T
TM	mean of normalized breakthrough curve, T
u	fracture velocity, L/T
U	maximum velocity in parallel plate conduit, L/T
v	velocity, L/T
\bar{v}	average cross sectional velocity, L/T
V	total volume, L ³
V _c	total conductive void volume, L ³
VLIN	average linear velocity, L/T
VPORE	calculated mean pore velocity, L/T
[α]	geometric dispersivity tensor, L
α_1	longitudinal geometric dispersivity for isotropic medium, L
α_L	longitudinal geometric dispersivity, L
α_t	transverse geometric dispersivity for isotropic medium, L
ζ	angle between scanline and fracture pole, degrees
η	ordinate for coordinate system inside fracture, L
θ	angle of flow, degrees
θ_T	theoretical angle of flow, degrees
λ_1	linear fracture density, 1/L
λ_A	set areal density, 1/L ²
μ	fluid viscosity, M/LT
μ_i	mean of i
ξ	abscissa for coordinate system inside fracture, L

ρ	fluid density, M/L ³
σ_i	standard deviation of i
σ^2	variance of normalized breakthrough curve, T ²
τ	tortuosity
ϕ	total porosity
ϕ_H	hydraulic effective porosity
ϕ_R	rock effective porosity
ϕ_T	theoretical total porosity
Φ	hydraulic head, L

Acknowledgments

Acknowledgment is due to U. S. Department of Energy for support of this study under contract number DE-AC03-76F0098.

I should like to express my appreciation to Professor Paul A. Witherspoon who served as my major advisor in this study. I should also like to thank Professor Robert L. Wiegel and Professor Malcolm McPherson the other two members of the dissertation committee.

CHAPTER 1

INTRODUCTION

Concerns about radioactive waste storage and the injection of toxic pollutants deep underground have focused interest on the problems of fluid flow and mass transport in groundwater systems. The disposal of pollutants in or near a rock mass where fractures constitute the major conduits of groundwater movement is a central problem. The primary objective of this research is to determine when a fractured rock mass may be treated as an equivalent porous medium for transport studies.

In porous media, the size, shape, and degree of interconnection of the intergranular pores regulate fluid flow and transport. The void region is well connected and the number of pores per volume of porous medium is very large, so that the medium may be treated as a continuum in which macroscopic fluid flow and transport properties are considered without regard for the actual movement of individual fluid particles. The number of connected fractures per volume of rock is much less in a fractured rock mass than in a porous medium: therefore, a larger sample of rock may be required before the porous medium approach is applicable. When the porous medium approach is not appropriate, a discrete model which simulates transport in each fracture of the network must be used. The discrete approach requires detailed information on the geometry of the fracture system and hence may require an excessive amount of data and computational effort. Thus, the continuum approach is preferable if it can be shown to be appropriate.

In order to evaluate whether the continuum approach is applicable, one must demonstrate that the fracture system has the same transport behavior as that of an equivalent porous medium. However, fracture systems may be anisotropic and transport in anisotropic media is not fully understood. The reason is that no solution is available to determine the components of the dispersivity tensor in an anisotropic medium (Freeze and Cherry, 1979, pp. 552).

However, mechanical transport, the component of transport that is due to the movement

of fluid through the conductive flow channels, can be evaluated for anisotropic media. Thus, the conditions under which fracture networks behave like equivalent porous media can be investigated by focusing on mechanical transport.

The directional variations of the ratio of fluid flux to mean velocity, tortuosity, and longitudinal mechanical dispersion must be understood to evaluate mechanical transport. In an anisotropic medium, the ratio of flux to mean velocity is assumed to be independent of direction of flow and equal to porosity. Thus, a test for equivalent porous medium behavior is to determine if the ratio of flux to velocity is constant in all directions. Less is understood about the directional dependence of tortuosity and mechanical dispersion in anisotropic porous media. The prevailing practice is to treat an anisotropic porous medium as an equivalent isotropic medium in transport studies, implying that each transport parameter has no directional dependence. This work introduces the concept that longitudinal mechanical transport and tortuosity are both dependent on the direction of flow. Thus, the evaluation of these parameters in anisotropic fracture networks will lead to a better understanding of the transport phenomenon in all permeable media.

The fact that fluid flow and mechanical transport are coupled processes makes it necessary to also investigate equivalent porous medium behavior for fluid flow. The directional properties of specific discharge are used to investigate equivalent continuum behavior for fluid flow. When the fracture system exhibits continuum behavior, specific discharge can be predicted in any direction from a permeability tensor.

A numerical model is used in this research to simulate mechanical transport in discrete fracture networks. We assume that fluid flow is restricted to planar fractures within an impermeable rock matrix and that mechanical transport is the only transport process. The simulation of mechanical transport uses a new streamtubing technique which traces the detailed movement of fluid within streamtubes from inflow to outflow boundaries along the fracture system.

CHAPTER 2

LITERATURE REVIEW

2.1. INTRODUCTION

Tracer injected into a groundwater aquifer will not migrate downstream retaining its shape, but will spread and mix with the ambient fluid. Dispersion of the tracer is caused by microscopic mixing occurring within the pores of the medium. This literature review will: 1) introduce the transport processes and parameters used to model dispersion in porous media; 2) present key areas of research in porous media transport and; 3) review mechanical transport models for fractured rock masses.

The primary objective of this research is to determine when a fractured rock mass can be treated like an equivalent porous medium. Porous media transport modeling is reviewed so that continuum parameters characterizing transport can be evaluated. Areas of uncertainty where research is needed are also discussed. Two specific problem areas, applicability of the Fickian dispersive approach and dispersion in anisotropic media, will be investigated.

Three earlier discrete mechanical transport models are discussed below. The modeling techniques and principles used in each model are reviewed in detail. A new model which simulates mechanical transport in fractured rock masses is developed in Chapter 4. This new model is based on the physics of fluid flow to provide a sound and realistic simulation of mechanical transport.

2.2. DISPERSION IN POROUS MEDIA

The porous media dispersion model consists of an advective transport process coupled with a dispersive transport process. The advective process accounts for transport by the mean motion of flow. Advective transport alone causes no distortion in the shape of a pollutant plume as pollutant is merely transported with the mean flow. The dispersive process allows for the spread of a pollutant resulting from complex microscopic mixing that occurs within the pores. In the next two sections, modeling of the advective and the dispersive processes are

discussed. Section 2.2.3 reviews the fairly recent approach of stochastic transport modeling for porous media. A numerical stochastic model of mechanical transport will be developed in Chapter 4.

2.2.1. The Advective Transport Process

In the advective process, a pollutant moves with the mean flow velocity. In porous media modeling, the mean rate of advection is expressed in terms of the quantity of fluid flowing through the medium because fluid flow parameters are generally much easier to determine than transport parameters. The hydraulic effective porosity is used in this study to express the relationship between fluid flow and transport, and is defined as the specific discharge divided by the average linear velocity. The average linear velocity is the ratio of the straight or linear travel length to the mean flow travel time. Considerable laboratory work has been carried out to determine the relationship between hydraulic effective porosity and total porosity. Von Rosenberg (1956) conducted tracer experiments in packed columns of Ottawa sand and found that for this homogeneous and isotropic medium the hydraulic effective porosity was nearly equal to the total porosity. Biggar and Nielsen (1960) obtained mixed results when they investigated a set of four porous media: glass beads, Oakley sand, Columbia silt loam, and Yolo loam. In the case of the glass beads, the total porosity provided a good estimate of the hydraulic effective porosity. However, the hydraulic effective porosity was less than the porosity for the three other porous media. Biggar and Nielsen (1960) attributed this deviation to the presence of stagnant void regions. In contrast to the findings of Biggar and Nielsen, Ellis et al. (1968) found that, in laboratory tracer experiments involving packed sand columns, the hydraulic effective porosity was generally larger than the porosity. The hydraulic effective porosity may be greater than the porosity if microscopic regions of slow movement exist which have a minor influence on the total flow rate passing through the medium, but have a major influence on the travel time for particles flowing into these zones. The slow movement in these zones produces a very large mean flow travel time which can result in the hydraulic effective porosity being larger than the porosity.

Well testing methods provide a means of evaluating the hydraulic effective porosity in the field. Hazzaa et al. (1965, 1966) applied the two-well pulse method to predict the hydraulic effective porosity for an inhomogeneous aquifer of sand and gravel interbedded with clay lenses. Hazzaa et al. in a series of tests concluded that the hydraulic effective porosity was less than the porosity.

Grove and Beetem (1971) used an innovative recharging-discharging well technique to determine the hydraulic effective porosity for a fractured carbonate aquifer of Culebra dolomite. In this technique, water is pumped from one well and injected into another well at the same flow rate until a steady state hydraulic head distribution is established in the aquifer. Tracer is then introduced into the recharging well, and the breakthrough curve measured at the discharging well. The hydraulic effective porosity was found to be within the range of the estimated porosity.

The standard multiple well method of injecting tracer into a recharging well and monitoring concentration at strategically located observation wells was employed by Hoehn and Roberts (1982). The multiple-well test was conducted in a vertically homogeneous, poorly-sorted alluvial gravel aquifer. It was concluded that the hydraulic effective porosity was less than the porosity.

Thus, both field and laboratory tests have demonstrated that the hydraulic effective porosity (ϕ_H) is not necessarily equal to the total porosity (ϕ). Experimental evidence from the laboratory indicates that the relationship between ϕ_H and ϕ is dependent on the type of porous medium. Where there is a well-ordered pore structure (i.e. glass beads), ϕ_H is approximately equal to ϕ . However, where the pore structure is irregular and nonuniform, the hydraulic effective porosity differs from the total porosity and is usually less than ϕ because of the presence of stagnant void regions.

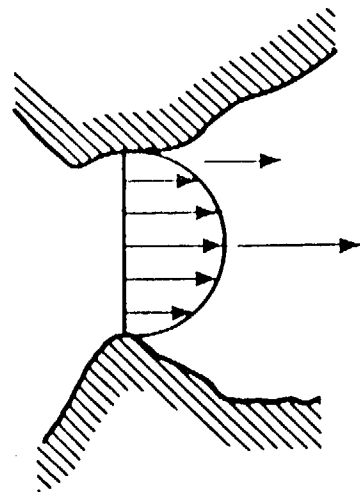
2.2.2. The Dispersive Process

The distortion in the shape of a contaminant plume for a conservative pollutant is caused by the interaction of molecular diffusion and mechanical dispersion. Molecular diffusion is the

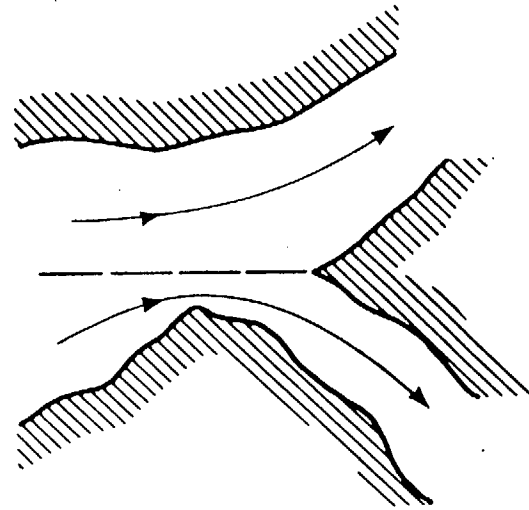
mixing caused by the kinetic energy of randomly moving solute particles. Mechanical dispersion is the mixing induced by the movement of fluid through the conductive channels of the medium. The principle microscopic mechanisms of mechanical dispersion, as illustrated in Figure 2-1, are the velocity distribution across a flow channel which causes particles to move faster in the center than along the sides of the channel; the flow rate variation from one channel to another which dictates the direction particles will travel; and the geometry of the pores which causes particles to travel along tortuous paths. Molecular diffusion controls dispersion when the flow velocity is very low; mechanical dispersion rapidly becomes the governing mode of transport as flow velocity increases.

Presently, the classical approach is widely used to characterize the dispersive process because of the simplicity of this approach, and because this approach has been used with moderate success in analyzing laboratory tracer experiments. The classical approach was formulated from Fick's law for molecular diffusion. In this approach, the mass flux dispersing across a unit area is equal to the product of a second-order dispersion tensor consisting of constant coefficients and the negative of the concentration gradient. Von Rosenberg (1956) presented qualitative justification for applying the classical approach to porous media dispersion based on Taylor's analysis (1953) of dispersion in a pipe. Taylor demonstrated that after an initial period, the Fickian approach may be used to model longitudinal dispersion in a pipe.

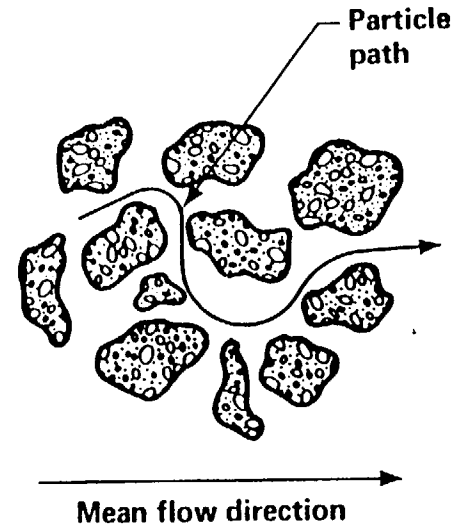
The laboratory tracer experiments that confirmed the classical dispersive approach were generally conducted using packed columns of isotropic, homogeneous porous media. A porous medium sample was carefully placed into an open-ended cylinder and constant hydraulic head boundary conditions were applied across the inlet and the outlet of the packed column to create a uniform flow field. A consistent uniform flow field throughout the sample was required to evaluate meaningful transport parameters from the tracer experiment. Tracer was then introduced at the inlet to the column and concentration was measured at various points within the column or at the outlet. Perkins and Johnston (1963) present a comprehensive review of laboratory dispersion studies that were based on this classical approach.



Velocity distribution
in flow channel



Flow variation



XBL 827-7177

Figure 2-1 Three Microscopic Mechanisms in Mechanical Transport.

Dispersion studies have also been conducted in the field. Two general techniques are used to evaluate dispersion from field measurements. In the first technique, tracer tests are conducted and concentration measurements are used to evaluate dispersion coefficients. A multitude of different types of single-well or multiple-well methods can be applied in this approach. The type of tracer test to use depends on the scale of the test and intended accuracy. Fried (1975) describes the different types of field tracer tests and their range of applicability. The second technique of evaluating dispersion coefficients is known as the inverse method. In the inverse method, dispersion coefficients are determined by simulating the time history migration of pollutant in an aquifer. This is accomplished by varying the parameters in the dispersion model until the calculated concentration contours match the historical data. A major limitation of the inverse method is that because of the large number of parameters used in transport modeling a unique solution is often not obtainable. Anderson (1979) presents a detailed discussion on the application and limitations of the inverse method.

Dispersion in anisotropic porous media is not well understood. No experimental or analytical technique is available for evaluating all nine components of the classical dispersion tensor for an anisotropic medium (Anderson, 1979; Freeze and Cherry, 1979). Consequently, dispersion in anisotropic porous media cannot be modeled accurately. The current practice is to treat an anisotropic medium as an equivalent isotropic porous medium in dispersion studies. This simplification is made because the two independent coefficients of the dispersion tensor for an isotropic porous medium can be evaluated. These two independent coefficients are the dispersion coefficient in the direction of flow called the longitudinal dispersion coefficient, and the dispersion coefficient perpendicular to the direction of flow called the transverse dispersion coefficient. All references cited in this literature review make the assumption that dispersion takes place in an isotropic porous medium.

One of the main reasons dispersion in anisotropic porous media is indeterminable is that the proper flow field to use in a tracer experiment has not been recognized. The direction of flow coincides with the direction of the hydraulic gradient for an isotropic porous medium;

hence, it is easy to create a uniform flow field as discussed earlier. However, for an anisotropic porous medium, the direction of flow and the direction of the hydraulic gradient do not coincide. Thus, when the hydraulic boundary conditions used in a tracer experiment for an isotropic medium are applied to an anisotropic medium, a nonuniform flow field is created. The appropriate flow field to use in tracer experiments to evaluate mechanical transport for anisotropic porous media will be introduced in Chapter 3.

There has been no justification to qualify the treatment of an anisotropic medium as an equivalent isotropic medium. Evidence from field experiments suggests that this simplification may lead to serious errors in transport prediction. The dispersion coefficients calculated from field tests are found to be many times larger than dispersion coefficients measured in laboratory experiments (Anderson, 1979; Fried, 1981; Cherry et al., 1978). The difference between the two measured coefficients could be attributed to directional transport properties of the medium.

Another important finding is that the classical dispersion coefficients computed for field data commonly increase with time (Pickens and Grisak, 1981). The transient behavior of dispersion coefficients are commonly explained based on the scale of testing. Mechanical dispersion, commonly the controlling mode of dispersion, is caused by zones of velocity variations which cause particles to move at different rates and spread out spatially. The size of these zones of velocity variations is referred to as the scale of heterogeneity. As the scale of heterogeneity increases, the initial period of non-Fickian dispersion increases. Laboratory samples are fairly homogeneous and dispersion is caused by velocity variations within the microscopic pores. Field tests are conducted on a very large scale, so that dispersion results from macroscopic heterogeneous zones which are much larger than a pore. The large scale of heterogeneity influencing a field test results in measurements of transient dispersion coefficients which indicate that the period of testing is within the initial period of non-Fickian dispersion.

In summary, Fickian dispersion for anisotropic porous media cannot be accurately modeled because the second-order dispersion tensor cannot be evaluated. When dispersion

coefficients are computed by treating the medium as an equivalent isotropic medium, the calculated coefficients often increase with sample size. Both of these problems lead to difficulties in transport prediction. Methodology will be developed in Chapter 3 to evaluate both the hydraulic effective porosity and longitudinal mechanical transport coefficient for anisotropic porous media. The applicability of the Fickian approach to characterize mechanical transport for anisotropic fractured rock masses will be investigated in Chapters 5 and 6.

2.2.3. Stochastic Models for Porous Media Dispersion

The continuum approach is a black-box technique which computes the output from the box without analyzing what actually happens within the box. Stochastic modeling is a more detailed approach which analyzes the internal structure and actions within the box to determine the system's output. Analytical and numerical stochastic models are briefly reviewed to provide the concepts necessary in developing a stochastic model. A numerical stochastic model that simulates mechanical transport in fractured rock is developed in Chapter 4. Since stochastic modeling is a fairly recent approach one of the objectives of reviewing these studies is to show the approaches being used in research on porous media transport.

2.2.3.1. Analytical Stochastic Models of Dispersion

In analytic stochastic models, certain transport parameters, such as the mean rate of advection, are allowed to vary statistically throughout the porous medium. This results in a stochastic dispersion equation which is then solved to determine macroscopic dispersion within the medium. Gelhar et al. (1979) investigated dispersion in vertically-stratified media. The focus of their study was to determine whether macroscopic dispersion in the aquifer could be represented by the classical approach. Horizontal flow was produced in each layer by introducing a uniform hydraulic gradient in the direction of flow. Dispersion was primarily caused by the variation of permeability in the vertical direction. Each variable in the classical dispersion equation, except effective porosity, was expressed as a stationary random variable represented by its expected value plus a perturbation component. The stochastic equation for the concen-

tration perturbation was then derived neglecting all second-order perturbation terms. Spectral analysis was applied to solve this equation.

The results of their study, for a specific permeability spectrum, indicated that global dispersion was Fickian only after a period of non-Fickian dispersion. Initially, the variance of the plume increased much more rapidly than predicted by Fickian dispersion and the spatial distribution of the tracer cloud was highly skewed. The spatial distribution of the tracer cloud is symmetric when the Fickian approach is applicable. As time went on, Fickian transport was approached as the tracer cloud became more symmetric and the rate of spreading decreased.

Matheron and de Marsily (1981) analyzed dispersion in vertically stratified aquifers in which a vertical component of velocity existed. The following parameters in the dispersion equation were considered to be constants: vertical component of velocity, longitudinal dispersion coefficient, transverse dispersion coefficient, and effective porosity. This meant that the only stationary random variable in the dispersion equation was the horizontal component of velocity. The stochastic model traced the movement of a solute particle through the aquifer. This technique was equivalent to directly solving the dispersion equation because the probability density of the solute particle at a point was equal to the expectation of concentration at that point.

The spatial variance in the horizontal direction was found to be a function of the covariance in the horizontal velocity component. Fickian dispersion only occurred if this covariance satisfied certain conditions, and only after an initial period of non-Fickian dispersion. The vertical component of velocity caused the conditions for Fickian dispersion to be less stringent than if flow was strictly horizontal in the aquifer. Fickian dispersion occurred early when the vertical velocity component and vertical dispersion coefficient were large. In a practical example involving a sandstone aquifer, Fickian dispersion was approached at approximately 140 days, or after 600 meters of travel under natural flow conditions. This amount of time is often not feasible for a field tracer experiment.

A stochastic study of macrodispersion in three-dimensional heterogeneous porous media

was conducted by Dieulin et al. (1981). Macrodispersion is dispersion caused strictly by velocity variations within the heterogeneous porous medium. The velocity field was assumed to be a stationary random process in the Dieulin et al. study. The stochastic model traced the movement of a solute particle instead of directly solving the dispersion equation, the same technique used in the Matheron and de Marsily (1981) study. Dieulin et al. showed that the dispersion tensor can vary in magnitude with time, and after a sufficient initial period, the dispersion tensor may become constant.

2.2.3.2. Numerical Stochastic Models of Dispersion

Numerical stochastic dispersion modeling is a discrete approach to investigate dispersion in porous media. A porous medium is stochastically created within a problem domain by dividing the domain into a large number of small subregions and statistically generating the dispersion parameters for each subregion. Next, hydraulic boundary conditions are applied to the domain to create the desired flow field. Reference tracer particles are then introduced into the porous medium and the detailed particle movements are monitored to evaluate dispersion.

One of the first stochastic studies in porous media transport was conducted by Warren and Skiba (1964). This work focused on interpreting the effect of the scale of heterogeneity on Fickian mechanical transport. A cubic porous medium domain was subdivided into constant-sized blocks that were cubic or rectangular parallelepiped. Block sizes varied with each Monte Carlo run to examine the influence of the scale of heterogeneity on dispersion. Permeability was lognormally distributed within the blocks, and porosity was normally distributed within the blocks.

Boundary conditions were applied to the domain to induce flow in one direction between two opposing sides and reference particles were randomly introduced across the domain's inlet. The magnitude and direction a particle was displaced in a discrete time interval was determined by interpolating velocities in the blocks adjacent to that containing the particle. As particles exited the system, the travel time of each particle was recorded from which the breakthrough curve was constructed. The classical longitudinal dispersion coefficient was then

computed from this breakthrough curve.

Warren and Skiba found that the longitudinal dispersion coefficient increased as the ratio of the length of a block to the width of the domain decreased. This implies that the longitudinal dispersion coefficient is unique (Fickian dispersion) for all sample sizes only if this dimensionless length ratio remains constant. This also implies that for Fickian dispersion, the scale of heterogeneity must increase with sample size.

Schwartz (1977) investigated the validity of the Fickian approach for characterizing mechanical transport in heterogeneous porous media. In his study, two-dimensional rectangular porous media domains were constructed using equal-sized rectangular elements. Heterogeneity was created by distributing low-permeability elements within a background of high-permeability elements. Three types of porous media were simulated by distributing the low-permeability elements in different patterns: random, regular, and aggregated, in which the low-permeability elements appeared as clusters within the domain. A one-dimensional flow field was established, and reference particles were introduced across the inlet to the domain. Schwartz investigated the applicability of the classical approach by computing the spatial variance of the particle distribution with time. The spatial variance increases linearly with time when the longitudinal dispersion coefficient is unique.

Schwartz found that the applicability of the classical approach was dependent on the type of porous medium. In a stratified medium, created by generating three layers of low permeability elements within the domain, Schwartz found that a unique dispersion coefficient did not exist. A unique dispersion coefficient was approached as the number of elements within the domain increased and as the distribution pattern for the low-permeability elements became random. The longitudinal dispersion coefficient increased with increased permeability contrast and with increased randomness of the low permeability elements.

In general, the Fickian longitudinal dispersion coefficient computed by Schwartz (1977) overestimated the spatial variance of the particle distribution in early stages of dispersion, and underestimated it in later stages for a given realization. The particles moved with about the

same velocity in the early stages of dispersion so the rate of dispersion was small. However, with time, the heterogeneities caused the particles to move at different rates and, consequently, the spatial variance increased rapidly.

Smith and Schwartz (1980,1981a,b) extended the earlier work of Schwartz (1977). A two-dimensional porous medium domain was created using a first-order nearest-neighbor stochastic model in which the permeabilities of neighboring elements were spatially correlated. The details are given in Smith and Schwartz (1980). A hybrid deterministic-probabilistic method governed the movement of tracer particles. The deterministic stage was similar in concept to Warren and Skiba (1964). The probabilistic stage accounted for the effects of microscopic dispersion such as molecular diffusion.

Two tests were performed to evaluate if macroscopic dispersion could be represented by a unique longitudinal dispersion coefficient. The first test, identical to Schwartz (1977), investigated the linear variation in the spatial variance with time. A stronger condition for Fickian dispersion is that the spatial particle distribution should be Gaussian. To test for this requirement, the chi-square test was used.

In a Monte Carlo simulation totaling 300 realizations, Smith and Schwartz found that less than 18 percent of the realizations satisfied the two criteria for Fickian dispersion. Smith and Schwartz stated the condition necessary for Fickian dispersion:

"Fundamental to the diffusional representation of dispersion (Scheidegger,1964) is the assumption that as the total particle travel time becomes much greater than the time interval during which its successive local velocities are still correlated, then the total displacement may be considered as the sum of a large number of elementary displacements statistically independent of one another."

The total particle travel times were too short in the Monte Carlo simulation for the Fickian representation of dispersion to be applicable. Multimodal particle distributions found in many realizations clearly showed that successive local velocities were correlated. Particles traveled along preferred pathways and thus, were sampling only a portion of the velocity field. Consequently, connected pathways of rapid movement/high permeability and slow movement/low permeability developed within the domain.

Stochastic dispersion studies have demonstrated that global dispersion in heterogeneous porous media is characterized by an initial period of non-Fickian dispersion. The spatial variance of the solute plume spreads very rapidly in this initial period such that an equivalent classical dispersion coefficient would have to increase with time in order to characterize dispersion. These conclusions agree with observations made from field tests. After this initial period, Fickian dispersion may occur depending on the statistical properties of the velocity field. Fickian dispersion is likely to occur in a porous medium with a small scale of heterogeneity and a random velocity field.

2.3. DISCRETE MECHANICAL TRANSPORT MODELS FOR FRACTURED ROCK MASSES

Three discrete mechanical transport models for fractured rock masses are reviewed in this section. Detailed discussions are presented on the approaches used to simulate mechanical transport in each model. A new discrete mechanical transport model will be developed in Chapter 4 that is based on fundamental principles of fluid flow.

Neretnieks (1980) analyzed mechanical transport in a set of parallel, planar, and continuous fractures. A one-dimensional flow field was established, parallel to the orientation of the set, by a uniform hydraulic gradient. Fracture apertures were distributed according to a known probability distribution. The velocity in each fracture was assumed equal to the average cross-sectional velocity which was proportional to the cubed power of the aperture. Thus, mechanical transport was caused by the variation in fracture velocities produced by the aperture distribution. The composite concentration distribution at the exit end of the problem domain was analytically solved for both a step and a pulse injection of concentration across the inlet to the domain. Neretnieks found that Fickian macroscopic transport did not occur for this fracture system because the longitudinal dispersion coefficient increased with sample size. This result was not surprising since this fracture system was equivalent to a stratified porous medium. The work of Neretnieks considered fractures which had no interactions with the other fractures

in the system. The following two studies dealt with more realistic networks of intersecting fractures.

In a series of four related papers (Castillo et al., 1972; Krizek et al., 1972; Karadi et al., 1972; and Krizek et al., 1973), a numerical model was developed to simulate transport in a fracture system consisting of two sets of parallel, planar, and continuous fractures of constant aperture and spacing. The principles incorporated in their model can be understood by following the migration of solute as it flows through the fracture system. Mechanical transport governs the movement of solute within an element:

$$\frac{\partial c}{\partial t} + u(\eta) \frac{\partial c}{\partial \xi} = 0$$

When solute exits an element at a node, it encounters solute from other elements flowing into the node. Krizek et al. used either the complete mixing condition or the partial mixing condition to distribute the inflowing solute to the outflow elements. In the complete mixing condition, all outflow elements receive the same concentration given by :

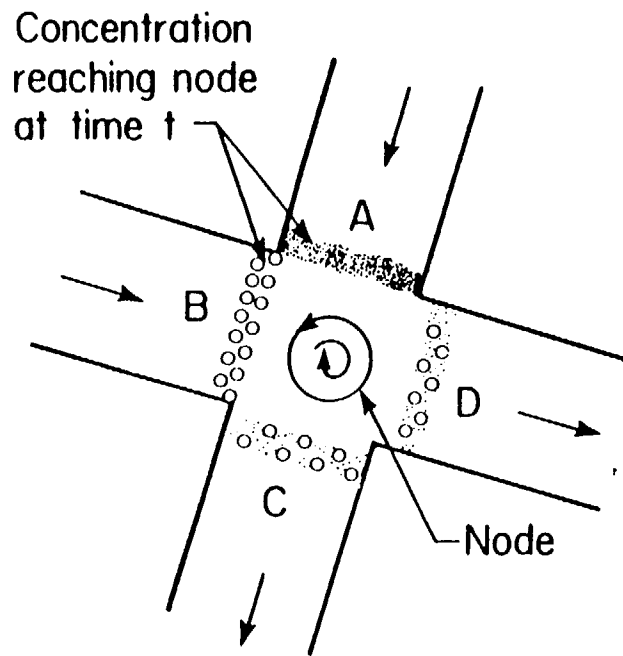
$$c_o(t) = \frac{\sum_i \int_0^b u_i(\eta) c_i(\eta, t) d\eta}{Q_N}$$

where the summation of i is for all inflow elements. The complete mixing condition is illustrated in Figure 2-2a.

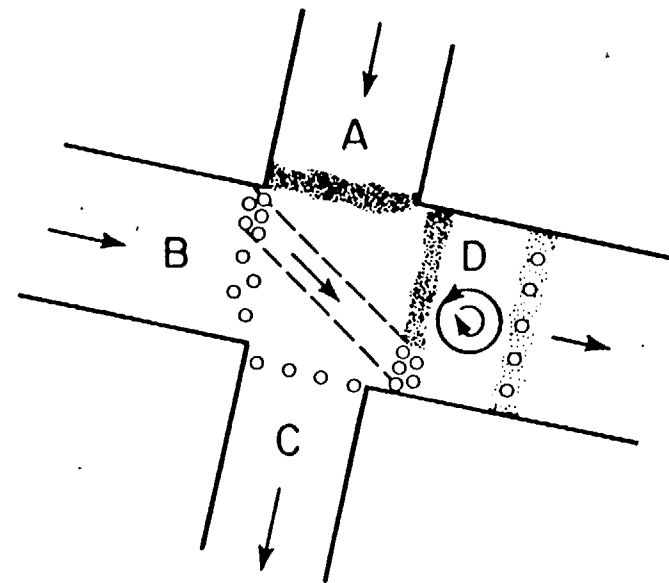
The partial mixing condition is illustrated in Figure 2-2b. Fluid enters the node from elements A and B, and exits through elements C and D. Element D is a large element such that the flow rate in element D consists of the total flow rate in element A and part of the flow rate in element B. The widths in elements A and B occupied by the flux flowing into element D are determined, and the mass of solute entering the node from these zones is calculated. This mass of solute is then distributed uniformly across the entrance to element D.

The travel time within a node is usually very short, such that the solute is primarily advected by the flow in a node. The physics of laminar flow suggest that the two mixing conditions above would not properly simulate transport within a node. In laminar flow, the fluid moves in layers, one layer flowing smoothly over the adjacent layers. A flow lamina cannot

→ Arrow indicates direction of flow



(a) Complete mixing condition



(b) Partial mixing condition

Figure 2-2 Graphical Representation of Mixing Conditions at a Node.

XBL 833-8772

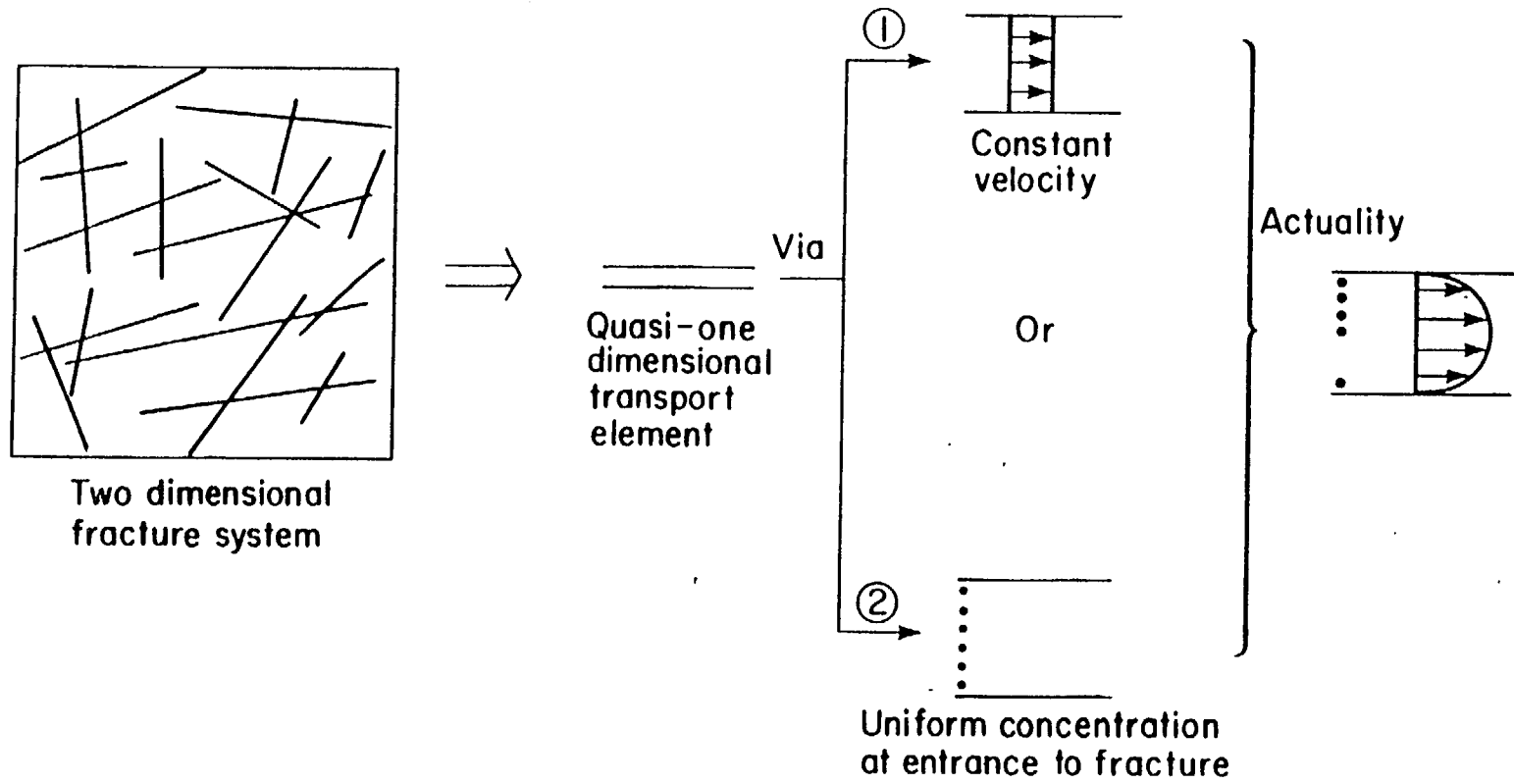
cross over into another layer, as assumed in the above model, to develop uniform concentrations across the entrance of outflow elements. Although laboratory experiments performed by Krizek et al. (1972) concluded that the complete mixing is valid for laminar flow, their experiments were not conclusive. These experiments were limited to the situation in which there was only one inflow element and all outflow elements had nearly identical flow rates. A more general set of experiments should be considered which involves more than one inflow element, with unequal flow rates and unequal concentrations in both inflow and outflow elements. Wilson (1970) conducted such an experiment using capillary tubes for Reynolds number on the same order as the experiments by Krizek et. al (1972) and demonstrated that fluid still flows within layers at intersections when the flow is laminar.

Schwartz et al. (1981) stochastically generated two orthogonal fracture sets in a rectangular domain. The number of fractures in each set within the domain was controlled by the areal density (the number of fractures per unit area). The fracture centers were randomly distributed in the domain and the fracture lengths and apertures were generated from exponential and log-normal distributions, respectively. Schwartz et al. avoided a major simplification made in previous transport studies of fracture systems by using fractures of finite length. Impermeable boundaries were created on two opposite sides of the rectangular domain and the two remaining sides consisted of constant-head boundaries. Tracer particles were assumed to propagate at a constant velocity within the elements and were also assumed to be completely mixed at the nodes, even though the flow was laminar. Molecular diffusion was considered to be negligible within a fracture and therefore, was not modeled.

Schwartz et al. (1981) found that the spatial particle distribution in the average direction of flow was non-Gaussian and positively skewed. The skewness is attributed to a combination of channels of rapid movement oriented in the direction of flow, and channels of slow movement oriented normal to the direction of flow. The bulk of the fluid moves in the direction of gradient, and most of the particles travel in this direction. However, as time proceeds, the probability of a particle flowing into a slow channel increases. As particles move through the slow

channels, an asymmetrical particle distribution develops.

Consequently, previous mechanical transport models simulate transport in two-dimensional fracture networks by linking together one-dimensional or quasi-one-dimensional mechanical transport models for each element in the network as shown in Figure 2-3. The model is one-dimensional because a constant velocity is assumed to exist in the element or a nodal mixing condition which distributes concentration uniformly across the entrance of out-flowing elements is used. Completely or partially neglecting the effects of the velocity distribution across a fracture ignores an important microscopic mechanism of mechanical transport. The nodal mixing conditions used in these models are not based on the physics of laminar flow. In laminar flow, the fluid moves in layers, one layer flowing smoothly over the adjacent layers. A flow lamina cannot cross over another layer, as assumed in these models, by uniformly distributing concentration across the entrance of the outflow elements at a node. A two-dimensional mechanical transport model for each element is developed in Chapter 4 to provide a more realistic understanding of mechanical transport.



XBL-829-4506

Figure 2-3 Modeling Conditions Used in Earlier Mechanical Transport Models for Fracture Networks.

CHAPTER 3

THEORETICAL DEVELOPMENT

3.1. INTRODUCTION

Transport is considered at the microscopic, pore, and continuum levels in the first part of this chapter. Transport is modeled within a very small differential control volume at the microscopic level. Consequently, all transport processes are accurately modeled at this level. In porous media modeling, it is extremely difficult to use a microscopic transport model because of the complex flow pattern within the pores and the irregular structure of the pores. The only practical way of modeling transport in a porous medium is to treat the medium as a continuum and analyze the macroscopic behavior of the medium, disregarding the detailed behavior occurring within the pores. Both rock and fluid properties vary smoothly and continuously throughout the continuum as there is no physical boundary between solid and fluid phases. However, the concepts of continuum modeling can lead to difficulties in accurately modeling transport processes. Transport models are derived at the microscopic, pore, and continuum levels to demonstrate the assumptions and simplifications that are needed to model transport at each level.

No experimental technique is available which can evaluate dispersion in anisotropic porous media, and consequently, an anisotropic medium is treated as an equivalent isotropic medium (Anderson, 1979). This simplification assumes that there is no directional dependence in each transport parameter. A set of tracer experiments will be presented in this chapter that allow the directional characteristics of mechanical transport for anisotropic media be evaluated. The design, execution, and determination of mechanical transport parameters from the set of experiments are presented in this chapter.

A discrete model is developed in Chapter 4 to simulate fluid flow and mechanical transport in fractured rock masses. An important objective of this research is to determine if a fracture system can be treated as an equivalent porous medium continuum. The conditions

required for equivalent porous medium behavior are discussed below. Tests are developed, based on these conditions, to detect when a fracture system can be treated like an equivalent porous medium. These tests are incorporated into the numerical model developed in Chapter 4.

3.2. MICROSCOPIC LEVEL TRANSPORT

To develop a transport model at the microscopic level, a conservative solute with the same viscosity and density as the ambient fluid is migrating in a porous medium. The model is derived below, taking into account the cubic differential control volume shown in Figure 3-1. The two microscopic transport processes occurring are molecular diffusion and advection. Molecular diffusion is the mixing caused by the random motion of solute molecules produced by the concentration gradient. Advective transport is caused by the movement of fluid within the pores. The modeling of each transport process at the microscopic level is presented below.

The diffusive mass flux is defined as the mass of solute diffusing across a unit area in a unit time. The diffusive mass flux is governed by Fick's law which states:

$$\vec{d} = -D\nabla c$$

The net mass flux diffused into the control volume in the x direction in Figure 3-1 is equal to:

$$\left[\text{mass flux diffused into face 1} \right] - \left[\text{mass flux diffused out of face 2} \right]$$

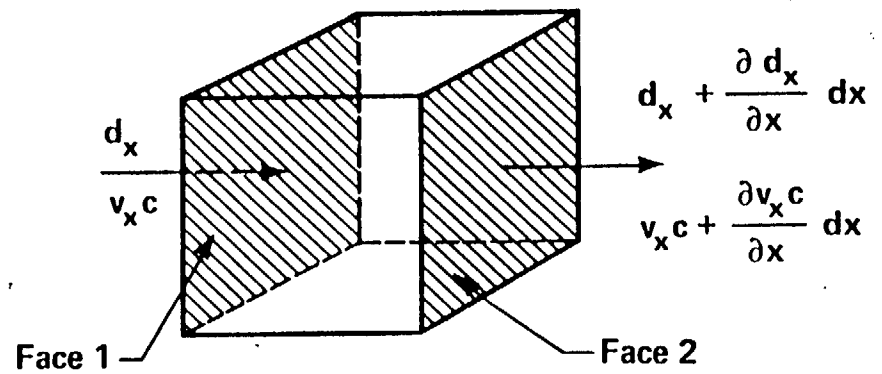
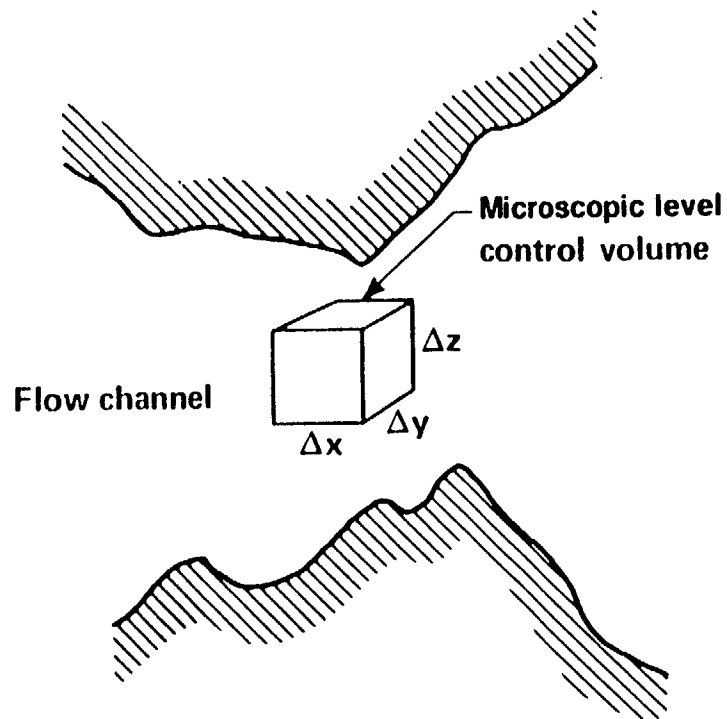
which is equal to:

$$\left[d_x - \left(d_x + \frac{\partial d_x}{\partial x} dx \right) \right] dydz = \frac{\partial \left(D \frac{\partial c}{\partial x} \right)}{\partial x} dx dy dz$$

Similarly, the net mass flux diffused into the control volume in the y and z directions are, respectively:

$$\frac{\partial \left(D \frac{\partial c}{\partial y} \right)}{\partial y} dy dx dz \quad \text{and} \quad \frac{\partial \left(D \frac{\partial c}{\partial z} \right)}{\partial z} dz dx dy$$

The advective mass flux is defined as the mass of solute advecting across a unit area in a unit time. The total mass advected into the control volume per unit time across face 1 is equal to the advective mass flux at face 1 ($v_x c$) multiplied by the area of face 1:



XBL 827-7149

Figure 3-1 Modeling of Transport Within a Control Volume at the Microscopic Level.

$$(v_x c) dydz$$

Following a similar procedure for net advective transport as demonstrated for diffusive transport, the net mass flux advected into the control volume in the x, y, and z directions are, respectively:

$$-\frac{\partial (v_x c)}{\partial x} dx dy dz, \quad -\frac{\partial (v_y c)}{\partial y} dx dy dz, \quad -\frac{\partial (v_z c)}{\partial z} dx dy dz.$$

The mass conservation of solute within the control volume states that:

$$\left[\begin{array}{l} \text{net mass flux of} \\ \text{solute diffused} \\ \text{into control volume} \end{array} \right] + \left[\begin{array}{l} \text{net mass flux} \\ \text{advected into} \\ \text{control volume} \end{array} \right] = \left[\begin{array}{l} \text{net accumulation of} \\ \text{solute in control} \\ \text{volume per unit time} \end{array} \right]$$

Substituting the appropriate terms into the equation above and simplifying yields:

$$D \nabla^2 c - \left(\frac{\partial v_x c}{\partial x} + \frac{\partial v_y c}{\partial y} + \frac{\partial v_z c}{\partial z} \right) = \frac{\partial c}{\partial t} \quad (3.1)$$

which is the partial differential equation governing transport at the microscopic level. The first term on the left hand side of equation 3.1 is called the dispersive term and the bracketed term is called the advective term. Equation 3.1 is extremely difficult to solve for a porous medium because of the complicated flow pattern within the pores and the complex boundary conditions arising from the random geometry of the pores. Therefore, the continuum approach is almost exclusively used to model porous media transport. The analysis of the microscopic flow field within the pores is avoided in the continuum approach because macroscopic properties of the medium are evaluated. Also, there is no need to define the detailed geometry of the pores because both rock and fluid properties vary continuously throughout the continuum, since there is no physical boundary between fluid and solid phases. Before the transport model for porous media is developed, transport models are discussed for smaller scale transport within a single flow conduit (i.e. pipe or a single conductive pore within a porous medium). These pore transport models must simulate the velocity field within a pore.

3.3. PORE TRANSPORT MODELS

The first pore transport model presented is the dispersed plug flow model. The flow velocity in equation 3.1 is replaced by the average cross-sectional velocity in the dispersed plug flow

model. This means that in this model solute is advected at the same rate across the cross section of a flow channel. Consequently, the dispersive term in the dispersed plug flow model must account for both molecular diffusion and mechanical dispersion produced by the cross-sectional velocity distribution. Since dispersion is greater in the longitudinal direction than in the transverse direction, because of mechanical dispersion, the constant coefficient, D , in equation 3.1 is replaced by a second-order dispersion tensor $[D_F]$ to account for the anisotropic rate of dispersion. Thus, the apparent simplification made to the advective term is somewhat negated by the added complexity introduced into the dispersive term.

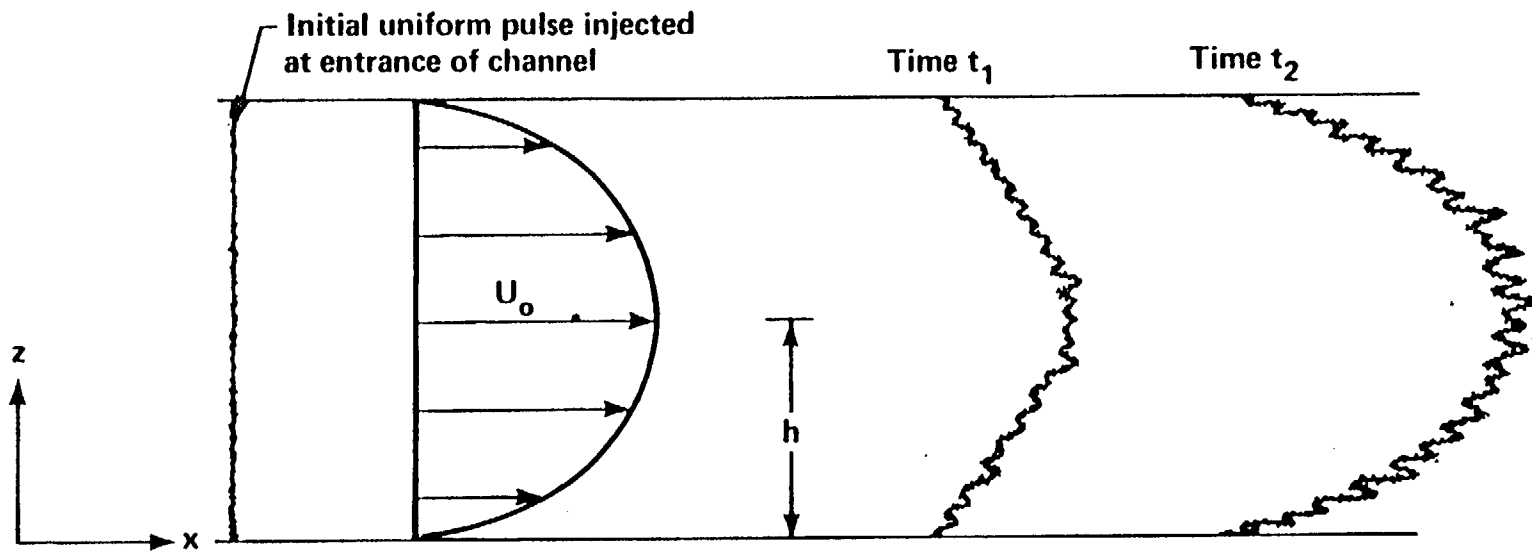
Consider, for example, transport in a parallel plate conduit with the channel axis corresponding to the x direction as shown in Figure 3-2. The dispersed plug flow model for the parallel plate conduit is:

$$\frac{\partial c}{\partial t} + \bar{v} \frac{\partial c}{\partial x} = \nabla \cdot ([D_F] \nabla c)$$

The second pore transport model presented is the axial dispersed plug flow model. The axial dispersed plug flow model makes an additional simplification to the dispersed plug flow model by assuming that concentration is uniformly distributed across each section such that no concentration gradient exists in the transverse direction. Consequently, dispersion occurs only in the longitudinal direction and the dispersive coefficient, which is multiplied by $\nabla^2 c$ in the dispersive term, is a scalar, D_L . The axial dispersed plug flow model for transport in a parallel plate conduit is:

$$\frac{\partial c}{\partial t} + \bar{v} \frac{\partial c}{\partial x} = D_L \frac{\partial^2 c}{\partial x^2}$$

The axial dispersed plug flow model cannot simulate transport during the initial period of transport. For example, consider the laminar flow problem of transport in a parallel plate conduit when a pulse of solute is instantaneously injected uniformly across the entrance to the conduit, as shown in Figure 3-2. The axial dispersed plug flow model is applicable when there is no concentration gradient in the transverse direction. In the early stages of transport, the solute distribution will violate this condition because advective transport is dominant, as shown in Figure 3-2. However, as time increases, molecular diffusion slowly reduces the concentration



XBL 827-7181

Figure 3-2 Early Stages of Transport When a Uniform Pulse is Injected Between Two Parallel Plates Under Laminar Flow Conditions.

gradient in the transverse direction. Gill et al. (1969) used a numerical technique to show that, for times greater than h^2/D , the axial dispersed plug flow is applicable.

Gill et al. (1969) demonstrated that the axial dispersed plug flow model cannot simulate early-time transport. The averaging of the flow velocity and avoidance of transverse dispersion indicate that a start-up time is required before the axial dispersed plug flow model is applicable. This initial period is similar to the period of non-Fickian dispersion commonly observed in porous media field tests. The cause of this period of non-Fickian dispersion in porous media is related to the macroscopic averaging of properties in the transport model for porous media. The derivation of the porous medium transport model is presented in the next section.

3.4. POROUS MEDIA TRANSPORT MODEL

The transport model for porous media is derived by considering mass conservation within a cubic continuum control volume much larger than a pore consisting of solid and fluid phases. The dimensions of this continuum and the coordinate system used in this derivation will be identical to those shown in Figure 3-1. In a continuum, fluid and solid phases exist at every point within the medium such that both rock and fluid properties are smooth and continuous functions throughout the medium. The porous media transport model consists of an advective transport process coupled with a dispersive transport process. The advective transport process will be modeled first.

The mass of solute advected into the control volume per unit time across face 1 is $Q_x c$. The flow rate Q_x is usually expressed in terms of the specific discharge. The specific discharge is defined as the flow rate crossing a unit area of porous medium continuum and is governed by Darcy's law which states:

$$\bar{q} = \frac{\rho g}{\mu} [k] \bar{J} = [K] \bar{J}$$

The specific discharge is often misconstrued as representing a type of velocity, because the dimensions of \bar{q} are the same as the dimensions for velocity. However, the specific discharge is the quantity of fluid flowing across a unit area per unit time, and should never be confused with velocity. The flow rate crossing a given area of porous medium written in terms of the

specific discharge is:

$$Q = \bar{q} \cdot \bar{A} = [K] \bar{J} \cdot \bar{A}$$

Consequently, the mass of solute advected into the control volume across face 1 per unit time can be expressed as:

$$(q_x dydz)c \tag{3.2}$$

It is apparent from equation 3.2 that the transport model for porous media can be classified as a dispersed plug flow model because solute is being advected across face 1 into the control volume at a constant rate of $q_x dydz$. In reality, solute is advected into the control volume from the pores at different rates. The microscopic variations in the advective rate of transport are accounted for in the dispersive term.

The net mass flux advected into the control volume in the x direction is:

$$\left[q_x c - \left(q_x c + \frac{\partial q_x c}{\partial x} dx \right) \right] dydz = - \frac{\partial (q_x c)}{\partial x} dx dydz$$

Similarly, the net mass flux advected into the control volume in the y and z directions are, respectively:

$$- \frac{\partial (q_y c)}{\partial y} dy dx dz \quad \text{and} \quad - \frac{\partial (q_z c)}{\partial z} dz dy dx$$

Advective transport alone causes no distortion in the shape of a pollutant plume. The distortion and spreading of a plume is caused by microscopic variations in the advective rate of transport, termed mechanical transport, and by molecular diffusion. Thus, the dispersive term accounts for the combined interaction of mechanical dispersion and molecular diffusion known as hydrodynamic dispersion.

The principle microscopic mechanisms of mechanical transport, as discussed in section 2.2.2 and illustrated in Figure 2-1 are: the velocity distribution across a pore which causes a fluid particle to move faster in the center than along the sides of the pore; the flow rate variation from one channel to another which dictates the direction a fluid particle will travel; and the random geometry of the pores which causes a particle to meander through the pore region. The mechanical dispersive flux is the mass of solute mechanically transported across a unit area

in a unit time. The mass flux of solute mechanically dispersed into the control volume across face 1 is:

$$m_x \left(\phi_R dydz \right)$$

where ϕ_R is the rock effective porosity defined as the conductive void volume per volume of rock. The net mass flux mechanically dispersed into the control volume in the x direction is:

$$-\frac{\partial m_x}{\partial x} \phi_R dx dy dz$$

Similarly, the net mass flux mechanically dispersed into the control volume in the y and z directions are, respectively:

$$-\frac{\partial m_y}{\partial y} \phi_R dx dy dz \quad \text{and} \quad -\frac{\partial m_z}{\partial z} \phi_R dx dy dz$$

The Fickian expression developed by Scheidegger (1961) is commonly used to represent the mechanical dispersive flux:

$$m_i = -M_{ij} \frac{\partial c}{\partial x_j}$$

where

$$M_{ij} = \alpha_{ijmn} \frac{v_m v_n}{V L I N}$$

The fourth-order geometric dispersivity tensor has a total of 81 components. Scheidegger showed that $[\alpha]$ possesses two symmetric properties, namely:

$$\alpha_{ijmn} = \alpha_{ijnm} \tag{3.3}$$

and

$$\alpha_{ijmn} = \alpha_{jimn} \tag{3.4}$$

so that there are 36 independent components in $[\alpha]$.

Presently, there is no experimental or numerical technique that will allow evaluation of all 36 independent components in $[\alpha]$ for an anisotropic porous medium. Consequently, an anisotropic porous medium is generally treated as an equivalent isotropic medium because there are only two measurable components in $[\alpha]$ for an isotropic medium: 1) the longitudinal dispersivity α_L , and 2) the transverse dispersivity α_T . The Fickian mechanical dispersion tensor for an isotropic medium with the direction of flow corresponding to the x direction is:

$$[M] = \begin{bmatrix} \alpha_1 V_{LIN} & 0 & 0 \\ 0 & \alpha_1 V_{LIN} & 0 \\ 0 & 0 & \alpha_1 V_{LIN} \end{bmatrix}$$

The mass flux diffused into the control volume is governed by Fick's law. Fluid flows along nonlinear paths in a porous medium due to the irregular geometry of the pores as shown in Figure 3-3 for a single pore. However, the concentration gradient is considered in the linear directions aligned in the directions of the cartesian coordinate system (x,y,z). To account for the nonlinear path of fluid movement in the diffusive mass flux, the free solution molecular diffusion coefficient, D, is divided by the tortuosity (Gilham and Cherry, 1982). The tortuosity is defined as the ratio of the mean path length of fluid flow to the linear length of travel. Thus the diffusive mass flux is:

$$\vec{d} = -\frac{D}{\tau} \nabla c = -D_0 \nabla c$$

The total void volume in a porous medium consists of isolated zones, dead-end spaces, and conductive void regions. Molecular diffusion occurs within the dead-end and conductive void spaces. However, mechanical transport occurs only within the conductive void volume. The conductive void volume and total void volume are assumed to be equal in porous media transport modeling because of the difficulty of accurately differentiating the three void spaces. This assumption is generally valid because porous media are commonly highly interconnected such that dead-end zones and isolated segments usually occupy only a small portion of the total void volume. Thus, the net mass flux diffused into the control volume in the x, y, and z directions are, respectively:

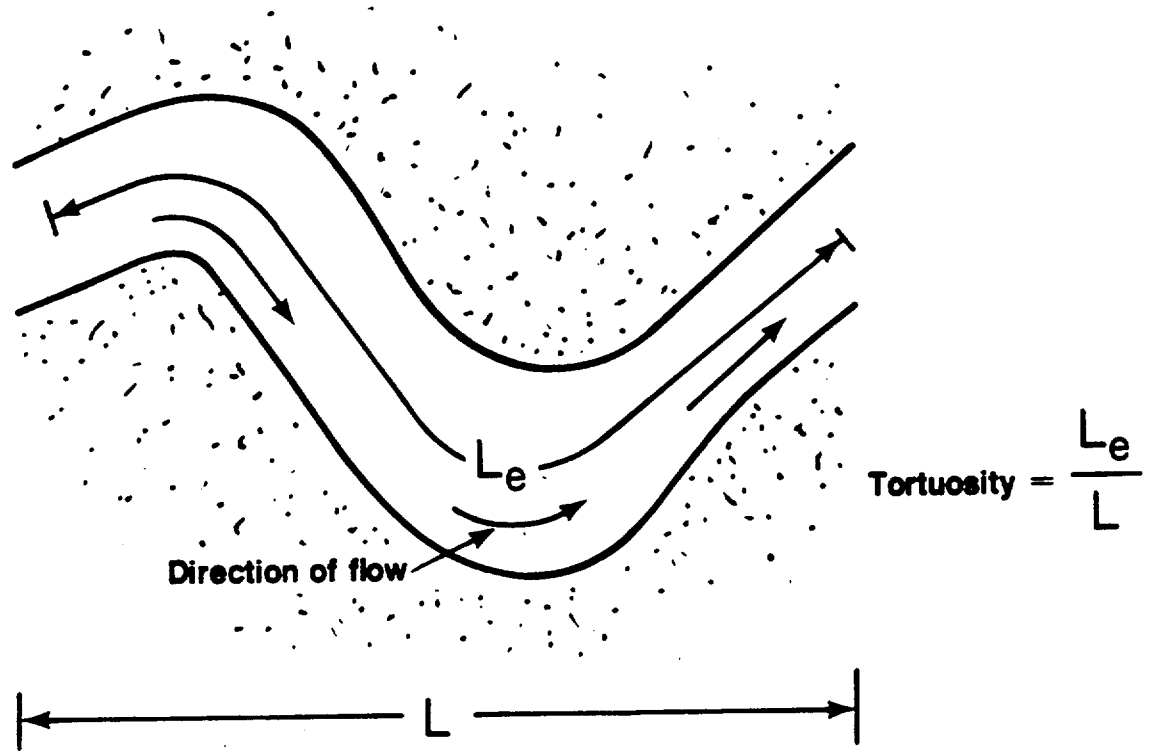
$$D_0 \frac{\partial^2 c}{\partial x^2} \phi_R dx dy dz, \quad D_0 \frac{\partial^2 c}{\partial y^2} \phi_R dx dy dz, \quad D_0 \frac{\partial^2 c}{\partial z^2} \phi_R dx dy dz$$

The net increase in the mass of solute within the control volume per unit time is:

$$\frac{\partial c}{\partial t} \phi_R dx dy dz$$

The mass balance in the control volume states that:

$$\left[\begin{array}{l} \text{net mass flux of} \\ \text{solute dispersed} \\ \text{into control volume} \end{array} \right] + \left[\begin{array}{l} \text{net mass flux} \\ \text{advected into} \\ \text{control volume} \end{array} \right] = \left[\begin{array}{l} \text{net accumulation of} \\ \text{solute in control} \\ \text{volume per unit time} \end{array} \right]$$



XBL 838-554

Figure 3-3 Tortuosity for a Single Pore.

which, when substituted by the appropriate terms yields:

$$\frac{\partial c}{\partial t} + \frac{1}{\phi_R} \left(\frac{\partial q_x c}{\partial x} + \frac{\partial q_y c}{\partial y} + \frac{\partial q_z c}{\partial z} \right) = D_o \nabla^2 c - \nabla \cdot \bar{m} \quad (3.5)$$

Equation 3.5 represents molecular diffusion and mechanical transport. The two terms on the right hand side of equation 3.5 constitute the dispersive term, while the bracketed term on the left hand side is the advective transport component.

This particular research is concerned with pure mechanical transport. The governing mechanical transport equation is:

$$\frac{\partial c}{\partial t} + \nabla \cdot \bar{m} + \frac{1}{\phi_R} \left(\frac{\partial q_x c}{\partial x} + \frac{\partial q_y c}{\partial y} + \frac{\partial q_z c}{\partial z} \right) = 0 \quad (3.6)$$

The three primary reasons for investigating mechanical transport are: (1) an insufficient understanding of hydrodynamic dispersion because no solution is available for the equation governing transport in an anisotropic medium, (2) the use of mechanical transport parameters, such as tortuosity, in modeling hydrodynamic dispersion, and (3) the need to determine when fracture systems can be treated like equivalent porous media. New principles and techniques will be introduced such that directional mechanical transport parameters can be evaluated for anisotropic media. The directional characteristics of hydraulic effective porosity will be used to develop the conditions under which fracture systems exhibit porous media equivalence. Consequently, the investigation of the fundamental mode of mechanical transport will lead to a better understanding of dispersion in all permeable media.

A series of tracer experiments must be conducted to evaluate directional mechanical transport for anisotropic porous media. The operation of the set of tracer experiments is discussed in two parts. First, two key steps in designing the tracer experiment are discussed: the proper flow field to use in a tracer experiment, and the appropriate test section to measure mechanical transport from a tracer experiment. Then, the execution of the set of tracer experiments is discussed.

3.5. PROPER FLOW FIELD AND APPROPRIATE TEST SECTION USED IN A TRACER EXPERIMENT

Two key steps in designing a tracer experiment to measure mechanical transport are: 1) selecting the proper flow field to use in the experiment and; 2) determining the appropriate test section within the sample in which to measure mechanical transport. The macroscopic flow characteristics within the flow region must be consistent in order for general mechanical transport properties to be measured from a tracer experiment. The flow characteristics are consistent when the flow field is uniform such that the specific discharge is constant throughout the flow region. If \bar{q} varies from point to point in the medium, equation 3.6 becomes nonlinear and difficult to solve.

To establish this desired flow system, certain hydraulic boundary conditions must be maintained on the flow region. Figure 3-4 illustrates the hydraulic boundary conditions that are designed to create a uniform flow field for an anisotropic, homogeneous porous medium. First, as shown in Figure 3-4a, constant hydraulic heads of H and 0 , respectively, are fixed on sides 2 and 4 of the flow region. Then, constant hydraulic gradients are maintained along sides 1 and 3. A constant hydraulic gradient in the flow field is needed to guarantee that \bar{q} is uniform throughout the flow region in accordance with Darcy's law.

Figure 3-4 also illustrates how flow net theory can be used to describe the flow field in a homogeneous, anisotropic porous medium. Figure 3-4b shows the flow net in the transformed isotropic space (Freeze and Cherry, 1979, pp. 174-178), and Figure 3-4c shows the uniform flow field for the anisotropic medium. The direction of flow is parallel to the streamlines and the hydraulic gradient is normal to the equipotential lines.

The proper test section within the flow region to conduct measurements of mechanical transport must be selected. The tracer experiment will monitor the detailed movement of fluid that enters the flow region on side 2 in Figure 3-4a, and exits on side 4. In the proper test section, the linear length of travel is constant for the fluid which flows continuously between sides 2 and 4. This requirement guarantees that mechanical transport properties are measured from

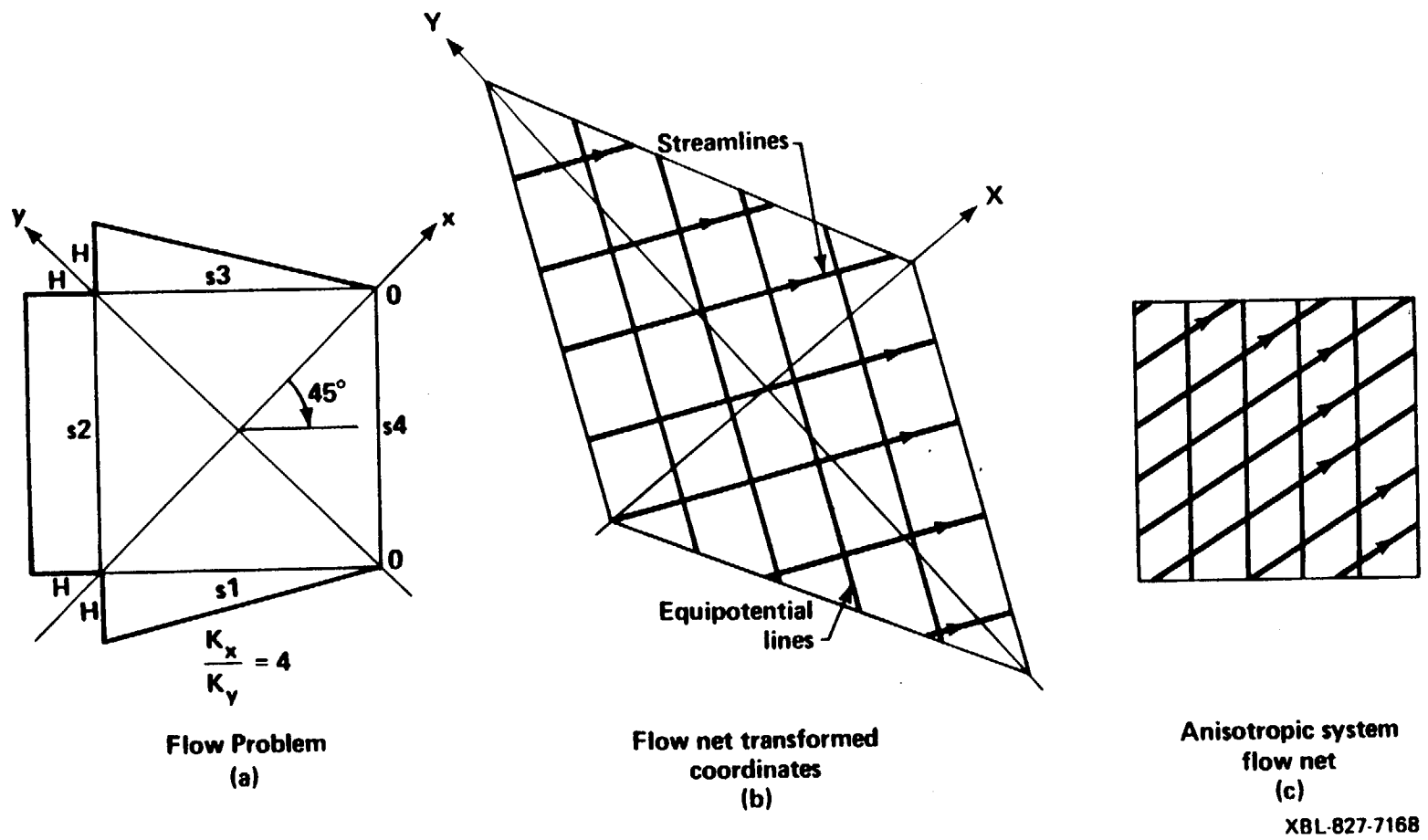


Figure 3-4 Determination of the Flow Field for an Anisotropic Porous Medium With a Constant Hydraulic Gradient Using Flow Net Theory.

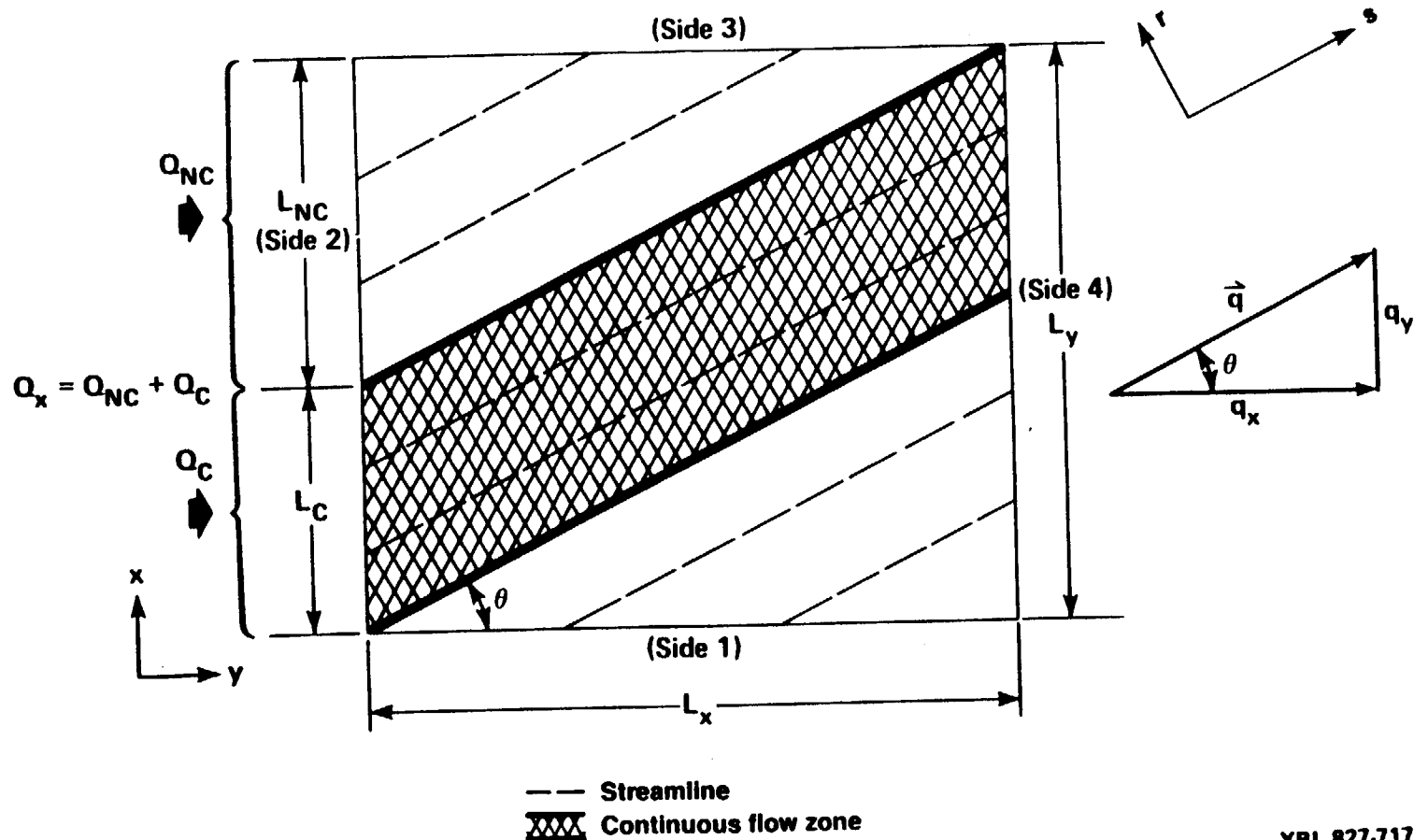
fluid which has traveled over the same linear distance. This linear length of travel is equal to the length of a streamline that begins on side 2 and ends on side 4 (Figure 3-4c). The linear travel length is constant within the cross-hatched area between sides 2 and 4 in Figure 3-5. Consequently, measurements of mechanical transport can be conducted in this cross-hatched zone called the test section. Thus, once the hydraulic boundary conditions have been established as illustrated in Figure 3-4a, measurements of mechanical transport can be made within the cross-hatched area shown in Figure 3-5.

3.6. EXECUTING THE SET OF TRACER EXPERIMENTS TO MEASURE DIRECTIONAL MECHANICAL TRANSPORT

This section describes the procedure for executing a set of tracer experiments that will allow evaluation of directional mechanical transport for anisotropic porous media. The first step in this procedure sets up a tracer experiment. This step is initiated by selecting a particular orientation of the porous medium to conduct the tracer experiment (Figure 3-6a). Next, the hydraulic boundary conditions shown in Figure 3-4a are applied to a flow region aligned in this direction to create the desired uniform flow field.

In the second step, the tracer experiment is performed by monitoring the detailed movement of fluid within the cross-hatched test section shown in Figure 3-5. This tracer experiment is numerically simulated in this research, but the same task may be performed experimentally by instantaneously injecting non-diffusive, dyed water uniformly across side 2 of the flow region as shown in Figure 3-6a. The dyed water will flow to side 4 only if it travels within the test section. The breakthrough curve for the fluid flowing in the test section is then measured by recording the concentration of dyed water on side 4 as illustrated in Figure 3-6a. Steps 1 and 2 constitute the procedure for conducting a single tracer experiment. The measurements made from this tracer experiment correspond to a particular direction of flow B_1 (Figure 3-6b).

Step three begins the investigation of the directional nature of mechanical transport for the medium. In this step, the orientation of the porous medium is rotated as shown in Figure 3-6c and a second set of measurements of mechanical transport is made by repeating steps 1



XBL 827-7173A

Figure 3-5 Example of Groundwater Flow in an Anisotropic Porous Medium Showing a Cross-Hatched Zone Where Travel Length is Constant.

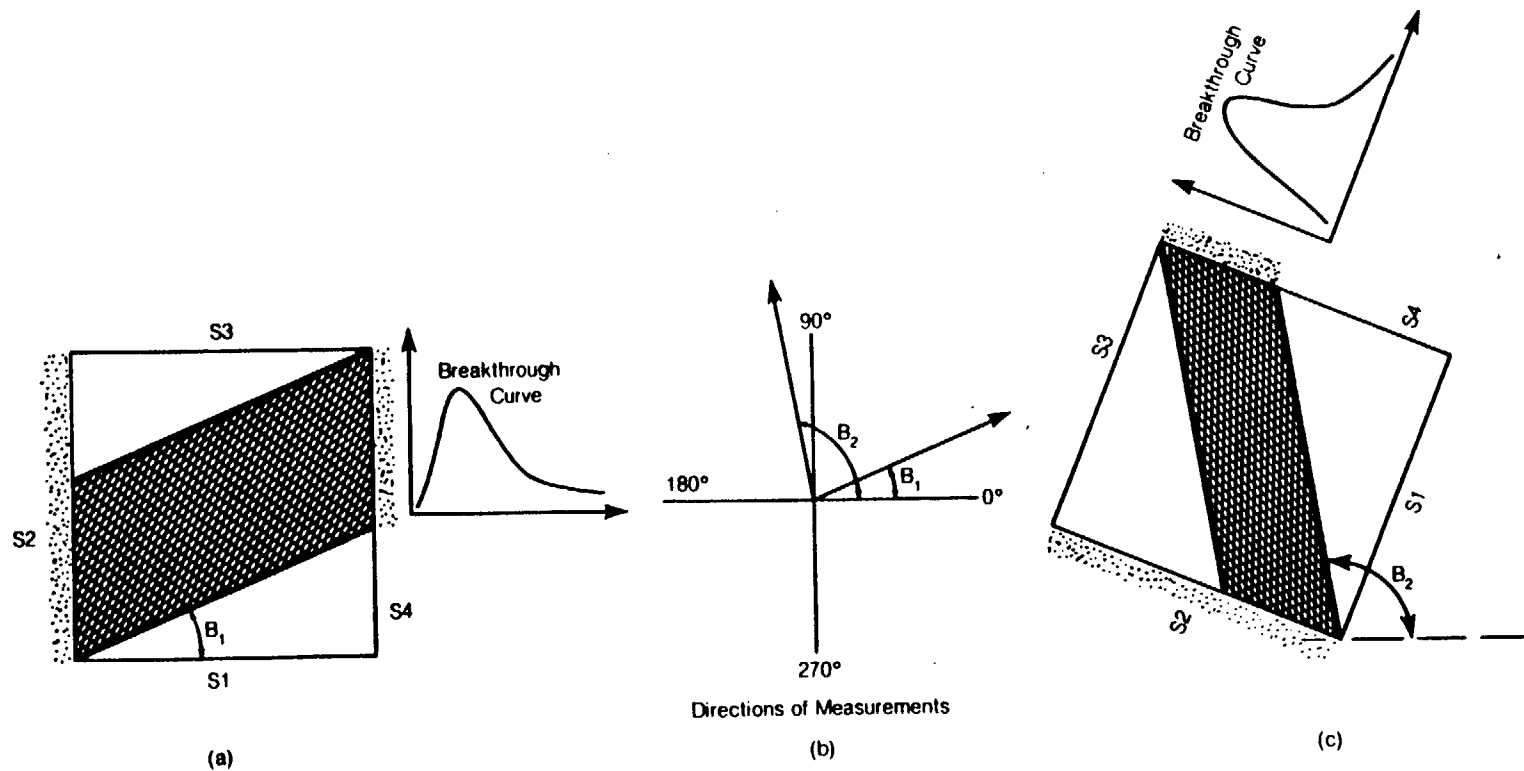


Figure 3-6 Procedure Used in Conducting a Set of Tracer Experiments to Measure Directional Mechanical Transport for an Anisotropic Porous Medium.

XBL 841-386

and 2 for the new direction of flow B_2 (Figure 3-6b). Next, step 3 is systematically repeated for selected orientations of the porous medium until a representative sample of directional mechanical transport for the medium is obtained. These steps constitute the execution of the set of tracer experiments needed to evaluate directional mechanical transport for an anisotropic porous medium.

3.7. MEASURING MECHANICAL TRANSPORT WITH THE BREAKTHROUGH CURVE

The purpose of this section is to show how mechanical transport parameters governing both the advective and dispersive processes in equation 3.6 can be evaluated from the tracer experiments described in the previous section. A tracer experiment is conducted by injecting a pulse of dyed water uniformly across side 2 of the flow region shown in Figure 3-5. At side 4, measurements are made of the concentration of dyed water in relation to time. The time distribution of the outlet concentration is known as the breakthrough curve or exit-age distribution for the test section. The statistical properties of the breakthrough curve are used to evaluate mechanical transport, as described below.

3.7.1. Mean of the Breakthrough Curve

The mean of the breakthrough curve is:

$$\bar{\tau} = \frac{\int_0^{\infty} \tau c \, d\tau}{\int_0^{\infty} c \, d\tau} = \int_0^{\infty} \tau E \, d\tau$$

The relationship between the mean of the breakthrough curve and the mean advective rate of movement q/ϕ_R is derived in this section. The area under the normalized breakthrough curve from t_1 to ∞ represents the percent of fluid residing in the test section longer than t_1 . The volumetric quantity of fluid flowing into the test section in the differential time interval dt is Qdt . Thus, the volume of fluid still residing in the test section that first entered t_1 earlier is:

$$Qdt \int_{t_1}^{\infty} E \, d\tau \quad (3.7)$$

The total conductive void volume in the test section is found by integrating equation 3.7 from t equals 0 to ∞ (i.e. for all fluid that enters the test section):

$$V_c = \int_0^{\infty} Q dt \int_1^{\infty} E d\tau = Q \int_0^{\infty} \int_1^{\infty} E d\tau dt \quad (3.8)$$

Reversing the order of integration in equation 3.8 yields:

$$V_c = Q \int_0^{\infty} \int_0^{\tau} E dt d\tau = Q \int_0^{\infty} E_{\tau} d\tau$$

So

$$\frac{V_c}{Q} = \int_0^{\infty} \tau E d\tau = \bar{\tau}$$

The average linear velocity is defined as the linear path length of fluid flow divided by the mean travel time. VLIN is an ideal velocity a fluid particle would have if it were constrained to move only in a straight path in the direction of flow:

$$VLIN = \frac{L}{\bar{\tau}} = \frac{QL}{V_c} = \frac{qAL}{V_c} = \frac{qV}{V_c} = \frac{q}{\phi_R} \quad (3.9)$$

The mean advective rate of movement will be determined from tracer experiments in this study because rock effective porosity is normally difficult to evaluate directly from laboratory experiments and because transport parameters should be predicted whenever possible from transport data (i.e. breakthrough curve).

The relationship in equation 3.7 assumes that the transport of all particles is characterized by a single breakthrough curve. In this equation, Q represents all fluid particles entering the test section per unit time and the breakthrough curve represents the probability distribution for residence in the test section for every particle. Since the time of residence in the test section for all particles is controlled by a single exit age distribution, fluid transport is homogeneous. Thus, ϕ_R will equal $q/VLIN$ when the transport of fluid particles is homogeneous.

Field and numerical studies indicate that transport may be inhomogeneous for homogeneous porous media. Childs et al. (1974) and Hoehn and Roberts (1982) presented field evidence of inhomogeneous transport in homogeneous porous media. Childs et al. used a detailed three-dimensional array of sampling points to monitor the movement of waste plumes in an operational homogeneous, sand aquifer. The measured concentration patterns showed that the waste plumes bifurcated, and moved along preferred pathways of travel that were not aligned in the direction of the regional flow. The conventional single plume model could not accurately characterize the pollutant migration and there was no indication as to the cause for the

bifurcation of the waste plumes. The study of Hoehn and Roberts (1982) found that in a vertically-homogeneous aquifer a two-domain model was needed to simulate transport. The domains in their model consisted of two separate zones (no interaction between zones) with vastly differing rates of movement. Hoehn and Roberts stated that no geological evidence supported the use of the two-domain model and noted that the two domains may be distinguishable only at the microscopic level.

Smith and Schwartz (1981a) conducted numerical mass transport studies for statistically-homogeneous porous media which were reviewed in section 2.2. In their Monte Carlo study, it was generally observed that, in a given realization, the bulk of the mass migrated along a definite path. This connected path linked together the high-permeable elements within the problem domain where the transport velocities were large. In some cases, the effects of the preferred paths of travel were clearly evident by bimodal breakthrough curves.

Thus, the following conclusions can be made. The actual rate of advection is controlled by the microscopic velocity field within the pores. If regions of vastly differing rates of movement or large variations in pore velocities exist in the medium, then transport is inhomogeneous. These contrasting domains of transport may be distinguishable only at the microscopic level.

The effect of inhomogeneous transport on the mean advective rate of transport is demonstrated by considering a test section consisting of two separate transport domains: a slow zone of movement and a fast zone of movement. The flow rate through the slow zone is QS . The particles flowing into the slow zone will produce a different breakthrough curve than the particles flowing into the fast zone. The mean of the breakthrough curve will be larger in the slow zone than in the fast zone, and the composite breakthrough curve for the test section is the sum of the breakthrough curves for the fast and slow zones. The total conductive void volume is given by:

$$V_c = QS \int_0^{\infty} E_{ST} d\tau + (Q-QS) \int_0^{\infty} E_{FT} d\tau$$

So,

$$\frac{q}{\phi_R} = \frac{L}{\frac{QS}{Q} \int_0^{\infty} E_{S\tau} d\tau + \frac{(Q-QS)}{Q} \int_0^{\infty} E_{F\tau} d\tau} \quad (3.10)$$

The mean of the composite breakthrough curve ($E = E_S + E_F$) is:

$$\bar{T} = \int_0^{\infty} \tau(E_S + E_F) d\tau$$

which is not equal to the denominator in equation 3.10. Therefore, the average linear velocity will not equal q/ϕ_R if preferential paths of movement exist in the test section.

The hydraulic effective porosity is defined to provide a general way of relating the actual rate of transport VLIN to the flow parameter q :

$$\phi_H = \frac{q}{VLIN} \quad (3.11)$$

In porous media transport models, the hydraulic effective porosity is usually assumed to be equal to ϕ_R or ϕ . The rock effective porosity is a stable rock property that does not vary with direction. The relationship indicated above is valid when transport is homogeneous. Field and numerical studies indicate that transport occurs along preferred paths of travel. When transport is inhomogeneous, the hydraulic effective porosity may deviate from the rock effective porosity. The deviation will increase as the number and size of the microscopic zones of contrasting movement increase. This research will investigate the directional nature of the hydraulic effective porosity for anisotropic media.

3.7.2. Variance of the Breakthrough Curve

The type of tracer experiment chosen in this research was carefully selected such that Fickian longitudinal mechanical transport can be evaluated from the variance of the breakthrough curve. The first objective of this section is to prove that longitudinal mechanical transport can be analyzed for the tracer test chosen in this study by developing the relationship for longitudinal mechanical transport. The second objective of this section is to show how the variance of the breakthrough curve can be used to evaluate longitudinal mechanical transport.

3.7.2.1. Longitudinal Dispersion for Pure Mechanical Transport

The equation governing longitudinal mechanical transport is derived in this section. It

will be shown that the mechanical dispersive flux can be characterized by a single, measurable dispersion coefficient. By computing this coefficient, the directional nature of longitudinal mechanical transport can be evaluated from the set of tracer experiments discussed in sections 3.5 and 3.6.

Laminar flow is considered within the porous medium. Laminar flow is characterized by the movement of fluid in laminas or layers, one layer flowing smoothly over the adjacent layers. The streamlines in Figure 3-4c which are parallel in the flow region indicate the macroscopic direction of flow. The flow paths of the fluid elements are dictated by the streamlines and cannot cross over one another because the flow is laminar. The fluid particle paths will deviate about the mean flow direction due to the random geometry of the pores. However, the constraint imposed because the streamlines are colinear signifies that the mean direction of movement must be in the direction of flow. Suppose a flow region existed in which the particle paths diverged in many directions such as for flow region b in Figure 3-7. If this flow region is part of a regional homogeneous, anisotropic medium in which the hydraulic gradient is constant, as shown in Figure 3-7, the directions of flow would vary in the adjacent flow regions. However, this flow situation cannot exist as the direction of flow is constant when the hydraulic gradient is constant in a homogeneous medium.

The fact that the macroscopic direction of movement for all fluid particles is in the direction of flow signifies that there can be no net transport of fluid perpendicular to the direction of flow. Applying this principle to the test section in Figure 3-5, the Fickian mechanical dispersive flux is:

$$\begin{bmatrix} m_s \\ m_r \end{bmatrix} = - \begin{bmatrix} M_{11} & M_{12} \\ M_{21} & M_{22} \end{bmatrix} \nabla c$$

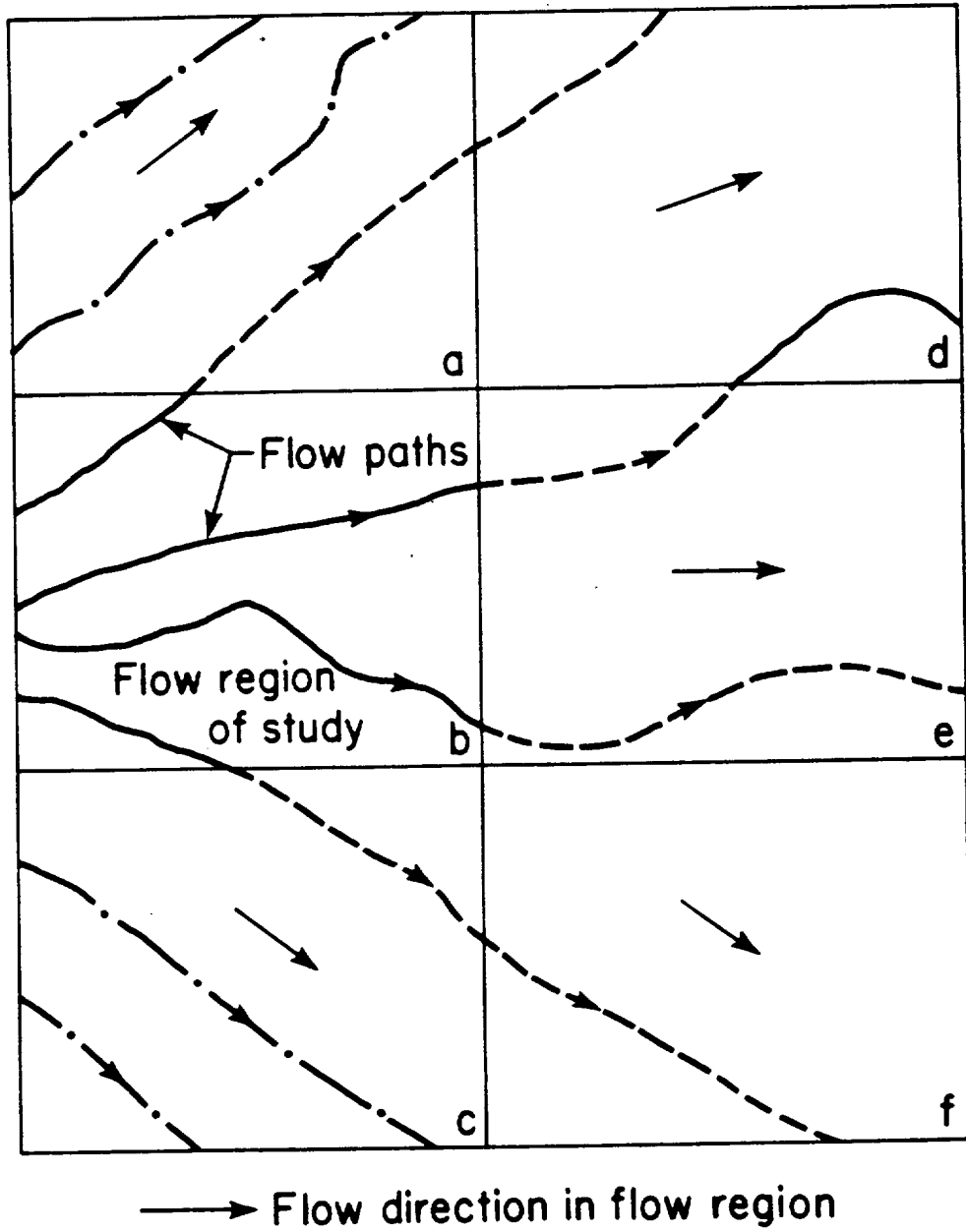
with

$$m_s = -M_{11} \frac{\partial c}{\partial s} - M_{12} \frac{\partial c}{\partial r} \quad (3.12)$$

and

$$m_r = -M_{21} \frac{\partial c}{\partial s} - M_{22} \frac{\partial c}{\partial r} = 0 \quad (3.13)$$

Equation 3.13 yields



XBL-829-4507

Figure 3-7 Divergence of Flow Paths in Flow Regions Within an Inhomogeneous Regional Flow System.

$$-\frac{M_{21}}{M_{22}} = \frac{\frac{\partial c}{\partial r}}{\frac{\partial c}{\partial s}} \quad (3.14)$$

Velocity is non-zero only in the s-direction such that:

$$M_{21} = \sum_{m,n} \alpha_{21mn} \frac{v_m v_n}{V_{LIN}} = \alpha_{2111} V_{LIN} \quad (3.15)$$

and

$$M_{22} = \alpha_{2211} V_{LIN} \quad (3.16)$$

Equation 3.14 can be expressed using equations 3.15 and 3.16 as:

$$-\frac{\alpha_{2111}}{\alpha_{2211}} = \frac{\frac{\partial c}{\partial r}}{\frac{\partial c}{\partial s}} \quad (3.17)$$

Substituting for $\frac{\partial c}{\partial r}$ from equation 3.17 into equation 3.12 yields:

$$m_s = -M_{11} \frac{\partial c}{\partial s} + M_{12} \frac{\alpha_{2111}}{\alpha_{2211}} \frac{\partial c}{\partial s}$$

or

$$m_s = - \left[\alpha_{1111} - \frac{\alpha_{1211} \alpha_{2111}}{\alpha_{2211}} \right] V_{LIN} \frac{\partial c}{\partial s}$$

Incorporating the symmetric relationship of equation 3.4 yields

$$m_s = - \left[\alpha_{1111} - \frac{(\alpha_{1211})^2}{\alpha_{2211}} \right] V_{LIN} \frac{\partial c}{\partial s} \quad (3.18)$$

The bracketed term in equation 3.18 is a constant, and thus, equation 3.18 may be written:

$$m_s = -\alpha_L V_{LIN} \frac{\partial c}{\partial s} = -M_L \frac{\partial c}{\partial s}$$

Note that for an isotropic porous medium, α_{1121} equals zero so that

$$\alpha_L = \alpha_{1111} = \alpha_1$$

where α_1 is the longitudinal geometric dispersivity for an isotropic porous medium defined in section 3.4. Substituting the expression for \bar{m} into equation 3.6 yields the equation governing Fickian longitudinal mechanical transport:

$$\frac{\partial c}{\partial t} + V_{LIN} \frac{\partial c}{\partial s} = M_L \frac{\partial^2 c}{\partial s^2} \quad (3.19)$$

Equation 3.19 is classified as an axial dispersed plug flow model because it is one-dimensional, a function only of the longitudinal variable s. Equation 3.19 shows that it is not necessary to

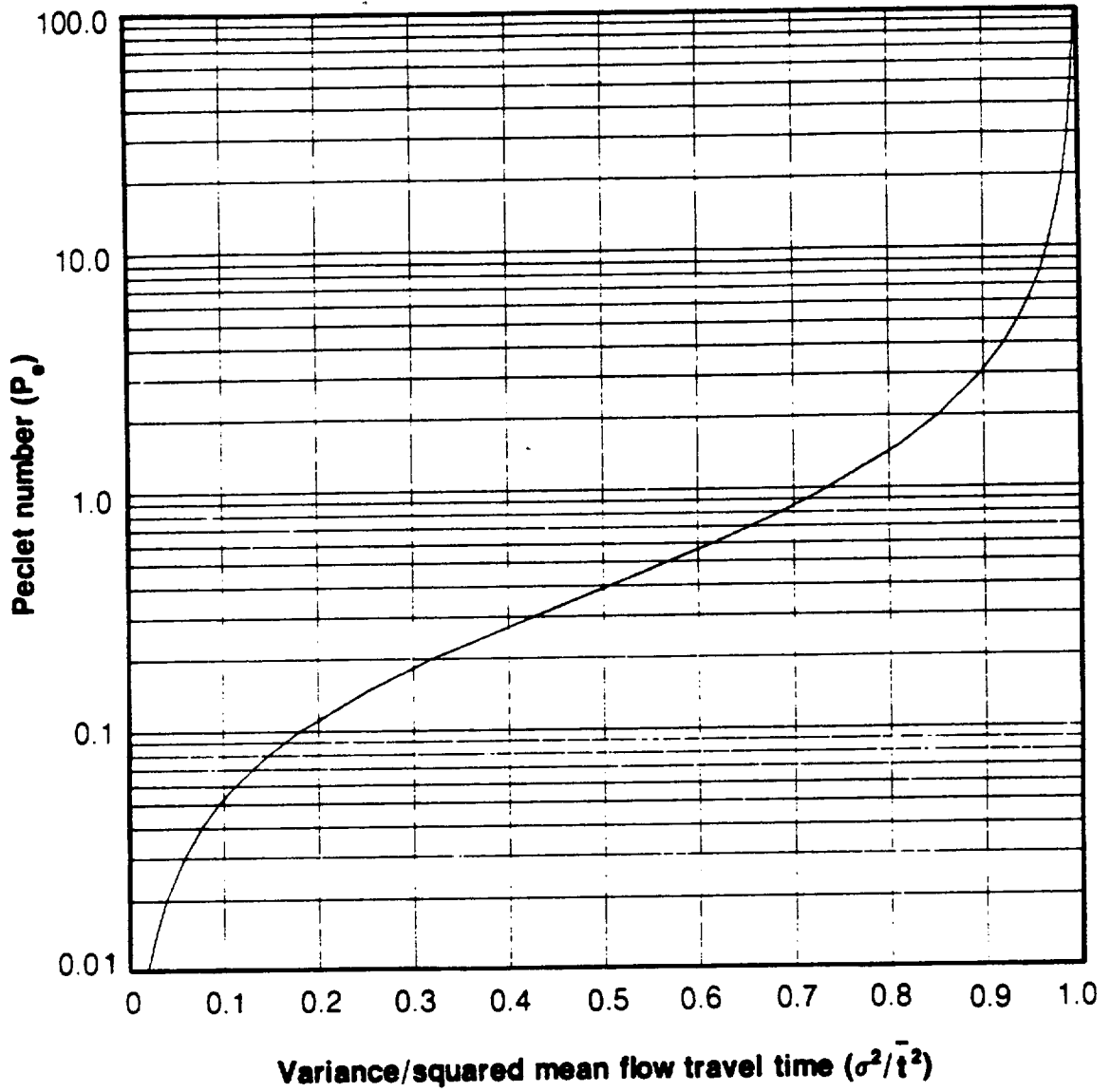
directly determine all 36 independent components of $[\alpha]$ to evaluate longitudinal dispersion for pure Fickian mechanical transport. M_L can be evaluated in a tracer experiment even though the three independent components of $[\alpha]$ which are functions of M_L cannot be individually evaluated. The directional nature of α_L will be investigated for anisotropic media in this research.

3.7.2.2. Evaluation of the Longitudinal Mechanical Dispersion Coefficient

The longitudinal mechanical transport coefficient M_L can be calculated from the variance of the breakthrough curve based on some useful formulas derived by Van der Laan (1958) for the moments of this curve. The problem domain considered by Van der Laan consisted of an entrance and exit section whose properties (i.e. VLIN and M_L) were independent from those of a middle, test section. Van der Laan solved a number of transport problems by varying the boundary conditions imposed on the problem domain. In the tracer experiments considered in this research, dyed water is injected and carried across the entrance section/test section interface by the bulk flow. There can be no dispersion upstream of this interface. Within the test section, mechanical transport is governed by equation 3.19. At the test section/exit section interface, the concentration of dyed water is measured. Then, the fluid is advected downstream in the exit section. Van der Laan analyzed this particular problem using Laplace transformations. He found that the Laplace transform for concentration is a fairly complex expression, and hence, its inverse transformation back into real space was not performed. Fortunately, the moments of the breakthrough curve can be determined without performing this transformation. The variance of the breakthrough curve, a function of the first and second moments, is related to M_L in the following way:

$$\frac{\sigma^2}{\bar{t}^2} = 2Pe - 2Pe^2 \left[1 - e^{(-1/Pe)} \right] \quad (3.20)$$

where $Pe = \frac{M_L}{(VLIN)L}$. Thus, M_L can be implicitly solved from the variance of the breakthrough curve. The log of Pe versus $\frac{\sigma^2}{\bar{t}^2}$ is shown in Figure 3-8. Note that $\frac{\sigma^2}{\bar{t}^2}$ can never exceed unity.



XBL 838-553

Figure 3-8 Semilog Plot of Peclet Number Versus the Ratio of the Variance of the Break-through Curve to the Squared Mean Travel Time.

Figure 3-9 shows three breakthrough curves for different values of Pe that were constructed using numerical methods (Levenspiel (1972); Yagi and Miyauchi (1953)). The ordinate of these breakthrough curves corresponds to

$$E' = E\bar{T}$$

and the coordinate of the breakthrough curves corresponds to the normalized time

$$\frac{t - TM}{SD}$$

where $TM = \bar{T}$ and $SD = \sigma$. The notation changes were made to accommodate the computer graphic capabilities used in this research.

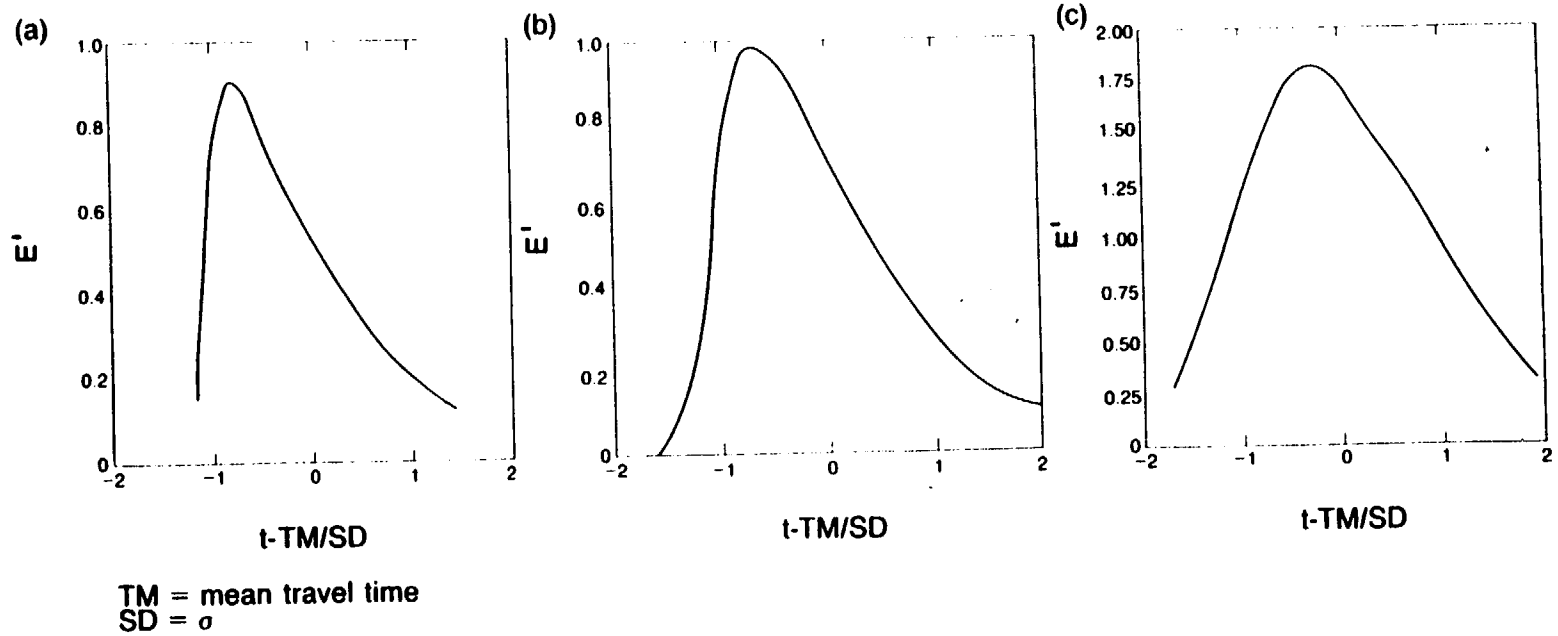
Figure 3-9 demonstrates that as Pe decreases, the peak concentration increases and shifts toward the right, and the skewness in the breakthrough curve decreases. The breakthrough curves are slowly converging to the Gaussian distribution as Pe decreases. The Gaussian distribution becomes a good approximation of the breakthrough curve when Pe is less than 0.01. For these small values of Pe:

$$M_L \approx \frac{1}{2} \frac{\sigma^2}{\bar{T}} (VLIN)L \quad (3.21)$$

3.8. EQUIVALENT POROUS MEDIUM BEHAVIOR

Up to this point, the porous medium continuum concept has been applied in order to evaluate fluid flow and mechanical transport. Another important objective is to determine if a fracture system can be treated like an equivalent homogeneous porous medium continuum. The requirements for continuum flow behavior are presented in this section, followed by a discussion of continuum behavior for hydraulic effective porosity.

In a porous medium, Darcy's law makes it possible to evaluate macroscopic fluid flux properties by treating the medium as a continuum. Fluid flow characteristics are analyzed for equivalent porous medium behavior in two ways. First, flow fields created from the boundary conditions shown in Figure 3-4a are individually evaluated for equivalent porous medium behavior. Then, directional flow is analyzed by synthesizing flow results in different directions. In a porous medium, macroscopic directional flow characteristics can be predicted from a unique permeability tensor.



XBL 8312 7427

Figure 3-9 Three Breakthrough Curves for a) Pe of 0.5, b) Pe of 0.2, and c) Pe of 0.025.

Any given flow field must satisfy the following two requirements in order to exhibit equivalent porous medium behavior:

- (1) The macroscopic flow field can be predicted by Darcy's law.
- (2) The specific discharge is stable and does not fluctuate with the size of the flow region.

As discussed in section 3.5, the flow field for an anisotropic porous medium is characterized by a uniform specific discharge. Because the specific discharge is a vector, the condition of uniformity implies that both its magnitude and angle of flow are constant. The use of macroscopic flow measurements are described below to determine if the magnitude and angle of \vec{q} are constant for the given flow field.

A uniform specific discharge means that parallel cross sections of equal area will have the same total fluid flux flowing across them. This means that in Figure 3-5 the flow rate into side 2 is equal to the flow rate out of side 4,

$$QS_2 = QS_4 \quad (3.22)$$

and the flow rate into side 1 is equal to the flow rate out of side 3,

$$QS_1 = QS_3 \quad (3.23)$$

Equations 3.22 and 3.23 constitute a continuity test to evaluate if the magnitude of the specific discharge is constant.

Two approaches are used to determine the angle of flow. Both approaches produce the same angle of flow if the specific discharge is uniform. In the first approach, the total flow rates into the sides of the flow region are used to compute the components of the specific discharge in the direction of the hydraulic gradient, and in the direction perpendicular to the gradient from which angle of flow is calculated. This calculation is not based on the path of the fluid. In the second approach, the conditions of the uniform flow field are used to compute angle of flow. As shown in Figure 3-5, the amount of fluid entering side 2 that exits on side 4 can be used to compute angle of flow. The remaining fluid entering side 2 must exit on side 3.

The first method of determining the angle of flow can be expressed mathematically using the two components of the specific discharge:

$$\vec{q} = q_x \vec{i} + q_y \vec{j}$$

or referring to Figure 3-5,

$$\theta = \tan^{-1} \frac{q_y}{q_x} = \text{ANFD} \tag{3.24}$$

For the flow region in Figure 3-5, the specific discharge in the x direction is obtained by summing the flow rate into side 2 from the individual flow channels and dividing by L_y . Similarly, the total flow rate into side 1 divided by L_x determines q_y .

The second method of determining the angle of flow is based on the uniformity of the specific discharge. For the anisotropic medium in Figure 3-5, a certain quantity of the fluid flux, Q_{NC} , flowing into side 2 must exit on side 3. Thus,

$$Q_{NC} = Q_{S3}$$

and

$$q_y = \frac{Q_{S3}}{L_x} = \frac{Q_{NC}}{L_x}$$

Substituting q_y into equation 5 yields:

$$\theta = \tan^{-1} \frac{Q_{NC}}{q_x L_x} = \text{ANFC} \tag{3.25}$$

This relationship is also obtained directly from the uniformity of the flow field. The cross-hatched area in Figure 3-5 designates the zone in which the fluid flows continuously from sides 2 to 4. Since the specific discharge is uniform, the following relationships hold on side 2:

$$\frac{Q_C}{L_C} = \frac{Q_{NC}}{L_{NC}} = \frac{Q_x}{L_y}$$

which means

$$L_{NC} = \frac{Q_{NC} L_C}{Q_C} = \frac{Q_{NC} L_y}{Q_x} = \frac{Q_{NC}}{q_x}$$

The relationship for the angle of flow is:

$$\tan \theta = \frac{L_{NC}}{L_x} = \frac{Q_{NC}}{L_x q_x}$$

so

$$\theta = \tan^{-1} \frac{Q_{NC}}{q_x L_x} \tag{3.26}$$

which is the same expression as equation 3.25.

Equation 3.26 is the second method of computing the angle of flow. The evaluation of ANFD and ANFC constitutes the angle of flow test. The direction of the specific discharge is a constant if ANFD is equal to ANFC.

The stability of the specific discharge, the second requirement for a flow field to exhibit porous medium behavior for a particular direction of flow, is tested by slowly increasing the size of the flow region and measuring the specific discharge. Initially, the specific discharge may be expected to fluctuate significantly. In small flow regions, the number of channels (fractures) may be too small so that the flow region does not behave like a representative elementary volume of a porous medium. However, as the size of the flow region increases, the fluctuations in the specific discharge may dampen out and eventually a stable value may be reached. When the specific discharge is stable, the flow field behaves hydraulically like an equivalent porous medium.

The above tests can be used to examine equivalent porous medium behavior for a particular direction of flow. However, Darcy's law also specifies that the flow field in any direction can be predicted by a permeability tensor. If such a tensor exists the square root of permeability in the direction of flow plots as an ellipse. For example, the square root of K_x/K_y for the anisotropic porous medium considered in Figure 3-4a is shown in the polar plot on Figure 3-10. Thus, the shape of the plot of the square root of permeability is the test of whether directional flow for the system behaves like an equivalent porous medium.

To determine equivalent porous medium behavior for transport, one must examine the directional nature of the hydraulic effective porosity. The hydraulic effective porosity is generally assumed to be equal either to the rock effective porosity or to the total porosity in transport modeling. Since both porosities are independent of direction in a continuum, the hydraulic effective porosity should be constant in all directions. Thus, the test for equivalent porous medium behavior for transport is to examine the stability of ϕ_H with direction.

The tortuosity was first introduced when researchers were developing the theory relating permeability to the geometric properties of a porous medium. One of the first workers,

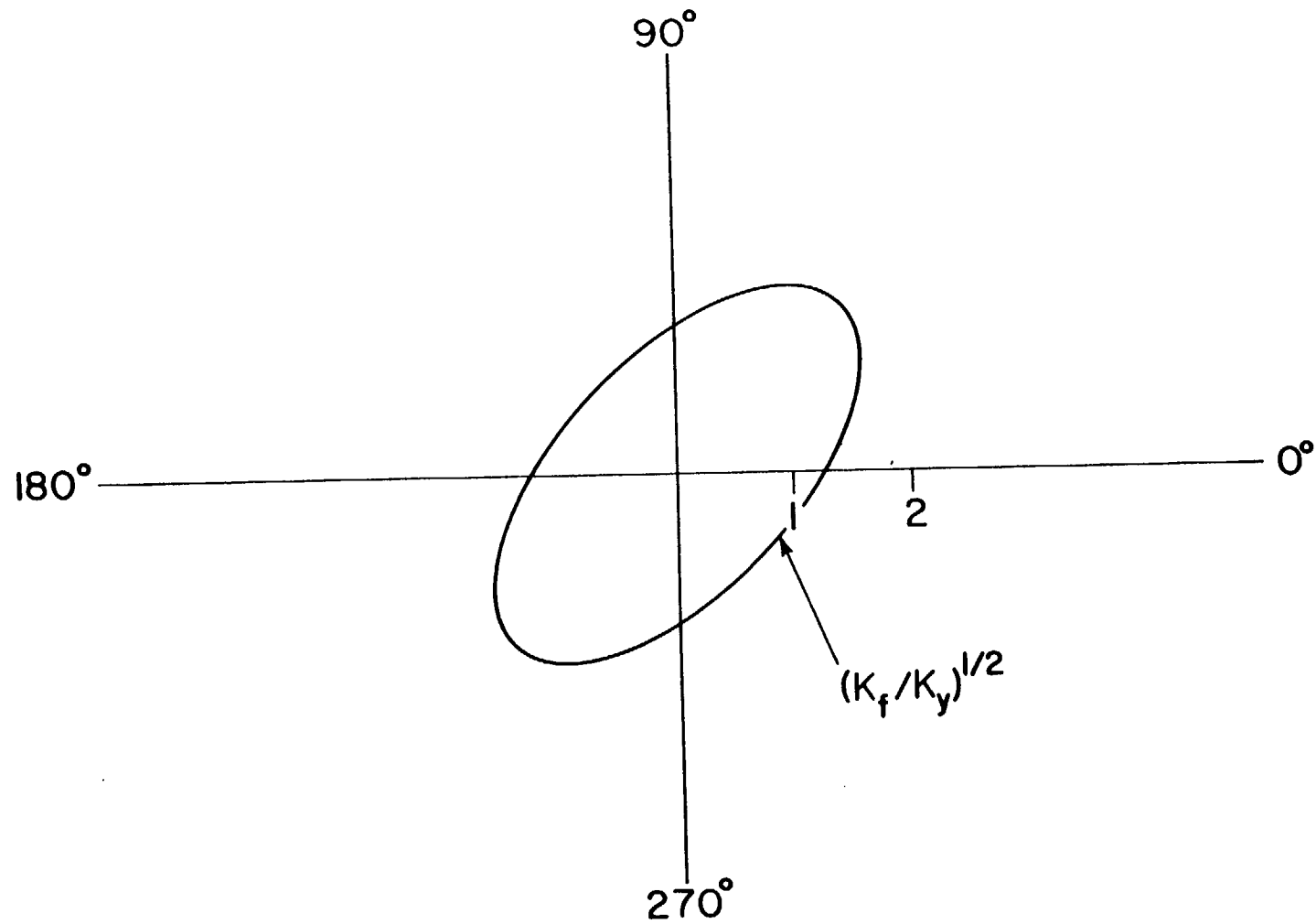


Figure 3-10 Square Root of Permeability in Direction of Flow for the Anisotropic Porous Medium Shown in Figure 3-4.

XBL 836-396

Kozeny, considered a simple porous medium model consisting of a bundle of capillary tubes to determine this relationship. The Kozeny-Carman expression for the intrinsic permeability for a medium of straight capillary tubes is:

$$k = \frac{\phi^3}{s_f S_s}$$

where $s_f = 32 \left(\frac{r_h}{d_c} \right)^2$ = shape factor

and r_h is the conductive volume divided by the wetted surface area, d_c is the diameter of a capillary tube, and S_s is the specific surface.

Kozeny, also accounted for the fact that fluid paths are nonlinear. The intrinsic permeability in this case (Carman, 1956) is:

$$k = \frac{\phi^3}{s S_s} \tag{3.27}$$

where $s = s_f \tau^2$

Tortuosity for isotropic porous media has been evaluated both analytically for random oriented flow channels (Haring and Greenkorn, 1970) and experimentally, by diffusion studies (Collins, 1961), to be $\sqrt{3}$ and $\sqrt{2}$, respectively. Dullien (1979) stated that τ should normally range between 1 and $\sqrt{3}$.

Tortuosity for anisotropic porous media is directionally dependent. Anisotropy (Rice et al., 1970) is caused by differences in path lengths of fluid particles and frictional resistance with direction resulting from the asymmetric shape of grains oriented in a particular direction. Longer paths of flow cause greater frictional resistance which subsequently reduces flow rate. The directional dependence of τ was shown experimentally by Sullivan and Hertel (1940) using a medium of glass wool. Sullivan and Hertel showed that the tortuosity parallel to the direction of the fibers was much less than τ measured in the direction perpendicular to the fibers.

Directional permeability from equation 3.27 is caused by variations in s . The shape factor s_f exhibits relatively small changes for different geometrically shaped conduits (Wyllie and Spangler, 1952) and normally falls between 2 and 3. Thus, only slight changes in s_f are expected with direction in an anisotropic medium. This means that directional permeability

strongly reflects changes in tortuosity. Since no known extensive study of directional tortuosity has been conducted, one would expect tortuosity to be inversely proportional to permeability for an equivalent porous medium.

CHAPTER 4

THE DISCRETE NUMERICAL MODEL

4.1. INTRODUCTION

A three-stage discrete numerical model written in FORTRAN specifically for the VAX-11/780 machines has been developed to evaluate mechanical transport in fracture systems. The first stage of the model is called fracture system generation. The function of this stage is to create a homogeneous, anisotropic fracture system for which the directional nature of mechanical transport can be investigated. In this stage, finite-element meshes are constructed for flow regions oriented in different directions so that the set of tracer tests used to evaluate directional mechanical transport can be simulated. The second stage is called the hydraulic head calculation. The hydraulic boundary conditions described in section 3.5 are applied to each flow region and a finite element method is used to calculate the hydraulic head at each fracture intersection within the flow region. The distribution of hydraulic head serves as input to the third stage of the numerical model called mechanical transport simulation. Mechanical transport is modeled in this stage using a new streamtubing technique which traces the detailed movement of fluid flow. At the end of this stage, macroscopic mechanical transport and fluid flow parameters are calculated. Each stage is discussed in detail in this chapter.

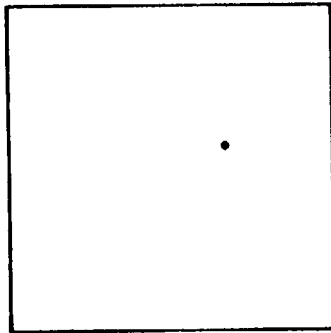
4.2. FRACTURE SYSTEM GENERATION STAGE

In the first stage of the numerical model, a two-dimensional fracture system is created in an area called the generation region. The procedure used in creating the fracture system was developed by Long (1983). The fractures in the generation region are created one set at a time, and the number of fractures in each set is controlled by an assigned areal density (number of fractures per unit area). The geometric parameters required to create each fracture are: its length, orientation, aperture, and location in the generation region. This information may be read directly into the computer program (deterministic approach) or may be generated stochastically. In a stochastic generation, each fracture is randomly located in the generation region to

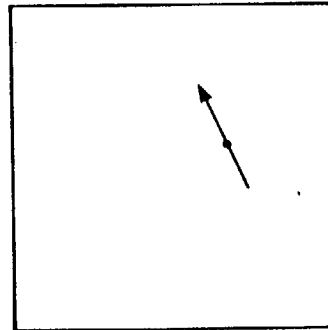
create a statistically homogeneous system. The three remaining geometric parameters are each created by probabilistic simulation. Probabilistic simulation can be conducted with either the Gaussian, lognormal or exponential probability distribution. The mean and standard deviation for the simulated distribution must be read into the computer program.

The stochastic generation of a fracture system consisting of two sets of fractures is illustrated in Figure 4-1. In Figure 4-1a, the size of a square generation region is defined, and the center of the first fracture for set 1 is randomly located in the generation region. This fracture is then assigned an orientation (Figure 4-1b) using probabilistic simulation. Next, the fracture is stochastically assigned a length and an aperture as shown in Figure 4-1c. The steps shown in this figure from 4-1a to 4-1c are used to create a single fracture. The number of fractures created for set 1 is controlled by its areal density. Each fracture for the first set is generated from the same set of geometric statistics (mean and standard deviation) for length, aperture, and orientation. After all the fractures have been created for set 1 (Figure 4-1d), the fractures for set 2 are created from a new set of geometric statistics. Figure 4-1e shows the complete fracture system consisting of two sets of fractures.

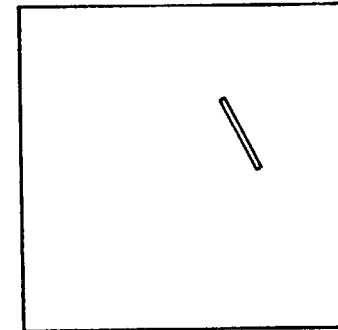
Flow regions within the generated fracture network are selected for fluid flow and mechanical transport studies. A flow region may be oriented in any direction as long as it fits within the boundaries of the generation region. A finite-element mesh is constructed for each flow region consisting of nodes, which are fracture intersections, and elements, which are fracture segments between nodes. Figure 4-1f shows a flow region within the generation region oriented at 45°. The finite element mesh for the flow region consists of 21 nodes and 22 elements. The hydraulic boundary conditions described in section 3.5 are applied to each flow region and the hydraulic heads for the nodes located along the boundary of the flow region are calculated. The finite-element mesh with the prescribed nodal hydraulic heads are stored in a data file. This file is read into the second stage of the computer program.



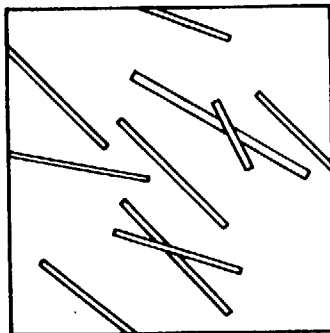
(a) Selection of generation region size with center of first fracture for set 1 randomly located in domain



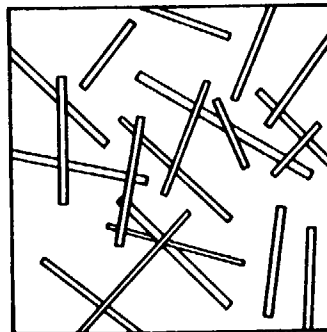
(b) Fracture orientation assigned



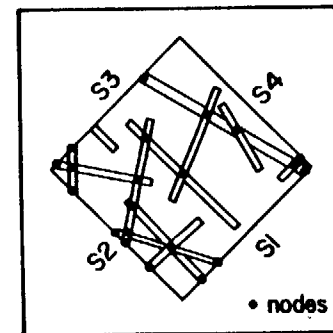
(c) Fracture length and aperture assigned



(d) Fractures for set 1 created



(e) Fractures for set 2 completes generation of fracture system



(f) Flow region oriented at 45° consisting of 21 nodes and 22 elements

Figure 4-1 Stochastic Generation of a Fracture System Consisting of Two Sets of Fractures.

XBL 836-395

4.3. HYDRAULIC HEAD CALCULATION

The steady state hydraulic heads at the nodes are calculated in the second stage using a finite-element technique developed by Wilson (1970). Laminar flow in each fracture is governed by the cubic law for fracture flow:

$$Q_e = - \frac{\rho g b^3}{12\mu} \frac{d\phi}{d\xi} \quad (4.1)$$

The finite element method first develops the necessary algebraic equations governing flow within each element by discretizing the derivative for ϕ in equation 4.1. The two equations governing flow into the two ends (nodes) of the element shown in Figure 4-2 are:

$$\text{Node i: } Q_{ei} = \frac{\rho g b^3}{12\mu L_e} (\phi_i - \phi_j) = a_F (\phi_i - \phi_j) \quad (4.2)$$

and

$$\text{Node j: } Q_{ej} = \frac{\rho g b^3}{12\mu L_e} (\phi_j - \phi_i) = a_F (\phi_j - \phi_i) \quad (4.3)$$

Equations 4.2 and 4.3 govern flow within a one-dimensional finite element called a line element. These two equations can be expressed in matrix notation as:

$$a_F \begin{bmatrix} 1 & -1 \\ -1 & 1 \end{bmatrix} \begin{bmatrix} \phi_i \\ \phi_j \end{bmatrix} = \begin{bmatrix} Q_{ei} \\ Q_{ej} \end{bmatrix}$$

or

$$[C_e] \{ \phi_e \} = \{ Q_e \} \quad (4.4)$$

A set of such equations is computed for each element in the flow region. Next, all the sets of equations governing flow at the element level are assembled into a global set of equations governing flow for the entire region. The matrix form of this global set of equations is:

$$[C] \{ \phi \} = \{ Q \} \quad (4.5)$$

The conductance matrix $[C]$ is simply calculated by adding all the 2×2 element submatrices into a square $n \times n$ matrix where n is the number of nodes. The conductance matrix for this problem is symmetric and banded. Both $\{ \phi \}$ and $\{ Q \}$ are $n \times 1$ column vectors of nodal hydraulic heads and prescribed flow rates, respectively. For the boundary conditions considered in section 3.5, $\{ Q \}$ is the null vector. After the known nodal hydraulic heads along the boundary of the flow region have been implemented into equation 4.5, a direct linear equation solver for symmetric banded matrices is used to calculate the nodal hydraulic heads. This

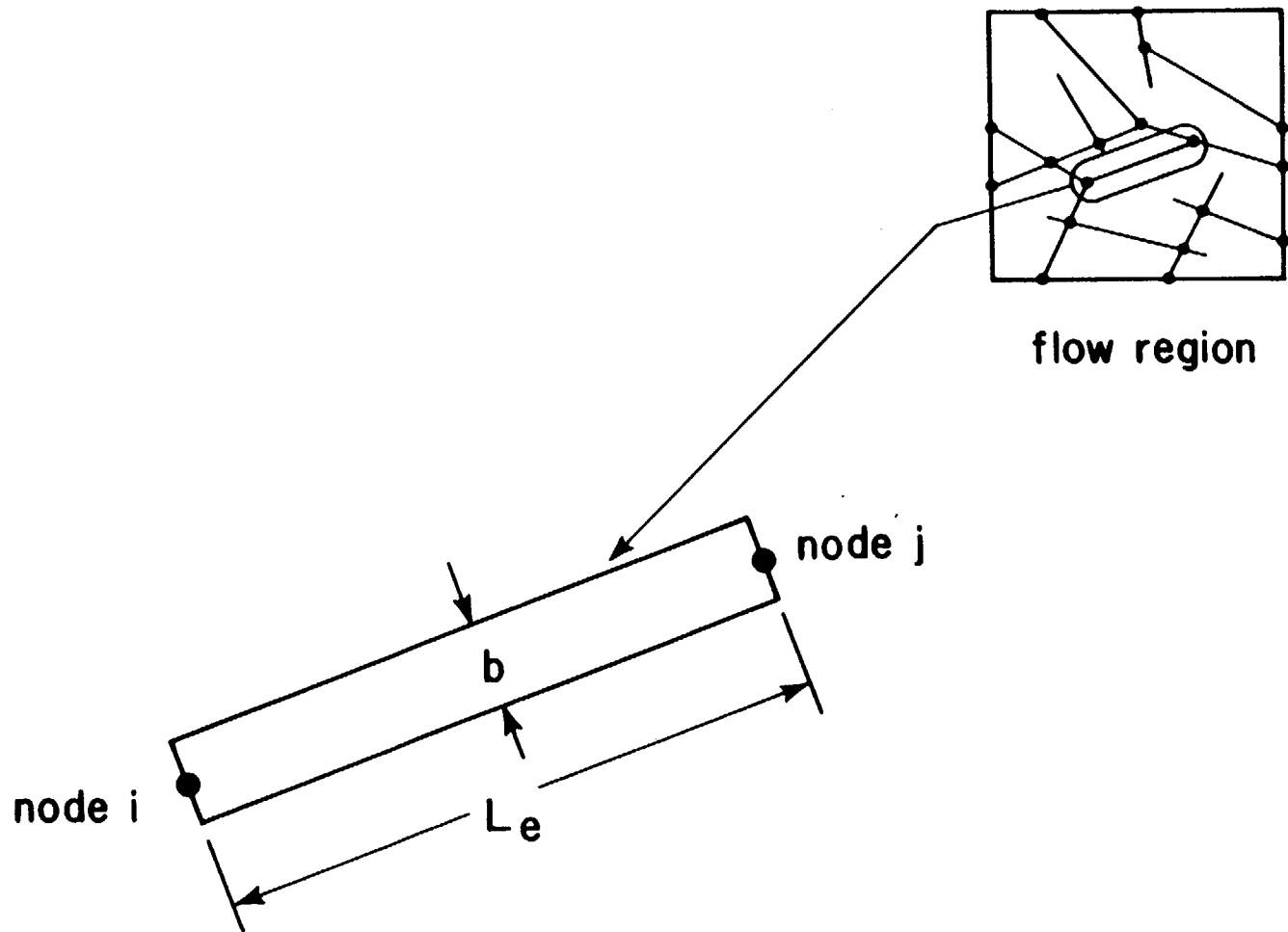


Figure 4-2 A Typical Line Element of Aperture b With Labeled Nodes.

XBL 836 - 397

constitutes the second stage of the numerical model.

4.3. MECHANICAL TRANSPORT SIMULATION

Mechanical transport is simulated for the elements in the flow region in the final stage of the program. A streamtube is defined as a flow conduit that is bounded by streamlines in which flow rate is constant. The model developed to simulate mechanical transport is used to determine the paths and flow rates for the streamtubes in the fracture network. Once all the streamtube paths have been determined, the total travel time from inlet to outlet for the fluid in each streamtube is computed by summing up the residence times in each element along the individual streamtubes. This procedure requires an evaluation of the path, the flow rate, and the width of the streamtube in each element. The time it takes the fluid in a streamtube to travel the length of an element will first be considered. Since fluid flows out of an element to a node, the way fluid flowing into a node exits out of the node will then be discussed.

As mentioned earlier, the flow rate in an element is governed by the cubic law for fracture flow. It can be shown that by solving the Navier-Stokes equation for laminar flow between parallel plates, an expression for the well-known parabolic velocity distribution across a planar element is obtained:

$$u(\eta) = \frac{\rho g}{\mu} \frac{d\Phi}{d\xi} \left[\frac{\eta^2}{2} - \frac{b}{2}\eta \right] \quad (4.6)$$

The flow rate in the element is obtained by integrating equation 4.6 across the width of the element:

$$Q_f = \int_0^b u(\eta) d\eta = -\frac{\rho g b^3}{12\mu} \frac{d\Phi}{d\xi}$$

This is the cubic law for fracture flow.

The time it takes the fluid in a streamtube to travel the length of an element is given by:

$$t_{ST} = \frac{L_T}{\frac{Q_{ST}}{\eta_{i+1} - \eta_i}}$$

where $\eta_{i+1} - \eta_i$ is the width of a streamtube in an element. Thus, to determine t_{ST} , the width that a streamtube occupies in an element must be computed. Integrating equation 4.6 between η_i and η_{i+1} yields:

$$Q_{ST} = \int_{\eta_i}^{\eta_{i+1}} u(\eta) d\eta = \frac{6Q_f}{b^3} \left[\frac{b(\eta_{i+1}^2 - \eta_i^2)}{2} - \frac{(\eta_{i+1}^3 - \eta_i^3)}{3} \right] \quad (4.7)$$

The width occupied by the streamtube can then be determined from the flow rate in the streamtube and the starting coordinate η_i . For example, the node in Figure 4-3 consists of three inflowing streamtubes labeled ST1, ST2, and ST3. Streamtube ST2 has a flow rate of 4 units and a starting coordinate, $\eta_{i,2}$, equal to zero in element E. The ending coordinate of ST2, $\eta_{i+1,2}$, is obtained using equation 4.7. That coordinate then becomes the starting coordinate for ST3 in element E from which the travel time for ST3 in element E is determined.

The principle of conservation of mass, and the fact that streamlines cannot cross one another in laminar flow, are used to calculate the downstream location of inflow streamtubes in outflow elements at a node. Travel times within a node are considered to be negligible. The upper outflow element D in Figure 4-3 has a flow rate of three units. The flow into this element must come from element A because if any of the other two streamtubes flowed into element D, they would have to cross the path of ST1. Using the same principle, ST2 must occupy the upper, and ST3 the lower, portion of element E. The order of the streamtubes and the flow rates in each streamtube are recorded for each outflow element. This information is needed to determine the travel time for the fluid in each streamtube.

The flux in an inflow streamtube can be distributed into more than one outflow element at the node, as is illustrated for ST1 in Figure 4-4. When this arises, the inflow streamtube must be subdivided such that a new streamtube is created for every outflow element that receives any portion of the inflow. For example, ST3 and ST4 are the result of the subdivision

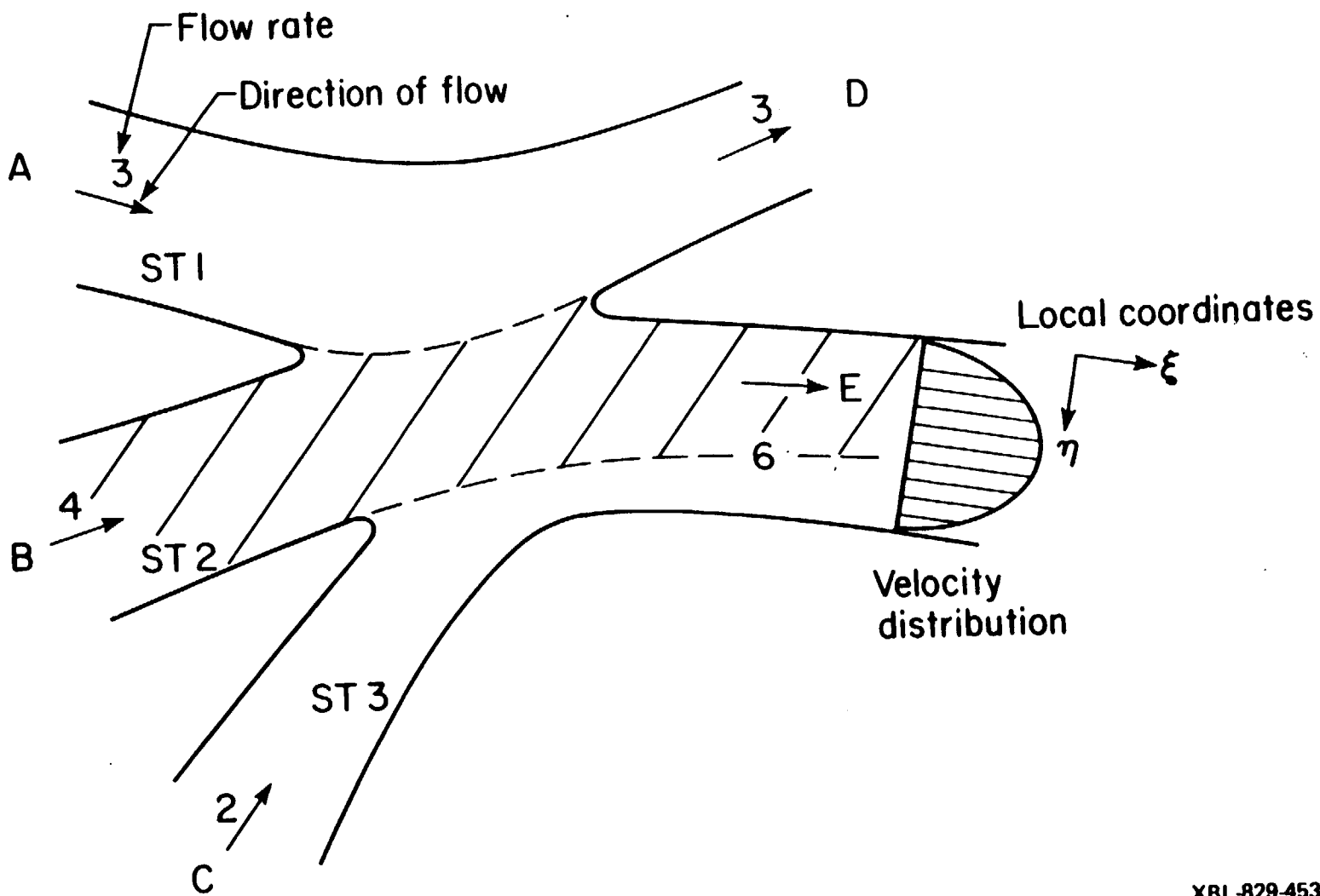


Figure 4-3 Redistribution of Streamtubes at a Node.

XBL-829-4534

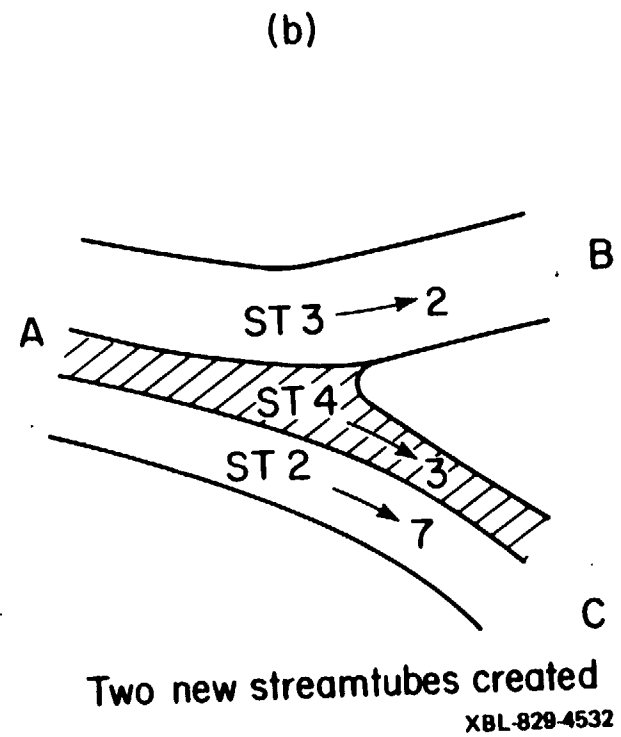
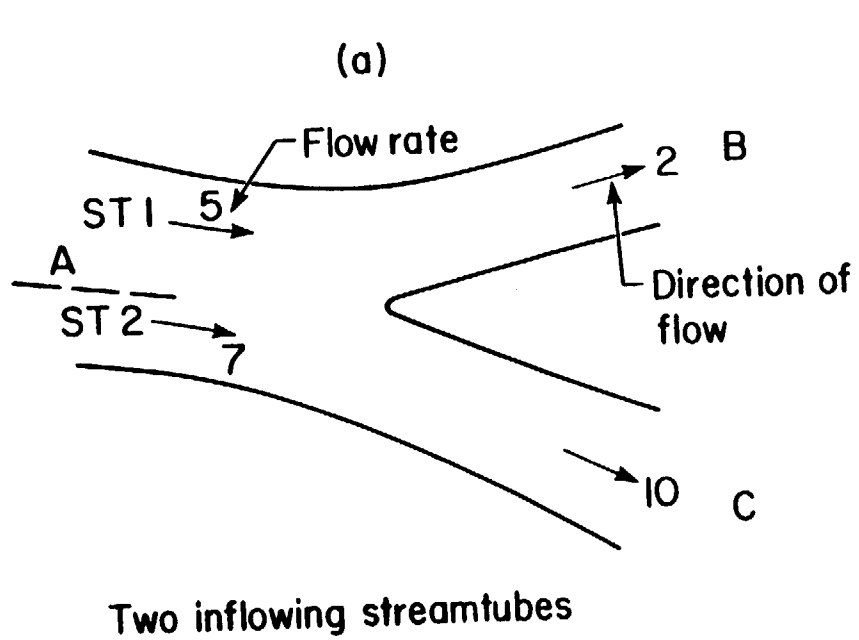


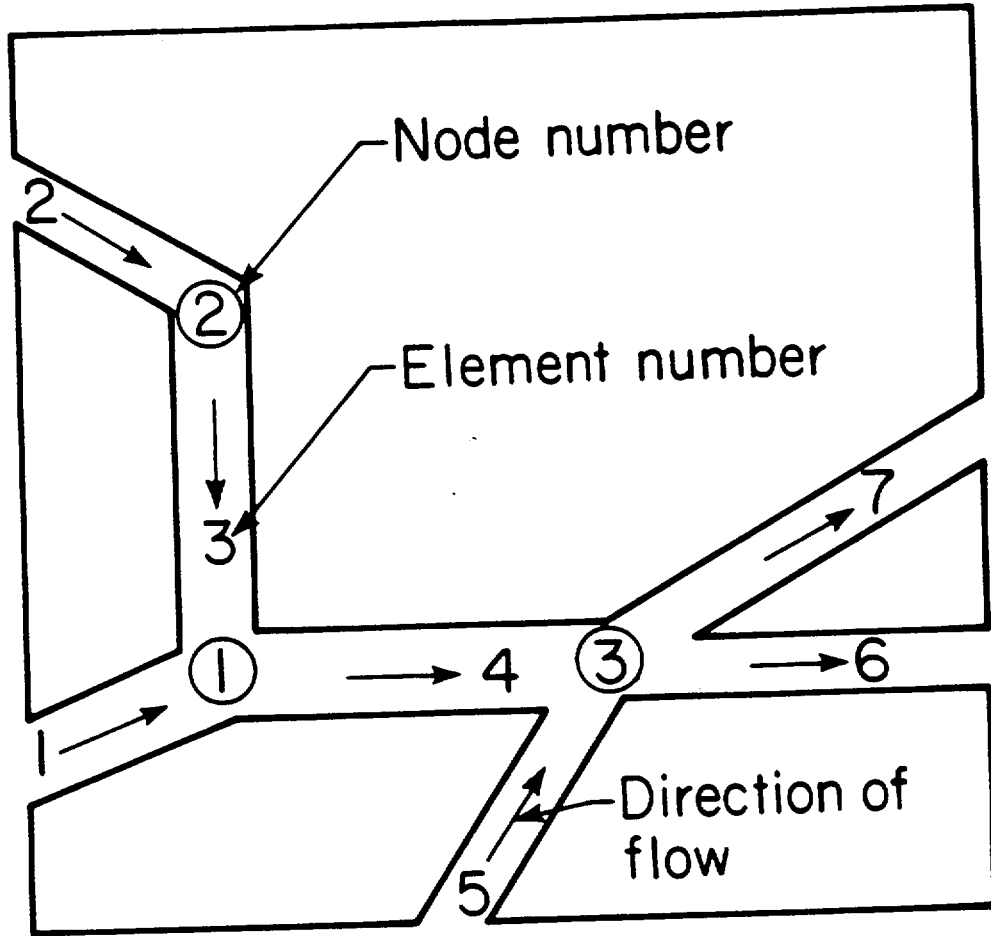
Figure 4-4 Creation of New Streamtubes at a Node.

of the discontinued streamtube ST1. The total travel time to this particular node for the fluid in a new streamtube is determined by backtracking along the path of ST1 to its origin.

The first step in tracing the location of streamtubes in the fracture network is to assign a streamtube to every inflow element on the boundary of the flow region. This assures that streamtubes exist in every conductive element within the flow region. For example, in the fracture network shown in Figure 4-5, streamtubes have been initiated in elements 1, 2, and 5. Each assigned streamtube is given a width equal to the aperture of the element it occupies, and a flow rate equal to that in the element.

The program then proceeds in sequential nodal order determining the outflow streamtubes at each node. The outflow streamtubes at a node can only be determined if the streamtubes are known in all inflow elements at the node. If streamtubes do not exist in an inflow element, the inflow element number and the node number are stored in memory. This situation arises when an inflow element at the node under consideration is an outflow element at a higher numbered node. The streamtubes in the inflow element at the current node can only be determined after proceeding to the higher node. In Figure 4-5, node 1 is the first node examined by the computer program and element 4 is the only outflow element at this node. The streamtubes in element 4 can only be calculated if the streamtubes are known in inflow elements 1 and 3. The streamtube in element 1 is known since a streamtube was assigned to this element in the first phase of the streamtubing procedure. However, at this point, the streamtubes in element 3 are unknown. Therefore, element 3 and node 1 are stored in memory and the program proceeds to node 2.

The streamtubes in the outflow elements at a node are determined when streamtubes exist in all inflow elements. After the streamtubes in all outflow elements have been determined, the program scans the elements stored in memory and removes any element that is an outflow element at the current node because the streamtubes are known in these elements. If an element is the only one stored for a particular node, then the streamtubes in the outflow elements at that node are determined. For example, at node 2 for the fracture network in Figure 4-5, the



XBL 833-1414 A

Figure 4-5 Fracture Network With Inflow Streamtubes Initiated in Elements 1, 2, and 5.

streamtube for the inflow element 2 is known. The streamtube in the outflow element 3 can therefore be computed knowing the streamtube in element 2. The program then removes element 3 from the list of stored elements because the streamtube in element 3 has been determined. Because element 3 is the only element stored in memory for node 1, the streamtubes in the outflowing element 4 at node 1 can now be calculated. As the network is scanned in this fashion, the number of streamtubes increases and the width of streamtubes decreases because new streamtubes are being created at nodes.

After the streamtubing procedure has been completed, the program computes the macroscopic fluid flow and mechanical transport parameters listed in Table 4-1.

Table 4-1. Macroscopic Parameters Calculated in Mechanical Transport Simulation Stage.
FLUID FLOW INFORMATION
Flow into side 2 (QS2)
Flow out of side 4 (QS4)
Flow into side 3 (QS3)
Flow out of side 1 (QS1)
Continuous flow from side 2 to 4 (Qc)
Magnitude of specific discharge (q)
Deviation in flow (DEVF)
Angle of flow based on flow uniformity (ANFC)
Angle of flow based of components of specific discharge (ANFD)
Deviation in angle of flow (DEVA)
Tortuosity (τ)
Breakthrough Curve Statistics
Mean flow travel time (\bar{t})
Variance (σ^2)
Porosity Information
Total porosity of flow region (ϕ)
Rock effective porosity (ϕ_R)
Hydraulic effective porosity (ϕ_H)
Velocity Information
Average linear velocity (VLIN)
Mean pore velocity (MPV)
Calculated mean pore velocity (VPORE)

There is no guarantee that a fracture system will behave like an equivalent porous medium and satisfy the continuity criterion discussed in section 3.8. Consequently, the specific

discharge is defined by recognizing that Darcy's specific discharge represents the average discharge crossing a unit area in the mean direction of flow. The magnitude of the specific discharge is thus computed by averaging the flux on the sides of the flow region in the following way:

$$q_x = \frac{QS2 + QS4}{2L_y} \text{ and } q_y = \frac{QS1 + QS3}{2L_x}$$

with

$$q = (q_x^2 + q_y^2)^{1/2}$$

It was shown in section 3.8 that for a porous medium:

$$QS2 = QS4 \text{ and } QS1 = QS3$$

The exact equality indicated by the two equations above will not necessarily hold for stochastically generated fracture systems. The relationship for the flow rate along the sides of the flow region can be written:

$$QS2 = QS4 + \Delta Q \text{ and } QS1 = QS3 + \Delta Q$$

The deviation in flow is defined to measure how well the continuity criterion is satisfied for the flow field within a flow region:

$$DEVF = \left(\frac{|\Delta Q|}{\text{TOTAL INFLOW}} \right) 100 \quad (4.8)$$

A small deviation in flow indicates that the continuity criterion is satisfied.

Two methods were presented in section 3.8 to compute the angle of flow. The continuous flow from side 2 to side 4 was used in calculating ANFC by equation 3.25. This method was based on the uniformity of the flow field. In the second method, the two components of the specific discharge were used in calculating ANFD by equation 3.24. The angle of flow for the specific discharge is thus computed by averaging ANFD and ANFC:

$$\theta = \frac{ANFD + ANFC}{2}$$

The deviation in angle of flow is defined to measure how well the flow field within a flow region satisfies the angle of flow criterion:

$$DEVA = |ANFD - ANFC| \quad (4.9)$$

ANFC will equal ANFD (DEVA = 0) if the fracture system behaves exactly like an equivalent

porous medium. Thus, DEVA and DEVF are both used to evaluate how well a flow field satisfies the flow requirements for equivalent porous medium behavior.

The breakthrough curve is constructed for the fluid that flows continuously between sides 2 and 4. The mean of this curve is used to compute VLIN in the following way:

$$VLIN = \frac{L}{\bar{t}} = \frac{L_x}{\cos\theta \bar{t}}$$

Next, VLIN is used to compute the hydraulic effective porosity as:

$$\phi_H = \frac{q}{VLIN}$$

The variance of the breakthrough curve can be used to compute the Fickian longitudinal mechanical transport coefficient from equation 3.20, once VLIN and L have been computed.

The mean pore velocity is the average microscopic velocity within the pores and is expressed mathematically as:

$$MPV = \frac{1}{V_c} \int_{V_c} v dV_c$$

A commonly accepted relationship associating the mean pore velocity with the specific discharge is the Dupuit-Forchheimer assumption (Scheidegger, 1960):

$$MPV \approx q/\phi_R$$

The rock effective porosity is computed by summing the volume of all conductive elements within the flow region and then dividing this term by the total volume. For homogeneous transport, q/ϕ_R is equal to VLIN, which means that the Dupuit-Forchheimer yields:

$$MPV \approx VLIN = \frac{L}{\bar{t}}$$

Fluid particles travel along nonlinear paths in a porous medium such that the mean pore velocity is larger than the average linear velocity. Consequently, a better estimate of MPV is provided in this study by VPORE. VPORE is computed using the tortuosity to account for the nonlinearity of fluid flow in the following way:

$$VPORE = \frac{L_s}{\bar{t}} = \tau VLIN$$

Tortuosity is computed as:

$$\tau = \frac{\sum_{i=1}^{NC} Q_{STi} L_{STi}}{Q_c L}$$

CHAPTER 5

INVESTIGATION OF CONTINUOUS FRACTURE SYSTEMS

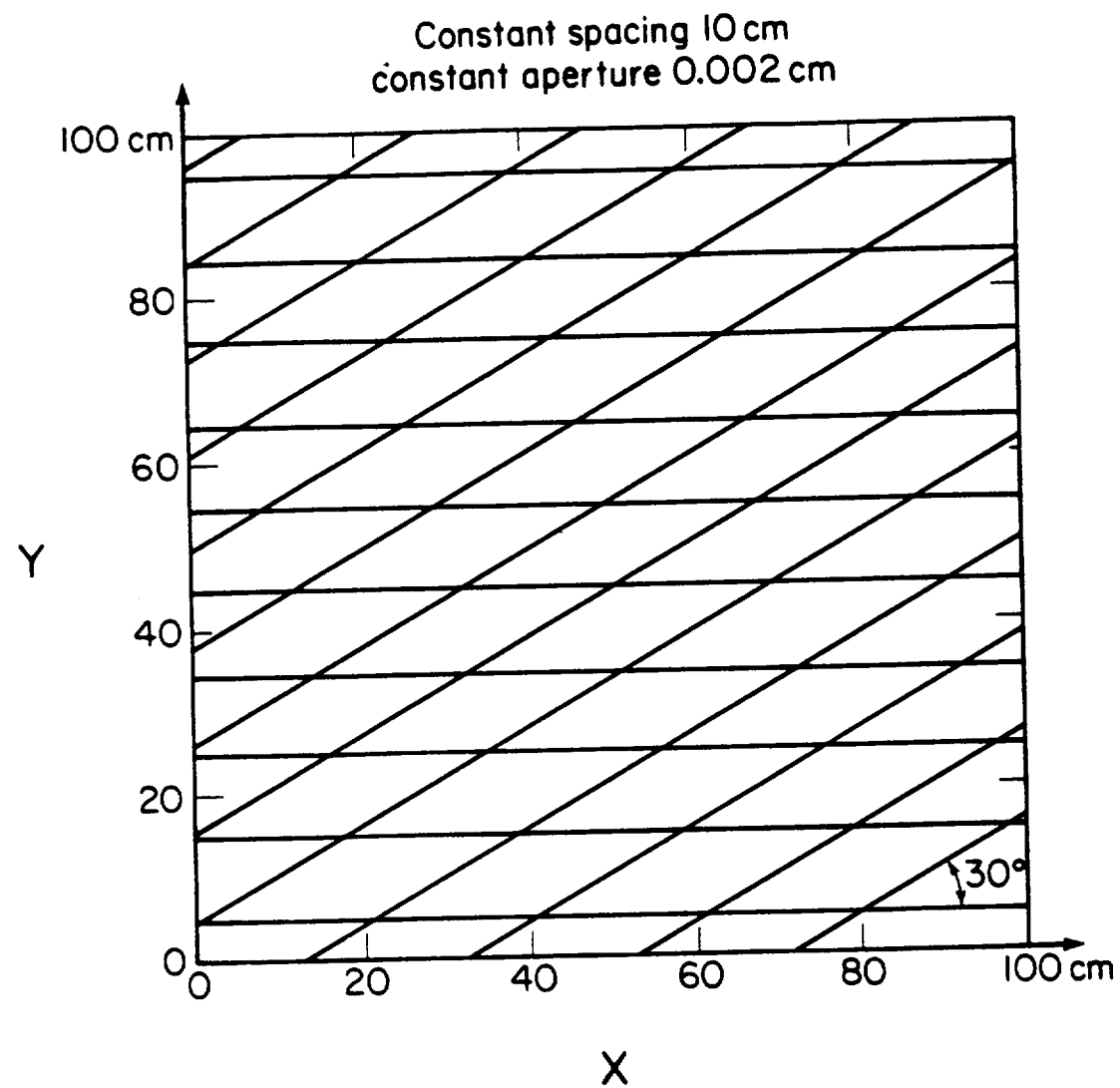
5.1. INTRODUCTION

Two regular continuous systems of infinitely long fractures were initially studied for two primary reasons. First, continuous fracture systems behave hydraulically as equivalent porous media with flow properties that can be analytically computed (Parsons [1966], Snow [1969]). The study of fracture systems with known continuum flow behavior can serve to demonstrate the tests developed to identify such behavior. Second, the possible directional dependence of mechanical transport can be investigated for anisotropic fracture systems in which the void region is totally connected. Such fracture systems simplify an understanding of the results because dead-end zones are excluded from the void region.

5.2. CONTINUOUS SYSTEM WITH TWO SETS OF CONSTANT-APERTURE FRACTURES

In the first investigation of networks with continuous fractures, the system consisted of two sets of parallel fractures oriented at 0° and 30° , as illustrated in Figure 5-1. All fractures had an aperture of 0.002 cm, and the spacing between fractures was a constant value of 10 cm.

Several different sized flow regions were analyzed to investigate the requirement that a fracture system that exhibits porous medium behavior should have a specific discharge that remains stable. This study was conducted by varying the size of several square flow regions oriented at 0° and observing if the numerical solutions for q and θ converge to their theoretical values as the size increases. The theoretical solutions for q and θ apply to flow regions of infinite dimensions. However, only finite-sized flow regions can be created using numerical models. Thus, the difference between the theoretical and numerical solutions for q and θ should decrease as size increases.



XBL-829-4542

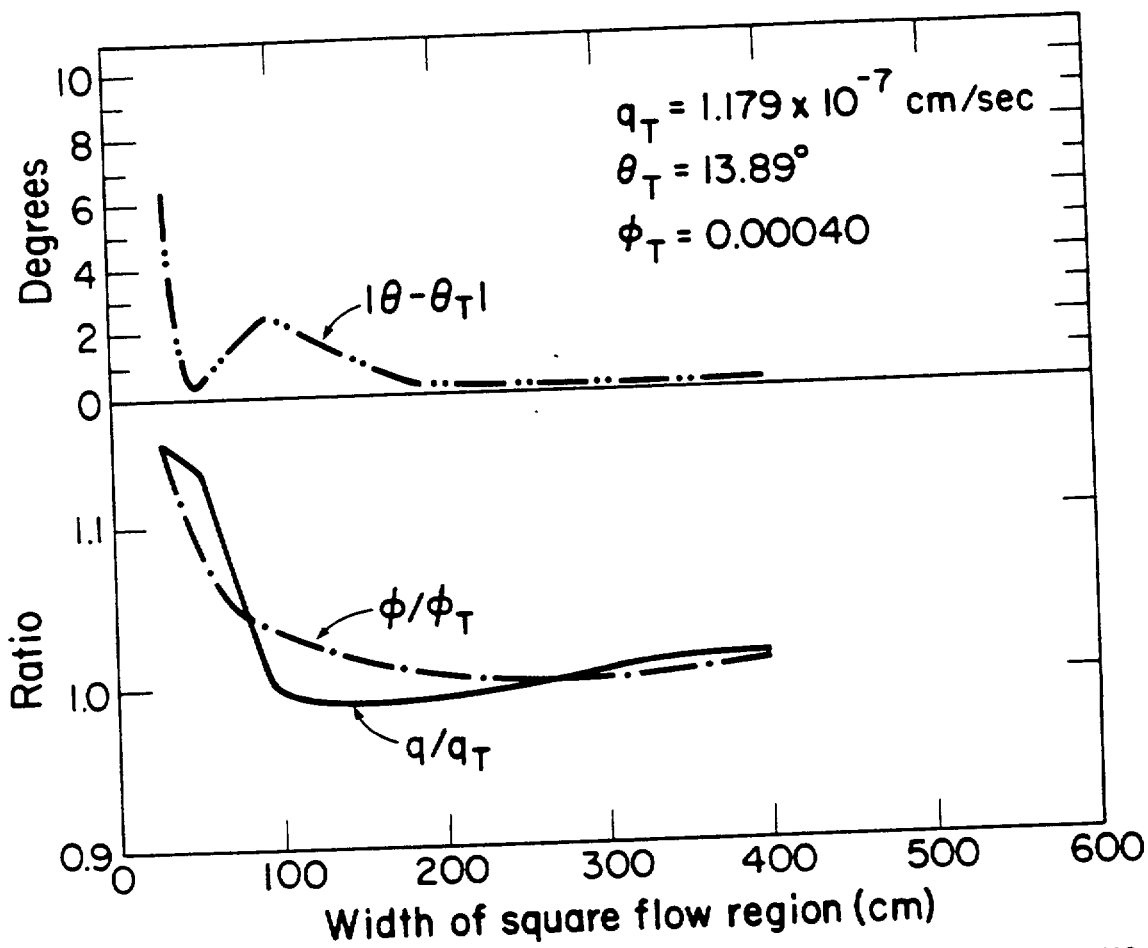
Figure 5-1 Fracture System With Two Sets of Parallel, Continuous, and Constant Aperture Fractures.

Figure 5-2 shows how the ratio of actual to theoretical specific discharge (q/q_T) approaches unity as the size of the flow region increases. Porous medium equivalence is also evident from the results for angle of flow. As shown in Figure 5-2, the deviation between actual and theoretical angles of flow ($|\theta - \theta_T|$) is negligible for flow regions larger than 200 x 200 cm. Further evidence that this size fracture network exhibits porous medium behavior can be obtained from the ratio of actual to theoretical porosity (ϕ/ϕ_T), which has also been plotted in Figure 5-2. Thus, the stability requirement is met for this particular fracture network when the size of the flow region is 200 x 200 cm or larger.

Next, flow results for different directions of flow were analyzed for equivalent porous medium behavior using the continuity test and the angle of flow test. Flow regions oriented at every 15°, beginning at orientation 0°, were used in this part of the study. Square flow regions of width 400 cm were used for orientations 0°, 15°, 30°, 45°, 60°, and 105°. Rectangular flow regions of size 186 x 400 cm were used for orientations 75° and 90°, because the angle of flow is greater than 45° for these two orientations. Side 2 had to be longer than side 1 to ensure that a zone of continuous flow existed from side 2 to side 4.

A comparison of numerical and theoretical values for q and θ is given in Table 5-1. The good agreement between numerical and theoretical values ($0.96 < q/q_T < 1.04$ and $|\theta - \theta_T| < 3^\circ$) is evidence that the stability requirement for porous medium behavior has been satisfied for all flow regions regardless of the orientation of the flow field. The angle of flow test is also satisfied for all orientations because the values computed for ANFC are essentially identical to those of ANFD. Furthermore, the continuity test is also satisfied because flow rates on opposing sides of the flow region are equal. This equivalence results from the fact that an equal number of fractures from each set intersect opposing sides of each flow region. Thus, each flow region that has been tested exhibits porous medium flow behavior.

Directional equivalent porous medium flow behavior can be shown using the flow results in Table 5-1. Marcus and Evenson (1961) have derived very useful relationships between specific discharge and direction of flow for porous media. If the hydraulic gradient is kept con-



XBL 833-1416

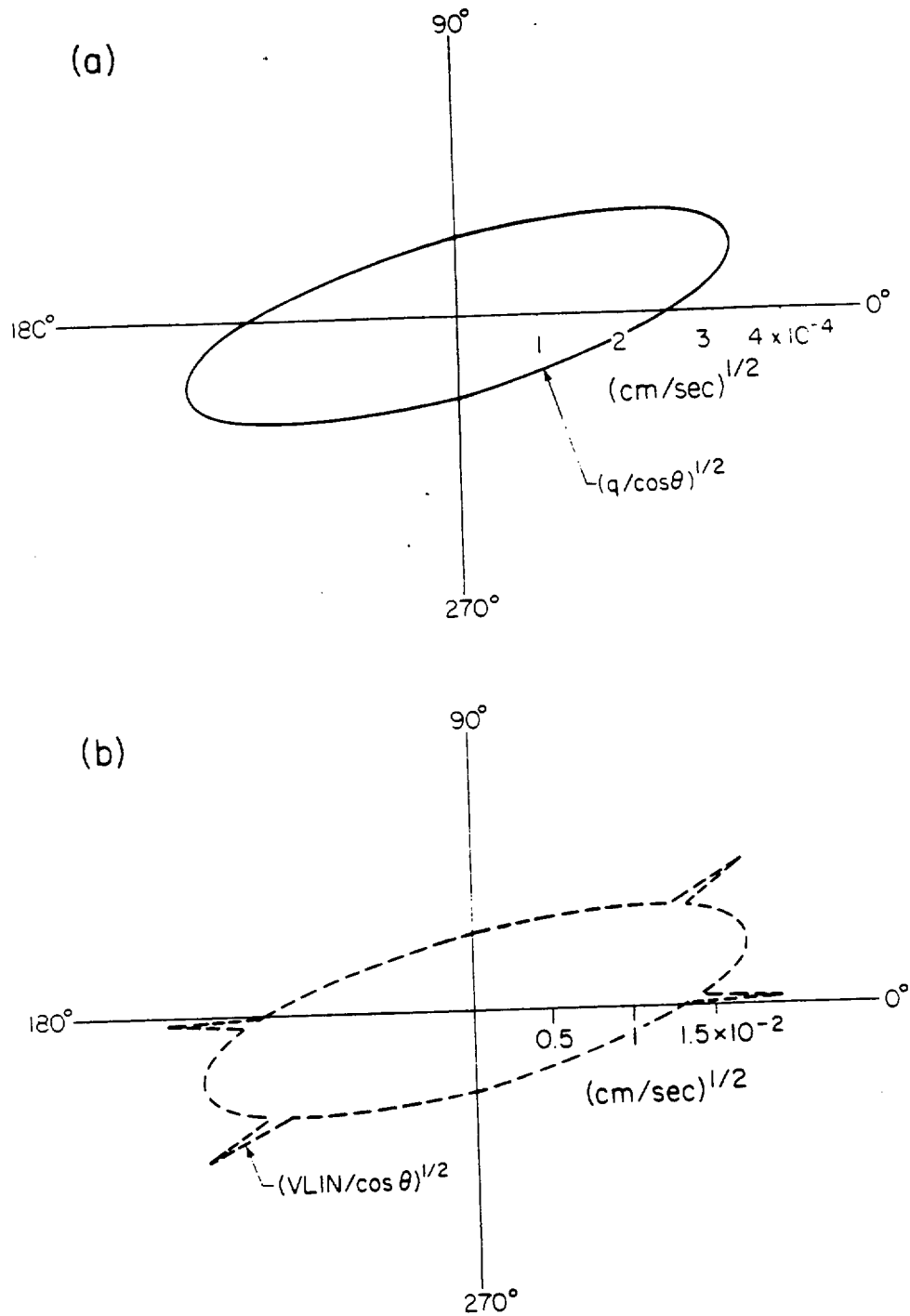
Figure 5-2 Convergence of Specific Discharge and Porosity to Their Theoretical Values as Size of Flow Region Increases (Ratio is q/q_T or ϕ/ϕ_T).

Orientation of Gradient degrees	Specific Discharge		Angle of Flow		
	Theoretical $10^{-7} \frac{\text{cm}}{\text{s}}$	Actual $10^{-7} \frac{\text{cm}}{\text{s}}$	Theoretical degrees	ANFC degrees	ANFD degrees
0	1.179	1.199	13.90	13.65	13.65
15	1.220	1.232	0	-1.47	0
30	1.179	1.184	-13.90	-13.84	-13.84
45	1.057	1.065	-27.63	-26.86	-26.86
60	0.8649	0.8706	-40.92	-40.82	-40.82
75	0.6147	0.6116	-52.91	-52.76	-52.76
90	0.3269	0.3406	-60.00	-61.32	-61.32
105	0.08759	0.0846	0	-2.87	-2.87

stant, as was done in this study, the square root of specific discharge divided by $\cos\theta$, $(q/\cos\theta)^{1/2}$, when plotted versus flow direction, forms an ellipse since $q/\cos\theta$ is equal to the product of K_f and the hydraulic gradient. Figure 5-3a shows the plot of $(q/\cos\theta)^{1/2}$ versus direction of flow. It may be seen that the specific discharge curve is an ellipse with directions of maximum and minimum permeabilities near 15° and 105° , respectively. The ellipse is symmetric about these two principal directions. As expected from theory, this particular network of continuous fractures has the same flow behavior as an equivalent porous medium.

Having demonstrated that this system of continuous fractures behaves like an equivalent porous medium for fluid flow, the model was next used to investigate continuum behavior for transport. For comparative purposes, one needs the total porosity of the fracture system. The porosity of each set is 0.0002, which is simply the 0.002 cm aperture divided by the 10 cm spacing, and therefore the total porosity for the two sets is 0.0004.

Figure 5-4 is a plot of the hydraulic effective porosity versus direction of flow, which was determined by adding the angle of flow to the orientation of the flow region. At orientation 90° (where the theoretical flow direction is 30°) and orientation 120° (where the theoretical flow direction is 180°) there is a dramatic reduction in ϕ_H . At either orientation, one set of fractures becomes nonconductive because it is perpendicular to the hydraulic gradient. The result is that $\phi_H = \phi/2$ in either flow direction. The directional dependence in the hydraulic effective porosity shows that this fracture system does not behave like an equivalent porous medium for



XBL 636-524A

Figure 5-3 Polar Plots of a) Specific Discharge and b) Average Linear Velocity Factor Versus Direction of Flow for System of Two Set of Parallel, Continuous, and Constant Aperture Fractures.

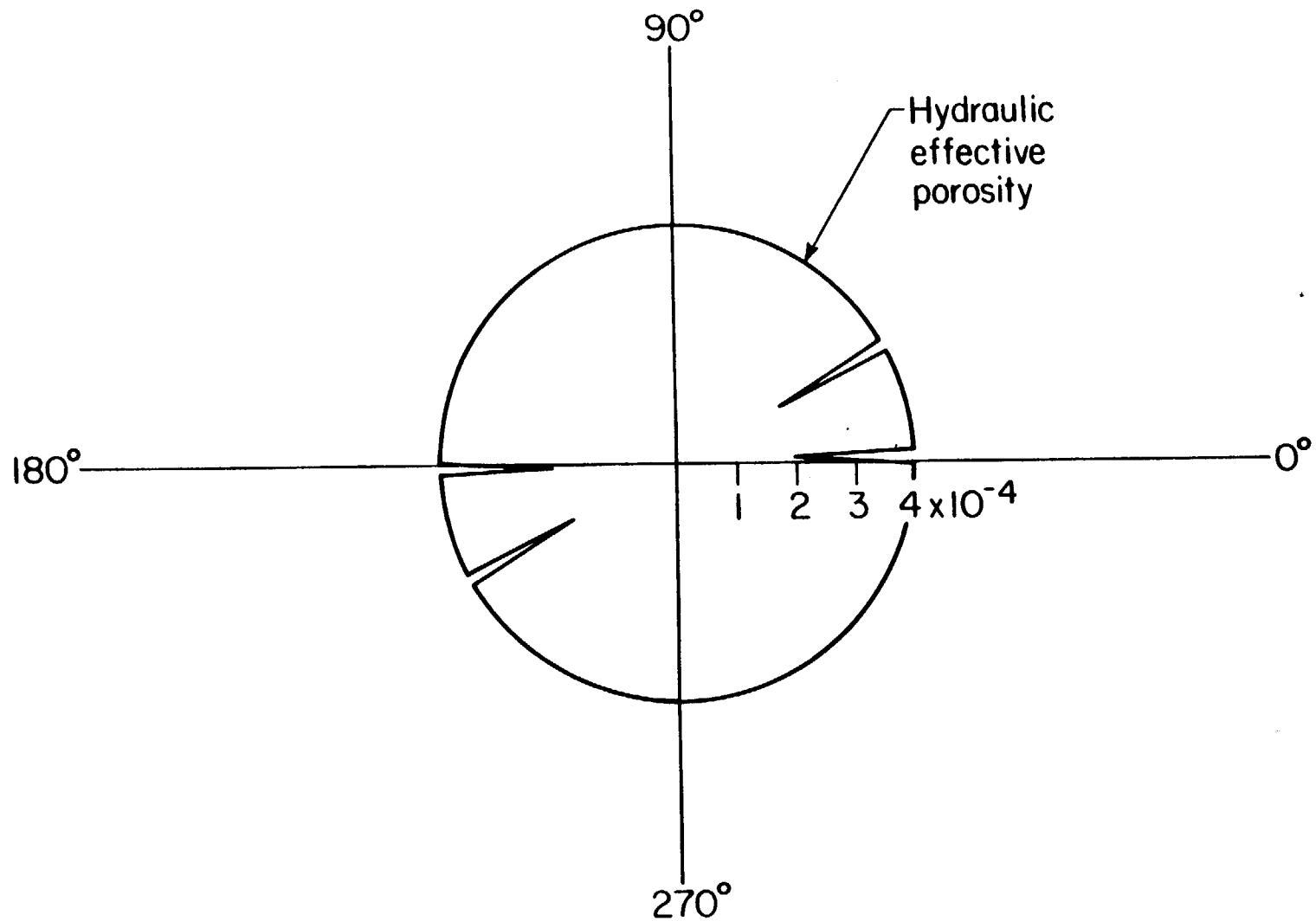


Figure 5-4 Polar Plot of Hydraulic Effective Porosity Versus Direction of Flow for System of Two Sets of Parallel, Continuous, and Constant Aperture Fractures.

XBL 833-1421

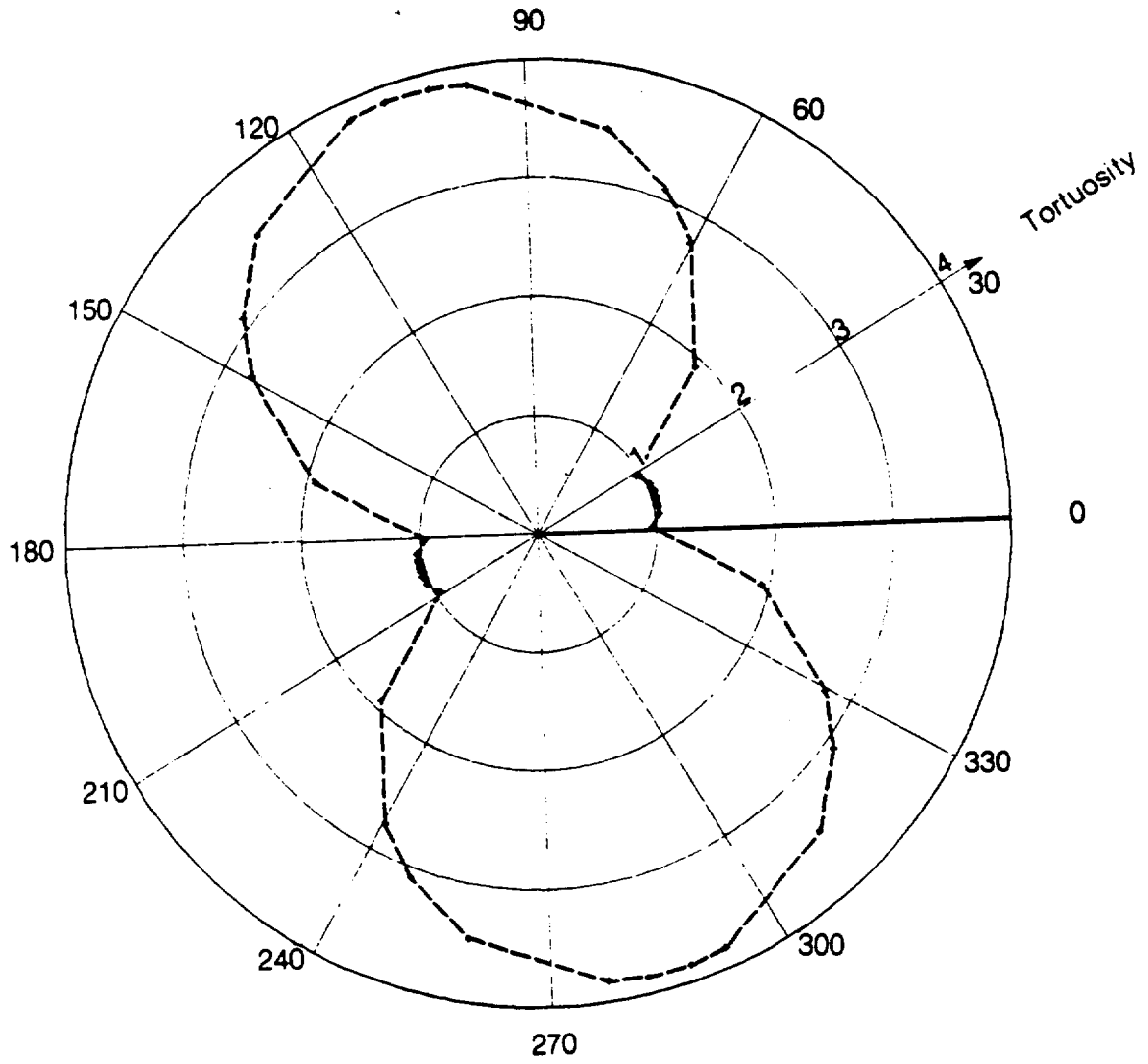
transport.

At orientation 105° , ϕ_H decreases slightly below ϕ and obtains a value of 0.000384. To check this result, two additional square flow regions of widths 320 and 450 cm were tested. The resulting ϕ_H were 0.000385 and 0.000409, respectively. This clearly indicates that ϕ_H is converging to ϕ and that the size of the mechanical transport continuum varies with direction. However, the convergence proceeds at different rates for different directions.

The change in convergence rate is directly related to the tortuosity. As tortuosity increases, travel paths become more irregular and deviate more from the flow direction. Consequently, larger flow regions are needed before representative mechanical transport behavior occurs. Figure 5-5 shows that the tortuosity is relatively stable at 1.04 between directions 0° to 30° . At direction 30° , the tortuosity reaches a theoretical minimum of 1.0. Tortuosity then increases rapidly to 3.86 near direction 105° . The bisection of the hydraulic gradient with the obtuse angle of 150° resulting from the intersection of the two fracture sets (Figure 5-1) caused tortuosity to be maximum in this direction. Thus, the large tortuosity in this direction results in a slight oscillation in ϕ_H . Tortuosity should be inversely proportional to permeability for an equivalent porous medium. Since tortuosity is relatively stable between directions 0° and 30° , tortuosity does not behave like it would for an equivalent porous medium. However, between 30° and 105° tortuosity does behave like it would for an equivalent porous medium.

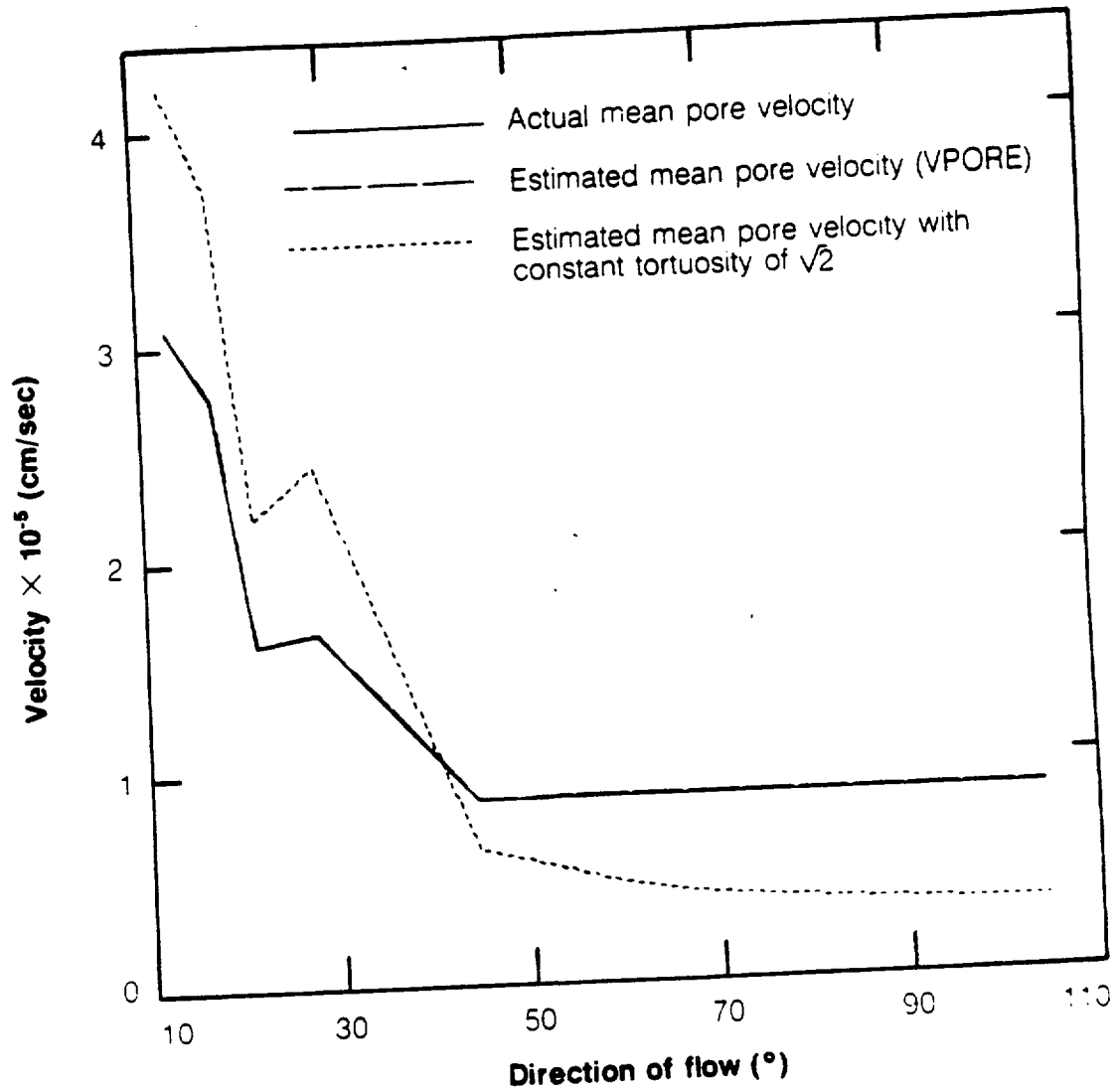
Figure 5-6 shows a plot of VPORE versus flow direction. This figure shows that there is no difference between VPORE and the mean pore velocity. In transport studies, tortuosity is rarely computed and normally assigned a value about $\sqrt{2}$. This figure also demonstrates that if a constant tortuosity of $\sqrt{2}$ had been used to compute VPORE, a serious error in the calculated mean pore velocity would have resulted.

If the hydraulic effective porosity is a constant, then the square root of the average linear velocity divided by $\cos\theta$, $(V_{LIN}/\cos\theta)^{1/2}$, should plot as an ellipse for an equivalent porous medium since $(q/\cos\theta)^{1/2}$ would plot as an ellipse. The plot of $(V_{LIN}/\cos\theta)^{1/2}$ in Figure 5-3b also demonstrates that this fracture system cannot be treated as equivalent porous medium for tran-



XBL 838-565

Figure 5-5 Tortuosity Versus Direction of Flow for Fracture System of Two Sets of Parallel, Continuous, and Constant Aperture Fractures.



XBL 838-564

Figure 5-6 Actual Mean Pore Velocity, Calculated Mean Pore Velocity, and Calculated Mean Pore Velocity With Tortuosity of $\sqrt{2}$ for Fracture System of Two Sets of Continuous, Parallel, and Constant Aperture Fractures.

sport. Although the VLIN curve coincides with the q curve in most directions, there are four sharp cusps in the directions where ϕ_H drops dramatically.

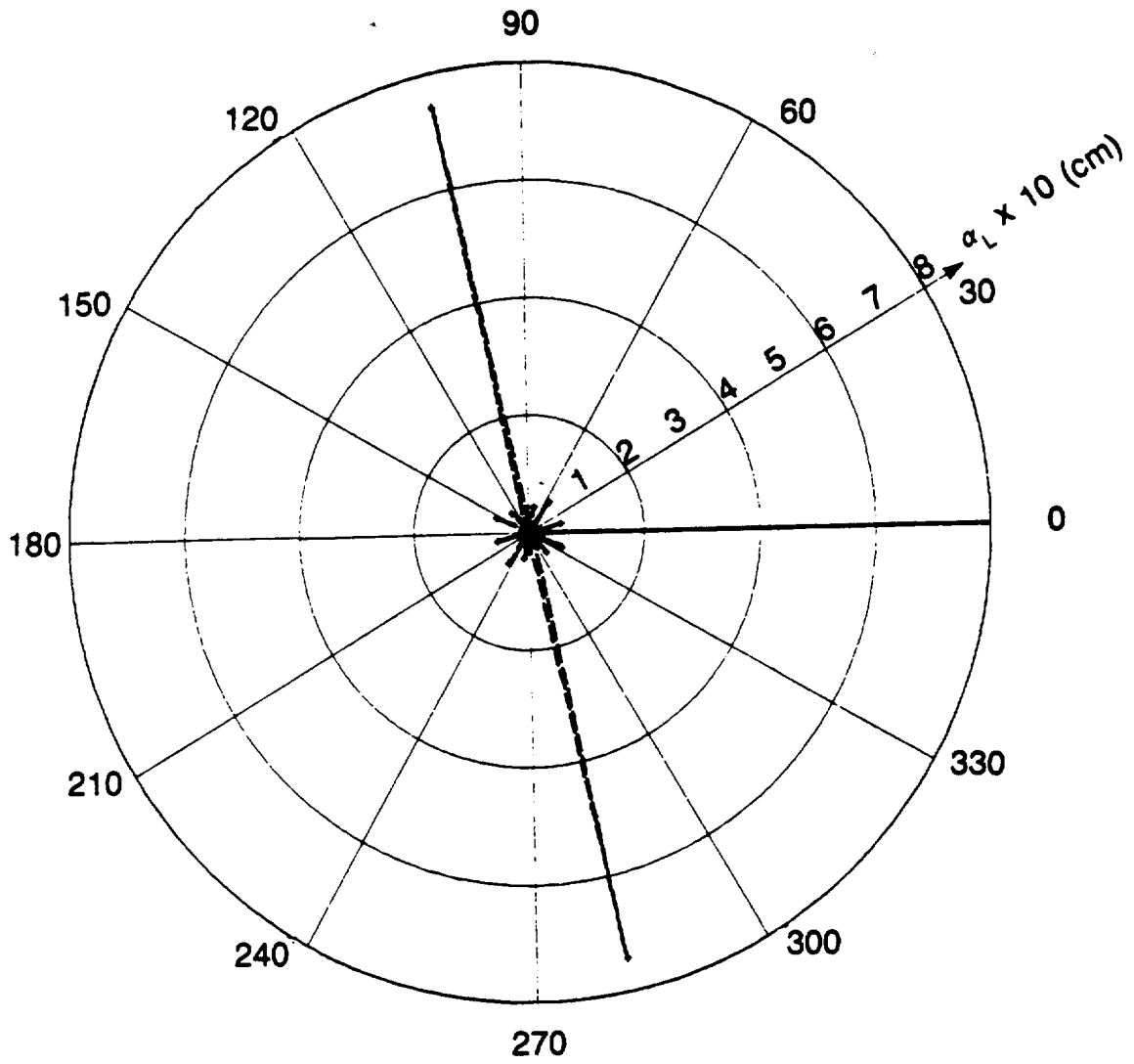
Figure 5-7 is the polar plot of the longitudinal geometric dispersivity. This plot definitely shows that α_L is directionally dependent. The maximum α_L of 74 cm occurs in the direction of minimum permeability. Longitudinal geometric dispersivity is much smaller in all other directions, but α_L is zero only near directions of flow 30° and 0° . Longitudinal geometric dispersivity is minimum in these directions because only one set conducts flow, and the velocity in each fracture of this set is constant.

The applicability of the Fickian dispersive approach was investigated for flow direction 18.3° (orientation 45°) using two square flow regions of widths 200 and 400 cm. When the Fickian approach is applicable, α_L will not vary with the size of the flow region. The longitudinal geometric dispersivities computed for the two sizes were 0.882 cm and 0.995 cm, respectively. The scale-dependent dispersivity shows that the Fickian approach cannot be applied at this scale.

5.3. SYSTEM WITH TWO ORTHOGONAL SETS OF CONTINUOUS FRACTURES

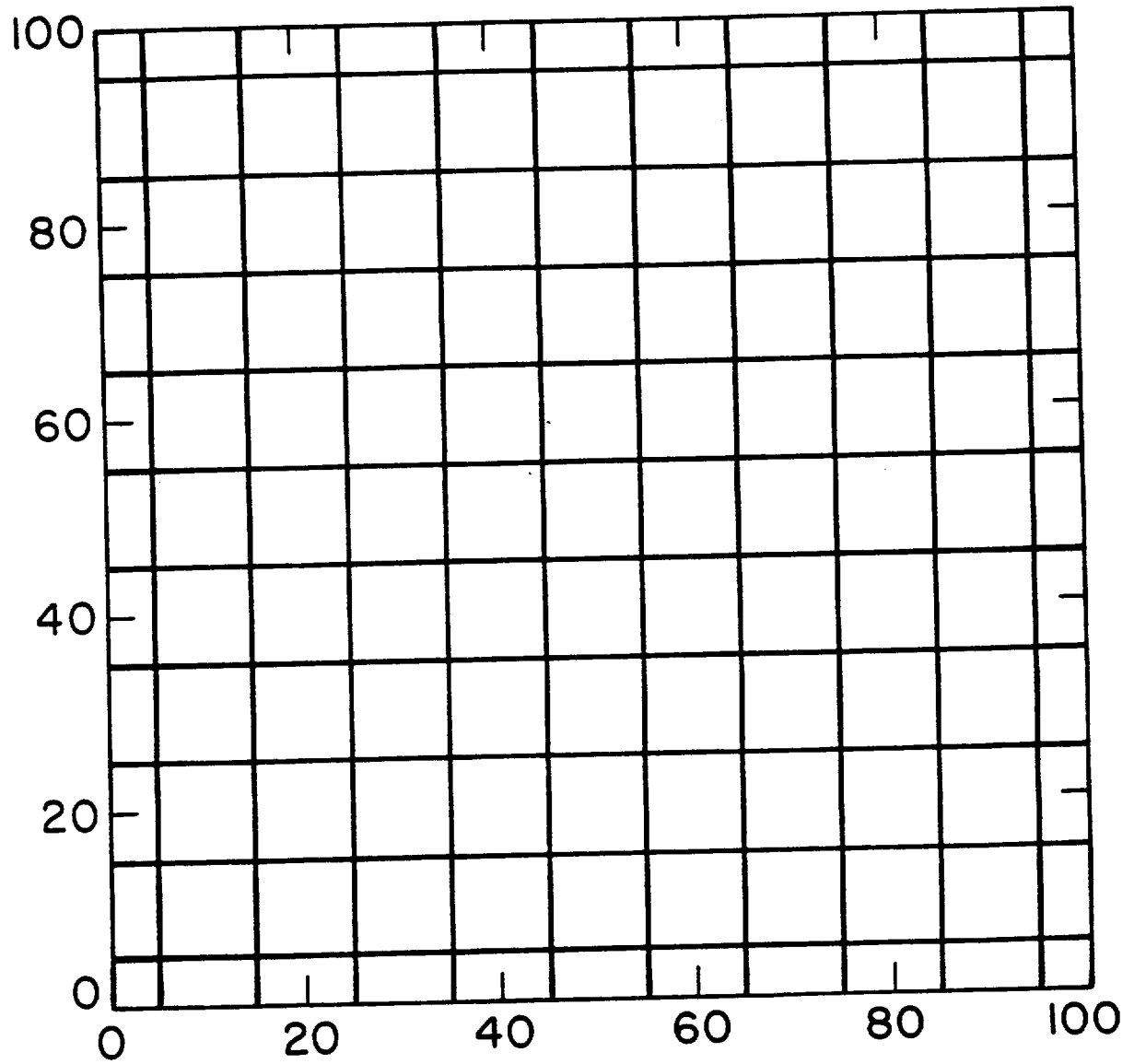
In the second investigation with this model, the system consisted of two sets of parallel fractures oriented at right angles to each other and all spaced 10 cm apart as shown in Figure 5-8. Anisotropy was achieved by using an aperture of 0.002 cm for the first set oriented at 0° , and an aperture of 0.004 cm for the second set oriented at 90° . Thus, the direction of maximum principal permeability is 90° , and the direction of minimum principal permeability is 0° . The hydraulic gradient along sides 1 and 3 (see Figure 3-4) was set at 0.01 for all flow regions. The total porosity is 0.0006; the porosity for the set oriented at 0° is 0.0002 and that for the set at 90° is 0.0004.

Sizes of flow regions were selected so that the number of elements and nodes in each region was nearly equal to that of the first study. It was anticipated that using the same number of elements and nodes would produce equivalent porous medium flow behavior in this orthogonal fracture system. Square flow regions of width 280 cm were used for orientations 0° ,



XBL 841-387

Figure 5-7 Polar Plot of Longitudinal Geometric Dispersivity for Fracture System of Two Sets of Continuous, Parallel, and Constant Aperture Fractures.



XBL 838-563

Figure 5-8 Fracture System With Two Orthogonal Sets of Continuous Fractures.

45°, 60°, 75° and 90°. Rectangular flow regions of 235 x 335 cm were used for orientations 15° and 30° because the angle of flow was greater than 45°.

A comparison of numerical and theoretical values for specific discharge is given in Table 5-2. The results demonstrate that each flow region behaves like an equivalent porous medium for fluid flow. Figure 5-9a illustrates directional equivalent porous medium behavior. The plot of $(q/\cos\theta)^{1/2}$ is an ellipse whose maximum axis coincides with the maximum principal permeability at 90° and whose minimum axis coincides with the minimum value of permeability at 0°. This is further evidence that this system of orthogonal fractures behaves like an equivalent porous medium for fluid flow.

Table 5-2. Specific Discharge Results for Fracture System With Two Orthogonal Sets of Fractures.

Orientation of Gradient degrees	Specific Discharge		Angle of Flow		
	Theoretical $10^{-7} \frac{\text{cm}}{\text{s}}$	Actual $10^{-7} \frac{\text{cm}}{\text{s}}$	Theoretical degrees	ANFC degrees	ANFD degrees
0	0.6538	0.6538	0	-0.31	-0.40
15	1.496	1.499	49.99	50.91	50.90
30	2.676	2.691	47.78	47.52	46.82
45	3.727	3.681	37.87	38.08	37.87
60	4.541	4.668	25.87	25.64	25.12
75	5.055	5.086	13.08	14.72	14.59
90	5.230	5.230	0	0	0

The model was next used to investigate continuum behavior for transport, and the results are shown in Figure 5-10. We again see a drastic reduction in hydraulic effective porosity when the direction of gradient is at right angles to either fracture set. Figure 5-10 clearly illustrates the directional dependence of hydraulic effective porosity for this orthogonal fracture system. The plot of $(VLIN/\cos\theta)^{1/2}$ in Figure 5-9b reveals an unexpected result. One would normally associate the direction of minimum principal permeability as an indication of the direction of the minimum velocity. However, the minimum value of VLIN does not occur at 0° because the minimum hydraulic effective porosity occurs in this direction. In dealing with fracture networks of this kind, one simply cannot associate directions of principal permeabilities with the directions of maximum or minimum linear velocities.

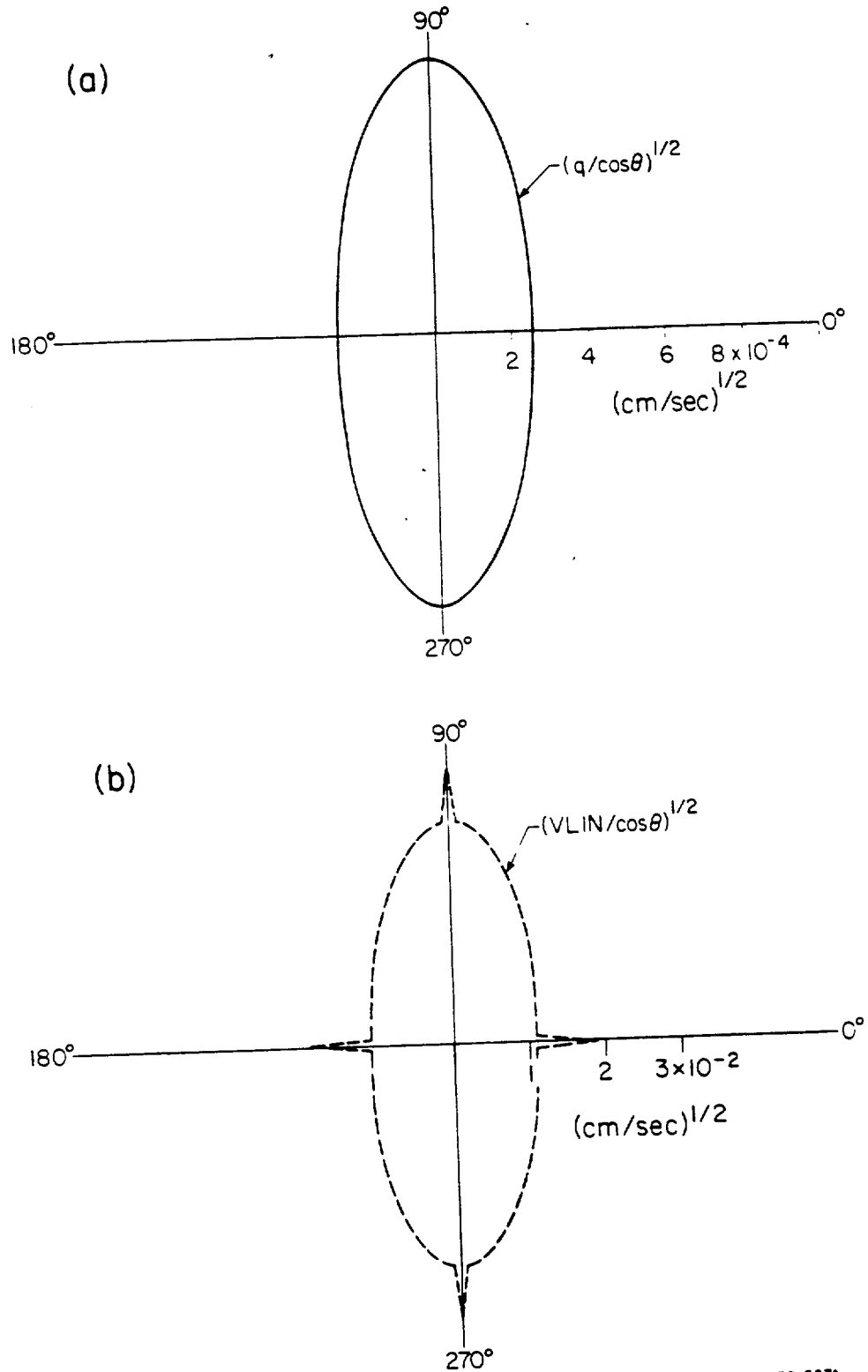
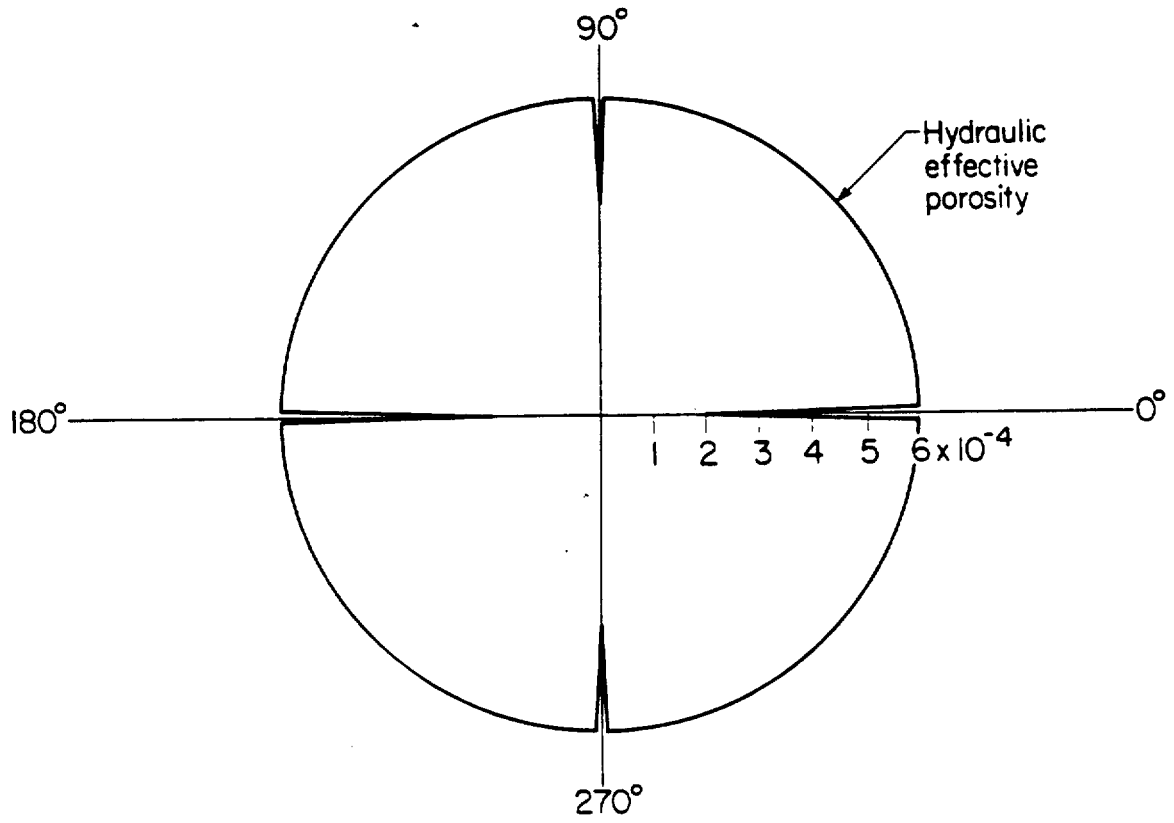


Figure 5-9 Polar Plots of a) Specific Discharge and b) Average Linear Factors Versus Direction of Flow for System With Two Orthogonal Sets of Continuous Fractures.

XBL 838-527A



XBL 833-1422

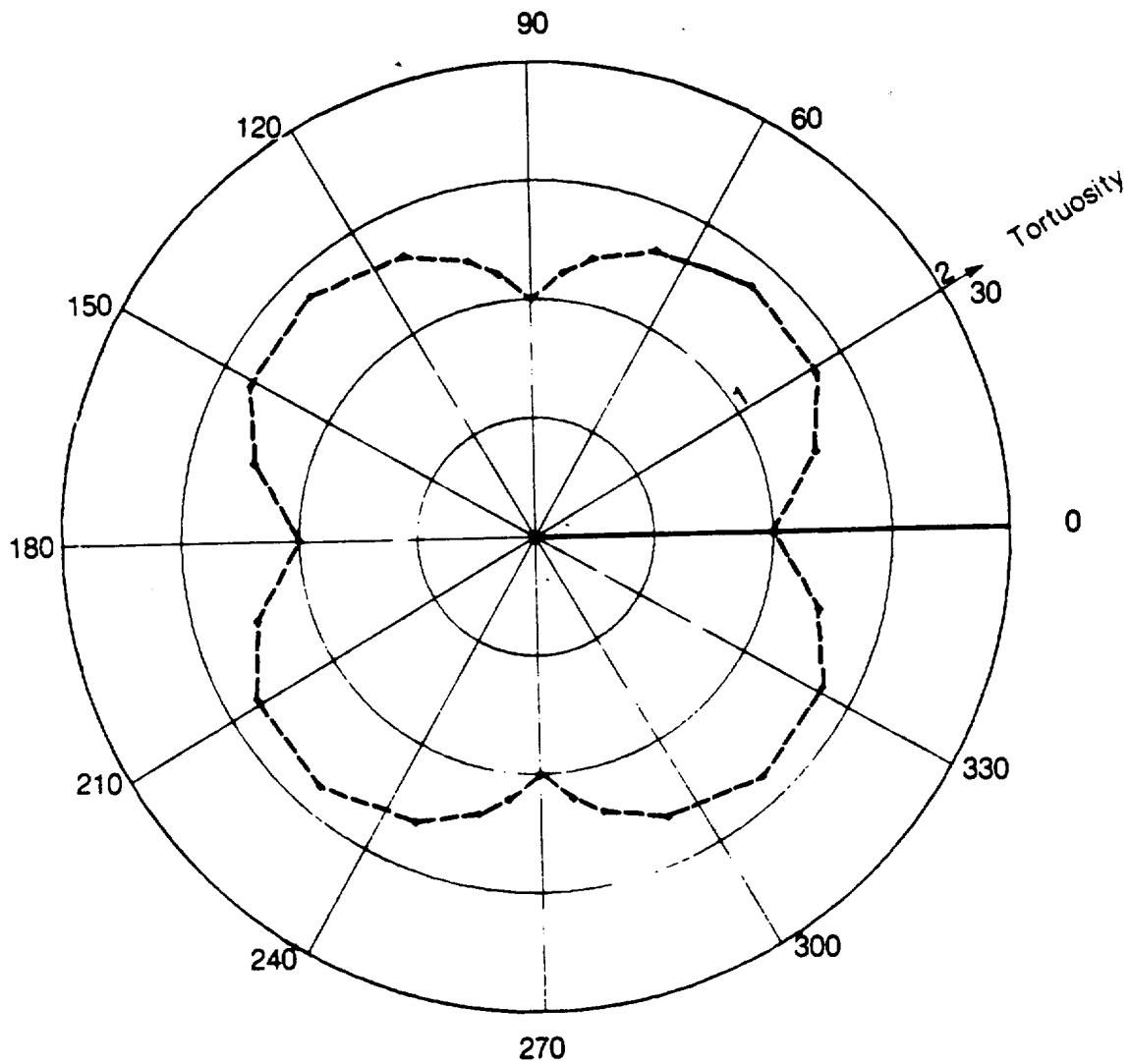
Figure 5-10 Polar Plot of Hydraulic Effective Porosity for System of Two Orthogonal Sets of Continuous Fractures.

The tortuosity versus direction of flow is shown in Figure 5-11. The directional nature in tortuosity shows that this parameter does not behave like it would for an equivalent porous medium. This is clearly evident in the direction of minimum permeability where tortuosity is minimum. This is exactly opposite of what one would expect for an equivalent porous medium.

The polar plot in Figure 5-12 shows that α_L is strongly directionally dependent. The maximum α_L of 26 cm is obtained in the four directions 7° from the direction of maximum permeability. In the two principal directions, α_L is zero because only one of the sets conducts flow, and the velocity in each fracture for this set is constant. Thus unlike the previous continuous system where α_L reached its maximum value in the direction of minimum permeability, α_L has a minimum value in the direction of minimum permeability.

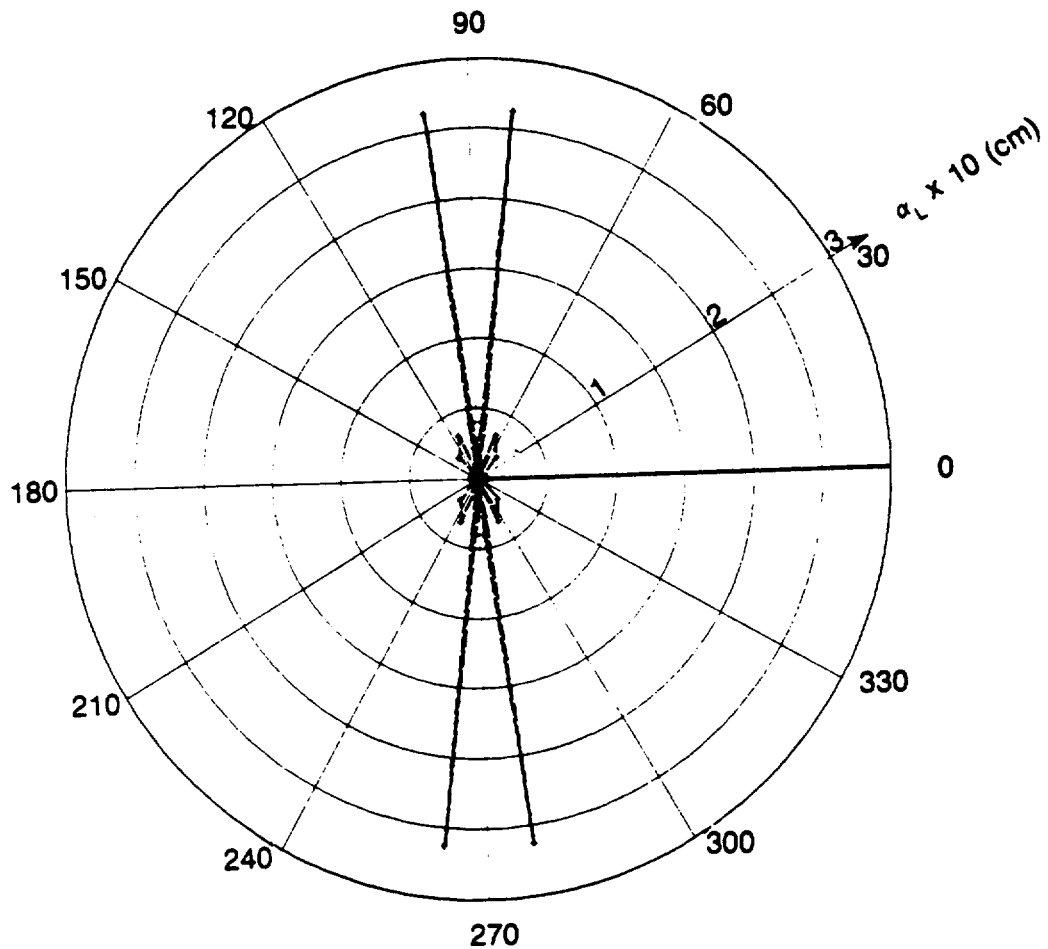
The polar plots of α_L for the two continuous fracture systems both show large directional variations in α_L . The maximum α_L is much larger in the first continuous system where anisotropy is greater. If a directionally-stable α_L is used to model transport for each system, serious errors in transport prediction would result. Yet, this type of modeling is presently practiced by treating an anisotropic medium as an equivalent isotropic medium.

This orthogonal fracture system can easily be made isotropic by making the apertures for both sets the same. Theoretically, α_L is directionally stable for an isotropic porous medium. If this fracture system were converted to an isotropic medium, a directionally stable α_L would not result. In directions of flow 0° and 90° , longitudinal geometric dispersivity would be zero. In all other directions, longitudinal geometric dispersivity would be nonzero. This clearly shows that a system which behaves like an equivalent isotropic porous medium for fluid flow, may not have a α_L which is directionally stable as theoretically expected.



XBL 838-562

Figure 5-11 Polar Plot of Tortuosity for Fracture System With Two Orthogonal Sets of Continuous Fractures.



XBL 841-388

Figure 5-12 Polar Plot of Longitudinal Geometric Dispersivity for System With Two Orthogonal Sets of Continuous Fractures.

CHAPTER 6

INVESTIGATION OF DISCONTINUOUS FRACTURE SYSTEMS

6.1. INTRODUCTION

A continuous fracture system is created in the generation region when all fractures are long compared to the size of the generation region. However, it is more likely that a fracture system must be studied in which the fractures do not span the width of the region. A fracture system consisting of finite-length fractures is called a discontinuous fracture system. Discontinuous fracture systems are much more difficult to analyze than continuous fracture systems. Continuous fracture systems have been shown to behave like equivalent porous media for fluid flow. This is not the case for discontinuous systems. The concepts developed in section 3.9 are used to evaluate equivalent porous medium flow behavior for discontinuous systems.

Mechanical transport is influenced by the paths of fluid flow in the conductive void spaces of a fracture system. Flow paths differ in discontinuous and continuous systems due to the structure of the void regions. In a continuous fracture system, all fractures are connected such that fluid can flow through the entire void region. However, conductive spaces are only part of the total void region in a discontinuous fracture system. The void region also consists of dead-end zones and isolated spaces where fluids cannot flow.

6.2. DISCONTINUOUS FRACTURE SYSTEM OF TWO SETS ORIENTED AT 0° AND 30°

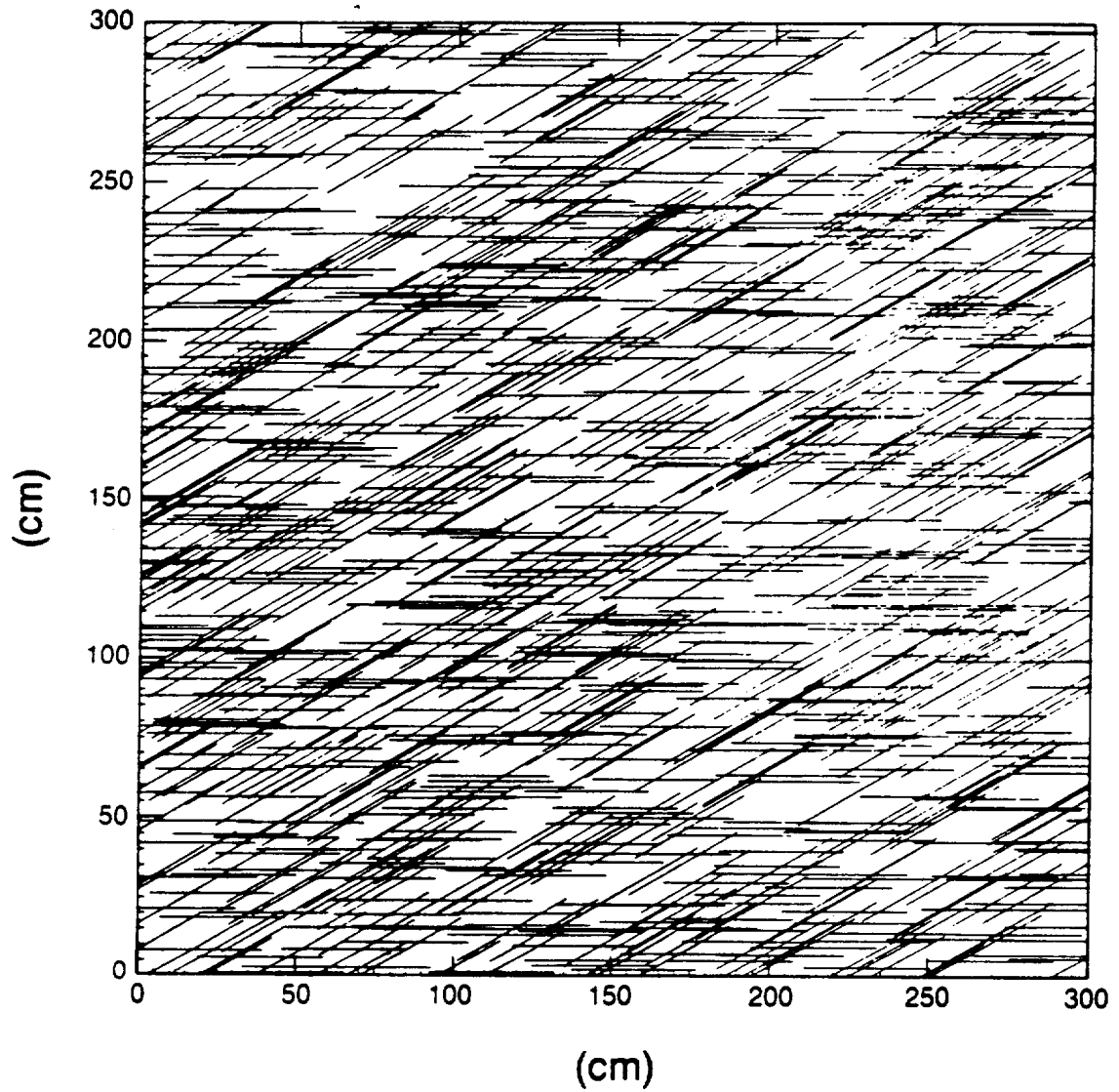
The first discontinuous fracture system studied was chosen to simulate the continuous fracture system in section 5.2. The discontinuous system consisted of two sets of fractures oriented at 0° and 30°. The areal density for each set was 0.00633 cm^{-2} . All fractures had an aperture of 0.002 cm and a length of 40 cm. A Monte Carlo simulation was required because fracture centers were randomly located in the generation region. The Monte Carlo simulation consisted of 10 realizations; the size of generation region used in each realization was 300 x 300

cm. Figure 6-1 shows the fracture pattern in the generation region for one of the realizations. The fracture pattern for the discontinuous fracture system differed considerably from the simulated continuous fracture system because of the random location of fracture centers and finite length of fractures.

The objective for each realization was to obtain a representative directional sample of mechanical transport and fluid flow properties. This required estimating the direction of flow for a given orientation of the hydraulic gradient. Since the angle of flow cannot be computed from first principles for discontinuous systems, the direction of flow for a given orientation of the hydraulic gradient was estimated from θ calculated for the simulated continuous fracture system. Based on these calculations, nine orientations of a uniform hydraulic gradient of 0.01 were selected to study fluid flow and mechanical transport. The nine orientations and estimated directions of flow are listed in Table 6-1.

The flow region sizes used in the Monte Carlo simulation were determined from a size study conducted in the first realization for orientation 15°. In the size study, the width of a square flow region oriented at 15° was slowly increased until the flow field exhibited the characteristics of an equivalent porous medium. This meant that the following conditions had to be satisfied: continuity test, angle of flow test, and stability of \bar{q} . When the width of the flow region was 180 cm, DEVF equaled 1.21, DEVA equaled 1.84°, and q was relatively stable. Consequently, a minimum flow region size of 32400 cm² was used in the Monte Carlo simulation. Table 6-1 lists the flow region sizes used to initiate the Monte Carlo simulation. The actual dimensions of the flow regions were selected such that a zone of continuous flow existed between sides 2 and 4 for the estimated direction of flow. Figure 6-2 shows the fracture pattern and connected fracture segments in a flow region oriented at 83° in one of the realizations.

Figure 6-3 is a polar plot of the mean square root of permeability in the direction of flow $\sqrt{K_f}$. Mean $\sqrt{K_f}$ was computed by averaging $\sqrt{K_f}$ for the ten realizations. For each mean $\sqrt{K_f}$, the standard error of the mean was computed. The standard error of the mean is a measure of the scatter in the data and is defined as the sample standard deviation divided by the



XBL 841-389

Figure 6-1 Fracture Network in the Generation Region for Discontinuous Fracture System of Two Sets of Fractures Oriented at 0° and 30° With Constant Aperture and Length.

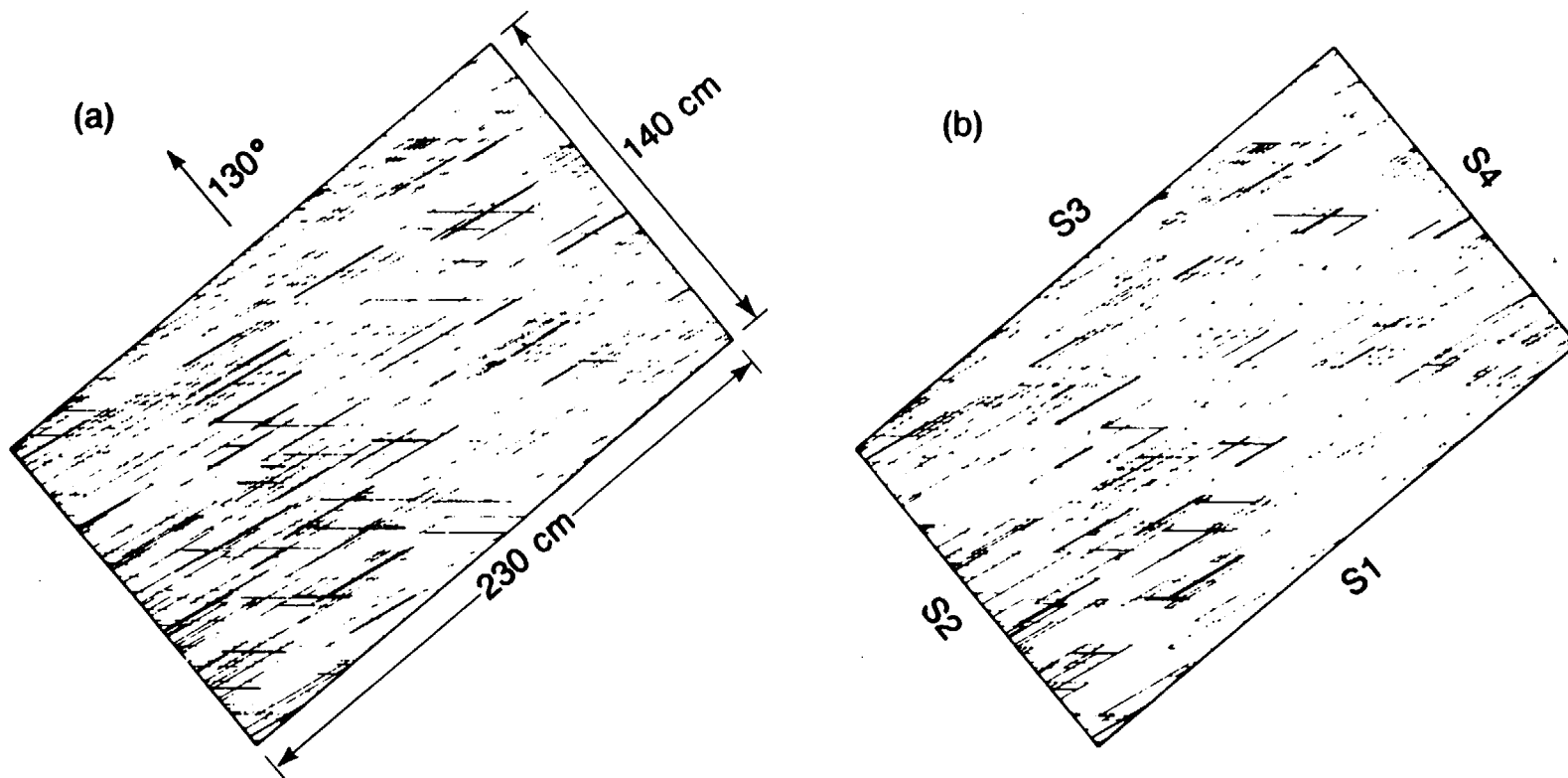


Figure 6-2 Networks of a) Fractures and b) Connected Fracture Segments in Flow Region Oriented at 130° for Discontinuous Fracture System of Two Sets Oriented at 0° and 30°.

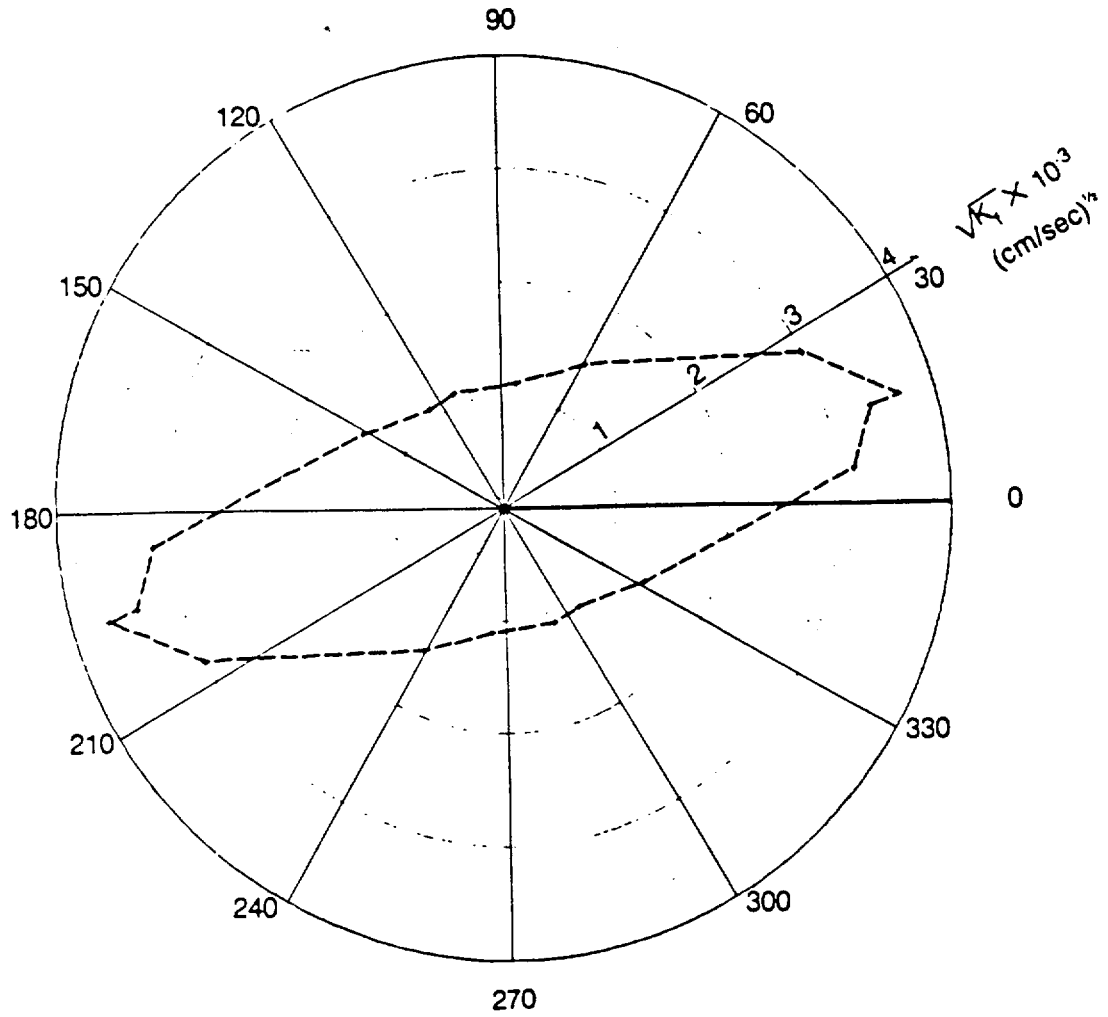
XBL 839-878A

Table 6-1. Orientations, Estimated Directions of Flow, and Flow Region Sizes Used in Monte Carlo Simulation of the Discontinuous System Consisting of Two Sets of Fractures Oriented at 0° and 30°.

Orientation of hydraulic gradient degrees	Direction of flow based on continuous system in section 5.2 degrees	Flow region size cm ²
15	15	180 x 180
83	25.08	140 x 230
100	54.37	170 x 188
104	91.34	180 x 180
105	105	180 x 180
106.5	125	170 x 188
110	155.6	170 x 188
130	186.2	140 x 230
160	192.1	180 x 180

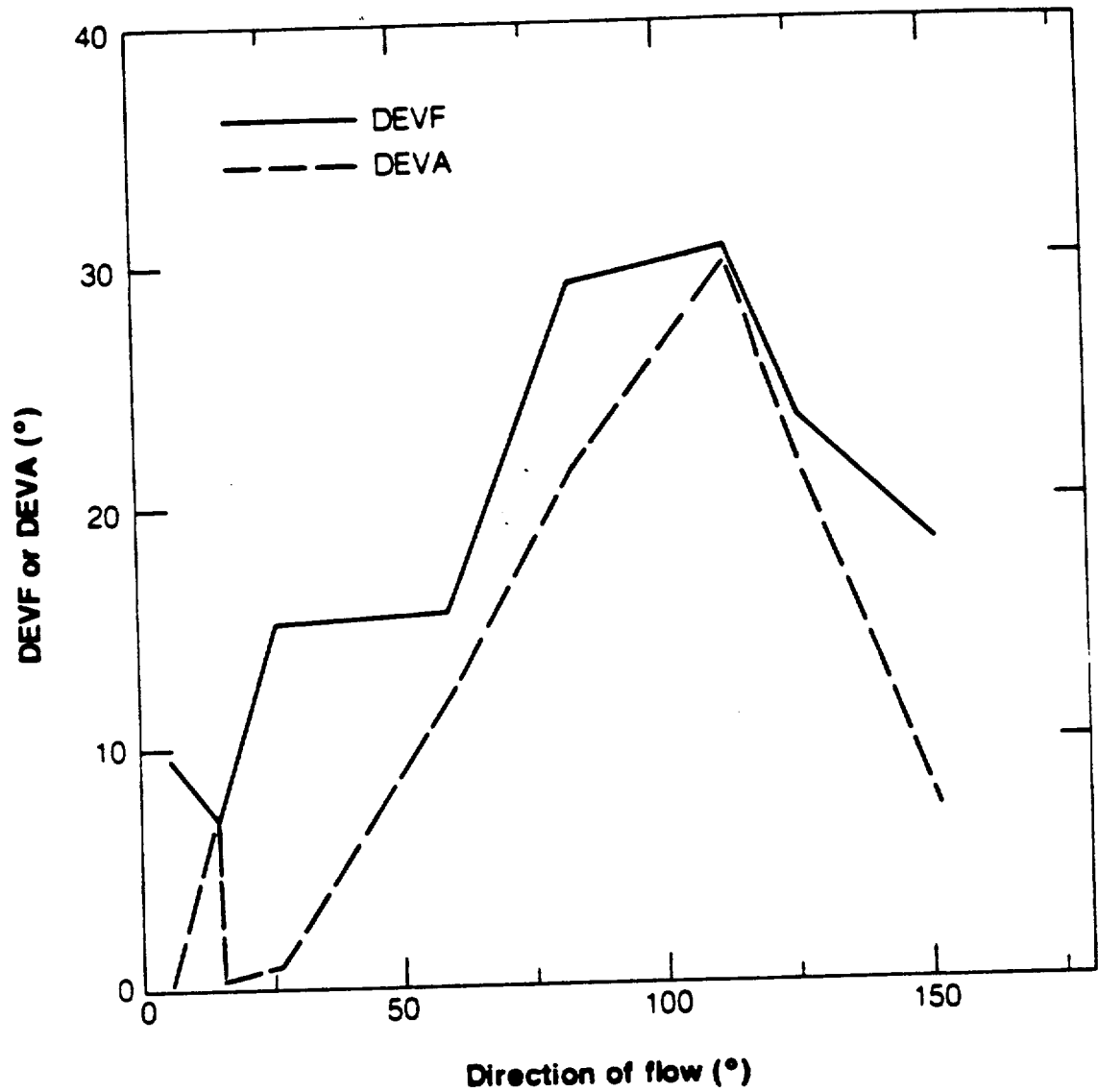
square root of the number of realizations (Topping, 1955; Baird, 1962). The computed mean from the data has a probability of approximately 68 percent of being within \pm one standard error of the true value. The standard error of the mean $\sqrt{K_f}$ was less than 0.00006 (cm/s)^{1/2} in all directions except in mean direction of flow 15.14° where the standard error was 0.00010 (cm/s)^{1/2}. In this direction, there is an irregularity in the $\sqrt{K_f}$ curve. The plot of mean $\sqrt{K_f}$ is similar to the plot of $(q/\cos\theta)^{1/2}$ for the simulated continuous fracture system (Figure 5-3). The shape of the mean $\sqrt{K_f}$ curve is approximately an ellipse with directions of maximum and minimum permeabilities near 15° and 105°, respectively. The ratio of K_x to K_y is about eleven. Thus, the directional flow characteristics for this fracture system behave like an equivalent porous medium.

Equivalent porous medium flow behavior was also evaluated for each direction of flow using the parameters DEVA and DEVF. When DEVA and DEVF are both small, equivalent porous medium behavior is likely to occur in that particular direction. Mean DEVA and mean DEVF are plotted versus direction of flow in Figure 6-4. DEVA exhibits two local maxima near each principal direction. The general tendency of the DEVA curve is for this parameter to increase as direction increases from the direction of maximum permeability to the direction of minimum permeability. DEVF also increases as direction of flow moves from the direction of maximum permeability to the direction of minimum permeability. Thus, porous medium



xBL 839-877

Figure 6-3 Polar Plot of Square Root of Permeability in Direction of Flow for Discontinuous Fracture System of Two Sets Oriented at 0° and 30°.



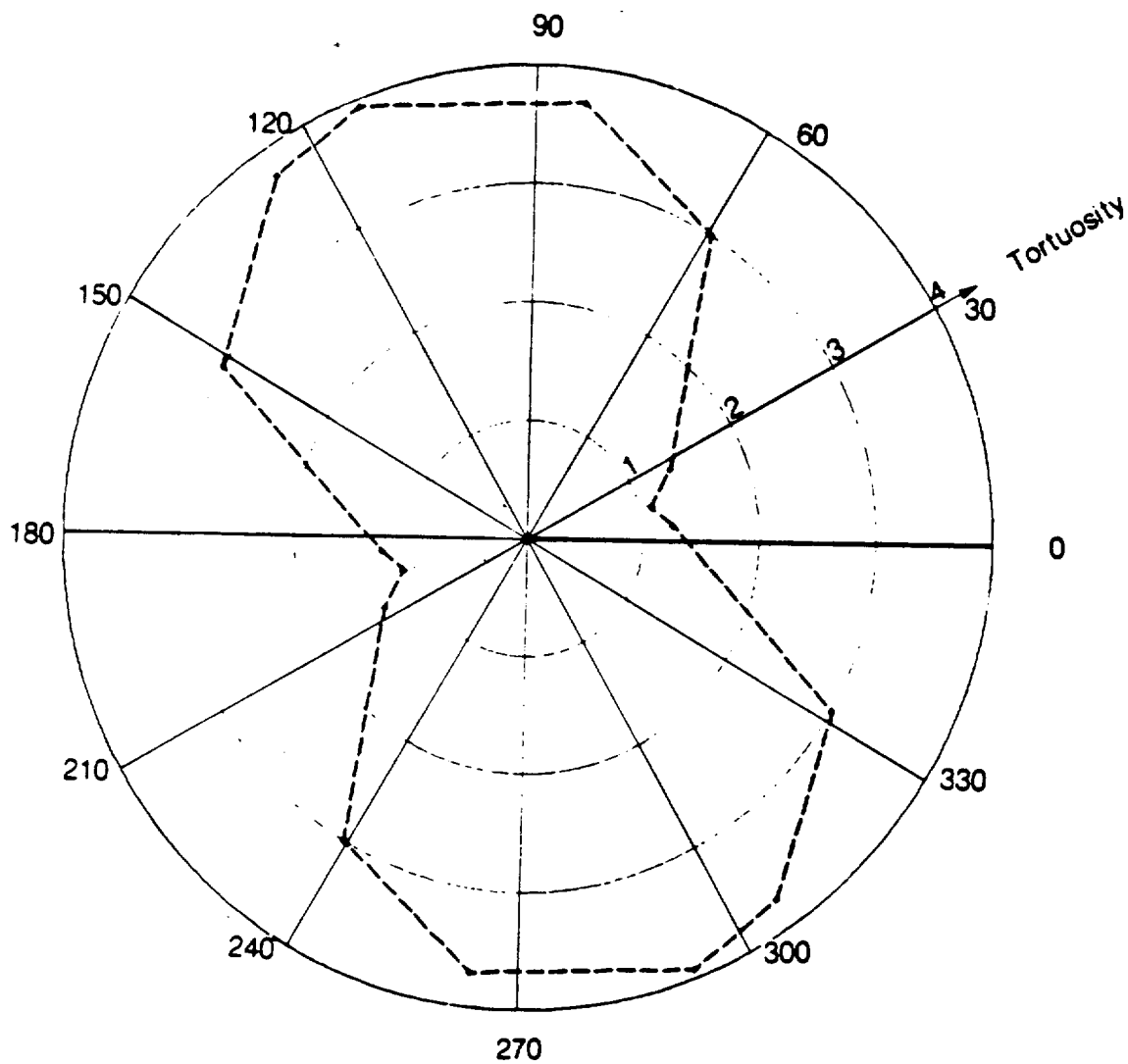
XBL 839-873

Figure 6-4 Mean DEVF and Mean DEVA Versus Direction of Flow for Discontinuous Fracture System of Two Sets Oriented at 0° and 30°.

equivalence is more likely to occur near the direction of maximum permeability than near the direction of minimum permeability.

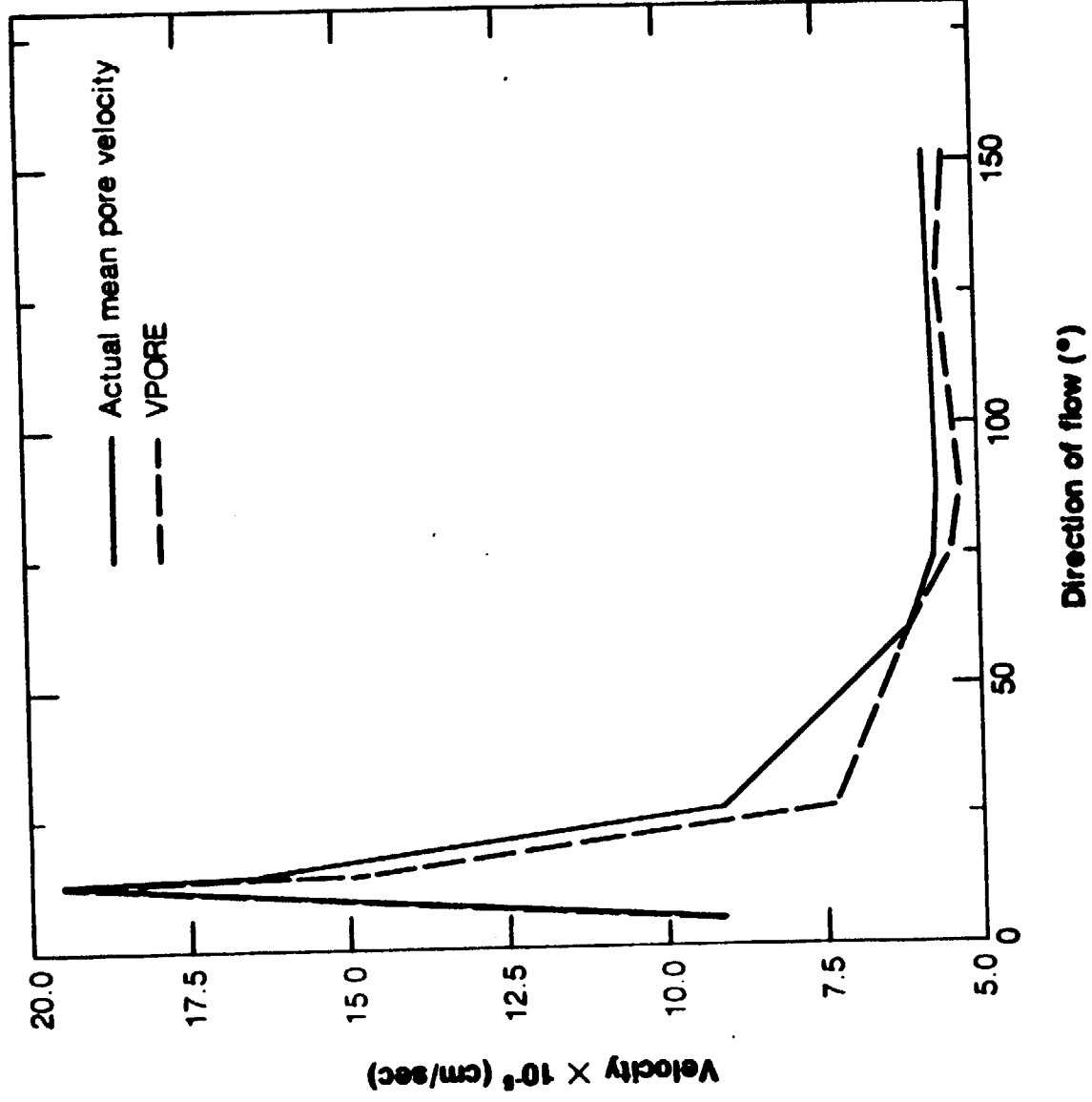
Figure 6-5 demonstrates that tortuosity is highly directionally dependent ranging from 1.10 to 3.93. The standard error of the mean τ was less than 4 percent of its mean value in any direction. The directional variation of tortuosity for this system is similar to tortuosity for the simulated continuous fracture system (Figure 5-5). However, there is one important difference. The minimum tortuosity occurs near the direction of maximum permeability and not at 30° , as found in the continuous system, such that tortuosity increases from the direction of maximum permeability to the direction of minimum permeability. Consequently, directional tortuosity for this system exhibits the characteristics one would expect for an equivalent porous medium. Tortuosity is used in this study to compute VPORE. Figure 6-6 shows how VPORE and MPV vary with direction of flow in the first realization. VPORE does not correspond exactly with MPV as found for the continuous fracture system. However, VPORE provides a good estimate of MPV from two mechanical transport parameters τ and VLIN. If tortuosity had been ignored in computing VPORE, a much lower estimate of the mean pore velocity would have resulted near the direction of minimum permeability.

The mean total porosity, rock effective porosity and hydraulic effective porosity are each plotted against direction of flow in Figure 6-7. Total porosity and rock effective porosity are both directionally stable. Hydraulic effective porosity exhibits no sharp cusps as found in ϕ_H for the simulated continuous fracture system, but there is some directional dependence. The minimum ϕ_H occurs near the direction of maximum permeability and the maximum ϕ_H occurs near the direction of minimum permeability. The mean ϕ_H is nearly equal to the average of ϕ and ϕ_R . Hydraulic effective porosity is computed as the product of q and \bar{T} , divided by L . So ϕ_H can be large when \bar{T} is large. In the direction of maximum permeability, mean travel time is small because this is the direction in which fluid flows the easiest. However, in the direction of minimum permeability, zones of low velocity and slow movement exist in the void region. Consequently, \bar{T} and ϕ_H are large in the direction of minimum permeability. However, the



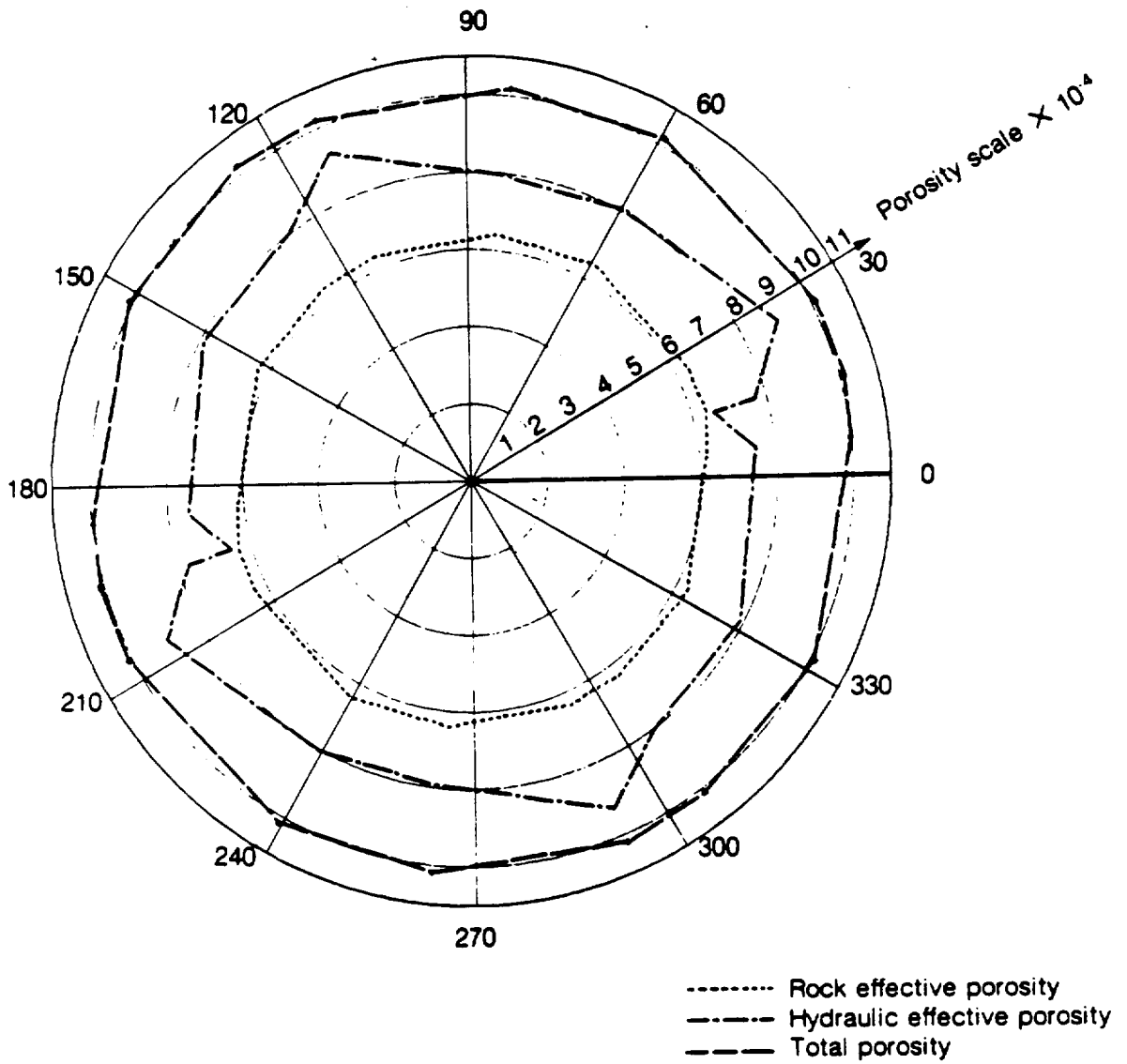
xBL039-875

Figure 6-5 Polar Plot of Tortuosity for Discontinuous Fracture System of Two Sets Oriented at 0° and 30°.



XBL 639-874

Figure 6-6 Actual Mean Pore Velocity and Calculated Mean Pore Velocity for First Realization of Discontinuous Fracture System of Two Sets Oriented at 0° and 30°.



xBL839-879

Figure 6-7 Polar Plots of Total Porosity, Hydraulic Effective Porosity, and Rock Effective Porosity for Discontinuous Fracture System of Two Sets Oriented at 0° and 30°.

mean hydraulic effective porosity of 0.00080 is a good estimate of ϕ_H in any direction, and transport can be predicted by treating this fracture system like an equivalent porous medium.

Three composite breakthrough curves are shown in Figure 6-8. Direction of flow increases from the direction of maximum permeability to the direction of minimum permeability as one proceeds down this figure. Near the direction of maximum permeability, the bulk of the fluid arrives at side 4 in a narrow time interval, with travel times less than \bar{T} . The right skewness in the curve is caused by a small part of the fluid that takes a long time to travel through the flow region. As direction of flow moves towards the direction of minimum permeability, a greater percent of the fluid have travel times larger than \bar{T} as more slow zones of movement develop within the flow region. Consequently, the breakthrough curve becomes more symmetric, but the right skewness in the breakthrough curve is still evident.

Figure 6-9 shows the directional variation in the longitudinal geometric dispersivity. The maximum α_L is obtained near the direction of maximum permeability. In the four directions midway between the directions of principal permeabilities, α_L decreases to minimum values. The minimum α_L is seven times less than the maximum α_L . This strong directional dependence in α_L means that this anisotropic medium cannot be treated as an equivalent isotropic medium for transport studies. The use of a directionally stable α_L for this fracture system would lead to serious errors in transport predictions.

Thus, the following conclusions can be made about the directional properties of this fracture system. The parameters DEVA and DEVF show that porous medium equivalence is more likely to occur near the direction of maximum permeability than near the direction of minimum permeability. Hydraulic effective porosity is relatively stable with direction so that the system can be treated like an equivalent porous medium for transport. The mean ϕ_H is not equal to either ϕ or ϕ_R , but approximately equal to the average of the two porosities. The importance of understanding the directional transport properties of this anisotropic medium is exhibited by α_L . Longitudinal geometric dispersivity is highly directionally dependent with the maximum α_L being at least seven times larger than the minimum α_L .

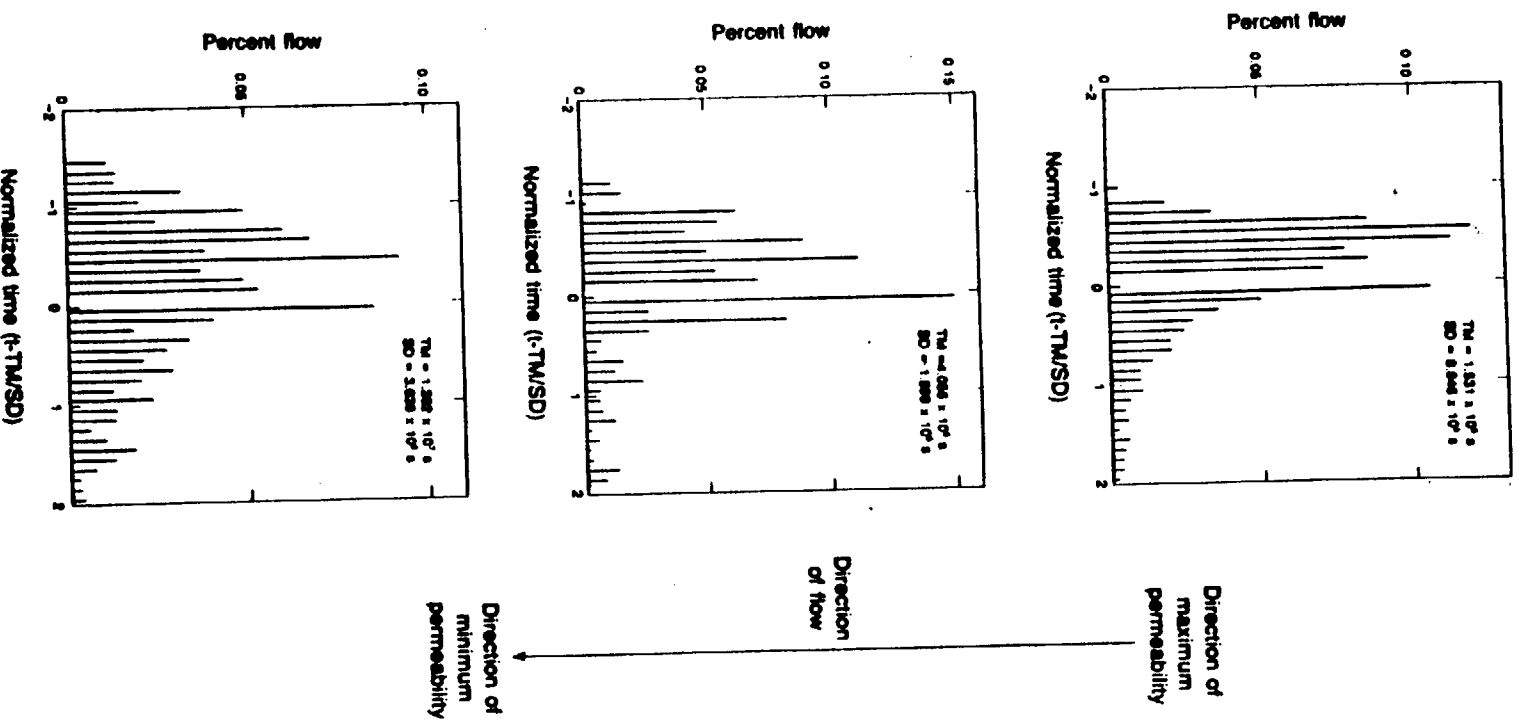
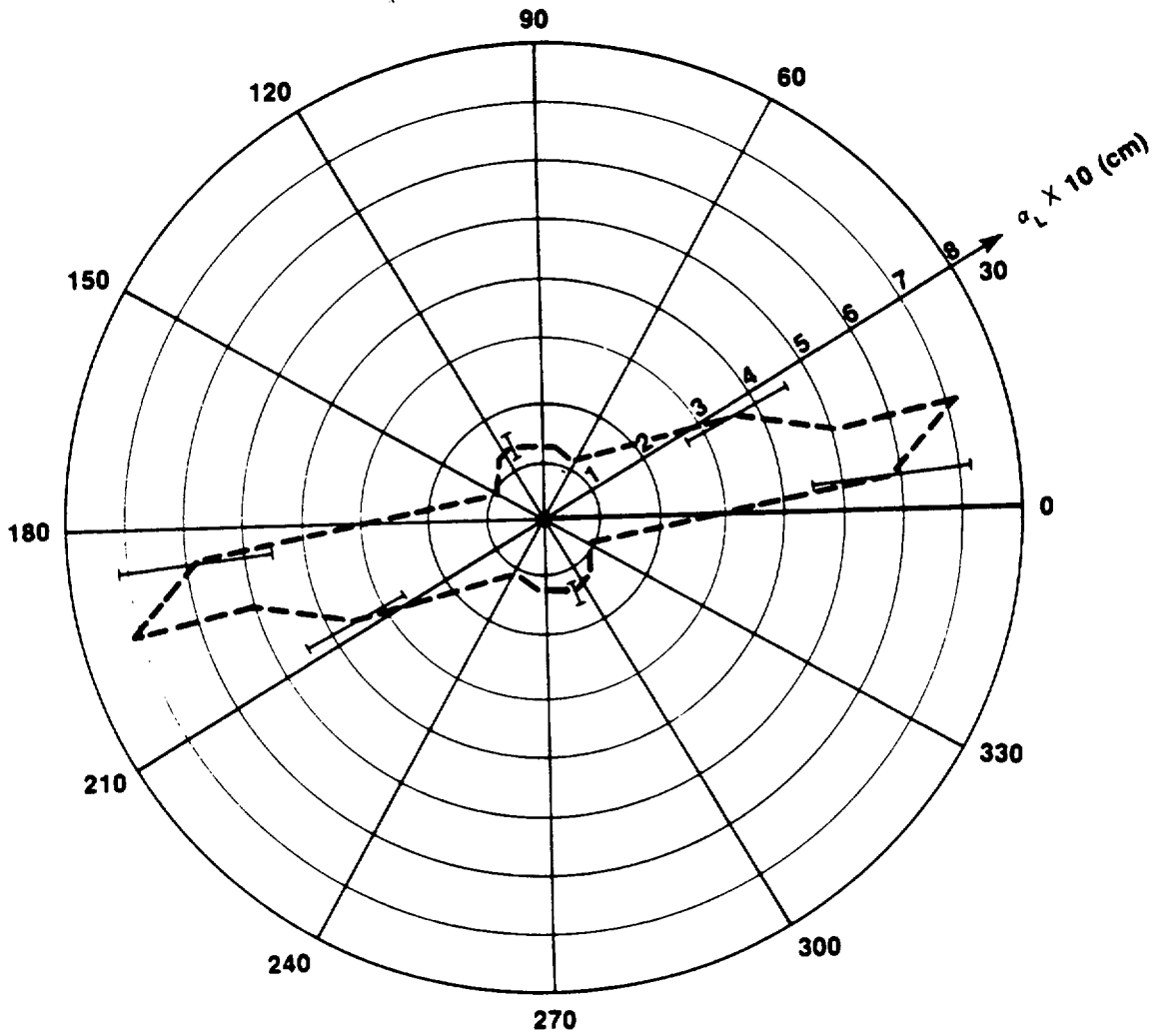


Figure 6-8
Three Breakthrough Curves for Directions of Flow Which Increase From the Direction of Maximum Permeability to the Direction of Minimum as One Proceeds Down the Figure.



XBL 8310-3304

Figure 6-9 Polar Plot of Longitudinal Geometric Dispersivity Versus Direction of Flow for Discontinuous System of Two Sets Oriented at 0° and 30°.

6.3. DISCONTINUOUS FRACTURE SYSTEM OF TWO SETS ORIENTED AT 0° AND 60°

The first Monte Carlo study was conducted for a discontinuous fracture system in which the three geometric parameters length (l), aperture (b), and orientation (o) were all constant. The following Monte Carlo study was conducted for a fracture system in which the three geometric parameters were all probabilistically simulated from the mean (μ) and the standard deviation (σ) for each parameter. The fracture system consisted of the following geometric parameters:

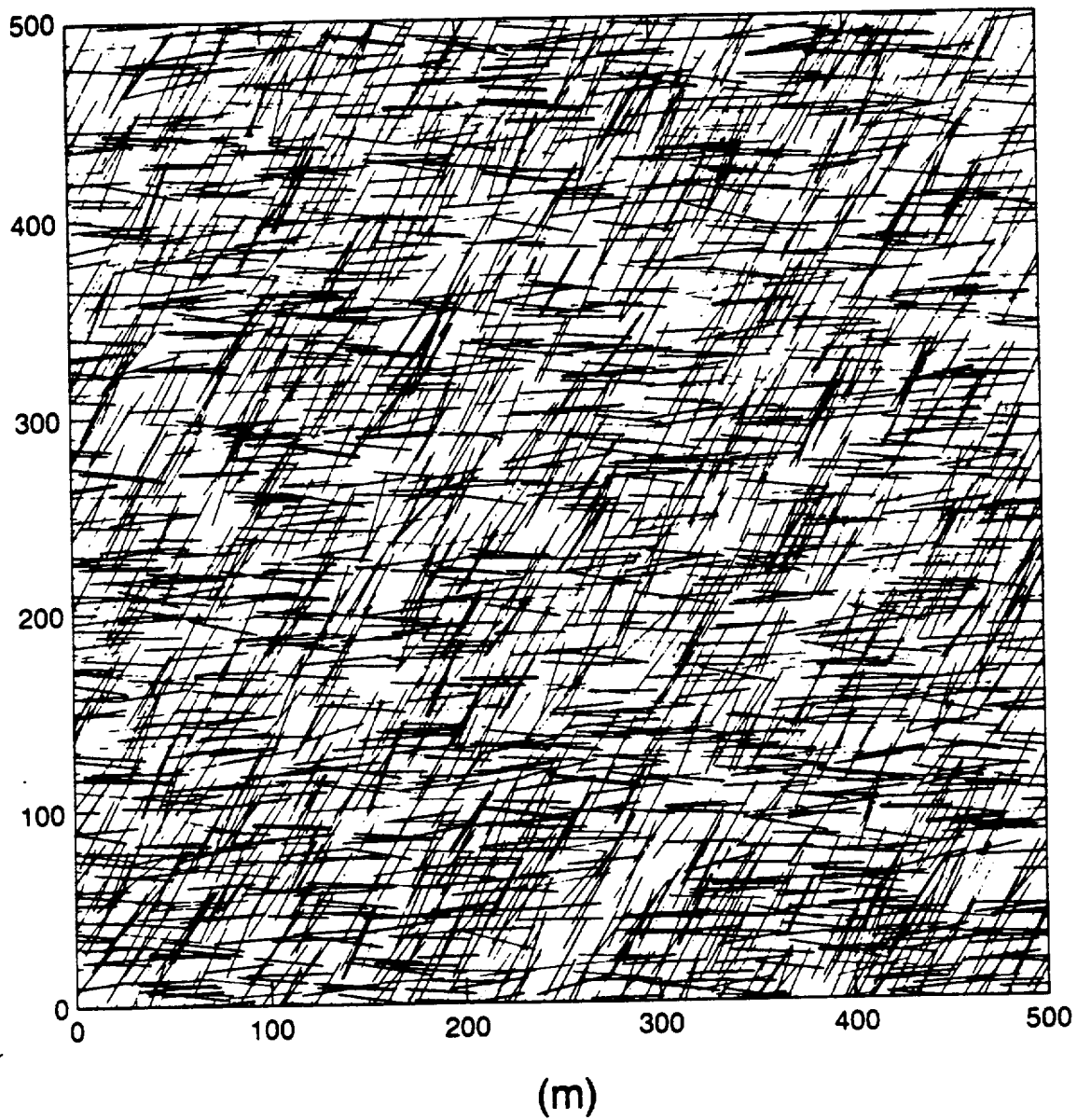
$$\mu_{o, \text{set } 1} = 0^\circ, \quad \sigma_{o, \text{set } 1} = 5^\circ$$

$$\mu_{o, \text{set } 2} = 60^\circ, \quad \sigma_{o, \text{set } 2} = 5^\circ$$

$$\mu_l = 40 \text{ m}, \quad \sigma_l = 4 \text{ m}$$

$$\mu_b = 0.00002 \text{ m}, \quad \sigma_b = 0.000002 \text{ m}$$

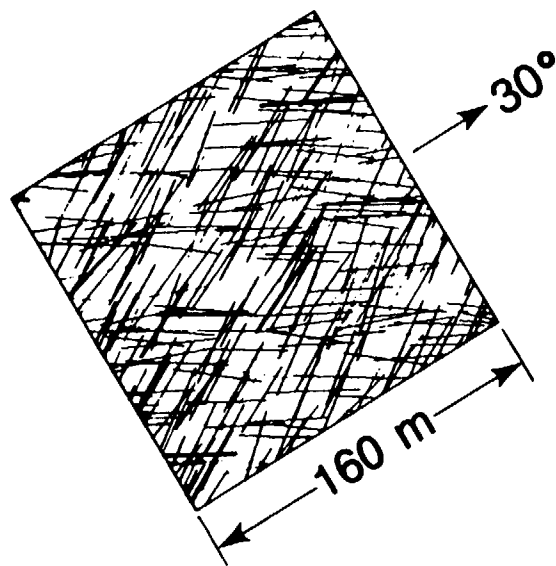
Ten orientations of the hydraulic gradient were selected for study in each realization. These orientations were selected in order to obtain a representative sample of mechanical transport in all directions. Direction of flow for each orientation was estimated based on calculations made for a continuous fracture system of two parallel sets of fractures oriented at 0° and 60°. Each fracture in this continuous system had the same aperture, and the spacing between fractures of the same set was constant. The ten orientations and estimated directions of flow are listed in Table 6-2. The estimated directions of maximum and minimum permeabilities are 30° and 120°, respectively. The estimated ratio of K_x to K_y is two. Flow regions of size 160 by 160 m (size limited by computer storage) were used for all orientations, and the hydraulic gradient along sides 1 and 3 was set at 0.01 for all flow regions. Figure 6-10 shows the fracture pattern in the generation region of 500 by 500 m for one of the realizations. Figure 6-11 shows the fracture pattern and conductive fracture segments in a flow region oriented at 30° for the same realization.



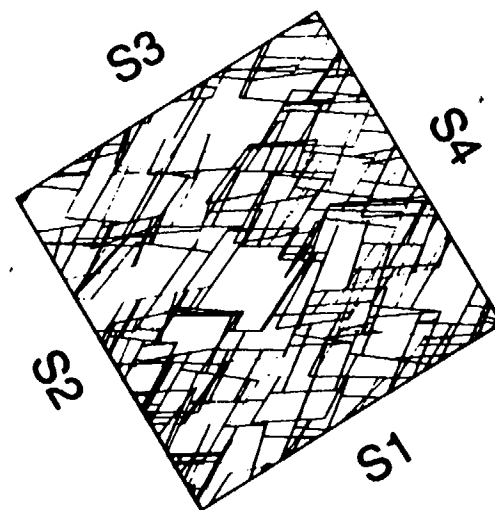
XBL 841-390

Figure 6-10 Fracture Network in the Generation Region for Discontinuous System of Two Sets Oriented at 0° and 60°.

(a)



(b)



XBL 8311-3454A

Figure 6-11 Networks of a) Fractures and b) Connected Fracture Segments in the Flow Region Oriented at 30° for Discontinuous System of Two Sets Oriented at 0° and 60° .

Table 6-2. Orientations and Estimated Directions of Flow Used in Monte Carlo Simulation of the Discontinuous System Consisting of Two Sets of Fractures Oriented at 0° and 60°.

Orientation of hydraulic gradient degrees	Angle of Flow based on continuous system degrees	Estimated Direction of flow degrees
30	0	30
75	-26.6	48.4
95	-29.4	65.6
107	-21.7	85.3
114	-11.5	102.5
120	0	120
126	11.5	137.5
138	21.7	159.7
145	29.4	167.4
165	26.6	191.6

The stability of hydraulic effective porosity determined the number of realizations for this Monte Carlo study. Figure 6-12 shows the mean hydraulic effective porosity for three orientations (30°, 75°, and 120°) plotted against the number of realizations. Orientations 30° and 120° were chosen because they were aligned in the estimated directions of principal permeabilities. For orientations 75° and 120°, mean ϕ_H fluctuated in the first ten realizations. However, mean ϕ_H was relatively stable for all three orientations after twelve realizations, and a slight directional dependence in ϕ_H was apparent. This Monte Carlo study ended after the seventeenth realization because hydraulic effective porosity in each of the three orientations was stable.

Figure 6-13 shows the plot of mean $\sqrt{K_f}$ versus direction of flow. The standard error of the mean $\sqrt{K_f}$ was less than 2.5 percent of its mean in any direction. The plot of the mean $\sqrt{K_f}$ can be approximated by an ellipse with directions of maximum and minimum permeabilities near 30° and 120°, respectively. This curve is nearly symmetric about the direction of minimum permeability, and the ratio of K_x to K_y is about 2.4. The elliptic shape of the $\sqrt{K_f}$ curve shows that the directional flow characteristics for this fracture system behaved like an equivalent porous medium. Table 6-3 lists the computed mean direction of flow and the standard error of the mean for each orientation of the hydraulic gradient. The fluid flow calculations made for the continuous fracture system gave good estimates of the fluid flow properties

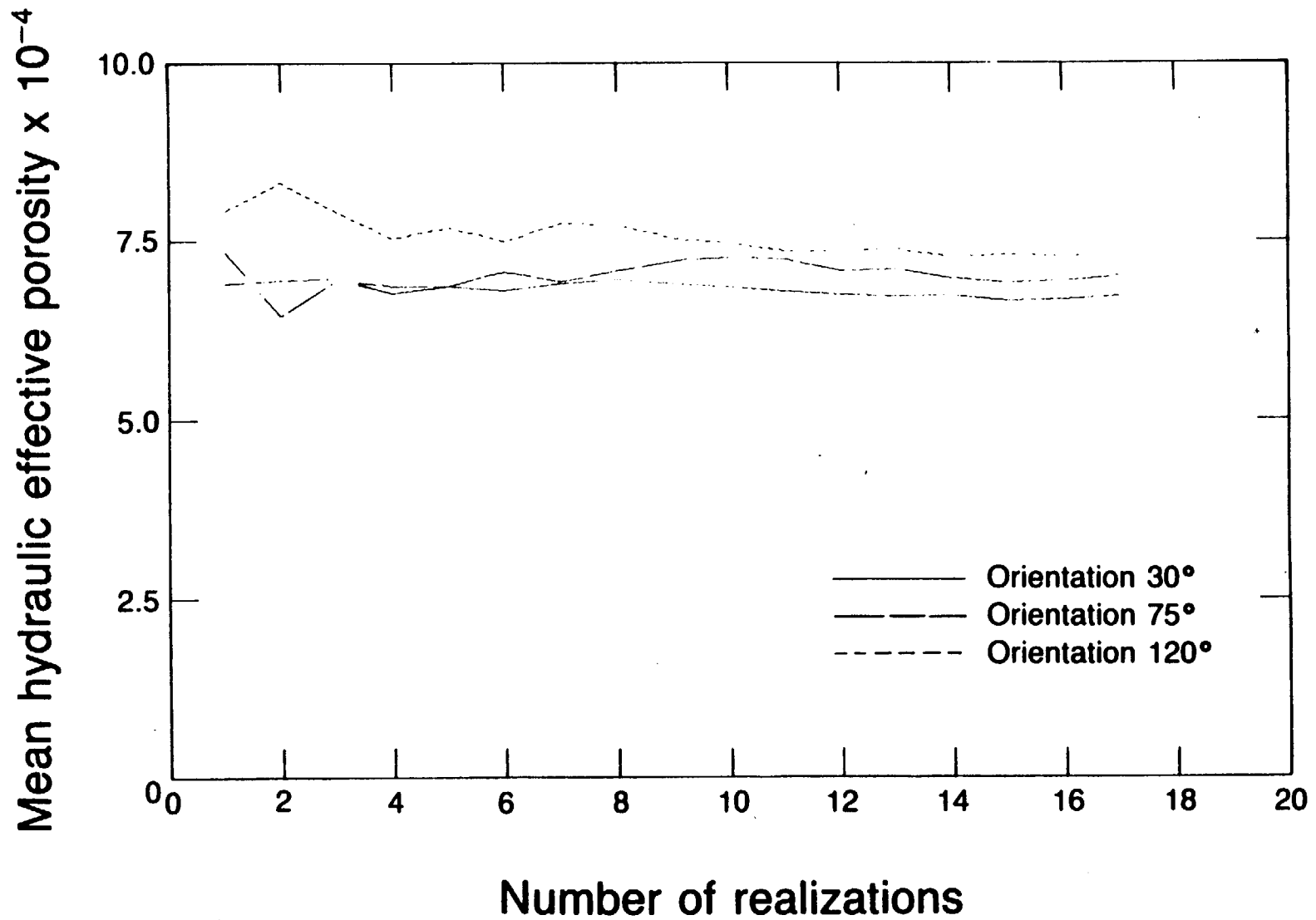
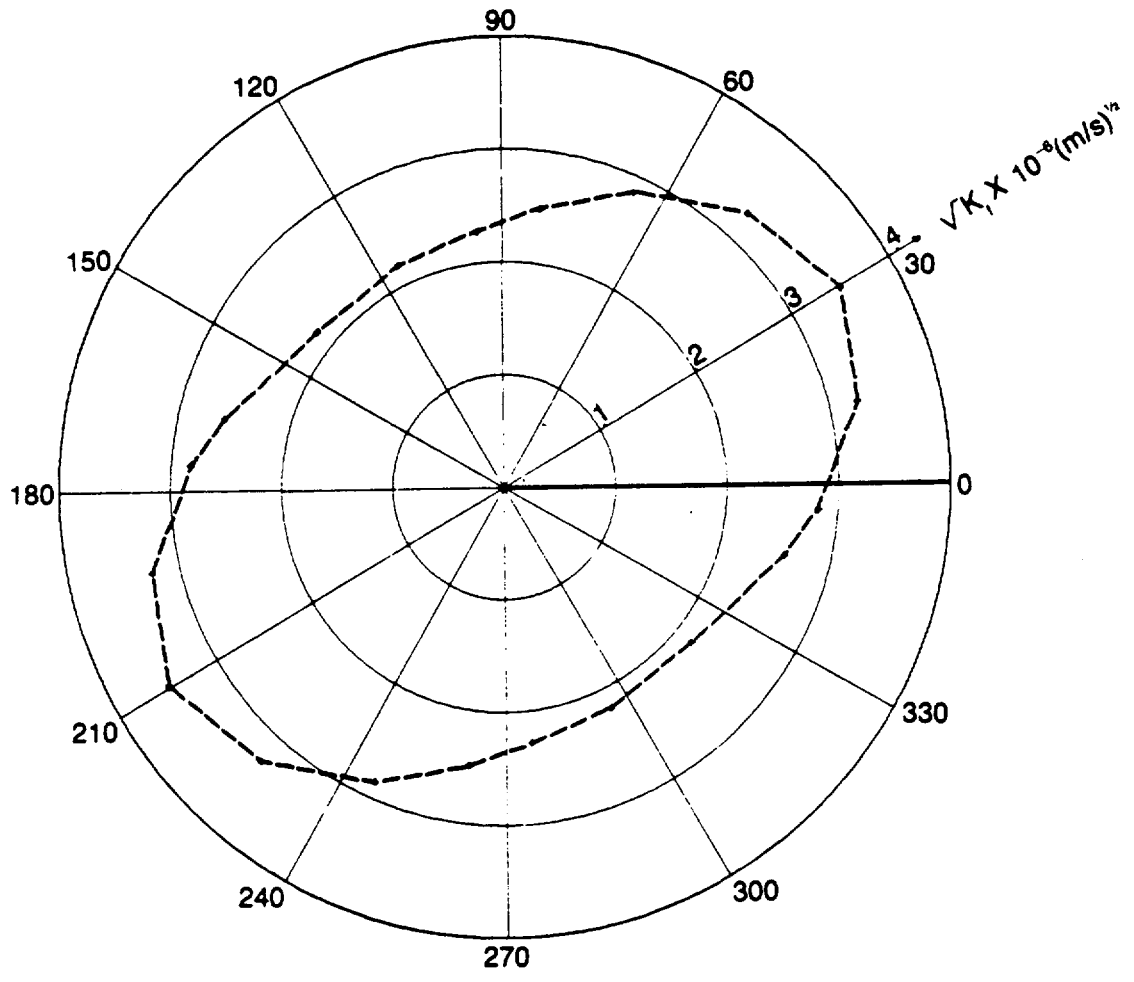


Figure 6-12 Mean Hydraulic Effective Porosity for Orientations 30°, 75°, and 120° Versus the Number of Realizations.

XBL 8311-7385



XBL 841-530

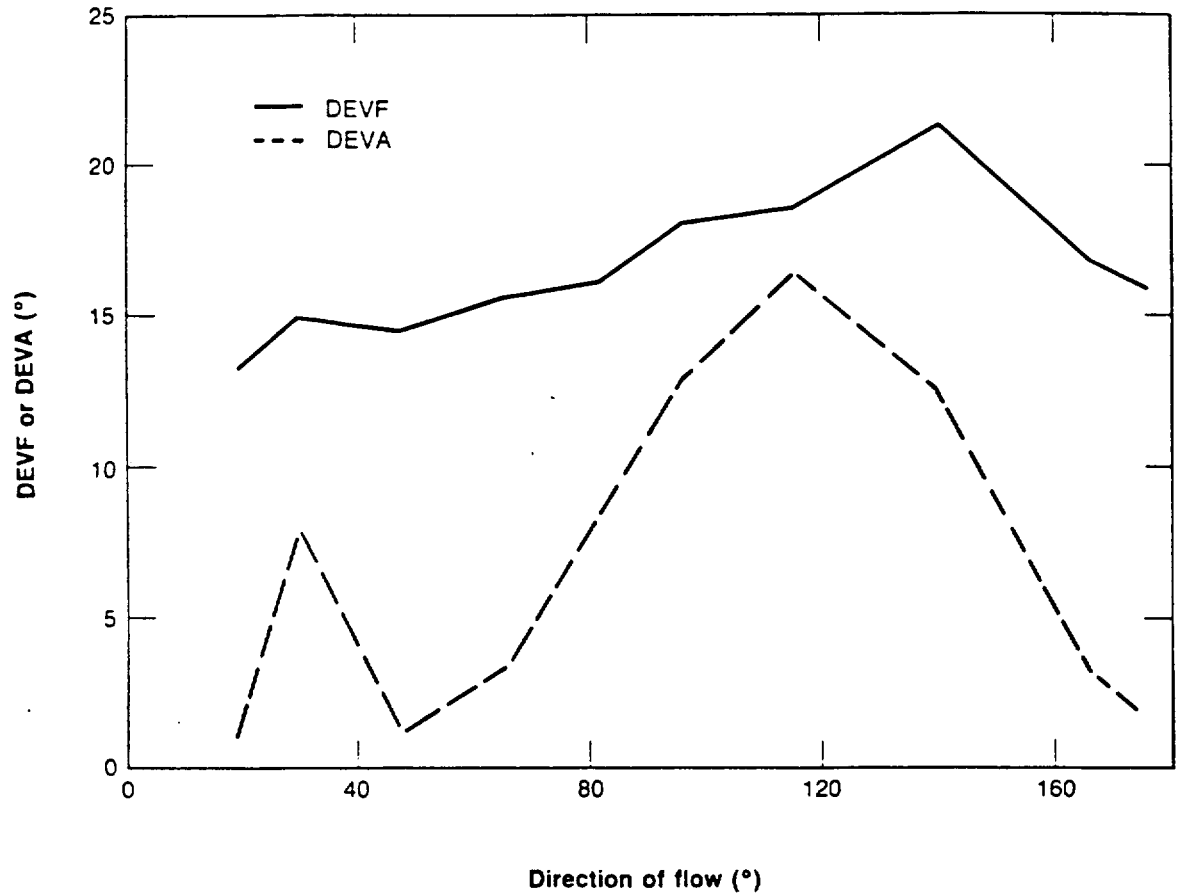
Figure 6-13 Polar Plot of Square Root of Permeability in Direction of Flow for Discontinuous System of Two Sets Oriented at 0° and 60°.

Orientation of hydraulic gradient degrees	Direction of flow degrees
30	29.69 ± 2.05
75	47.33 ± 0.62
95	65.37 ± 1.02
107	81.96 ± 1.16
114	95.96 ± 1.82
120	115.38 ± 2.90
126	140.00 ± 2.06
138	165.74 ± 0.81
145	175.25 ± 0.58
165	192.91 ± 0.46

for this system.

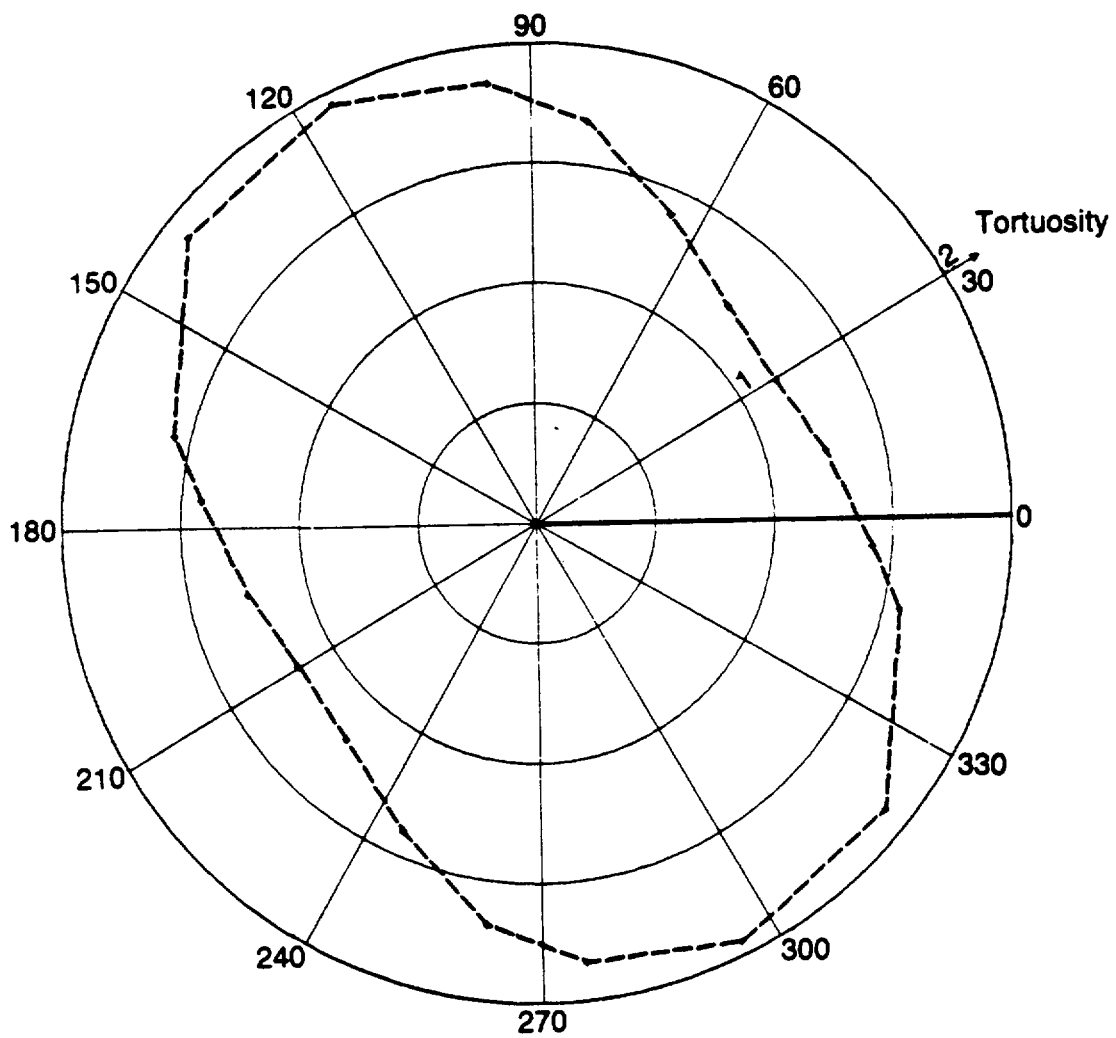
Mean DEVA and mean DEVF for this fracture system showed the same directional behavior (Figure 6-14) as the previous discontinuous system (Figure 6-4). DEVA exhibited two peaks, one near the direction of maximum permeability and the other near the direction of minimum permeability. The flow field was less uniform near the directions of principal permeabilities than in directions away from the principal directions. DEVF was inversely related to permeability, as DEVF steadily increased from the direction of maximum permeability to the direction of minimum permeability. Flow rate was large and fluid flowed easily in the direction of maximum permeability, as tortuosity was minimum (Figure 6-15), and DEVF was small. In the direction of maximum permeability, fluid flowed in a direction close to the orientations of the two sets. However, in the direction of minimum permeability, the orientation of the hydraulic gradient was not aligned favorably with the orientations of the sets. The mean orientations of both sets were not oriented in the direction of the hydraulic gradient, and fluid had to move in a particular direction that was controlled by the orientation of the hydraulic gradient. Tortuosity and DEVF were large in the direction of minimum permeability because fluid flowed in a direction nearly perpendicular to the orientations of the two sets.

Equivalent porous medium flow behavior for this fracture system is directional



XBL 8401-6786

Figure 6-14 Mean DEVF and Mean DEVA Versus Direction of Flow for Discontinuous System of Two Sets Oriented at 0° and 60°.



XBL 8401-8795

Figure 6-15 Polar Plot of Tortuosity for Discontinuous System of Two Sets Oriented at 0° and 60°.

dependent. Flow characteristics are better predicted by Darcy's law when the direction of flow is near the direction of maximum permeability than when it is near the direction of minimum permeability, as evidenced by the smaller DEVF and DEVA near the direction of maximum permeability. Since permeability is inversely proportional to tortuosity, the study of the fluid flow characteristics for this fracture system has shown that fluid flow continuum size is inversely related to tortuosity. The study of mechanical transport for the continuous fracture system oriented at 0° and 30° showed that mechanical transport continuum size was also inversely related to tortuosity (section 5.2).

Next, the relationship between mean pore velocity and VPORE was investigated. The estimate of mean pore velocity, VPORE, discussed in section 4.4, can be derived from the Kozeny equation (section 3.8). Kozeny formulated an expression relating pipe flow to porous media flow. The mean velocity in a pipe under laminar flow conditions is given by the Poiseuille equation:

$$\bar{v} = - \frac{r_h^2}{2\mu} \frac{dp}{dL}$$

The first key step in the formulation of the Kozeny equation was the acceptance that the Poiseuille equation was valid for porous media flow, with a few added modifications. The first modification accounted for the fact that fluid flows in only part (the conductive void region) of the total volume. The second modification accounted for the fact that fluid paths are nonlinear in a porous medium. The next key step in the formulation of the Kozeny equation was the development of the relationship between MPV and specific discharge. The mean pore velocity is expressed in the Kozeny equation as:

$$MPV = \frac{q}{\phi} \frac{L_a}{L} = - \frac{r_h^2}{\mu s_f} \frac{dp}{dL_a} \quad (6.1)$$

Theoretically,

$$MPV = \frac{1}{V_c} \int_{V_c} v dV_c \quad (6.2)$$

which is a very difficult equation to evaluate. In equation 6.1, mean pore velocity is related to macroscopic parameters (q , ϕ , L , and L_a) which are much easier to compute than is equation

6.2. Since L_a/L is the tortuosity, mean pore velocity can be written as:

$$MPV = \frac{q}{\phi} \tau$$

which for homogeneous transport is equal to:

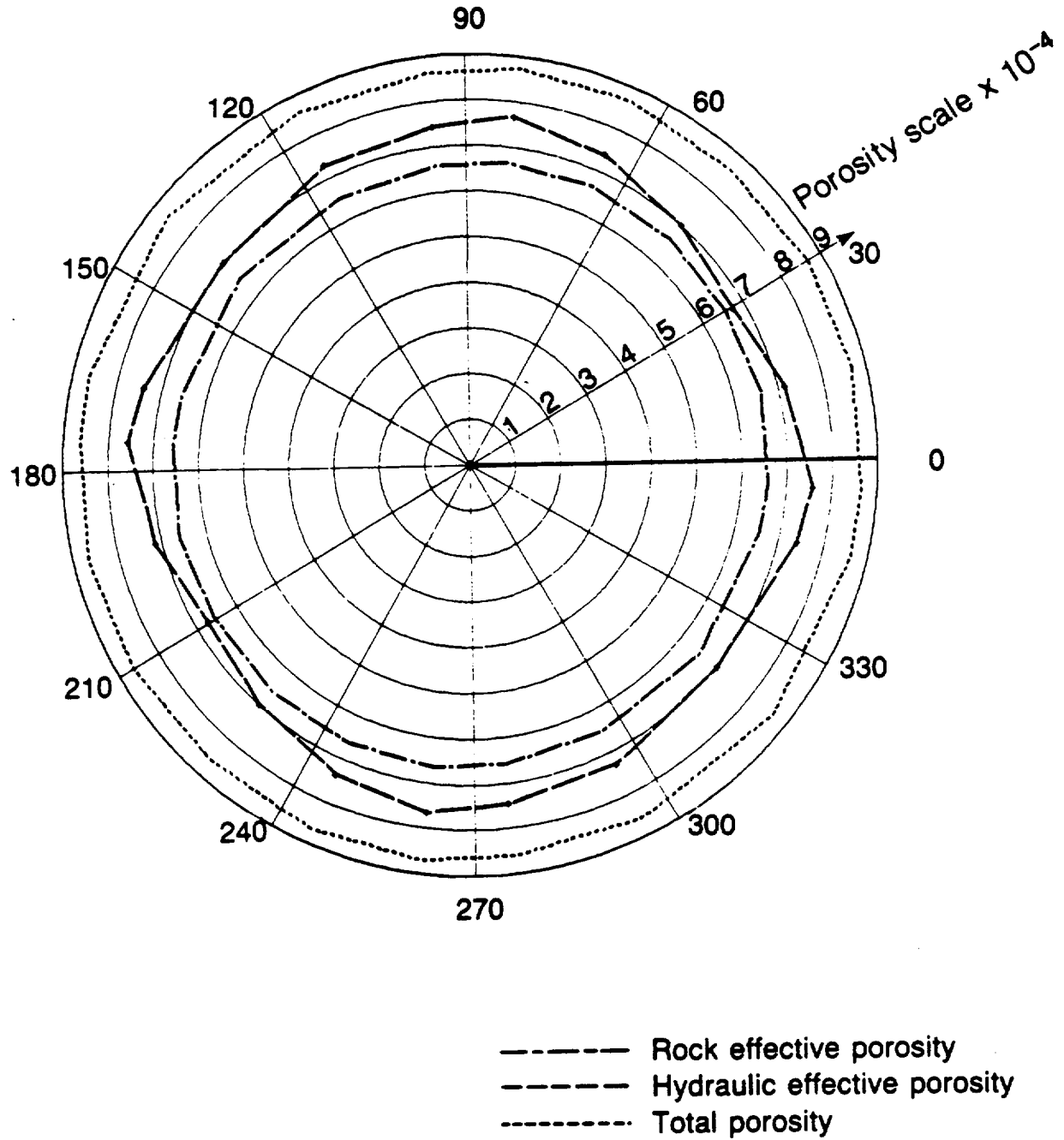
$$MPV = VLIN\tau = VPORE$$

Thus, VPORE is a function of two mechanical transport parameters that are measured in this study.

Tortuosity increased from 1.17 near the direction of maximum permeability to 1.95 near the direction of minimum permeability. The relationship between VPORE and mean pore velocity was investigated in three directions near the direction of minimum permeability, where tortuosity has a definite effect of VPORE. For the three directions of 82.0°, 96.0°, and 115.4°, mean tortuosities were 1.68, 1.80, and 1.95, respectively. Mean MPVs of 1.275×10^{-6} , 1.265×10^{-6} , and 1.248×10^{-6} m/s were calculated in these three directions, respectively. Mean VPOREs of 1.234×10^{-6} , 1.224×10^{-6} , and 1.240×10^{-6} m/s were also calculated in the same three directions, respectively. VPORE slightly underestimated MPV in the three directions. However, the difference between VPORE and MPV was less than 4 percent of MPV. Thus, VPORE provided a good estimate of the mean pore velocity.

Tortuosity has been found to be an important mechanical transport parameter. Tortuosity, as just shown, is an essential component in estimating VPORE. The continuum sizes for mechanical transport and fluid flow were found to be inversely related to tortuosity. Tortuosity is normally considered to range between 1 and 2. However, for the continuous and discontinuous fracture systems of two sets oriented at 0° and 30°, tortuosities as high as 3.8 were calculated. For discontinuous systems which exhibited continua behavior for directional fluid flow, tortuosity increased from a minimum value in the direction of maximum permeability to a maximum value in the direction of minimum permeability, as one would expect for equivalent porous media.

Total porosity, rock effective porosity, and hydraulic effective porosity are each plotted against direction of flow in Figure 6-16. Total porosity and rock effective porosity were both



XBL 8311-7383

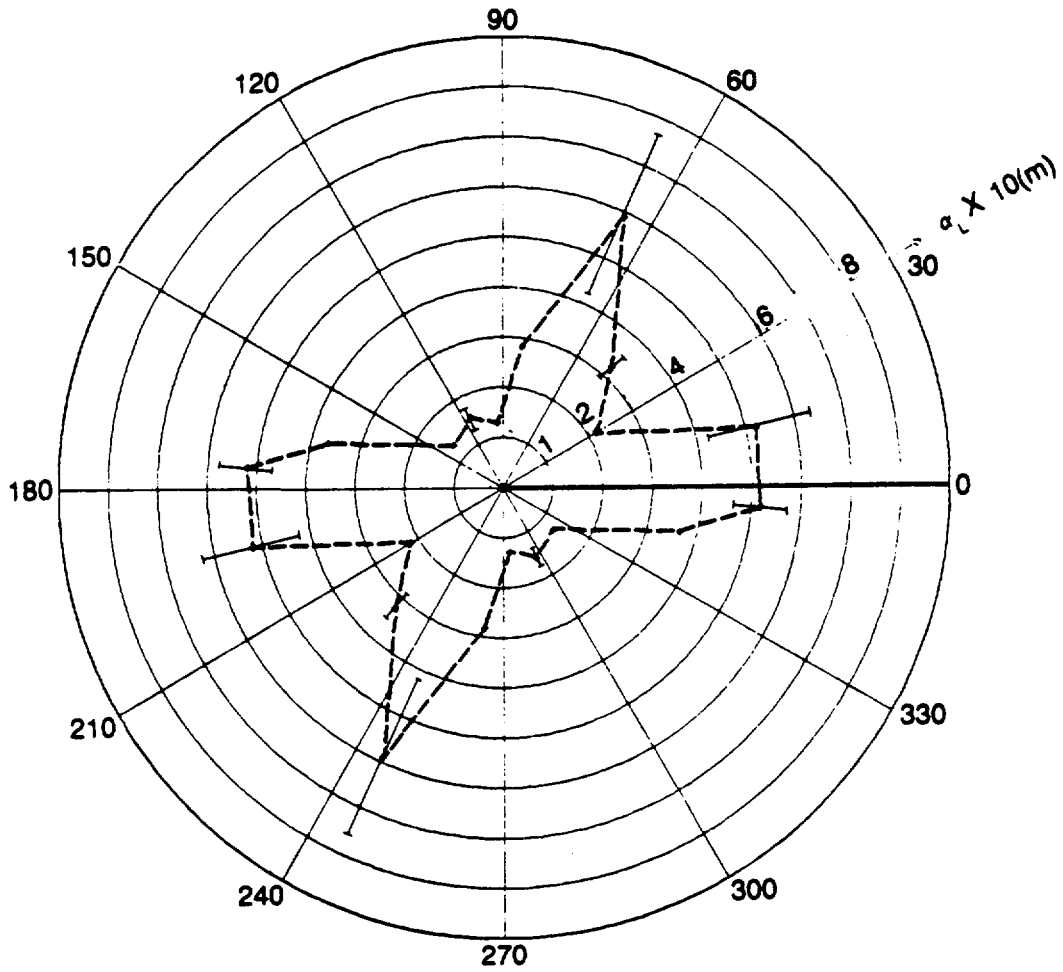
Figure 6-16 Polar Plots of Rock Effective Porosity, Hydraulic Effective Porosity, and Total Porosity for Discontinuous System of Two Sets Oriented at 0° and 60°.

stable with direction. Hydraulic effective porosity was slightly larger than ϕ_R , and the mean ϕ_H was 0.00000727. Hydraulic effective porosity showed a small directional dependence, with minimum ϕ_H occurring near the direction of maximum permeability, and the maximum ϕ_H occurring midway between the directions of principal permeabilities. The small directional dependence in hydraulic effective porosity indicates that this fracture system can be treated like an equivalent porous medium for transport.

The two Monte Carlo studies for discontinuous fracture systems showed that hydraulic effective porosity was larger than ϕ_R , but less than ϕ . Thus, q/ϕ_R would overestimate the average linear velocity for these two systems. Hydraulic effective porosity was larger than ϕ_R because zones of slow movement exist in the flow region which caused \bar{t} to be larger than theoretically expected. Hydraulic effective porosity exhibited a slight directional dependence, with the minimum ϕ_H occurring near the direction of maximum permeability. The abrupt changes in ϕ_H found in the regular continuous fracture systems were not observed in the discontinuous systems.

The directional variation of α_L for this fracture system is shown in Figure 6-17. The maximum α_L was obtained at a direction midway between the two directions of principal permeabilities. The minimum α_L was obtained near the direction of minimum permeability. The ratio of maximum to minimum α_L was four.

The following summarizes the results of the directional studies for the longitudinal geometric dispersivity. For the first continuous fracture system of two parallel sets oriented at 0° and 30° , the maximum α_L was obtained in the direction of minimum permeability. However, the minimum α_L of zero was obtained in the two principal directions for the next continuous system of two orthogonal sets. The discontinuous fracture system of two sets oriented at 0° and 30° had the maximum α_L in the direction of maximum permeability, and the minimum α_L at a direction midway between the two principal directions. For the discontinuous system just studied, the maximum α_L occurred at a direction midway between the two principal directions, and the minimum α_L occurred near the direction of minimum permeability. Thus, each system



XBL 841-531

Figure 6-17 Polar Plot of Longitudinal Geometric Dispersivity for Discontinuous System of Two Sets Oriented at 0° and 60°.

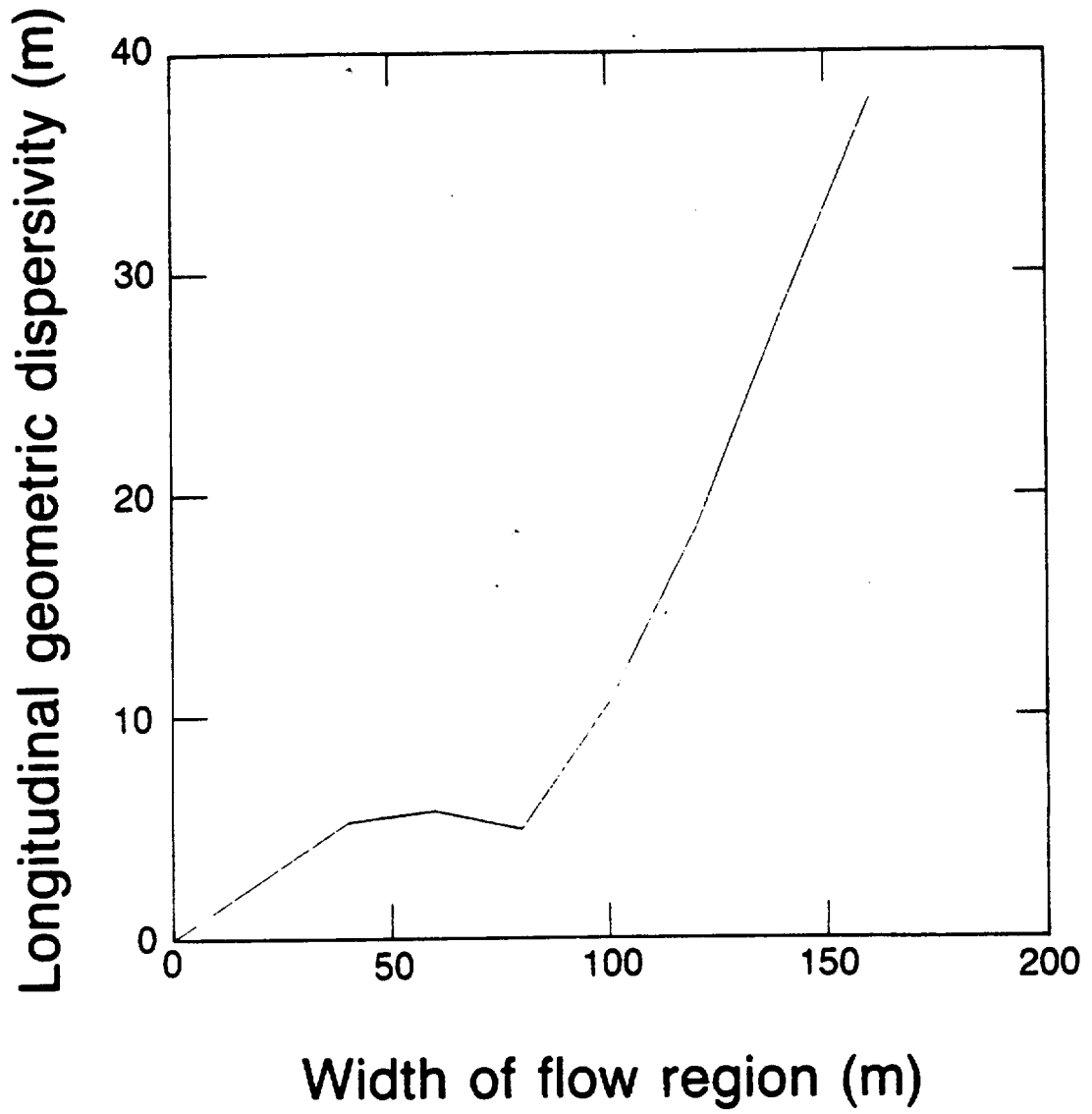
showed a unique directional dependence for α_L . The ratio of $\alpha_{L,max}$ to $\alpha_{L,min}$ for the two discontinuous systems was related to the degree of anisotropy (ratio of K_x to K_y).

The longitudinal geometric dispersivity will not vary with flow region size if the Fickian approach to characterizing dispersion is applicable. The applicability of the Fickian approach was studied using the fracture system in the last realization, as follows. The width of a square flow region oriented at 107° was increased in increments of 20 m, beginning at a width of 40 m. Orientation 107° was selected for this study because the fluid flow and mechanical transport parameters (K_f , ϕ_H , τ , α_L) for the last realization were all reasonably close to their mean values for the Monte Carlo study. For each flow region, the computer program was used to determine α_L . Computer storage limited the maximum width of the flow region to 160 m.

Figure 6-18 shows the variation in α_L with sample size. Since α_L increases with sample size, the Fickian approach cannot be used to characterize dispersion at this scale. The polar plot of the longitudinal geometric dispersivity shown in Figure 6-17 can only be used to predict transport for problems on the scale of 160 m. For problems on a larger scale, α_L is expected to be larger than α_L in Figure 6-17. Longitudinal geometric dispersivity varies linearly with size when the width of the flow region is greater than 75 m. Linearly varying dispersivities have been reported in the literature. Pickens and Grisak (1981a) had good success in matching the results of tracer experiments by Sudicky and Cherry (1979) and Pickens and Grisak (1981b) with linearly varying dispersivities. Presently, most transport models are based on the Fickian approach. However, the results of this study agree with a number of recent studies (Gelhar et al., 1979; Pickens and Grisak, 1981; Schwartz, 1977) which have demonstrated that dispersion coefficients initially increase with sample size.

6.4. SENSITIVITY ANALYSIS

A fracture system is created from the following geometric parameters: aperture (b), orientation (θ), length (l), and set areal density (λ_A). The first three geometric parameters are generally distributed and are modeled in this study using probabilistic simulation. This statistical procedure requires a knowledge of the mean and standard deviation for the simulated



XBL 841-391

Figure 6-18 Longitudinal Geometric Dispersivity Versus Width of Flow Region for Discontinuous System of Two Sets Oriented at 0° and 60°.

a mean geometric parameter. The fracture system in the first realization of the Monte Carlo simulation for the discontinuous fracture system of two sets oriented at 0° and 30° served as the control fracture system. This fracture system had the following constant fracture geometric parameters: 40 cm length, 0.002 cm aperture, 0° orientation for set 1, 30° orientation for set 2, and 0.00633 cm^{-2} areal density for each set. For each perturbed fracture system, measurements of mechanical transport and fluid flow were made for a flow region of $180 \times 180 \text{ cm}$ oriented at 160° . This orientation was selected because it showed a good probability of exhibiting equivalent porous medium flow behavior in the Monte Carlo study. The results for the perturbed fracture systems were then analyzed to evaluate sensitivity.

The connectivity sensitivity studies for mean orientation, set areal density, and mean fracture length were conducted with the following perturbed fracture systems. In the orientation sensitivity study, the orientation of set 2 was perturbed while the orientation of set 1 remained constant at 0° . Four orientations for set 2 of 26° , 28° , 32° , and 34° were used in this part of the study. The areal density sensitivity study was conducted by equally perturbing λ_A for both sets. The control fracture system had 570 fractures of each set in the generation region of $300 \times 300 \text{ cm}$. In the areal density sensitivity study, the number of fractures per set in the generation region ranged from 300 to 625 fractures. In the mean fracture length sensitivity study, five values of mean fracture length ranging from 30 to 45 cm were used.

Two perturbed systems were sufficient to conduct the conductivity sensitivity study for mean aperture because mean aperture is the only geometric parameter for which sensitivity can be computed. The two perturbed systems had mean apertures of 0.001 cm and 0.003 cm.

6.4.1.1. Connectivity Sensitivity Studies of Mean Fracture Length,

Mean Orientation, and Set Areal Density

The sensitivity studies for μ_1 , μ_2 , and λ_A were conducted together because the three parameters influence the connectivity of a fracture network. Connectivity clearly decreases as set areal density or fracture length decreases. The mean orientation of fracture sets can also influence connectivity. For example, consider a fracture system consisting of two fracture sets. The

minimum connectivity occurs when the two sets are parallel, and the maximum connectivity occurs when the two sets are orthogonal.

Mean sensitivity and relative sensitivity were computed to evaluate the sensitivity of a mean geometric parameter. The relative sensitivity (S) of a mechanical transport or fluid flow parameter (y) for a given value of a mean geometric parameter (x) was computed as:

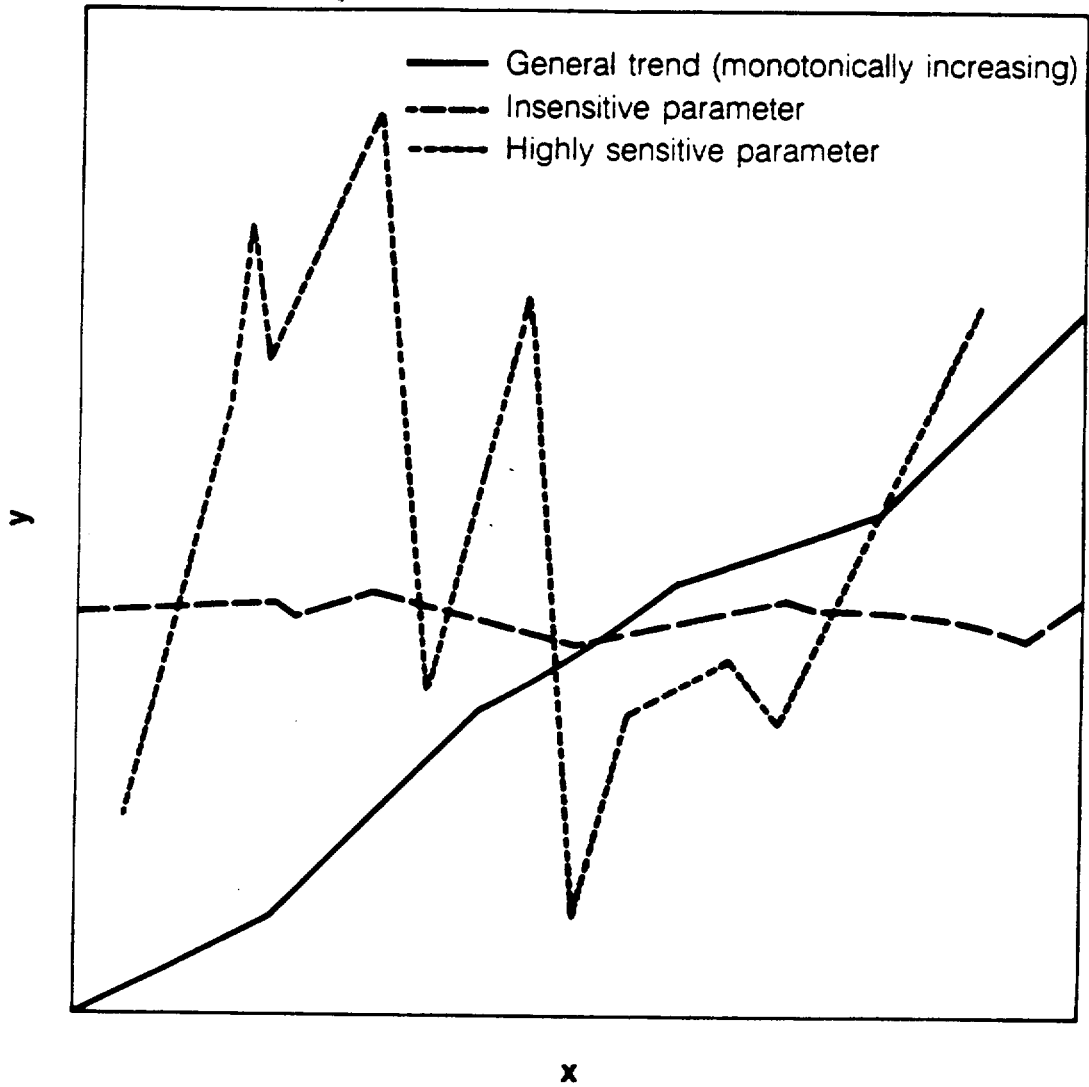
$$S = \frac{\frac{1}{y} \partial y}{\frac{1}{x} \partial x} \approx \frac{\frac{1}{y} \Delta y}{\frac{1}{x} \Delta x}$$

The relative sensitivity was defined so that the sensitivities of μ_1 , μ_0 , and λ_A could be compared on an equivalent dimensionless basis. Relative sensitivity was computed for each perturbed value of the studied geometric parameter. For the range of the studied geometric parameter (x_1, x_2), mean sensitivity was computed as:

$$S_m = \frac{1}{x_2 - x_1} \int_{x_1}^{x_2} S dx$$

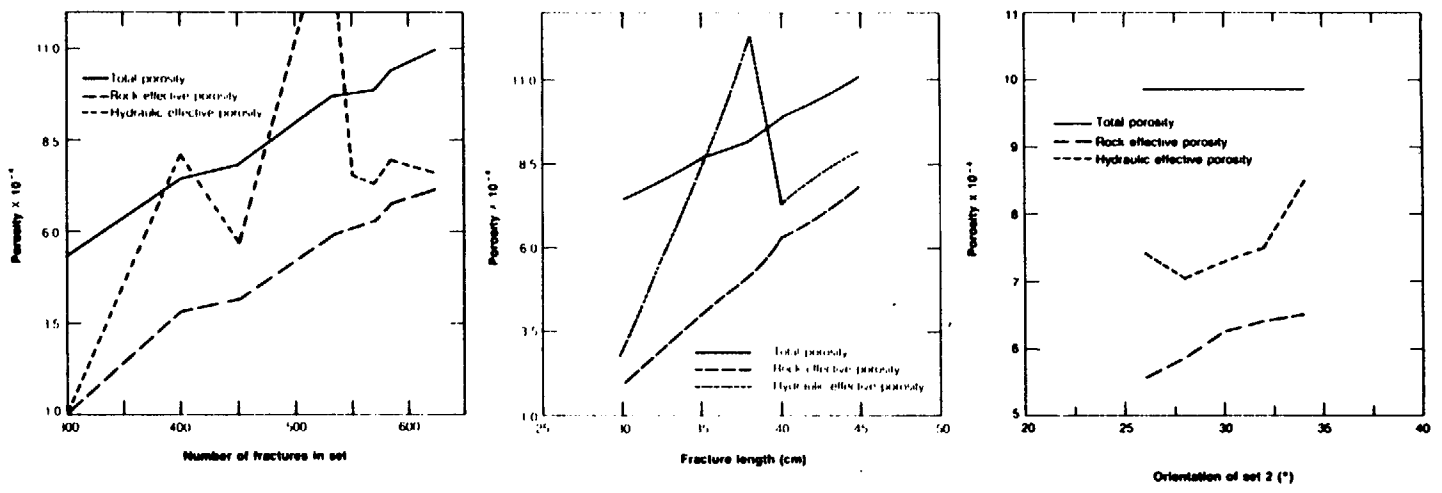
The relative sensitivities and mean sensitivity for a range of x were used to interpret a sensitivity study. Three types of relationships between y and x were observed. In the first type of relationship, y showed a tendency to increase or decrease with respect to x (solid line in Figure 6-19). Since relative sensitivities had the same sign (positive or negative), y was directly related to x. One can predict what will happen to y when x is perturbed for this type of relationship. In the second relationship, y was insensitive to x (dashed line in Figure 6-19). The relative sensitivities and mean sensitivity were small in magnitude, and the relative sensitivities had mixed signs. Even if there is a small error (perturbation) in the mean geometric parameter, y can be predicted fairly accurately. In the third relationship, y was highly sensitive to x (dotted line in Figure 6-19); y fluctuated with x and no general tendency was observed. This geometric parameter must be determined accurately to predict y.

Table 6-4 lists the mean sensitivity and maximum magnitude of relative sensitivity (max |S|) for the connectivity sensitivity study. Total porosity and rock effective porosity increased as fracture length and set areal density increased (Figure 6-20). The increase in both porosities reflected increases in connectivity. The mean sensitivity and max |S| of total porosity to



XBL 8310-3299

Figure 6-19 Three General Types of Sensitivity Relationships.



NBL 8310 3311A

Figure 6-20 Total Porosity, Rock Effective Porosity, and Hydraulic Effective Porosity Versus Number of Fractures in Set, Mean Fracture Length, and Orientation of Set 2.

mean orientation of set 2 were both zero. The nonsensitivity of ϕ to mean orientation of set 2 occurred because the number of fractures in the generation region did not change as the orientation of set 2 was perturbed. However, ϕ_R increased as the mean orientation of set 2 increased because connectivity increased. Total porosity and rock effective porosity were most sensitive to fracture length, and least sensitive to the mean orientation of set 2.

Table 6-4. Mean Sensitivity and Maximum Magnitude of Relative Sensitivity for Mean Orientation, Set Areal Density, and Mean Fracture Length Sensitivity Studies.

Parameter	Orientation		Areal Density		Fracture Length	
	max S	S _M	max S	S _M	max S	S _M
q	1.1	0.57	6.3	2.7	6.3	3.1
θ	0.04	0.04	0.59	0.02	0.65	-0.10
ϕ	0	0	1.3	0.88	1.4	1.0
ϕ_R	0.90	0.57	3.3	1.4	4.7	3.3
ϕ_H	2.1	0.11	18.3	0.57	10.0	2.2
τ	0.29	0.57	1.2	-0.09	1.1	-0.21
\bar{T}	1.4	0.18	25.0	-2.4	17.1	-0.90
σ^2	15.5	-3.7	52.1	1.9	28.9	-5.1

Specific discharge increased as μ_1 , λ_A , and $\mu_{0,set 2}$ increased (Figure 6-21). The max |S| of q was nearly equal for mean fracture length and set areal density. The max |S| of q to $\mu_{0,set 2}$ was almost six times less than the max |S| for μ_1 or λ_A . It was anticipated that the angle of flow would increase as the orientation of set 2 increased. However, the angle of flow was surprisingly insensitive to perturbations in $\mu_{0,set 2}$, μ_1 , and λ_A . Thus, q increased as connectivity increased, while θ was relatively insensitive to connectivity.

Rock effective porosity and specific discharge both increased as μ_1 , $\mu_{0,set 2}$, and λ_A increased. Thus, specific discharge and rock effective porosity were each plotted versus connectivity in Figure 6-22 using the results of the three sensitivity studies. The good correlation of both q and ϕ_R to connectivity shows that both parameters are fundamentally related to connectivity for this fracture system. Consequently, q and ϕ_R can be estimated from connectivity when the geometric parameters of this fracture system are perturbed.

Mechanical transport parameters were generally much more sensitive to μ_0 , μ_1 and λ_A than either q or ϕ_R . The three plots of mean travel time versus μ_1 , λ_A , and $\mu_{0,set 2}$ in Figure 6-23

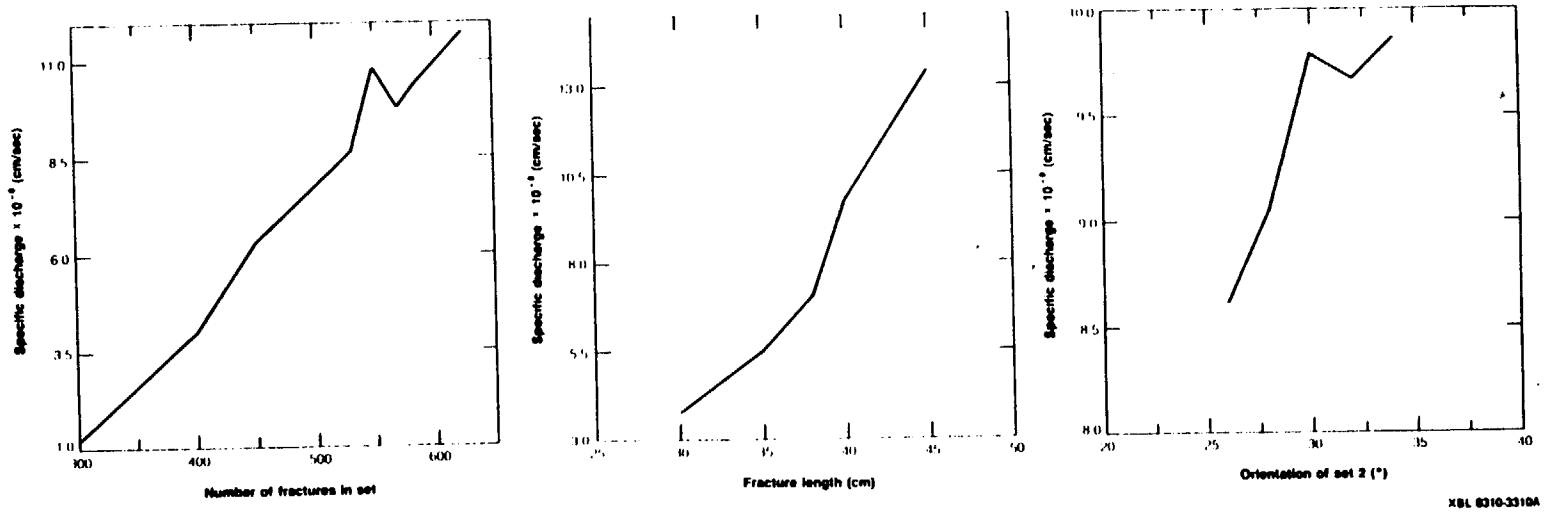
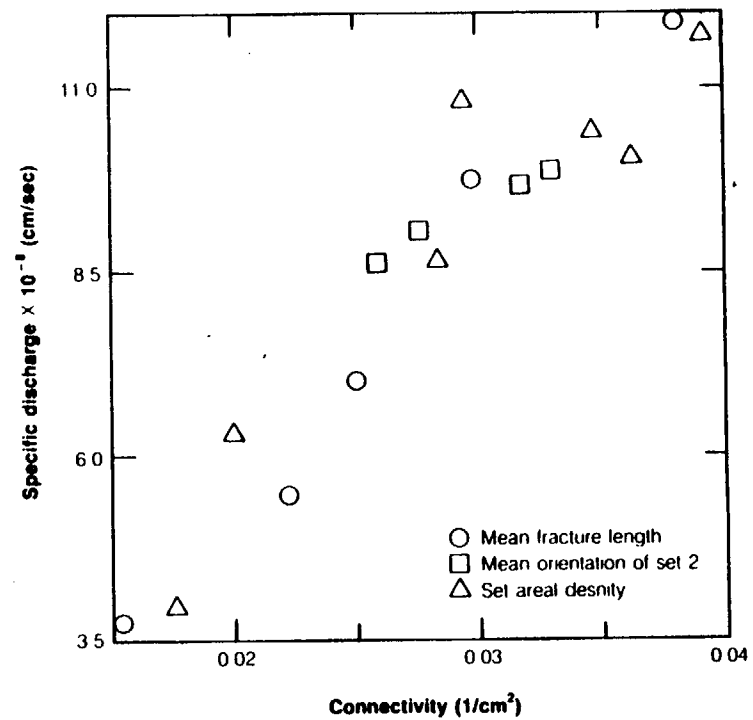
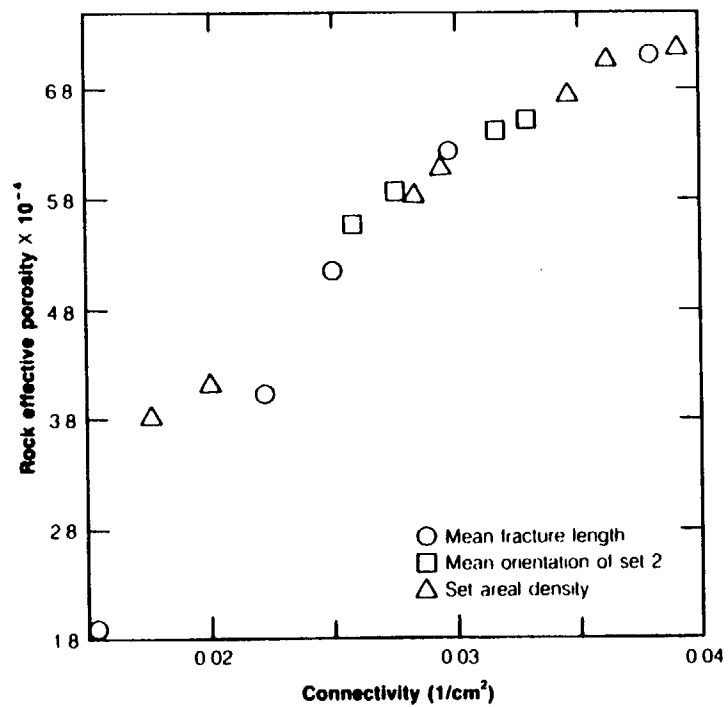


Figure 6-21 Specific Discharge Versus Number of Fractures in Set, Mean Fracture Length, and Orientation of Set 2.



XBL 8310-3306A

Figure 6-22 Rock Effective Porosity and Specific Discharge Versus Connectivity.

demonstrate the high sensitivity of mechanical transport to each parameter. Three different relationships between \bar{T} and connectivity are observed in this figure, and no general relationship between \bar{T} and any geometric parameter is observed. The high sensitivity of mechanical transport to connectivity is also evident in the variance of the breakthrough curve (Figure 6-24). The variance, σ^2 , was the most sensitive mechanical transport parameter, varying by as much as two orders of magnitude in a given sensitivity study. The shape of the σ^2 curve for a particular mean geometric parameter was similar to the shape of the \bar{T} curve for the same geometric parameter. Thus, σ^2 and \bar{T} showed the same type of relationship to each mean geometric parameter.

As each geometric parameter (μ_1 , μ_0 , λ_A) is perturbed, a different configuration of the conductive void region results. Specific discharge was found to be relatively insensitive to the configuration of the conductive void region, and fundamentally related to connectivity. However, mechanical transport was found to be highly sensitive to changes in the configuration of the conductive void region. Thus, mechanical transport parameters cannot be related to connectivity, for these parameters are highly dependent on the configuration of the conductive void region. These results imply the following on the use of double-porosity models. It may be possible to predict fluid flow using a double-porosity model, but it is less likely that such a model can be used to predict transport.

Mechanical transport parameters were generally least sensitive to the mean orientation of set 2, with the mean fracture length and the set areal density having about equal sensitivity to each mechanical transport parameter. For example, hydraulic effective porosity was highly sensitive to fracture length and set areal density, and ϕ_H became larger than ϕ in the two sensitivity studies (Figure 6-22). However, the max $|S|$ of ϕ_H to the mean orientation of set 2 was almost four times less than the max $|S|$ of ϕ_H to either the mean fracture length or the set areal density.

The connectivity sensitivity study has shown that q and ϕ_R are fundamentally related to connectivity. Specific discharge and rock effective porosity were least sensitive to the mean

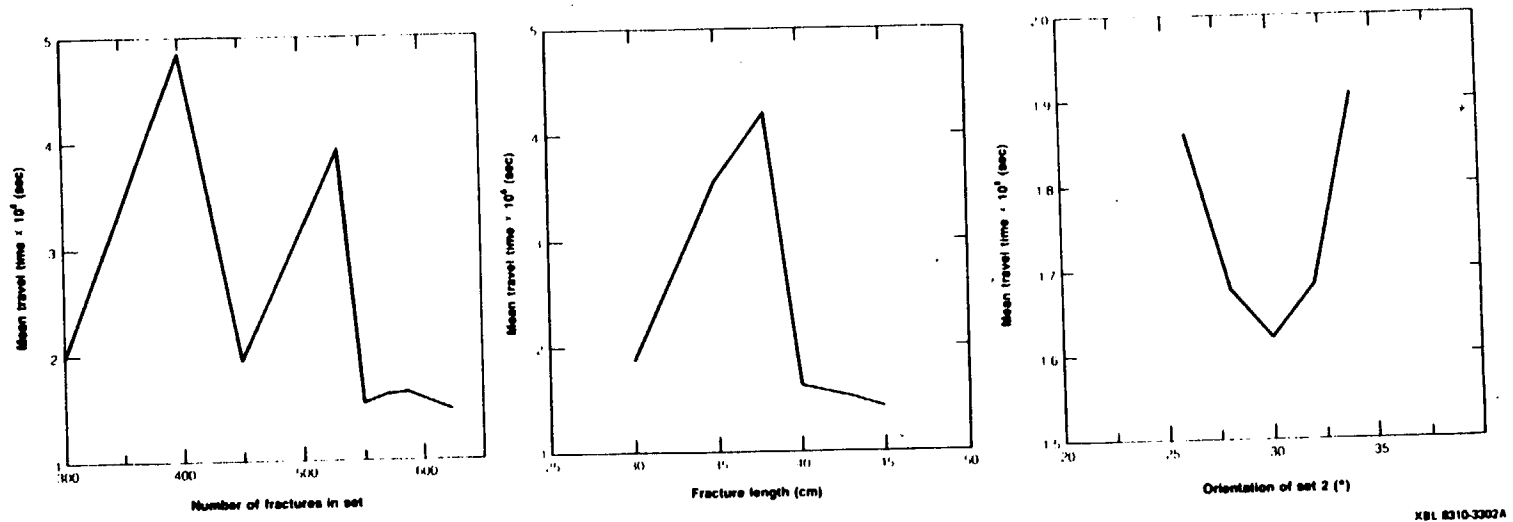
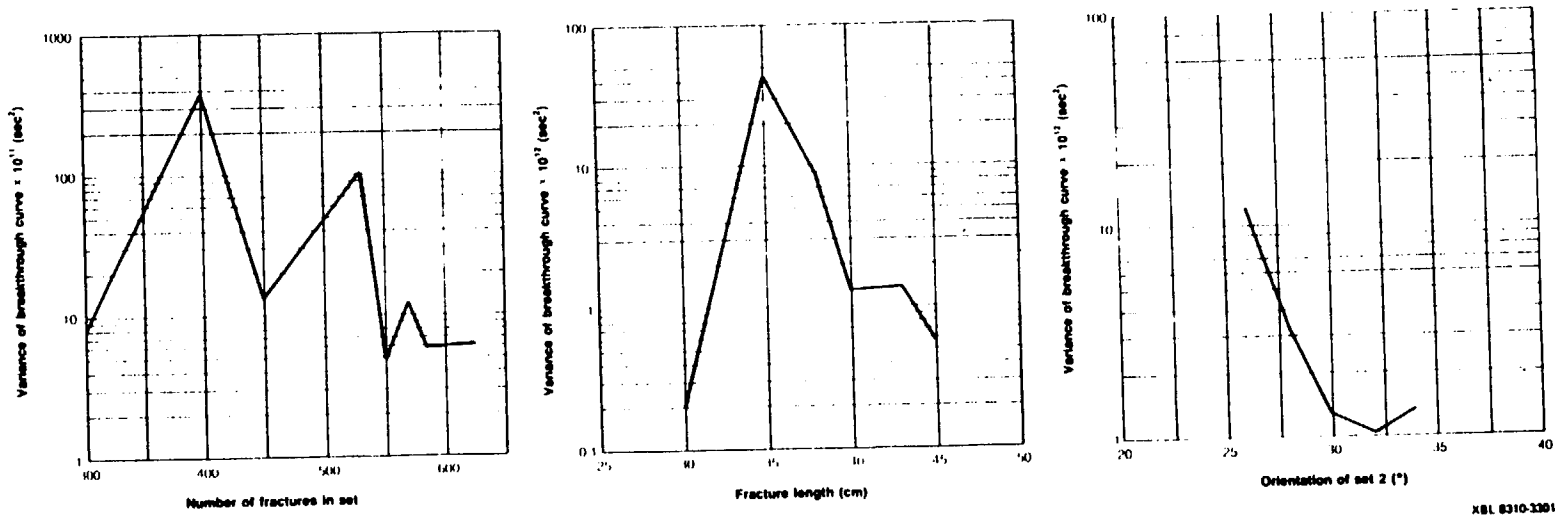


Figure 6-23 Mean Travel Time Versus Number of Fractures in Set, Mean Fracture Length, and Orientation of Set 2.



XBL 8310-3301A

Figure 6-24 Variance of the Breakthrough Curve Versus Number of Fractures in Set, Mean Fracture Length, and Orientation of Set 2.

orientation of set 2. Specific discharge exhibited nearly equal sensitivity to the mean fracture length and the set areal density. For this fracture system, angle of flow was relatively insensitive to connectivity.

Mechanical transport parameters were generally much more sensitive to the three connectivity parameters than either q or ϕ_R . No relationship was found between any of the mechanical transport parameters and connectivity, except for tortuosity. Mechanical transport parameters exhibited the least sensitivity to the mean orientation of set 2, and an equal sensitivity to the mean fracture length and the set areal density. The most sensitive mechanical transport parameter was σ^2 , and the least sensitive was τ .

6.4.1.2. Mean Aperture Sensitivity Analysis

Mean aperture is the only geometric parameter for which sensitivity can be evaluated. The following relationships were easily formulated for aperture:

a) $\phi \propto \mu_b$

b) $\phi_R \propto \mu_b$

c) $q \propto \mu_b^3$

d) $\theta \propto \mu_b^0$

e) $\tau \propto \frac{L}{\frac{q}{\phi_R}} = \frac{1}{\frac{\mu_b^3}{\mu_b}} = \frac{1}{\mu_b^2}$

f) $\phi_H = \frac{q}{VLIN} \propto \frac{\mu_b^3}{\mu_b^2} = \mu_b$

g) $\tau \propto \mu_b^0$

The relationships listed above were confirmed in the mean aperture sensitivity study which was conducted using two perturbed systems of aperture 0.001 cm and 0.003 cm.

The sensitivity of the variance of the breakthrough curve to aperture was not analytically derived. The mean aperture sensitivity study showed that σ^2 is proportional to μ_b^{-4} . The relationship of σ^2 to mean aperture was used to develop the relationships of both M_L and α_L to μ_b . Peclet number must be independent of mean aperture from equation 3.20 since the ratio of σ^2

to $\bar{\tau}^2$ is proportional to μ_b^0 . The relationship of M_L to mean aperture was determined from the Peclet number as:

$$M_L = Pe(VLIN)L$$

Since VLIN is proportional to μ_b^2 , M_L must also be proportional μ_b^2 . The longitudinal geometric dispersivity is equal to:

$$\alpha_L = \frac{M_L}{VLIN}$$

so α_L must be proportional to μ_b^0 since both VLIN and M_L are proportional to μ_b^2 . Thus, the mean aperture sensitivity study has shown that σ^2 , $\bar{\tau}$, and q are highly sensitive to mean aperture, while τ , θ , and α_L exhibit no sensitivity to mean aperture.

6.4.2. Sensitivity of Distributed Geometric Parameters

The previous sensitivity studies investigated the sensitivity of mean geometric parameters (μ). In this section, we shall investigate the effect distributed geometric parameters ($\sigma \neq 0$) have on mechanical transport and fluid flow. The sensitivity study for a distributed geometric parameter was conducted in the following way. First, a control fracture system (the same control fracture system used in the previous sensitivity study) was selected. Then, a distributed fracture system was created in which one of the three geometric parameters of length, orientation, or aperture was probabilistically simulated. The results for the distributed fracture system were then compared to the control fracture system to determine the effect the distributed geometric parameter had on mechanical transport and fluid flow.

6.4.2.1. Distribution of Fracture Orientation

The first distributed fracture system was created by distributing the fracture orientations in each set according to a normal distribution. The normal distribution for set 1 had a mean of 0° and a standard deviation of 3° , and the normal distribution for set 2 had a mean of 30° and a standard deviation of 3° . The distribution of fracture orientations produced a more random fracture pattern because fractures were oriented over a wider range of directions.

Connectivity increased with the randomness of the fracture pattern. As the number of fracture intersections increased, more fracture segments became conductive. The greater conductive void volume caused more fluid to flow through the system, and consequently, q and ϕ_R increased for this distributed system.

Deviation in angle of flow was greater for this system than for the control fracture system. The flow field became more nonuniform as paths of fluid particles became more irregular and deviated more from the mean direction of flow. The increased randomness of particle travel paths was reflected by a larger tortuosity. As the paths of particles became longer, the fluid needed more time to flow from side 2 to side 4. Consequently, mean travel time increased and the average linear velocity decreased. The increase in \bar{q} and decrease in VLIN resulted in an increase in ϕ_H . This increase in ϕ_H was expected since an increase in ϕ_R should correspond to an increase in ϕ_H . The variance of the breakthrough curve also increased because of the increased randomness in particle paths.

Thus, the distribution in fracture orientations created a more random fracture system which caused connectivity to increase. As the fracture pattern became more random, paths of fluid particles became more irregular. The following parameters increased because of the distribution in fracture orientation: ϕ_R , \bar{q} , DEVA, τ , $\bar{\tau}$, and σ^2 . The average linear velocity decreased for the fracture system with distributed orientations.

6.4.2.2. Distribution of Fracture Aperture

The second distributed fracture system was created by distributing the fracture apertures for each set according to a lognormal distribution with a mean of 0.002 cm and a standard deviation of 0.0001 cm. The purpose of this study was to show how small aperture fractures created by the distribution control both mechanical transport and fluid flow.

A fluid stream flows through a series of fractures of different apertures in a fracture network. The cubic law states that the flow rate in a fracture is proportional to b^3 . Consequently, the flow rate in a series of fractures is governed by the fracture with the smallest aperture, so that small aperture fractures will negate the large flow capabilities of large aperture fractures.

Flow rate would only increase if connected pathways of large aperture fractures existed across the fracture network. However there is only a small probability of these highly conductive paths developing in a fracture network.

The effect of small aperture fractures was demonstrated by the reduction in \bar{q} for this system, as compared with the control fracture system. The smaller flow rate, coupled with the fact that tortuosity did not change, meant that fluid particles took a longer time to travel through the flow region. Consequently, \bar{T} increased and VLIN decreased. Since both q and VLIN decreased, hydraulic effective porosity did not change.

The distribution of apertures caused a greater variation in the velocities within elements. This resulted in a larger difference in the flow rate on opposing sides of the flow region, and a wider distribution in particle travel times in the breakthrough curve. Consequently, both DEVF and σ^2 increased.

6.4.2.3. Distribution of Fracture Length

The third distributed fracture system was created by probabilistically simulating the fracture lengths of both sets according to a lognormal distribution with a mean of 40 cm and a standard deviation of 4 cm. Connectivity was greatly reduced for this fracture system as a larger portion of the void region became dead-end zones and isolated spaces. The short length fractures caused these nonconductive void regions to develop in the fracture network. Rock effective porosity and specific discharge decreased as connectivity decreased, and DEVF increased as only a few flow paths were continuous between sides 2 and 4.

6.4.2.4. Summary

The study of distributed geometric parameters has shown that a distribution in fracture orientation caused the fracture network to become more random. The increased randomness in the fracture network caused connectivity, q , ϕ_R , and ϕ_H to increase. When fracture lengths were distributed, connectivity decreased. The short length fractures caused an increase in dead-end zones and isolated void spaces. The reduced connectivity caused both q and ϕ_R to decrease,

and DEVF to increase. The distributed aperture study demonstrated that mechanical transport and fluid flow are controlled by the small aperture fractures. The distribution of aperture caused q to decrease and both $\bar{\tau}$ and σ^2 to increase.

CHAPTER 7

INVESTIGATION OF MECHANICAL TRANSPORT AT RESEARCH SITE IN MANITOBA, CANADA

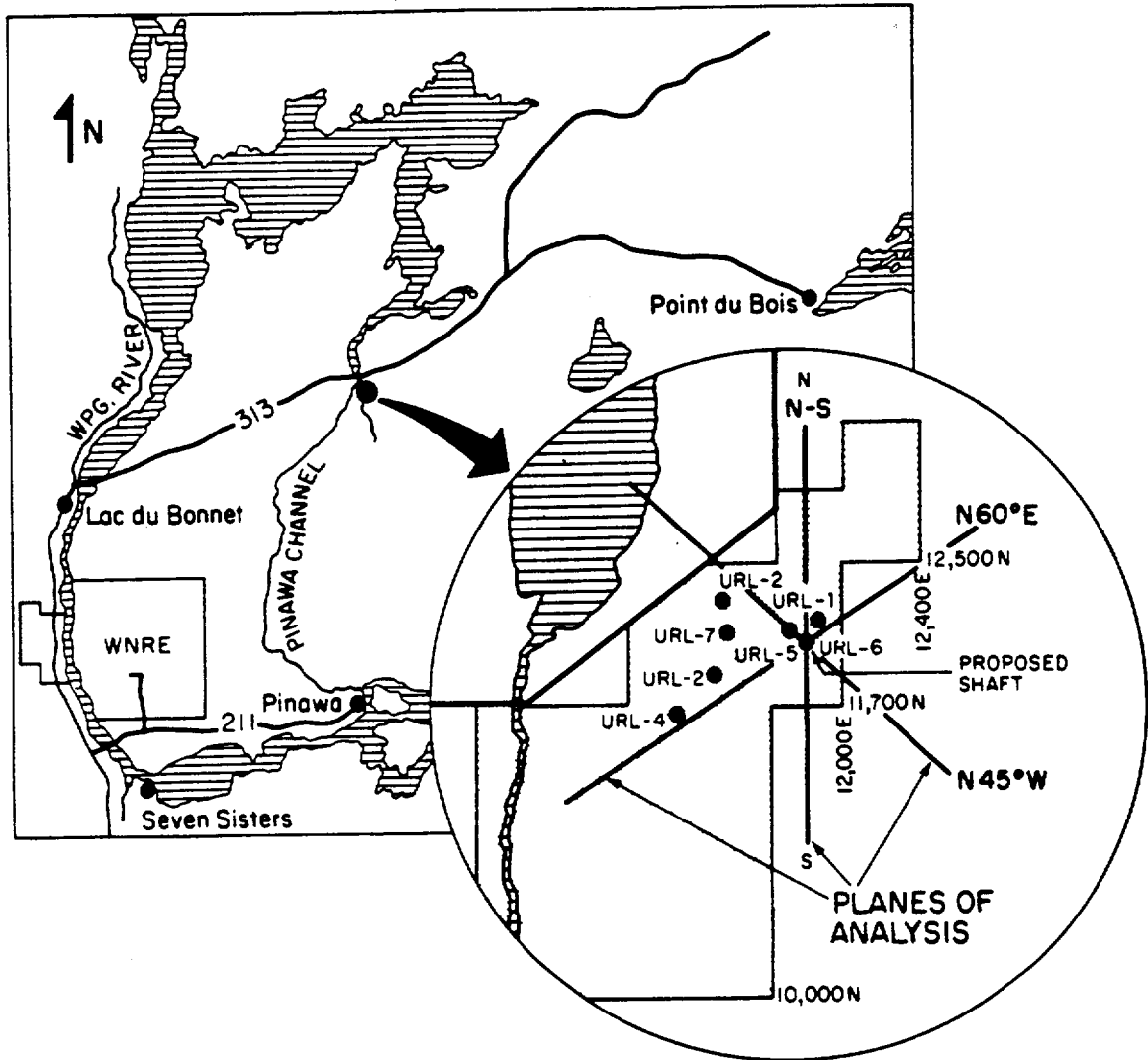
7.1. INTRODUCTION

The Atomic Energy of Canada Limited is conducting hydrologic research at a site located in the province of Manitoba (Figure 7-1). The research program, called the Canadian Nuclear Fuel waste Management Program, has two objectives: 1) to understand fluid flow in a fractured zone in the Lac du Bonnet granitic batholith, and 2) to understand mechanical transport in the same area. The study of fluid flow is being conducted by Long (1984). This chapter presents the study of mechanical transport for this fractured zone.

The computer program described in Chapter 4 was used to study mechanical transport for two vertical planes oriented at N-45-W and N-S in a sparsely fractured zone. Each plane intersected the location of the proposed shaft (insert to Figure 7-1). Fracture information must be read into the program to simulate the fracture pattern for the two vertical planes. This information for each plane consists of:

- 1) The number of fracture sets.
- 2) μ_0 and σ_0 for each set, and the type of probability distribution for fracture orientation.
- 3) μ_b and σ_b for each set, and the type of probability distribution for fracture aperture.
- 4) The areal density for each set.
- 5) μ_l and σ_l for each set, and the type of probability distribution for fracture length.

These geometric parameters were determined from hydrogeologic data collected at the site. A detailed discussion of the analysis of the field data is given by Long (1984). The field data consisted of borehole T.V. logs, core logs, and data from well tests for permeability. The borehole T.V. logs and core logs were used to determine the number of fracture sets, and the mean and



XBL 839-2214

Figure 7-1 Map of Hydrogeological Research Site in Manitoba, Canada.

standard deviation for the fracture orientations of each set. The fracture orientation statistics in both vertical planes were nearly identical such that only a single set of fracture orientation statistics (μ_o and σ_o for each set) was needed for both planes. Fracture orientations in each set were assumed to follow the Gaussian distribution.

The well testing data were used to determine the mean and standard deviation for the fracture apertures of each set. The aperture statistics for each set were assumed to be identical. Subsequently, the limited well testing data did not have to be analyzed separately for each set. The following geometric parameters were determined from the analysis of the field data:

- 1) The number of sets is 2.
- 2) $\mu_{o, \text{set } 1} = 0^\circ$, $\sigma_{o, \text{set } 1} = 30^\circ$
- 3) $\mu_{o, \text{set } 2} = 90^\circ$, $\sigma_{o, \text{set } 2} = 35^\circ$
- 4) $\mu_b = 0.00005 \text{ m}$, $\sigma_b = 0.00005 \text{ m}$

The set areal density, mean fracture length, and standard deviation of fracture length could not be determined from the borehole data. Thus, a length-density sensitivity analysis was conducted to investigate how length and density influences mechanical transport. In this analysis, each fracture set was assumed to have the same areal density and the same fracture length statistics, with the standard deviation of length assumed equal to μ_l . Fracture lengths were assumed to be lognormally distributed. The following relationship was used to relate mean fracture length and set areal density (Long, 1984):

$$\frac{\lambda_l}{\mu_{\cos\zeta}} = LD = \mu_l \lambda_A \quad (7.1)$$

The linear density λ_l is the number of fractures intersecting a unit length of scanline. Linear density was computed in this study by counting the number of open fractures intersecting each borehole, and then dividing by the total length of the boreholes. The mean of $\cos\zeta$ is a correction factor used to account for the fact that fractures that are perpendicular to the scanline have a greater probability of intersecting the scanline than fractures that are parallel to this line. From λ_l and $\mu_{\cos\zeta}$, the constant length-density parameter LD was computed to be 0.1 m^{-1} . As

an example of the use of this length-density relationship, a fracture set with a mean fracture length of l_a would have the following length statistics and set areal density:

$$\mu_l = l_a, \quad \sigma_l = l_a$$

$$\lambda_A = 0.1/l_a$$

Two series of length-density sensitivity studies were conducted: 1) the constant aperture series and; 2) the distributed aperture series. The constant aperture series was conducted to investigate mechanical transport caused strictly by the configuration of the fracture pattern, ignoring the heterogeneity that results by distributing apertures. Two studies were conducted in the distributed aperture series because the aperture distribution has a great influence on mechanical transport: 1) study with μ_b and σ_b both equal to 0.00005 m and, 2) study with σ_b equal to $0.3\mu_b$. The mean b^3 (cubic law) was held constant in the two series so that the expected permeability would be the same in the two series. In the first distributed aperture study, fracture apertures were lognormally distributed in both sets, with a mean of 0.00005 m and a standard deviation of 0.00005 m. The mean b^3 for this probability distribution is $1 \times 10^{-12} \text{ m}^3$. Consequently, this mean b^3 was maintained in both series such that an aperture of 0.0001 m was used in the constant aperture series.

7.2. CONSTANT APERTURE LENGTH-DENSITY SERIES

Fracture systems with different fracture lengths and set areal densities were created using equation 7.1:

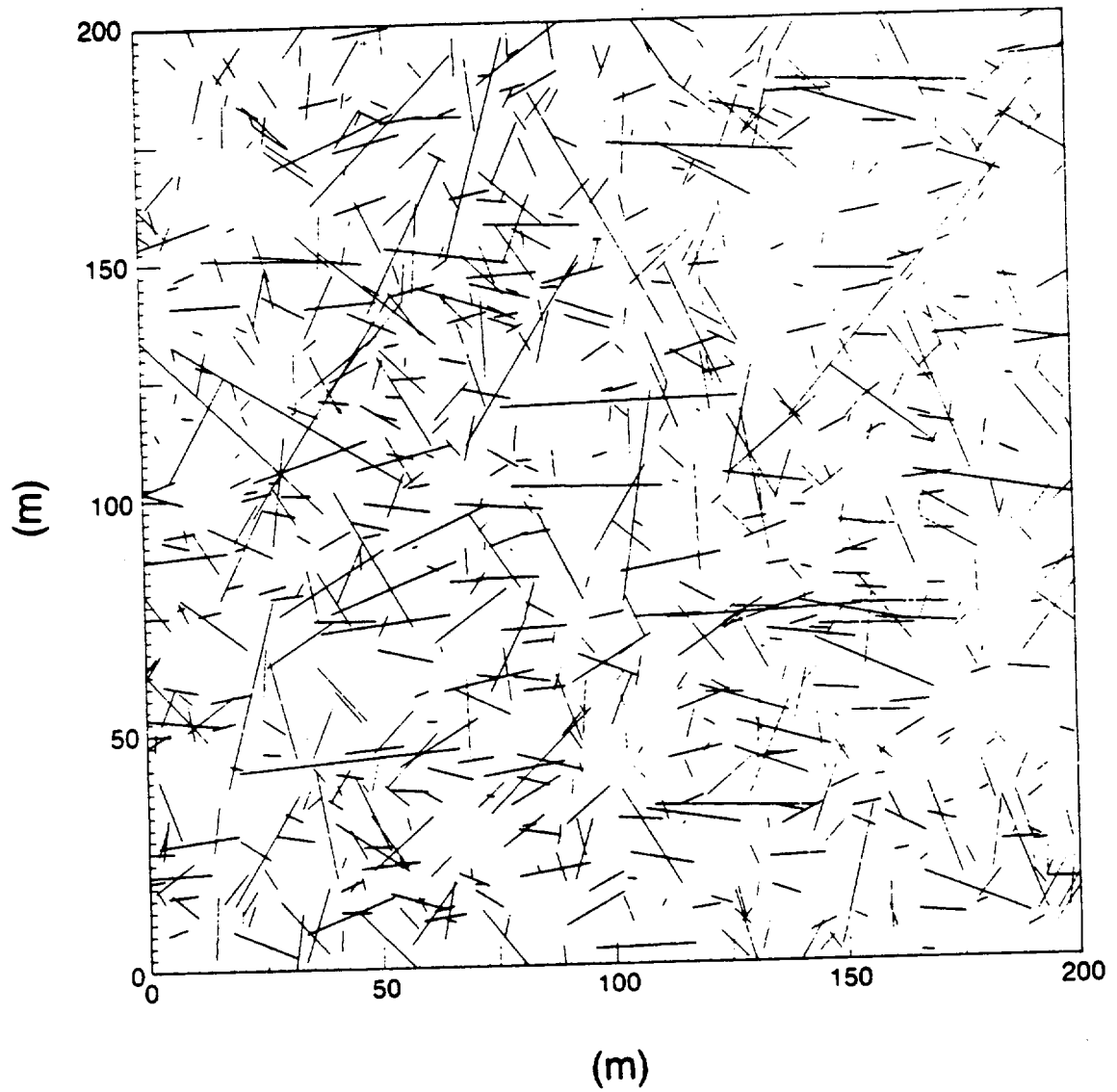
$$LD = 0.1 = \lambda_A \mu_l$$

Each fracture system consisted of two fracture sets with the same λ_A . The fracture orientations for set 1 were distributed using a normal distribution with a mean of 0° and a standard deviation of 30° . The fracture orientations for set 2 were distributed using a normal distribution with a mean of 90° and a standard deviation of 35° . All fractures had an aperture of 0.0001 m, and fracture lengths were distributed using a lognormal distribution with a mean of μ_l and a standard deviation also equal to μ_l . Each set had an areal density of $0.1/\mu_l$.

The width of the square generation region used in each length study was twenty times larger than μ_1 . Square flow regions of width ten times μ_1 , oriented at every 15° , were created for each fracture system to study mechanical transport. The hydraulic gradient on sides 1 and 3 for all flow regions was set at 0.01:

The first two fracture systems were created with μ_1 equal to 10 m ($\lambda_A = 0.01 \text{ m}^{-2}$) and μ_1 equal to 20 m ($\lambda_A = 0.005 \text{ m}^{-2}$). The fracture pattern in the generation region for the fracture system with μ_1 of 10 m is shown in Figure 7-2. The fracture pattern and network of connected fracture segments for the flow region oriented at 0° for this fracture system are both shown in Figure 7-3. Both fracture systems were so sparse that a zone of continuous flow did not develop between sides 2 and 4. Thus, neither system behaved like equivalent porous medium. In a porous medium, a continuous zone of flow exists in a square flow region unless the angle of flow is greater than 45° . The geometric parameters for the two systems indicate that both systems should be fairly isotropic, such that the angle of flow will not exceed 45° . No study of mechanical transport was conducted for the two systems because of the absence of the continuous zone of flow between sides 2 and 4 in any flow region. The fracture system with μ_1 of 30 m was the first system studied which had a continuous zone of flow between sides 2 and 4. In addition to the fracture system with μ_1 of 30 m, two other discontinuous systems with μ_1 of 35 m and 50 m were studied. For the fracture system with μ_1 of 50 m, the width of the flow region was reduced to seven times μ_1 because of computer storage. The fracture pattern in the generation region for the fracture system with μ_1 of 35 m is shown in Figure 7-4. The fracture pattern and network of connected fracture segments for the flow region oriented at 0° for this system are shown in Figure 7-5.

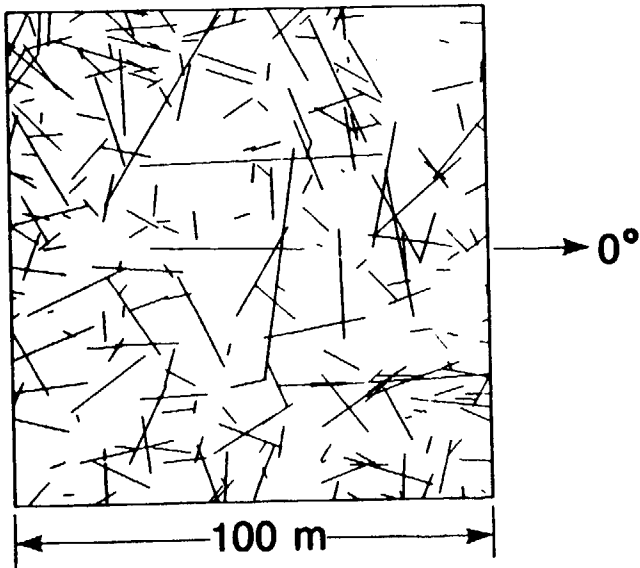
A continuous fracture system ($\mu_1 = \infty$) was also created to study mechanical transport. This system was created in the following way. For each set, a scanline was drawn perpendicular to the mean orientation of the set across the entire generation region. The square generation region had a width of 650 m. This scanline passed through the center of the generation region. The fracture centers of the set were then randomly located on this scanline. The number of



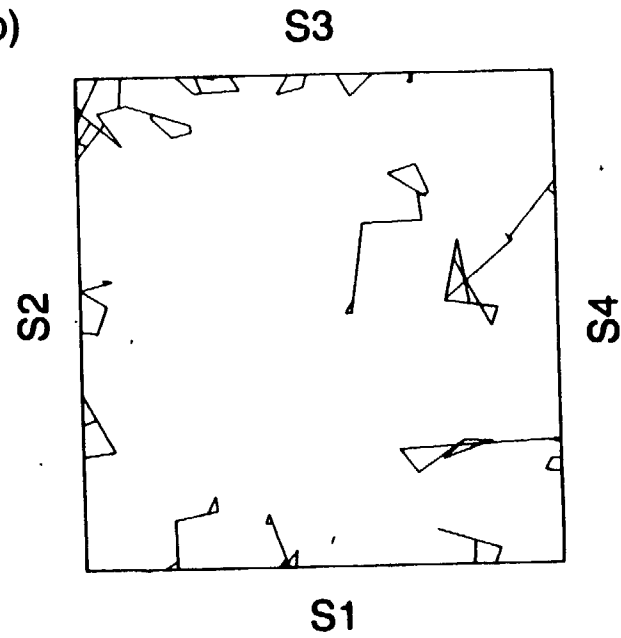
XBL 841-392

Figure 7-2 Fracture Network in the Generation Region for Discontinuous System With Mean Fracture Length of 10 m.

(a)

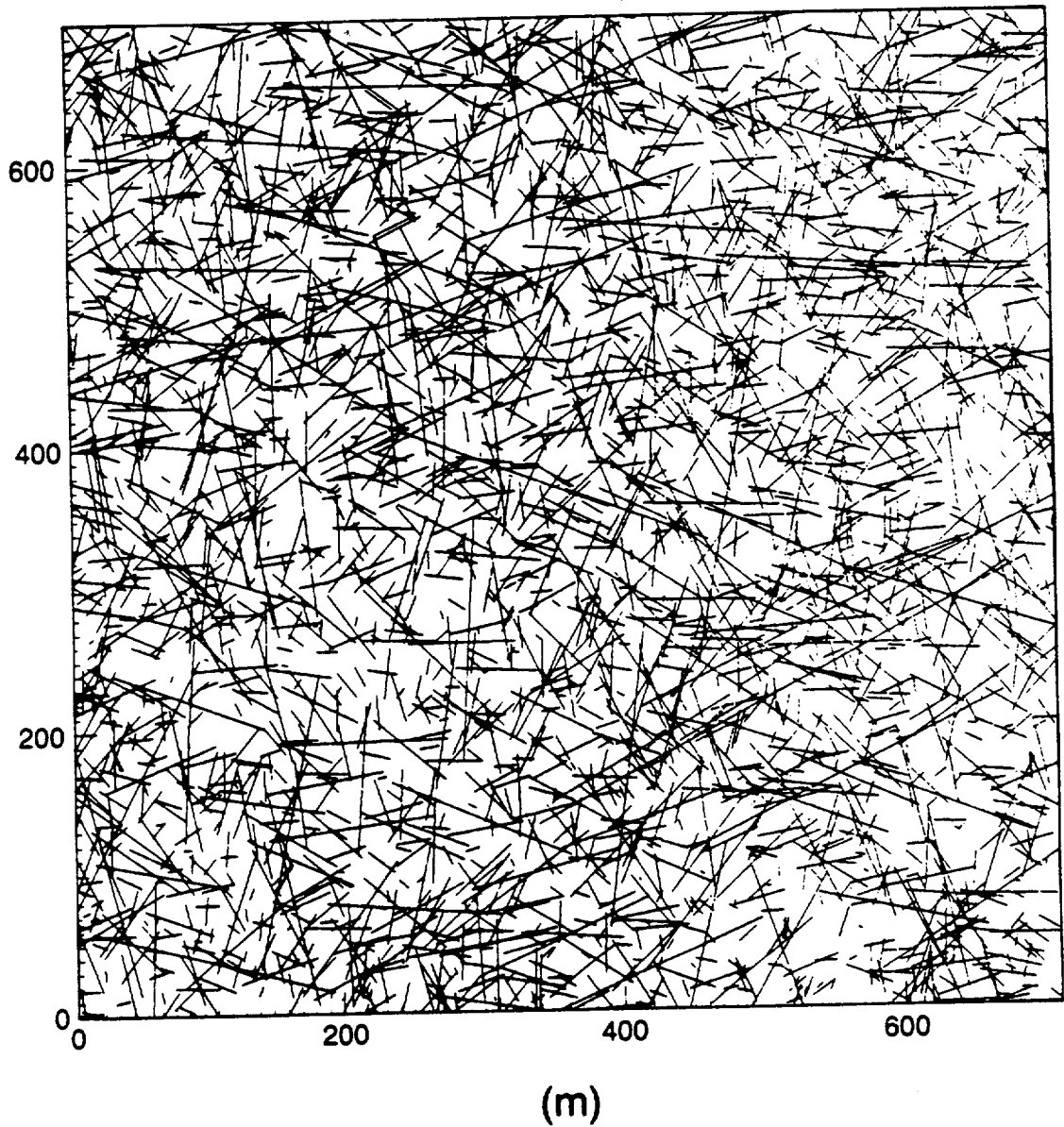


(b)



XBL 8311-3452

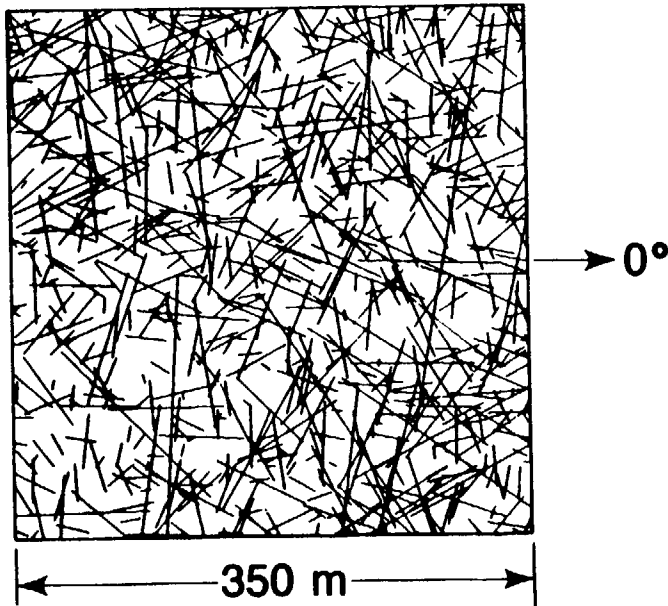
Figure 7-3 Network of a) Fractures and b) Connected Fracture Segments in the Flow Region Oriented at 0° for Discontinuous System With Mean Fracture Length of 10 m.



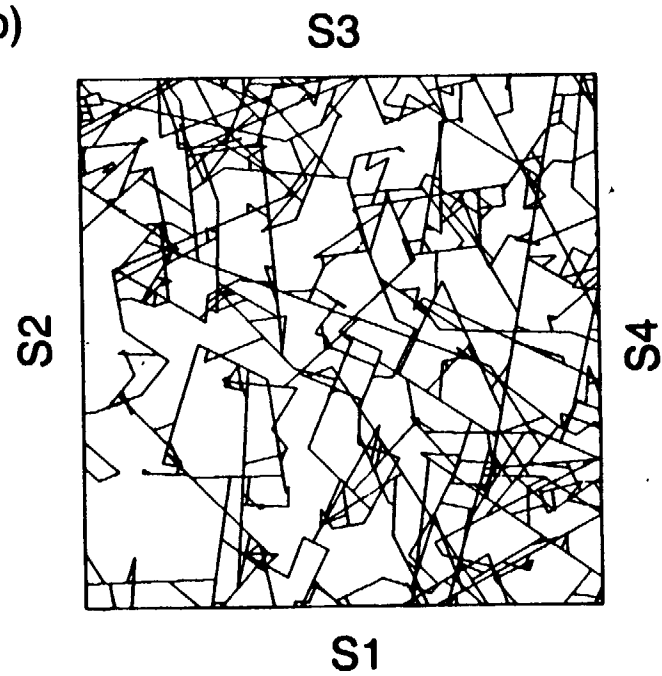
XBL 841-393

Figure 7-4 Fracture Network in the Generation Region for Discontinuous System With Mean Fracture Length of 35 m.

(a)



(b)



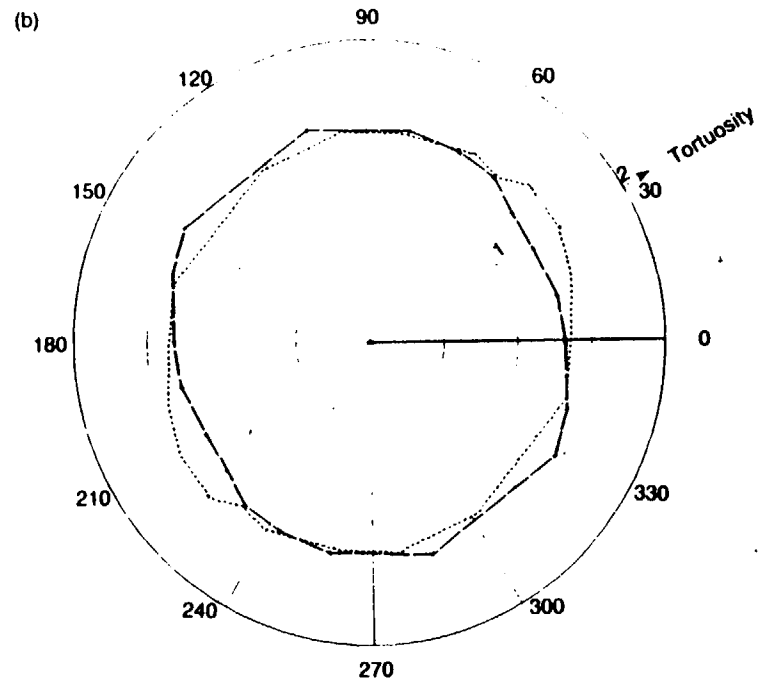
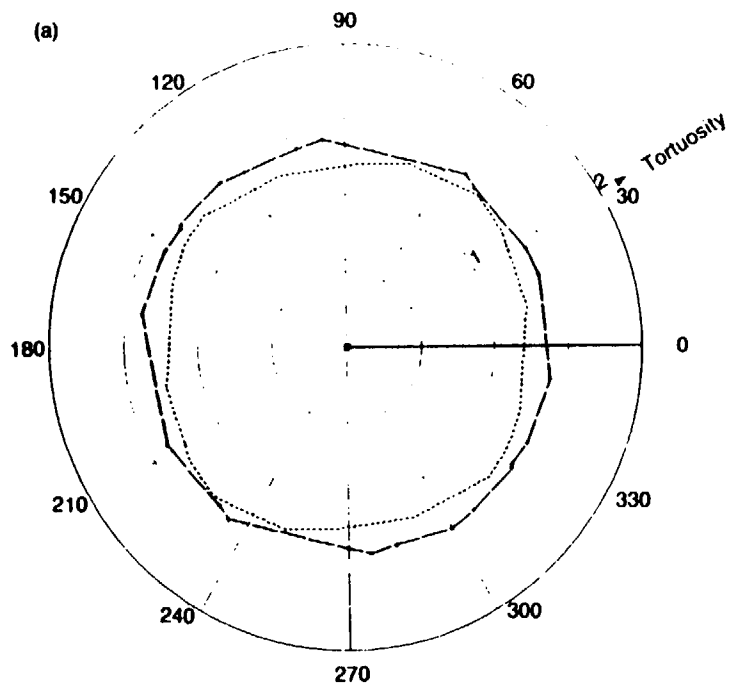
XBL 8311-3453A

Figure 7-5 Network of a) Fractures and b) Connected Fracture Segments in the Flow Region Oriented at 0° for Discontinuous System With Mean Fracture Length of 35 m.

fracture centers located on the scanline was equal to $(LD)(\mu_{\text{cos}\theta})LS$, where LS is the length of the scanline. Next, fracture orientations and apertures were distributed from Gaussian and lognormal distributions, respectively. Each fracture in the set was assigned a length much larger than the width of the generation region. After the completion of the fracture network, square flow regions of width 250 m, oriented at every 15° , were used to study mechanical transport.

Figure 7-6 shows the tortuosity versus direction of flow for the continuous fracture system and the three discontinuous systems. In all four cases, tortuosity is stable with direction. This indicates that these fracture systems are fairly isotropic. The permeability study conducted by Long (1984) also found that the four systems are fairly isotropic. Mean tortuosity does not vary significantly for the three discontinuous systems. The mean tortuosities were 1.367, 1.403, and 1.368 for the discontinuous systems with μ_1 of 30 m, 35 m, and 50 m, respectively. The mean tortuosity for the continuous system is 1.261. The fractures in the continuous system span across the entire flow region. Consequently, fluid flows in a more direct route across the flow region in the continuous fracture system than in any of the discontinuous systems. This caused tortuosity to be lower for the continuous system.

Hydraulic effective porosity is shown plotted against direction of flow in Figure 7-7. No directional dependence in ϕ_H is apparent for any of the four fracture systems. Since hydraulic effective porosity is relatively constant in all directions for the four systems, each system behaves like an equivalent porous medium for transport. The mean ϕ_H are 0.0000133, 0.0000141, and 0.0000147 for the three discontinuous systems with μ_1 of 30 m, 35 m, and 50 m, respectively. Rock effective porosity is constant at 0.000013 for the three discontinuous systems. Consequently, ϕ_H is greater than ϕ_R , and ϕ_H increases with μ_1 in the discontinuous systems. The mean ϕ_H is 0.0000213 for the continuous fracture system. This value is slightly less than the total porosity of 0.0000235. Hydraulic effective porosity is much greater for the continuous system than for the discontinuous system because no dead-end fracture segments exist in the continuous system. The void volume is totally connected for continuous systems. The total porosity for the three discontinuous systems of 0.0000195 is only slightly less than ϕ for

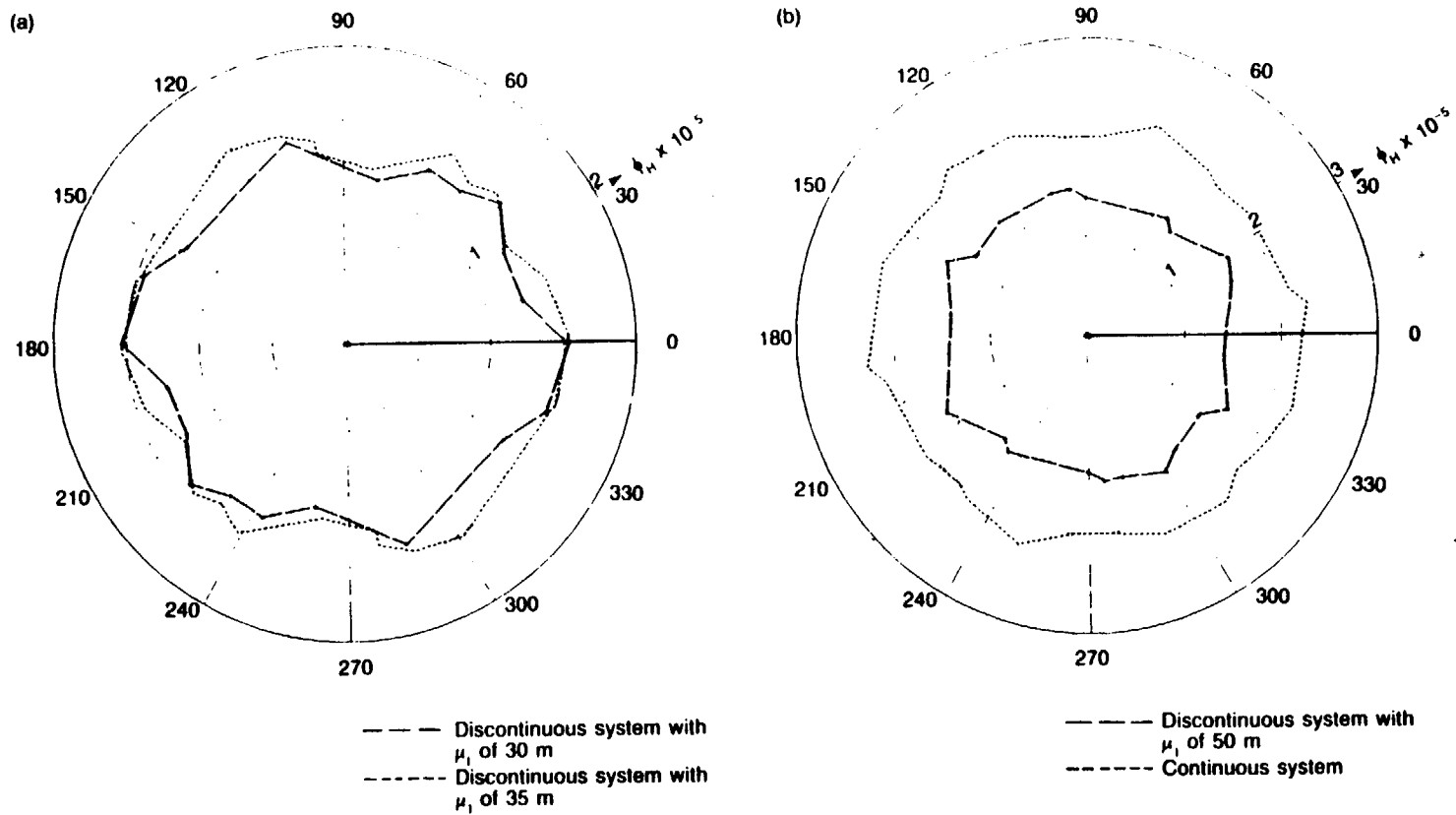


--- Discontinuous system with μ_l of 30 m
 - - - Discontinuous system with μ_l of 35 m

--- Discontinuous system with μ_l of 50 m
 - - - Continuous system

XBL 841-532

Figure 7-6 Polar Plots of Tortuosity for a) Systems With Mean Fracture Lengths of 30 and 35 m and b) System With Mean Fracture Length of 50 m and the Continuous Fracture System.



XBL 841-533

Figure 7-7 Polar Plots of Hydraulic Effective Porosity for a) Systems With Mean Fracture Lengths of 30 and 35 m and b) System With Mean Fracture Length of 50 m and the Continuous Fracture System.

the continuous system. However, only 67 percent of this void volume is conductive.

Figures 7-8 and 7-9 show the polar plots of longitudinal geometric dispersivity for the four systems. The discontinuous system with μ_1 of 30 m has a maximum α_L of 99 m at direction of flow 78° . The next largest α_L occurs in a direction which is nearly perpendicular to the direction of maximum α_L . The mean α_L for this system is 61.1 m, and the standard deviation in α_L is 18.4 m. The polar plot of α_L is very different for the discontinuous system with μ_1 of 35 m. Longitudinal geometric dispersivity shows large directional variations, as the α_L curve is very jagged. The ratio of $\alpha_{L,max}$ to $\alpha_{L,min}$ is four. The two largest values of α_L occur in directions that are nearly orthogonal to each other. The mean α_L for this system is 63.5 m, and the standard deviation in α_L is 36.0 m. The directional variation in α_L is less for the discontinuous system with μ_1 of 50 m than for the discontinuous system with μ_1 of 35 m. The ratio of $\alpha_{L,max}$ to $\alpha_{L,min}$ is three, and the standard deviation in α_L is 20.3 m. The mean α_L for this system is 66.4 m. For the continuous system, α_L shows a strong directional dependence. The ratio of $\alpha_{L,max}$ to $\alpha_{L,min}$ is nine. The two directions of maxima α_L are 0° and 90° . These two directions are the mean orientations for the two sets. The mean α_L is 30.3 m for the continuous system.

The following conclusions can be made about the α_L study. The direction of maximum α_L for each system is located between 80° and 170° . The next largest α_L for each system is obtained in a direction that is nearly perpendicular to the direction of maximum α_L . The polar plots of α_L are very different for each system, as α_L exhibits a unique directional variation in each system. However, the mean-directional longitudinal geometric dispersivities for the three discontinuous systems are nearly the same so that mean α_L is independent of mean fracture length.

The highly directional nature of α_L was not expected in this study. Theoretically, α_L should be constant in all directions in an isotropic porous medium. Therefore, we expected the polar plots of α_L to be nearly circular. To see if α_L approaches a directionally stable value, four additional realizations were studied for the discontinuous system with μ_1 of 50 m. The width of flow region used in these realizations was 330 m.

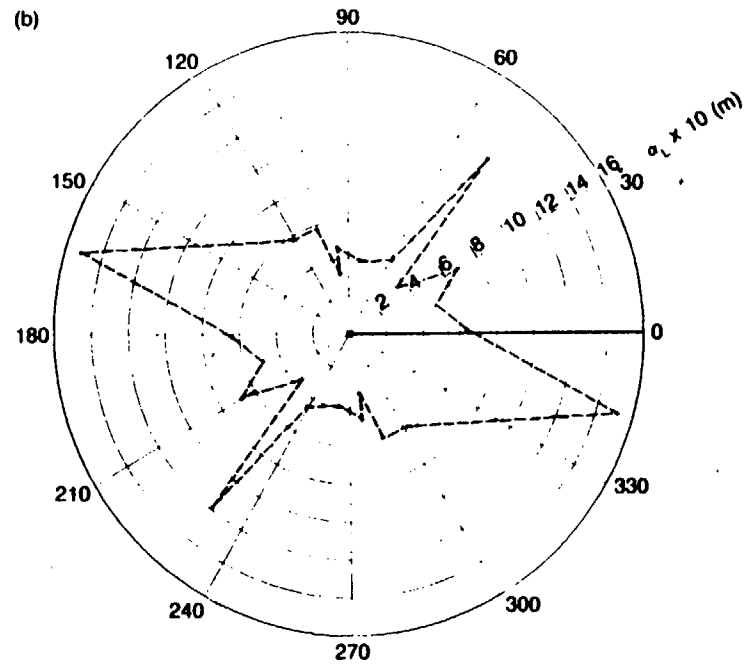
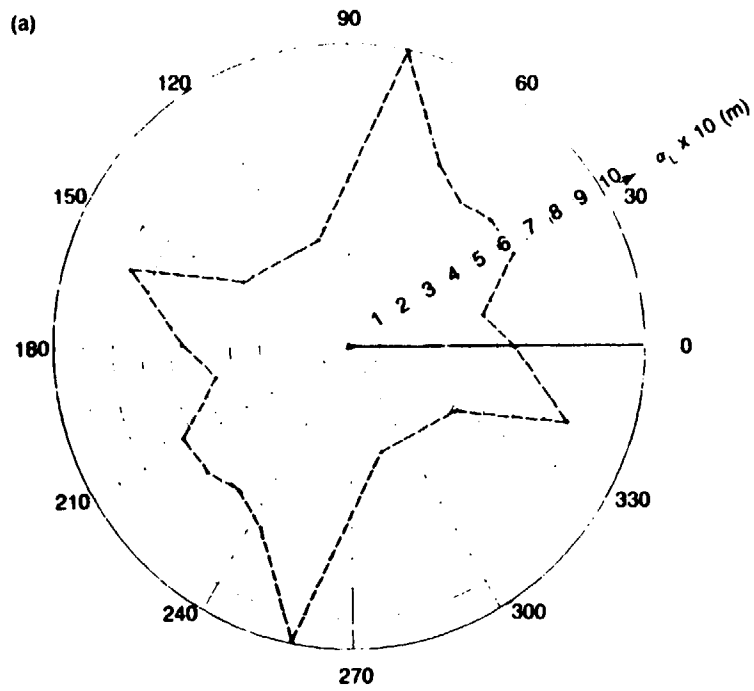
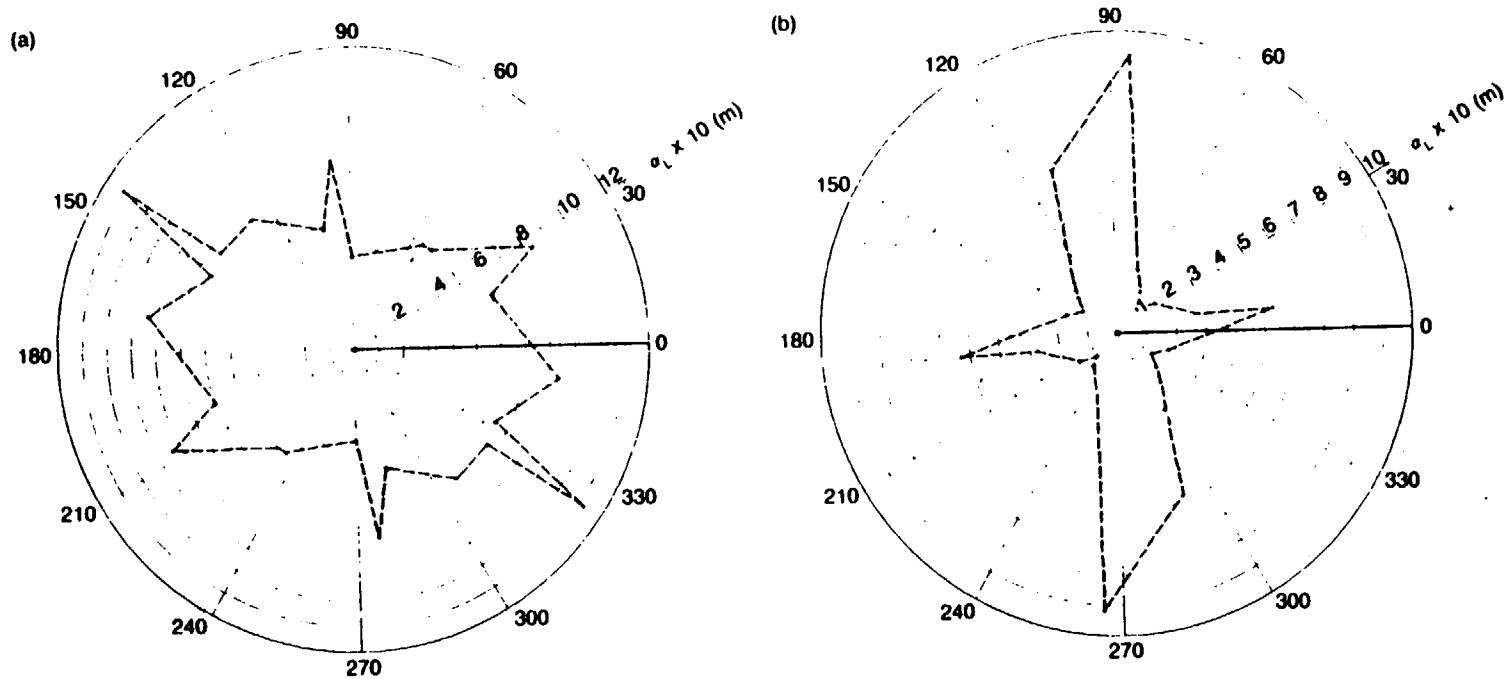


Figure 7-8 Polar Plots of Longitudinal Geometric Dispersivity for Systems With Mean Fracture Lengths of a) 30 m and b) 35 m.



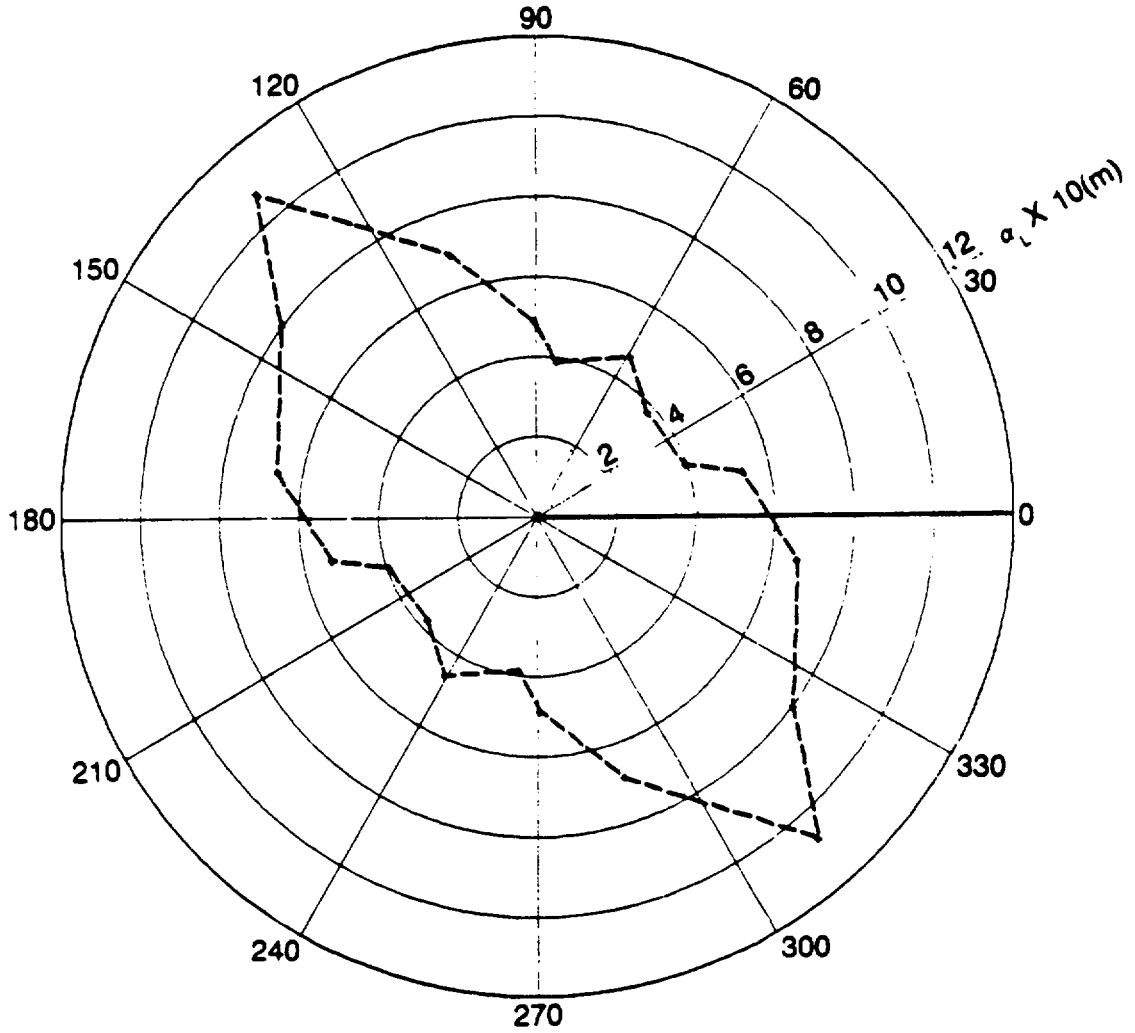
XBL 841-395

Figure 7-9 Polar Plots of Longitudinal Geometric Dispersivity for a) System With Mean Fracture Length of 50 m and b) the Continuous Fracture System.

All five realizations showed large directional variations in α_L . Figure 7-10 is a polar plot of the mean α_L for the five realizations. Longitudinal geometric dispersivity is directionally stable between 20° to 80° . As direction of flow varies from 80° to 130° , α_L increases rapidly to its maximum value of 110 m. The ratio of $\alpha_{L,max}$ to $\alpha_{L,min}$ is 2.8. Thus, longitudinal geometric dispersivity does not appear to be approaching a directionally stable value, as longitudinal geometric dispersivity is stable only between 20° to 80° . This was not the first fairly isotropic medium which had a directionally dependent α_L . It will be recalled from section 5.3 that α_L was directionally dependent for the continuous fracture system of two orthogonal sets with constant apertures which behaved like an equivalent isotropic medium for fluid flow. The mean α_L for the five realizations is 65.7 m. This value is about equal to the mean longitudinal geometric dispersivities measured earlier for the three discontinuous systems. We expect that if α_L were to converge to a directionally stable value, this value would be about 65 m.

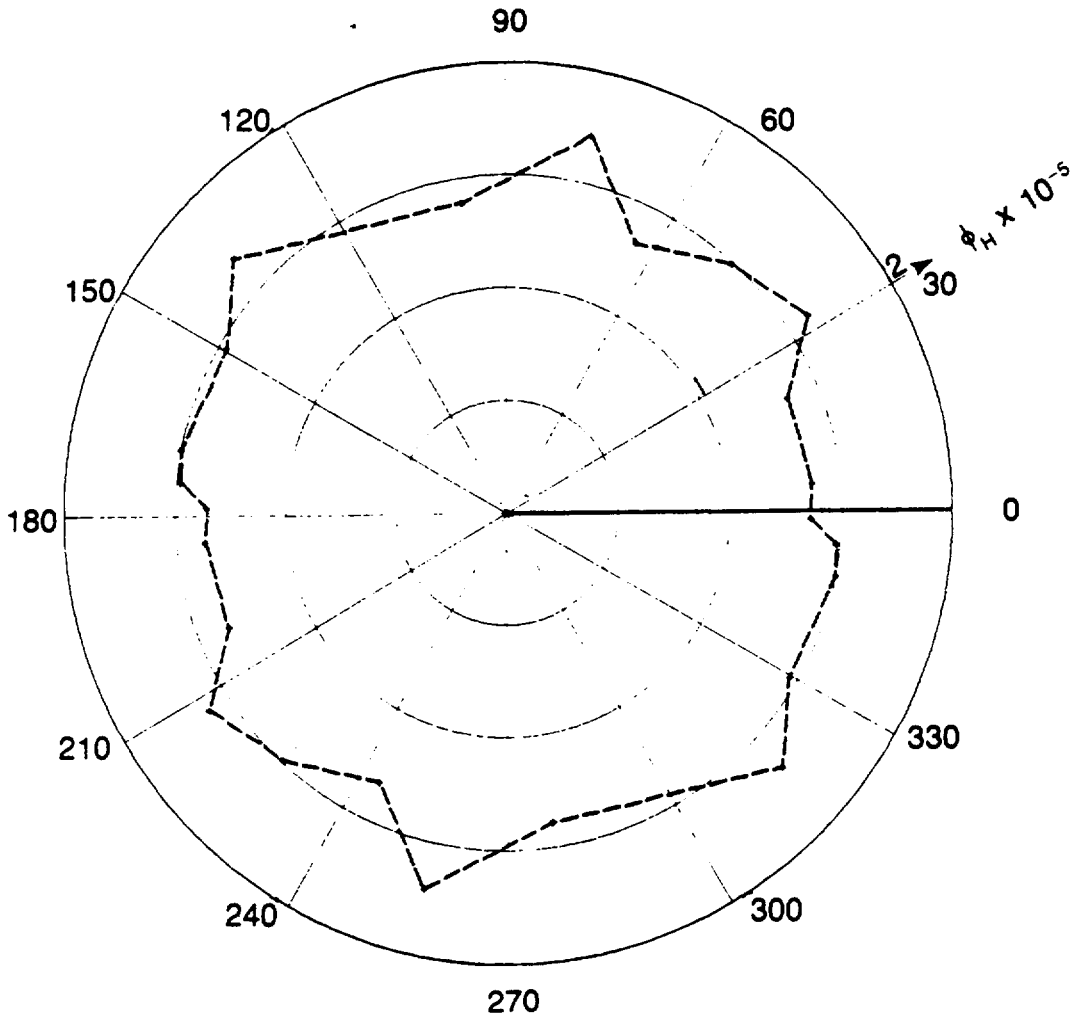
The four systems behaved like equivalent porous media for transport because ϕ_H was directionally stable in each system. A study was made to see what happens to ϕ_H when the fracture system does not behave like an equivalent porous medium. The fracture system in the last realization of the previous longitudinal geometric dispersivity study was used for this study. Square flow regions of widths 60 m, 175 m, and 330 m were oriented at every 15° , beginning at 0° within the generation region. For each flow region, the computer program was used to calculate hydraulic effective porosity.

Figure 7-11 is a polar plot of ϕ_H measured using flow regions of width 330 m. Hydraulic effective porosity is nearly the same in all directions. The mean ϕ_H is 0.0000148 and the standard deviation in ϕ_H is 1.28×10^{-6} . Figure 7-12 shows the polar plot of hydraulic effective porosity measured using flow regions of width 175 m. The mean hydraulic effective porosity is 0.0000149. Thus, the mean hydraulic effective porosity did not change as the size was lowered. The standard deviation in ϕ_H increased slightly to 1.35×10^{-6} . The polar plot of ϕ_H is still approximately a circle, and we can conclude that on this scale the system behaves like a continuum for transport. Figure 7-13 shows the polar plot of ϕ_H measured using flow regions of



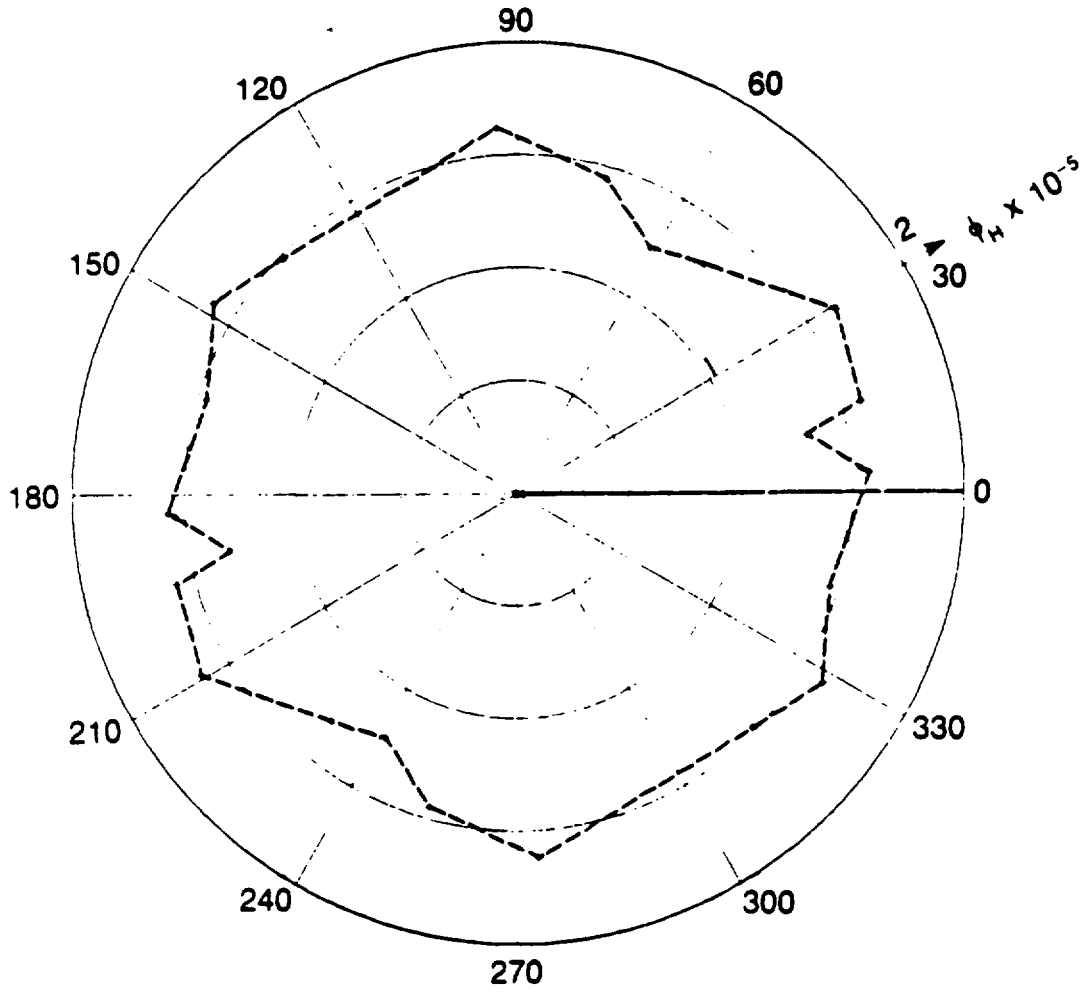
XBL 8401-6799

Figure 7-10 Polar Plot of Mean Longitudinal Geometric Dispersivity for Five Realizations of the System With Mean Fracture Length of 50 m.



XBL 841-384

Figure 7-11 Polar Plot of Hydraulic Effective Porosity for System With Mean Fracture Length of 50 m Using Square Flow Region of Width 330 m.



XBL 841-383

Figure 7-12 Polar Plot of Hydraulic Effective Porosity for System With Mean Fracture Length of 50 m Using Square Flow Region of Width 175 m.

width 60 m. The mean hydraulic effective porosity of 0.0000118 is less than computed at the two larger scales. The ϕ_H curve deviates from a circle as large fluctuations in ϕ_H are observed near 110°. The standard deviation in ϕ_H has increased to 1.73×10^{-6} . Thus, a flow region of this size behaves like a discontinuum for transport. As the flow region size decreases, the polar plot of ϕ_H begins to deviate from a circle and ϕ_H fluctuates with direction. As a consequence, the standard deviation in ϕ_H increases.

7.3. DISTRIBUTED APERTURE LENGTH-DENSITY SERIES

7.3.1. Distributed Aperture Length-Density Study with Standard

Deviation Equal to Mean Aperture

The previous constant aperture length-density study investigated mechanical transport caused by the configuration of the fracture network, ignoring heterogeneity that results by distributing apertures. In the first distributed aperture length-density study, fracture apertures were distributed using two techniques.

- 1) Apertures were lognormally distributed with a mean of 0.00005 m and a standard deviation of 0.00005 m.
- 2) Apertures were linearly correlated to fracture length in the following way:

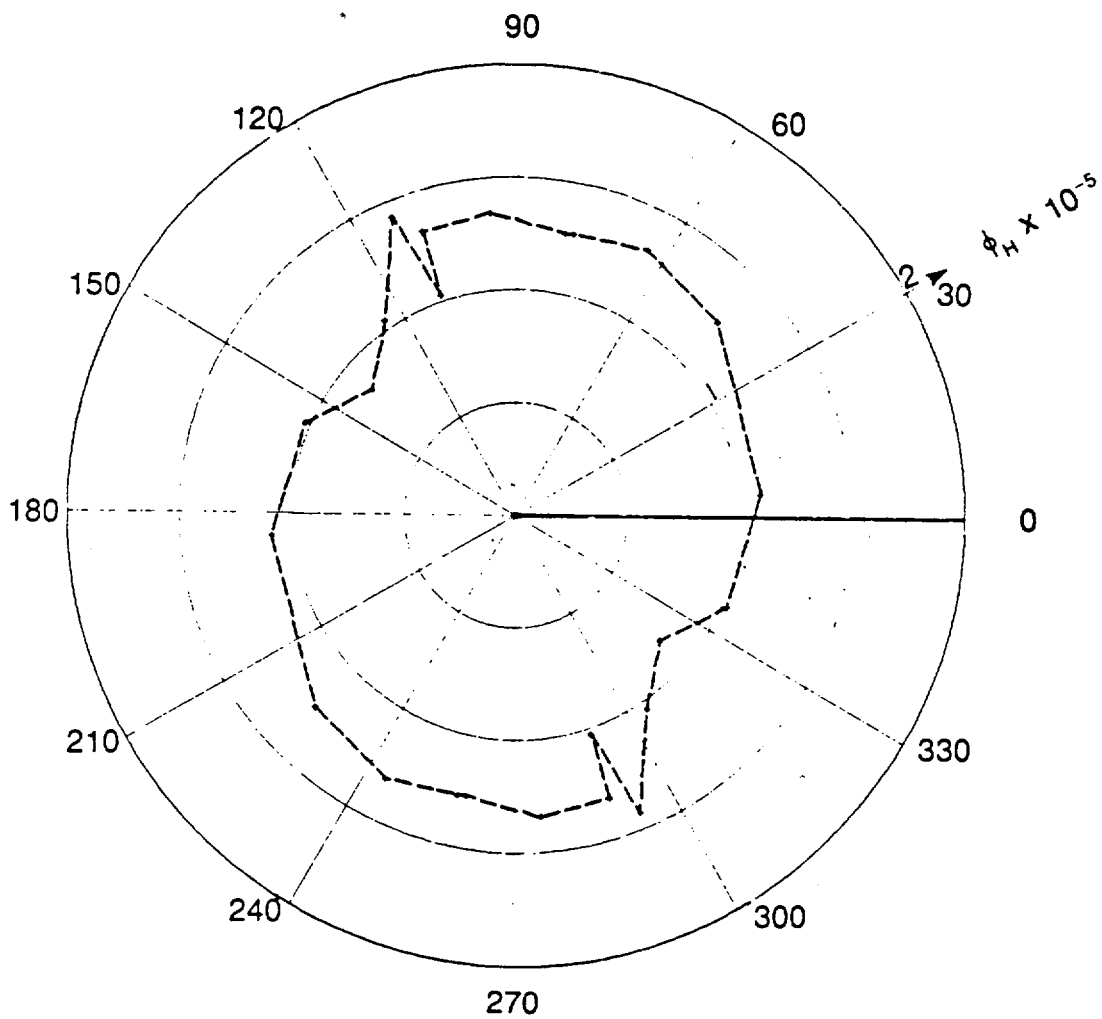
$$b = \frac{\mu_l}{\mu_b} l + \epsilon \quad (7.2)$$

where ϵ is a random variation in aperture and μ_b is equal to 0.00005 m.

Since fracture lengths were lognormally distributed with μ_l equal to σ_l , the linear correlation model was used so that μ_b would equal σ_b , similar to the lognormal distribution of apertures.

7.3.1.1. Continuous Fracture System

The fracture apertures were lognormally distributed for the continuous fracture system since fracture lengths which are infinitely long cannot be correlated with apertures. A Monte Carlo study was conducted because fracture apertures were probabilistically simulated. The



XBL 841-385

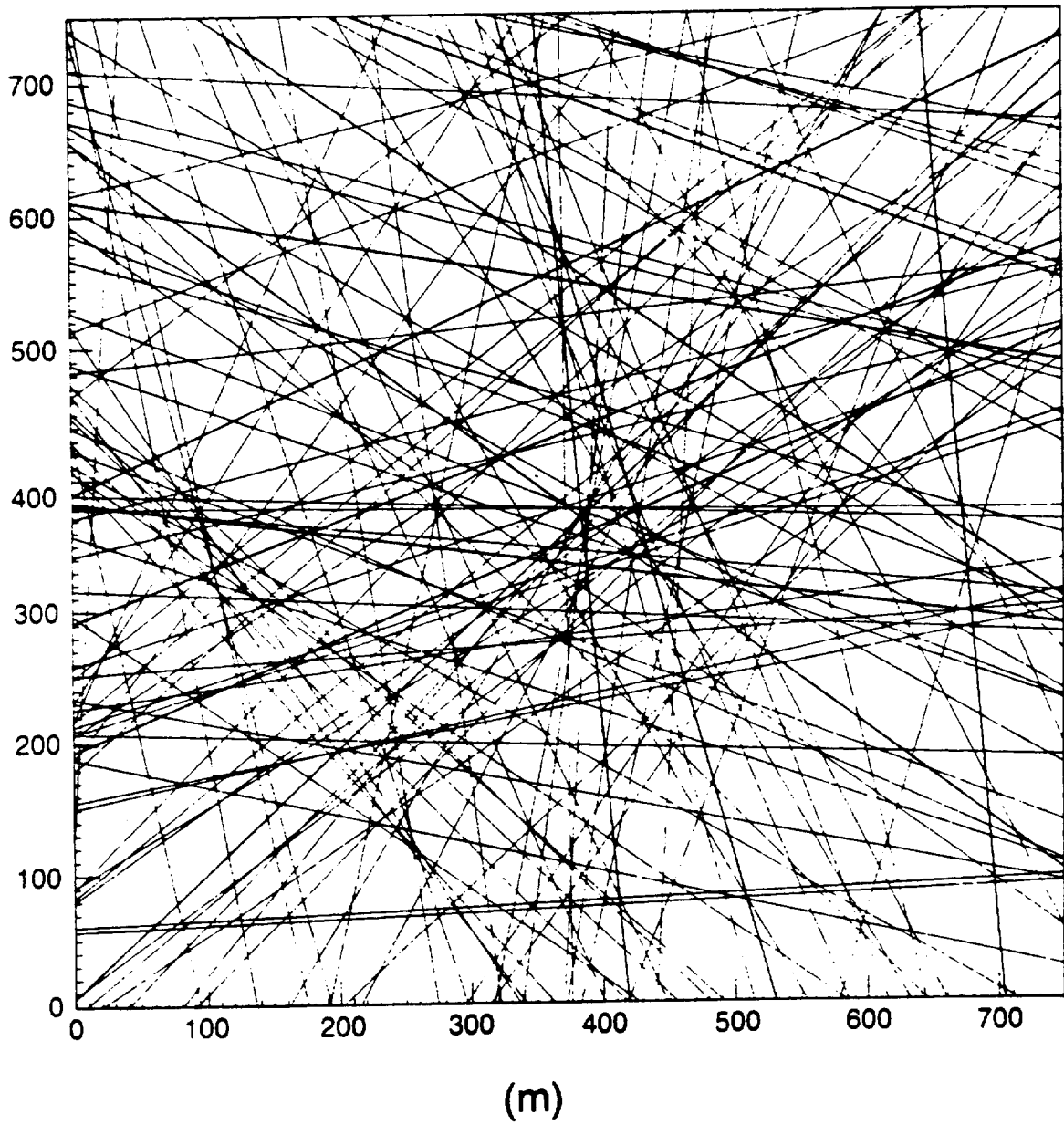
Figure 7-13 Polar Plot of Hydraulic Effective Porosity for System With Mean Fracture Length of 50 m Using Square Flow Region of Width 60 m.

continuous fracture system in each realization was created in the same way as in the constant aperture length-density study except that apertures were lognormally distributed. Figure 7-14 shows the fracture pattern in the generation region for one of the realizations. The intensity of each fracture (line) is directly related to the fracture's aperture.

The number of realizations for this Monte Carlo study was determined from: 1) the stability of the mean directional ϕ_H , and 2) the directional stability of ϕ_H . The mean directional ϕ_H was computed in the following way. For each realization, the hydraulic effective porosity in each direction was added up to obtain the sum of all hydraulic effective porosities for this realization. This total was next added to the previously calculated total of all hydraulic effective porosities. Mean directional hydraulic effective porosity was then computed by dividing the last total by the total number of measurements of hydraulic effective porosity. We expected that ϕ_H would be directionally stable as was found earlier in the constant aperture length-density study. When ϕ_H is directionally stable, the mean directional ϕ_H is equal to its directionally stable value.

Hydraulic effective porosity in each direction should converge to its stable value as the number of realizations increases. The directional stability of ϕ_H was tested using the polar plot of mean ϕ_H . When ϕ_H is directionally stable, the polar plots of ϕ_H for n realizations and $n+5$ realizations are identical. The mean directional ϕ_H tests the overall stability of the hydraulic effective porosity. The directional stability of ϕ_H requires that in every direction hydraulic effective porosity is stable.

Figure 7-15 is the plot of the mean directional hydraulic effective porosity versus the number of realizations. Initially, this mean ϕ_H increases rapidly as the number of realizations increase. Mean directional hydraulic effective porosity is then relatively constant for the next eight realizations. At realization 12, another sudden increase in this mean ϕ_H is measured. This sudden increase is followed by a gradual decrease in mean directional ϕ_H as the number of realizations increases. Mean directional hydraulic effective porosity is slowly approaching a stable value. This stable value is not equal to the total porosity of the system which is



XBL 8311-3457

Figure 7-14 Fracture Network in the Generation Region for Continuous System in the First Distributed Aperture Study.

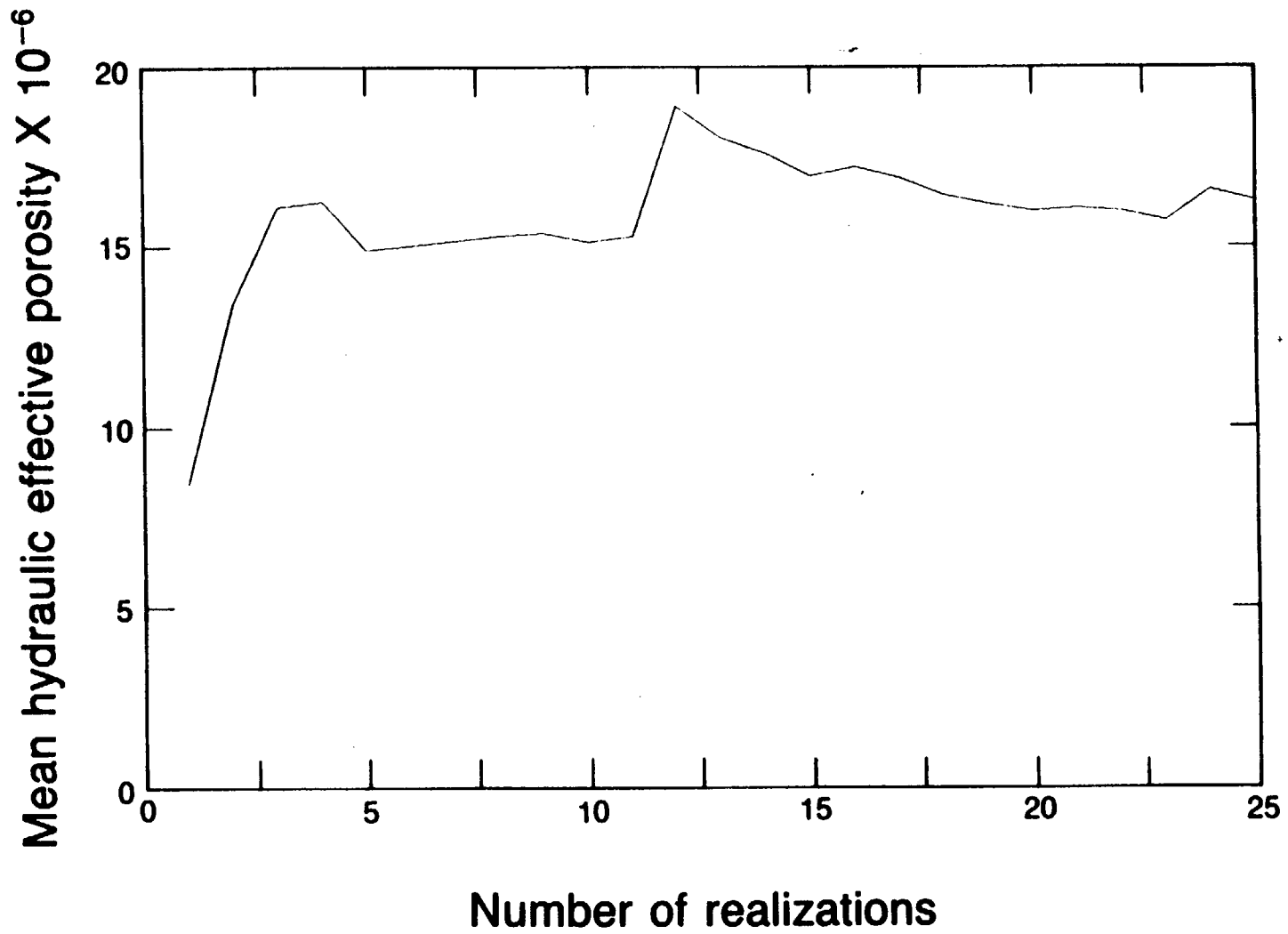


Figure 7-15 Mean Hydraulic Effective Porosity in All Directions Versus the Number of Realizations. XBL 841-534

0.0000106.

The standard error of the mean directional ϕ_H is plotted against the number of realizations in Figure 7-16. The large increases in the standard error of the mean directional ϕ_H at realizations 2 and 12 reflect the two sudden increases in this mean ϕ_H . After realization 12, the standard error slowly decreases as the number of realizations increases. This figure shows that in one out of ten realizations a fracture system is created in which the hydraulic effective is very large. Consequently, both mean directional ϕ_H and its standard error increase at this realization. This sudden increase is followed by a decrease and a slow stabilization in mean directional ϕ_H .

The sudden increase in mean directional ϕ_H at realization 12 is caused by two fractures with very large apertures (super conductors) within the fracture network (Figure 7-17). These two large apertures were created because of the large standard deviation in fracture apertures. Since travel time in a fracture is proportional to b^{-2} , fluid flowing in the large aperture fractures had a much smaller travel time from side 2 to side 4 as compared with the travel times for the rest of the fluid. Thus, two zones of contrasting fluid movement developed in the flow region. This type of transport is called inhomogeneous transport. The breakthrough curve for direction of flow 20° (Figure 7-18) shows that part of the fluid moves within a zone of fast movement, and have travel times that are less than $\bar{\tau}$. The remaining fluid moves within a zone of slow movement and have travel times that can be much larger than $\bar{\tau}$. The two large-aperture fractures also caused a large increase in specific discharge because q is proportional to b^3 . Mean hydraulic effective porosity suddenly increased at realization 12 because the product of q and $\bar{\tau}$ was large in relation to L .

Figures 7-19 and 7-20 show polar plots of mean ϕ_H after 5, 10, 15, and 25 realizations. After 5 and 10 realizations (Figure 7-19), ϕ_H exhibits large directional variations as each polar plot is very jagged. The two polar plots in Figure 7-20 for 15 and 25 realizations are more similar to each other than the two polar plots in Figure 7-19 for 5 and 10 realizations. This indicates that ϕ_H is slowly converging to its stable value in all directions as the number of reali-

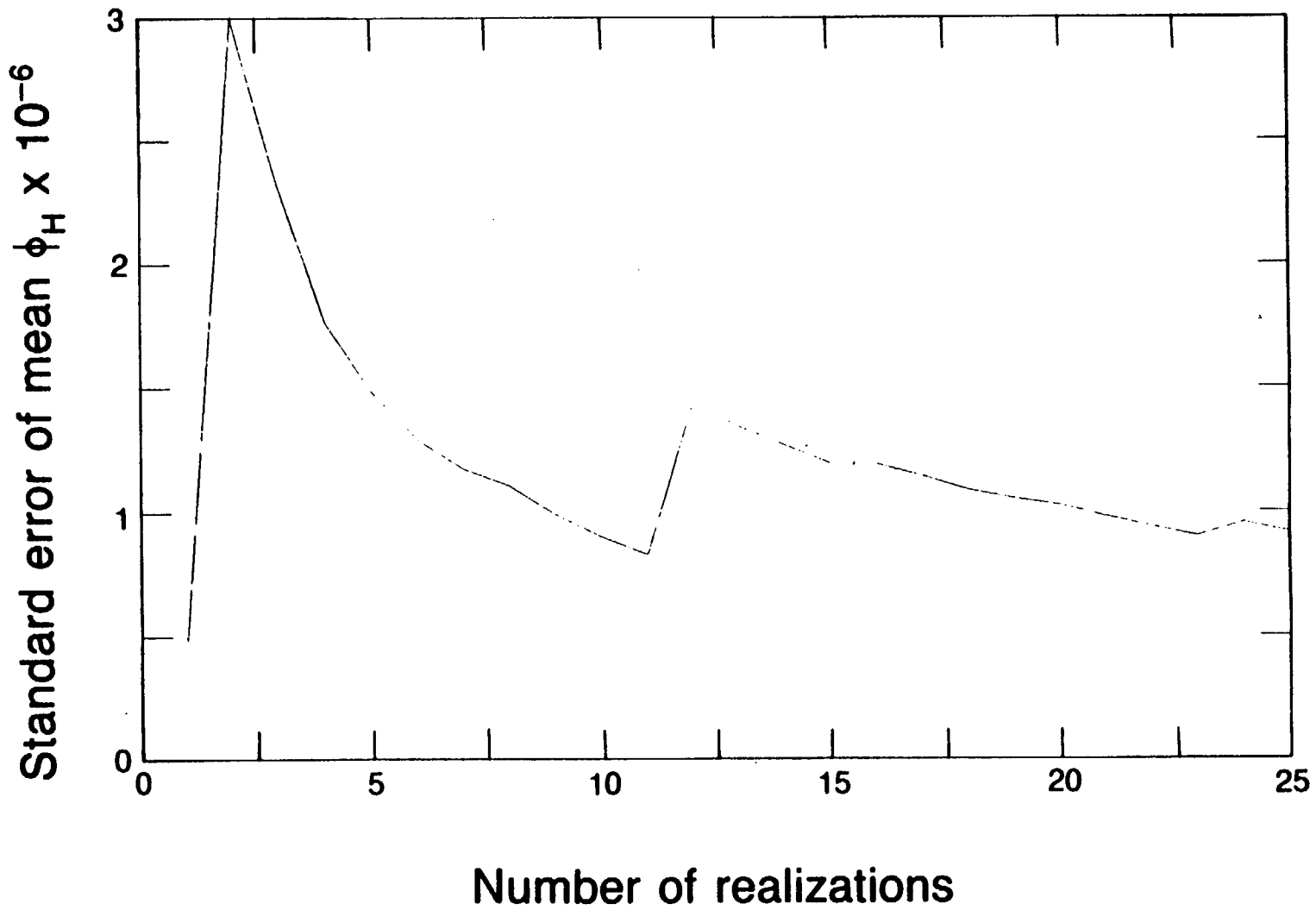
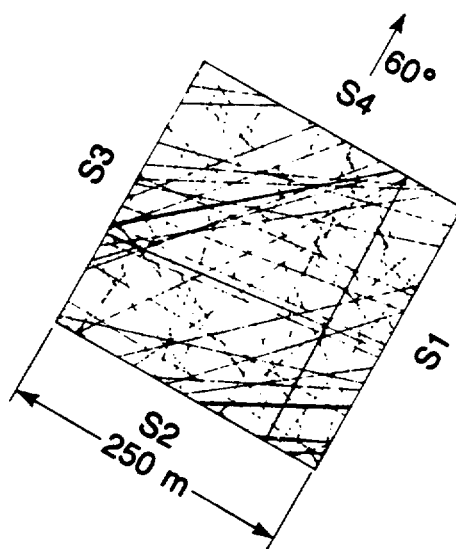
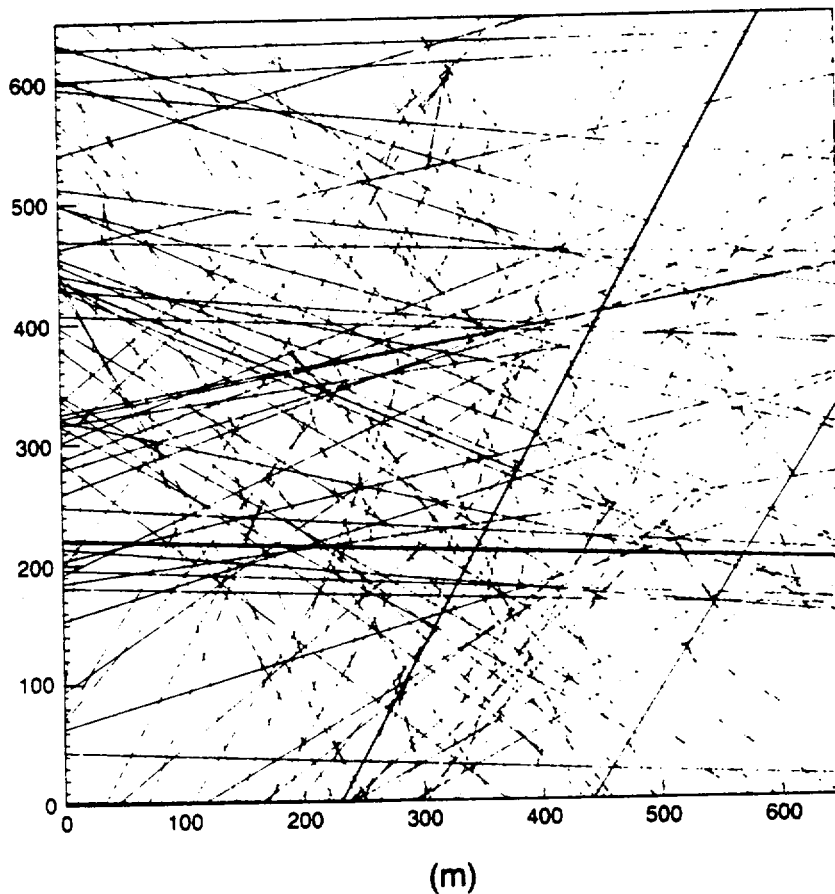
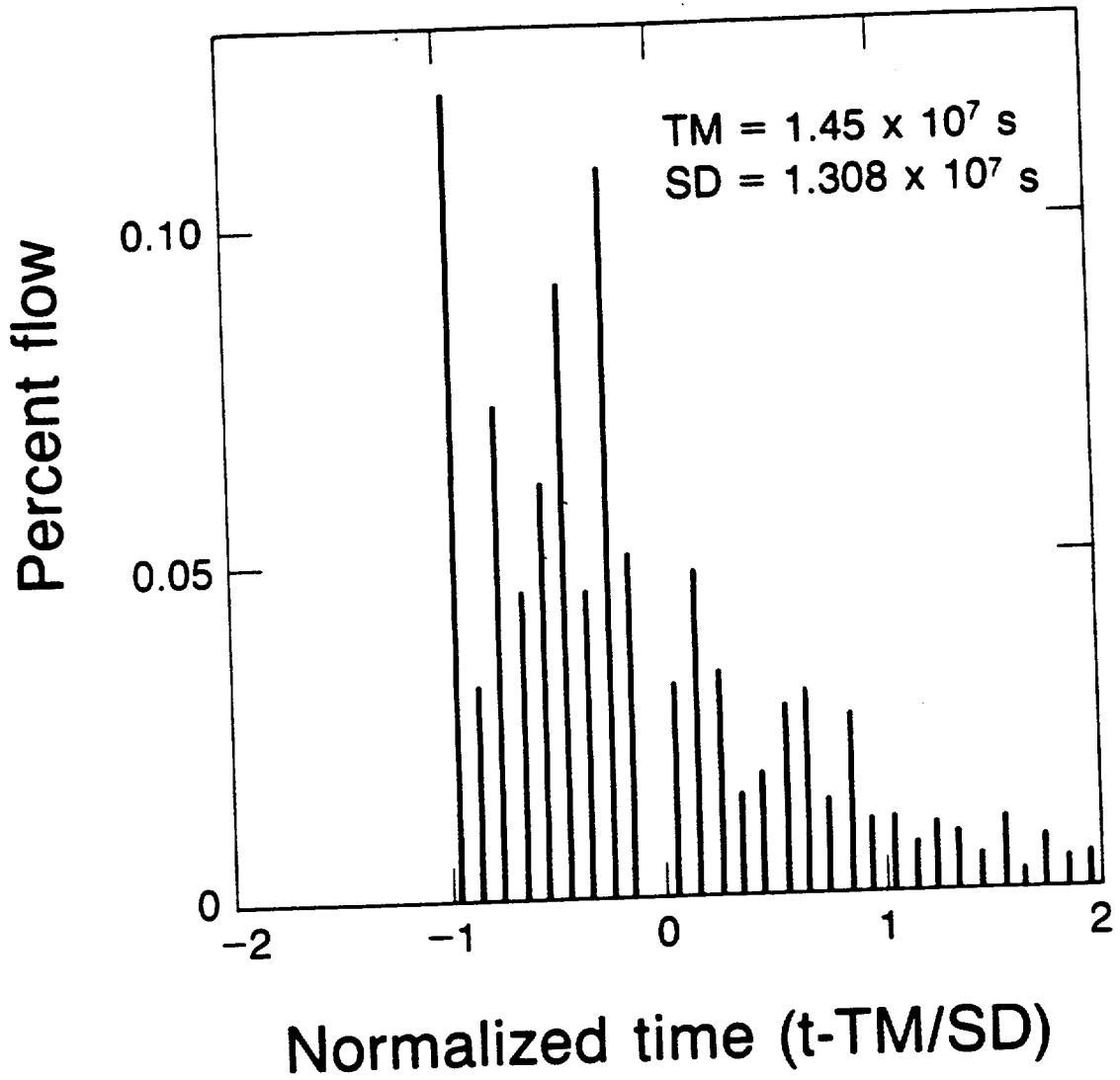


Figure 7-16 Standard Error in Mean Hydraulic Effective Porosity Versus the Number of Realizations. XBL 8311-7386



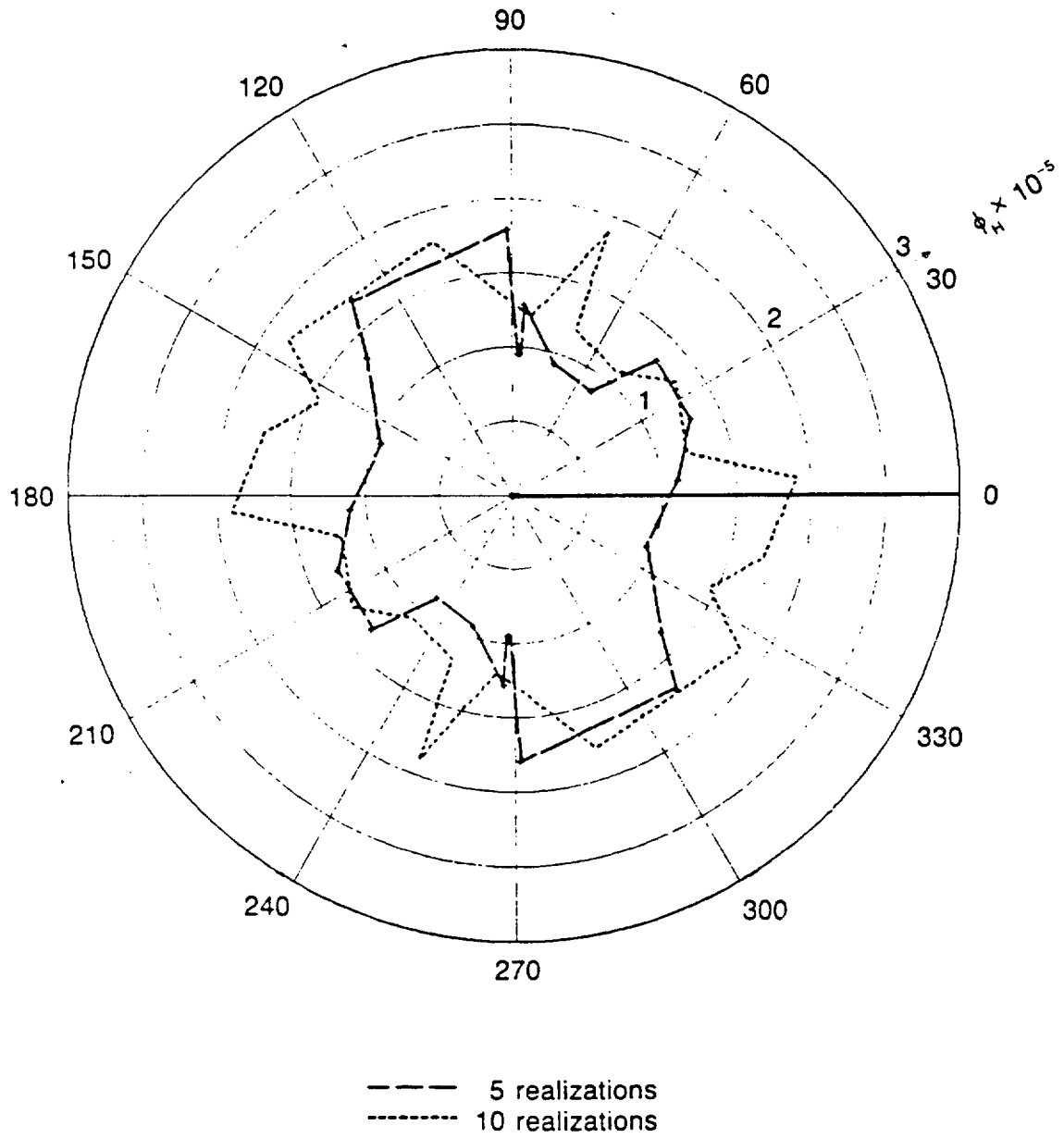
XBL 8311-3466A

Figure 7-17 Fracture Network in a) Generation Region and b) Flow Region Oriented at 60° for Realization 12 of the Continuous System in the First Distributed Aperture Study.



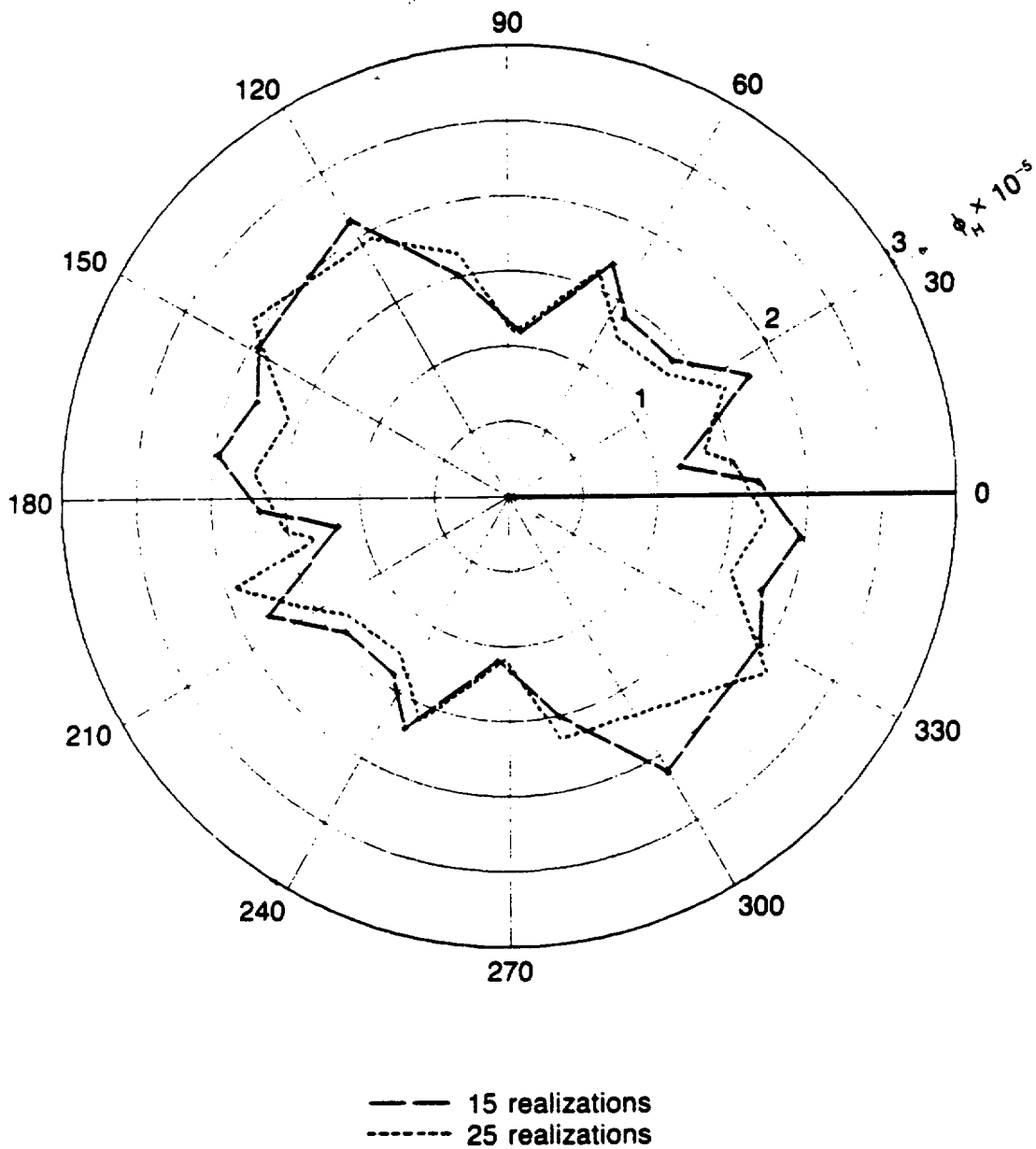
XBL 8311-3455

Figure 7-18 Breakthrough Curve for Direction of Flow 120° for Continuous System in the First Distributed Aperture Study.



XBL 8312-7420

Figure 7-19 Polar Plots of Mean Hydraulic Effective Porosity After Five Realizations and Ten Realizations.



XBL 8312-7423

Figure 7-20 Polar Plots of Mean Hydraulic Effective Porosity After Fifteen Realizations and Twenty-Five Realizations.

zations increase. The Monte Carlo simulation ended after 25 realizations because both mean directional hydraulic effective porosity and directional ϕ_H were stabilizing. However, after 25 realizations, hydraulic effective porosity is still directionally dependent, and the polar plot of ϕ_H is very jagged.

The polar plot of ϕ_H after 25 realizations indicates that at this scale the fracture system does not behave like an equivalent porous medium for transport. The characteristics of this polar plot are similar to the polar plot of ϕ_H for the discontinuous system of constant aperture with μ_1 of 50 m calculated using square flow regions of width 60 m. At a scale of 60 m, the discontinuous system did not behave like a continuum for transport. The polar plot of ϕ_H showed large fluctuations, and deviated from the nearly circular plots of ϕ_H found using larger flow regions of widths 175 m and 330 m. For this continuous fracture system, the flow region size was too small to be a good statistical sample for the distribution of apertures. Consequently, equivalent porous medium behavior for transport was not obtained at the scale of 250 m. Unfortunately, we could not increase flow region size because of the limitations of computer storage.

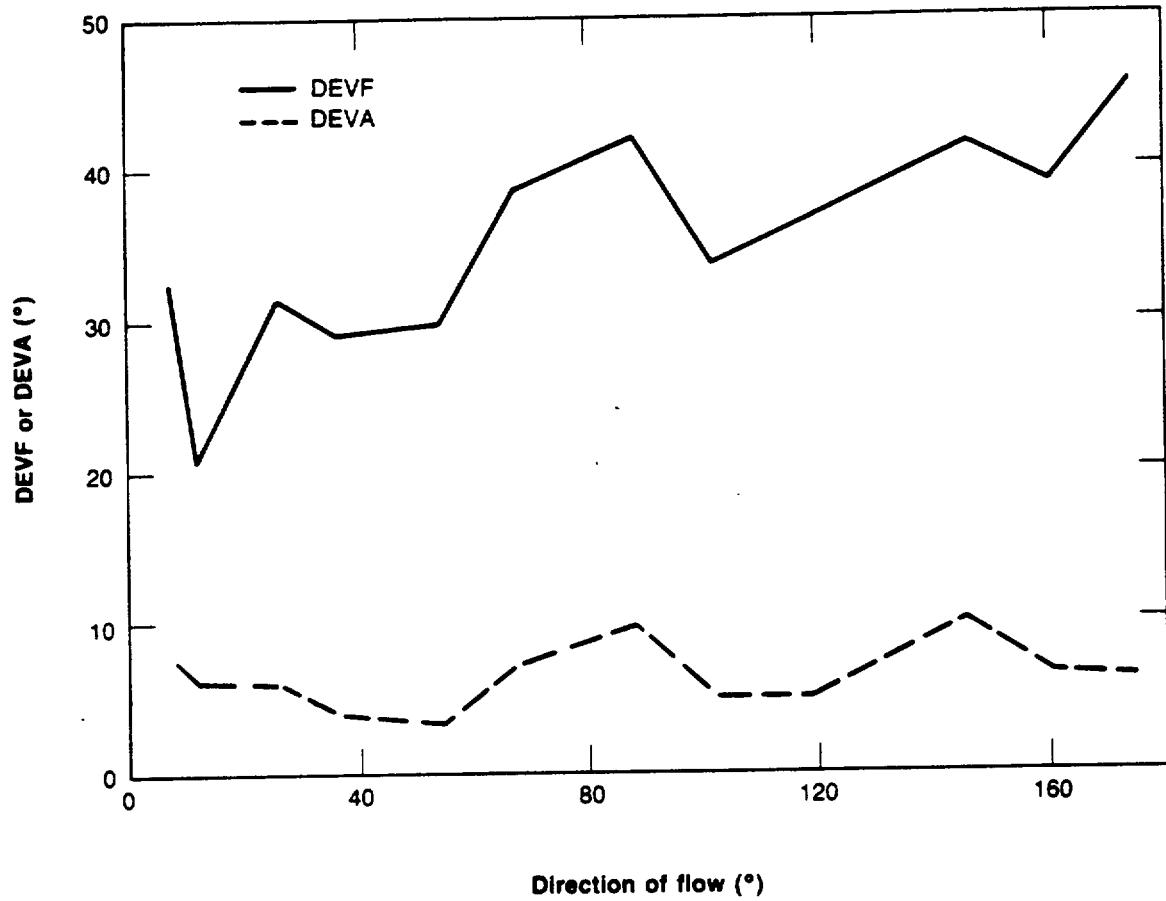
The polar plots of ϕ_H were constructed using flow regions of width 250 m. These polar plots show that ϕ_H is directionally dependent and that ϕ_H is greater than ϕ in all directions. Walter et al. (1983) reported large differences in travel times, depending on direction of flow, for tracer tests conducted in a fractured aquifer. Walter et al. questioned the meaning of "effective" porosity. We have shown that ϕ_H can be directionally dependent when a fracture system does not behave like an equivalent porous medium. In porous media, the mean rate of advection is often predicted by q/ϕ . This estimate would be two times faster than the mean rate of advection in direction of flow 120° , and 1.5 times faster than the rate in direction of flow 30° . Thus, the porous medium estimate q/ϕ is not a good estimate of the mean rate of advection in all directions at this scale. When field tracer tests are conducted at this scale, one should bear in mind that the transport properties may be directional.

The maximum ϕ_H occurs near direction of flow 120° . This direction coincides with the

direction of maximum α_L for the discontinuous system of constant aperture with μ_1 of 50 m. Longitudinal geometric dispersivity is large when the standard deviation of the breakthrough curve is large in relation to \bar{T} . A large standard deviation can be caused by inhomogeneous transport. The contrasting zones of movement lead to a wide distribution of travel times, and consequently, a large standard deviation for the breakthrough curve. For the discontinuous system of constant aperture with μ_1 of 50 m, ϕ_H was slightly larger than ϕ_R , so a small degree of inhomogeneous transport occurred. The movement of fluid in the contrasting zones caused by inhomogeneous transport did not affect the directional nature of ϕ_H , as hydraulic effective porosity was directionally stable. However, inhomogeneous transport had a major influence on σ^2 , as the spread in the breakthrough curve was greatest in direction of flow 120° . A larger deviation between ϕ_H and ϕ_R was measured for this continuous fracture system in this direction. Thus, a greater degree of inhomogeneous transport occurred because of the heterogeneity created by distributing fracture apertures. Unlike the discontinuous fracture system, inhomogeneous transport had a major directional effect on ϕ_H for this continuous fracture system.

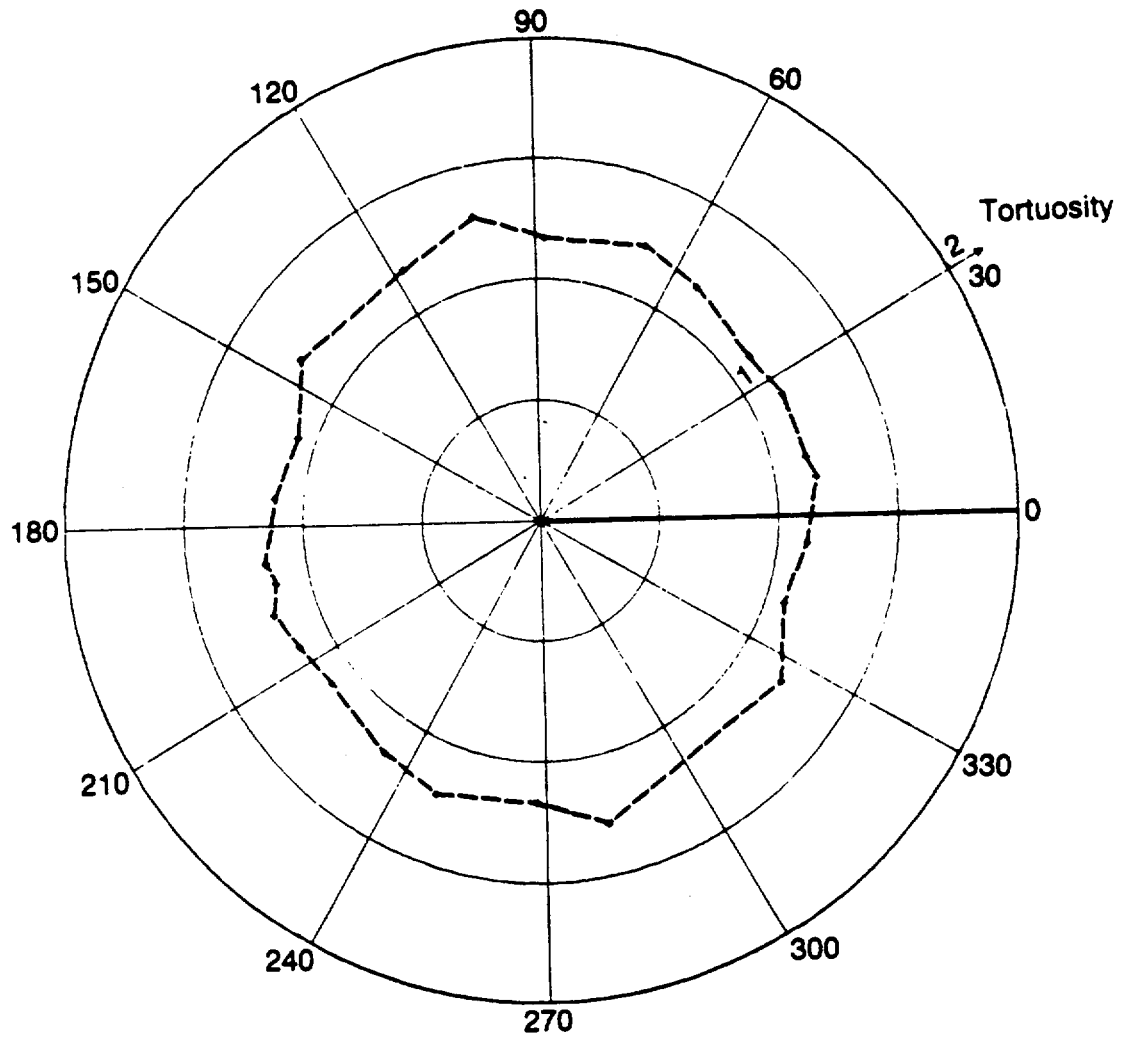
Equivalent porous medium flow behavior can be analyzed using DEVF and DEVA. Figure 7-21 is a plot of mean DEVA and mean DEVF versus direction of flow after 25 realizations. DEVF is much larger for this continuous system than for the discontinuous system of two sets oriented at 0° and 60° . A larger difference in flow rate on opposing sides of the flow region occurred because of the wide distribution in fracture apertures. A large-aperture fracture which intersects side 2, but does not intersect side 4 can cause this large flow difference. Thus, it is likely that this continuous fracture system does not behave like an equivalent porous medium for fluid flow at this scale. It will be recalled that the directional flow characteristics for the discontinuous system behaved like an equivalent porous medium.

Figure 7-22 is a polar plot of mean tortuosity after 25 realizations. The tortuosity curve is nearly circular which indicates that the medium is isotropic. Tortuosity is the only mechanical transport parameter that is similar in both the constant aperture and the distributed aperture length-density series. This result is not surprising, since the sensitivity analysis in Chapter 6



XBL 8401-6788

Figure 7-21 Mean DEVF and Mean DEVA Versus Direction of Flow for Continuous System in the First Distributed Aperture Study.



XBL 8401-8783

Figure 7-22 Polar Plot of Mean Tortuosity for Continuous System in the First Distributed Aperture Study.

showed that tortuosity was insensitive to both μ_b and σ_b .

In most realizations, longitudinal geometric dispersivity could not be computed in any direction of flow because σ^2/\bar{l}^2 exceeded unity. The variance in the breakthrough curve was very large because of the wide distribution in fracture apertures ($\mu_b = \sigma_b$). Travel time in a fracture is proportional to b^{-2} . Thus, the distribution in travel times was much wider than the distribution of apertures. Consequently, the ratio of σ to \bar{T} exceeded unity, which meant that M_L approached infinity. No polar plot of α_L was constructed because of the limited data.

7.3.1.2. Discontinuous System with Mean Fracture Length of 50 m

7.3.1.2.1. System with Linearly Correlated Apertures

The fracture system for each realization was created the same way as in the constant-aperture study except that apertures were linearly correlated with fracture lengths by equation 7.2. The linear correlation model was used to distribute apertures so that: 1) long fractures would be assigned large apertures and short fractures would be assigned small apertures and, 2) the mean aperture of 0.00005 m would equal the standard deviation of aperture. This mean was equal to the standard deviation because fracture lengths were lognormally distributed with the mean of 50 m equal to the standard deviation of fracture length. Square flow regions of width 330 m were oriented at every 15° so that mechanical transport could be studied.

Numerical precision problems were encountered in the mechanical transport stage of the computer program because of large hydraulic gradient differences in the elements intersecting a node. For example, consider two elements intersecting a node. Suppose element 1 has an aperture which is 30 times larger than the aperture of element 2. For this fracture system, the large aperture difference is caused by the wide distribution of apertures. Since both fractures have the same flow rate, the ratio of hydraulic gradients in the two elements is proportional to b^3 :

$$\frac{(\nabla\Phi)_2}{(\nabla\Phi)_1} = (30)^3 = 27000$$

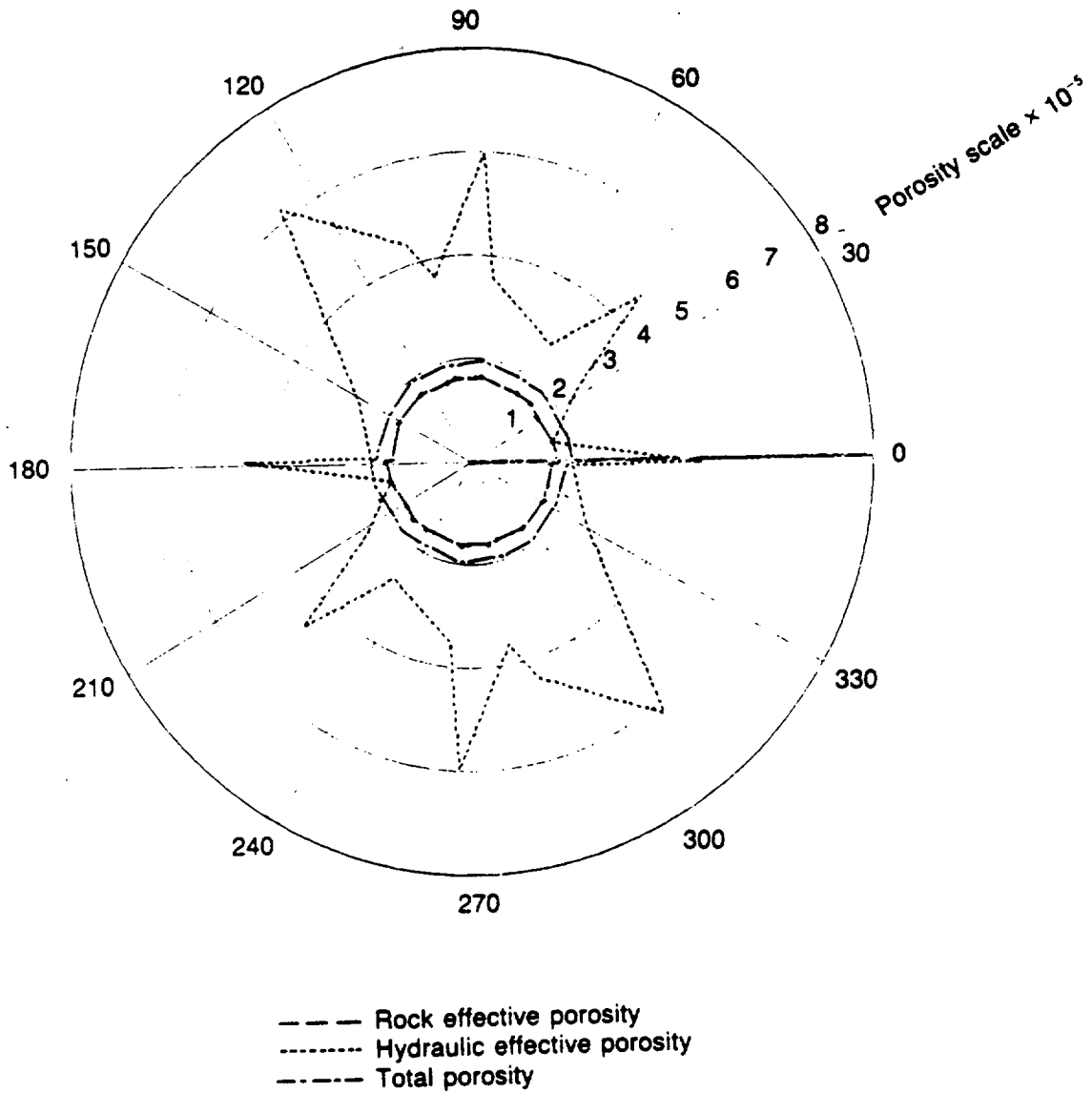
Consequently, it was difficult for the program to distinguish no flow elements (zero gradient) from low flow elements (very small gradient). This problem is similar to the problem one

encounters when modeling transient flow in an aquifer consisting partly of sand and partly of clay. Sand is much more permeable than clay. So, small time steps must be used in order for the numerical solution to be stable. Also, the conductive matrix for such a problem is a stiff matrix because the coefficients along the diagonal of this matrix vary significantly. Numerical solution is often difficult when the conductance matrix is a stiff matrix.

The problem of large hydraulic gradient differences at a node was not encountered in the study of the continuous fracture system of distributed apertures. Theoretically, the gradient along an infinitely-long fracture is equal to the product of the magnitude of the hydraulic gradient and the cosine of the angle between the fracture orientation and direction of the gradient. Since the gradient along the fracture was not related to aperture cubed, there were no extreme differences in hydraulic gradients at a node. For this system, with μ_1 of 50 m and linearly correlated apertures, five realizations were run for each orientation.

The rock effective porosity, hydraulic effective porosity, and total porosity are each shown in Figure 7-23. Both total porosity and rock effective porosity were directionally stable, but hydraulic effective porosity was highly directionally dependent. Hydraulic effective porosity did not show the characteristics of an equivalent porous medium, as the polar plot of ϕ_H was very jagged and ϕ_H showed large directional variations. These porosity results were based on five realizations, and consequently, may not be conclusive. However, we believe that hydraulic effective porosity will still exhibit directional tendencies when a large number of realizations are made because the same directional tendencies for ϕ_H were present after 5 and 25 realizations for the previous continuous system. The direction of maximum ϕ_H was near 120° . This direction was also the direction of maximum ϕ_H for the continuous fracture system with distributed apertures, and the direction of maximum α_1 for the discontinuous system with μ_1 of 50 m and constant apertures. The maximum ϕ_H had a value four times larger than the rock effective porosity. Consequently, the deviation between ϕ_H and ϕ_R is greater for this system than for the previous continuous system.

Hydraulic effective porosity was greater than total porosity because both q and T were



XBL 8312-7419

Figure 7-23 Polar Plots of Total Porosity, Hydraulic Effective Porosity, and Rock Effective Porosity for Discontinuous System With Mean Fracture Length of 50 m and Linearly Correlated Apertures.

large in relation to L . Specific discharge was large because long fractures with large apertures have a greater probability of conducting flow (intersecting other long fractures) than the short fractures with small apertures. Mean travel time was large because of the slow movement of part of the fluid. Figure 7-24 shows a breakthrough curve in a direction in which ϕ_H was three times larger than ϕ_R . Sixty-eight percent of the fluid arrived within the small time interval between the normalized times of -0.5 and 0.0. Between the normalized times of 0.0 and 0.5, another 22 percent of the fluid arrived. However, the 10 percent of the fluid that arrived between the normalized times of 0.5 and 2.0 caused the mean travel time to be large. The real time (t) is equal to:

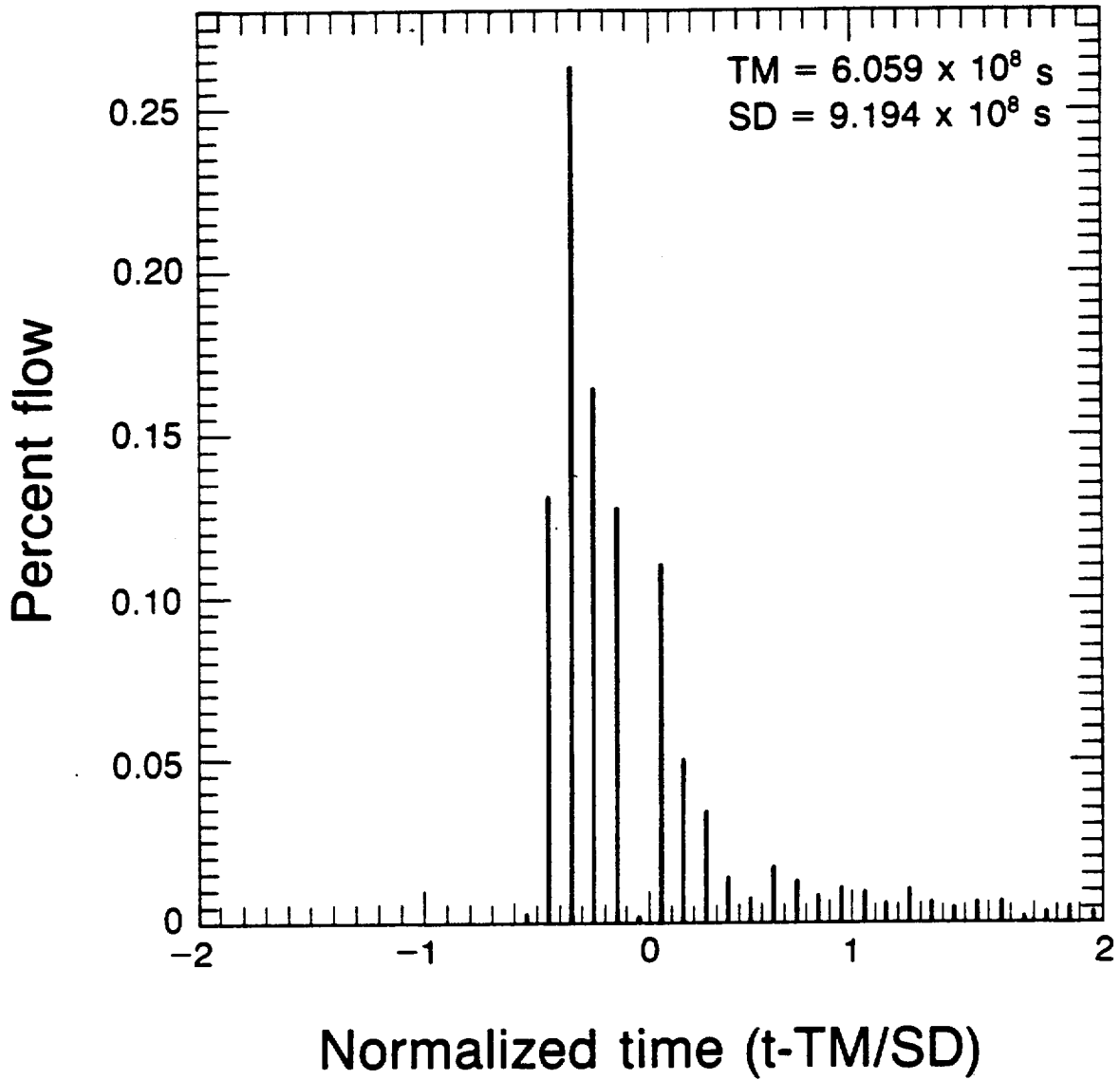
$$t = \bar{T} + \sigma(\text{normalized time})$$

Since the standard deviation of this breakthrough curve is larger than the mean travel time, real time rapidly becomes greater than \bar{T} as normalized time increases. The right skewness in the breakthrough curve reflects the movement of particles which had large travel times.

Mean DEVA and mean DEVF are shown plotted against direction of flow in Figure 7-25. Both DEVA and DEVF were much larger in this system than in any of the previous systems studied. The large DEVA and DEVF were caused by the heterogeneity of apertures. For the fracture system in the fifth realization of the constant aperture study with μ_1 of 50 m, mean directional DEVA and DEVF were only 10.5° and 12.4, respectively. The large values in DEVA and DEVF at this scale show that this fracture system does not behave like an equivalent porous medium for fluid flow.

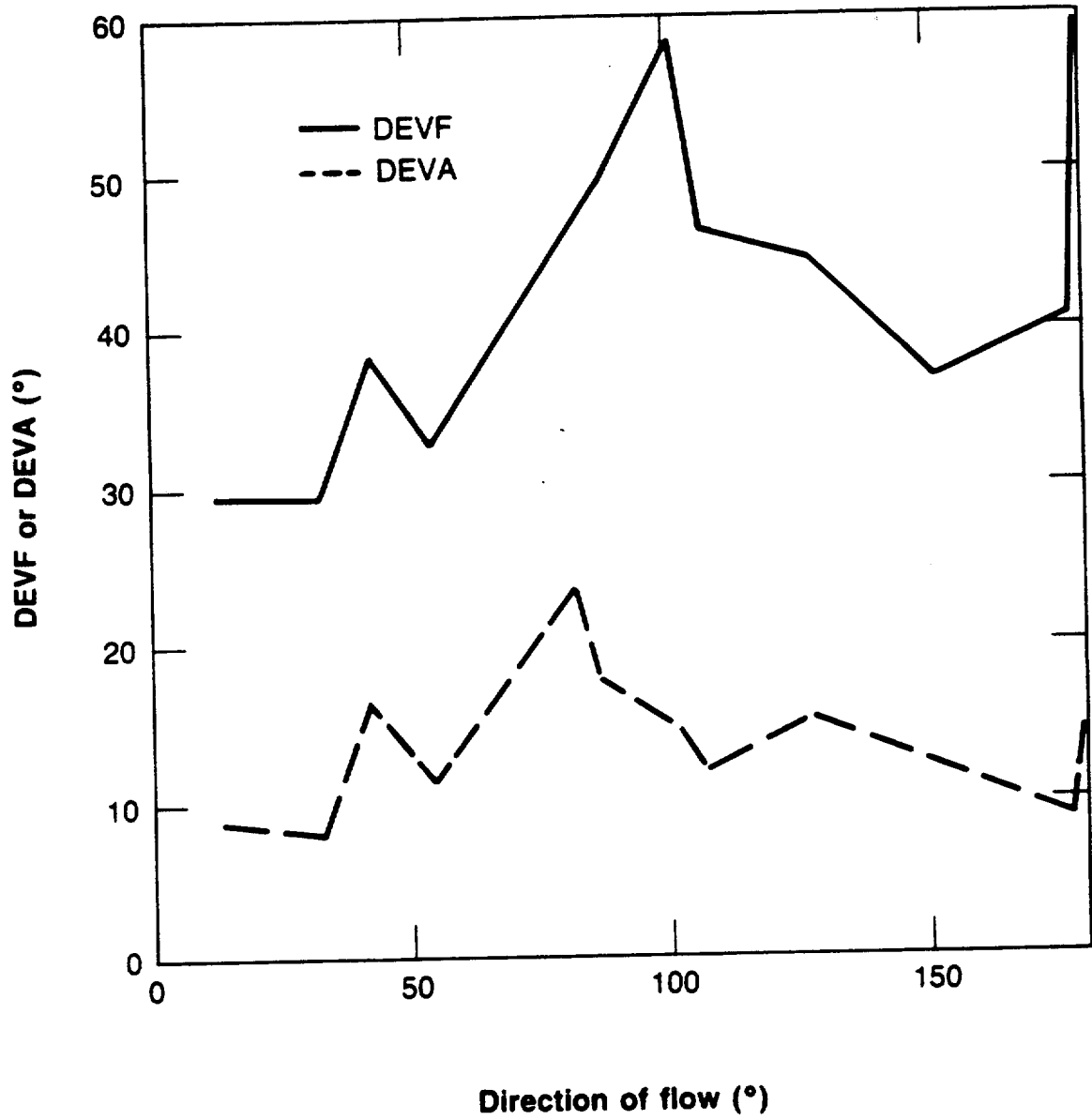
Figure 7-26 is a polar plot of mean tortuosity. Tortuosity is nearly constant in all directions, and the mean directional tortuosity is 1.28. Thus, even though hydraulic effective porosity showed large directional variations, tortuosity showed the same directional behavior as found in the constant-aperture study for the fracture system with μ_1 of 50 m, where the polar plot of hydraulic effective was nearly circular.

Longitudinal geometric dispersivity could not be computed for more than 90 percent of the realizations. The mean velocity within an element varied considerably in the flow region



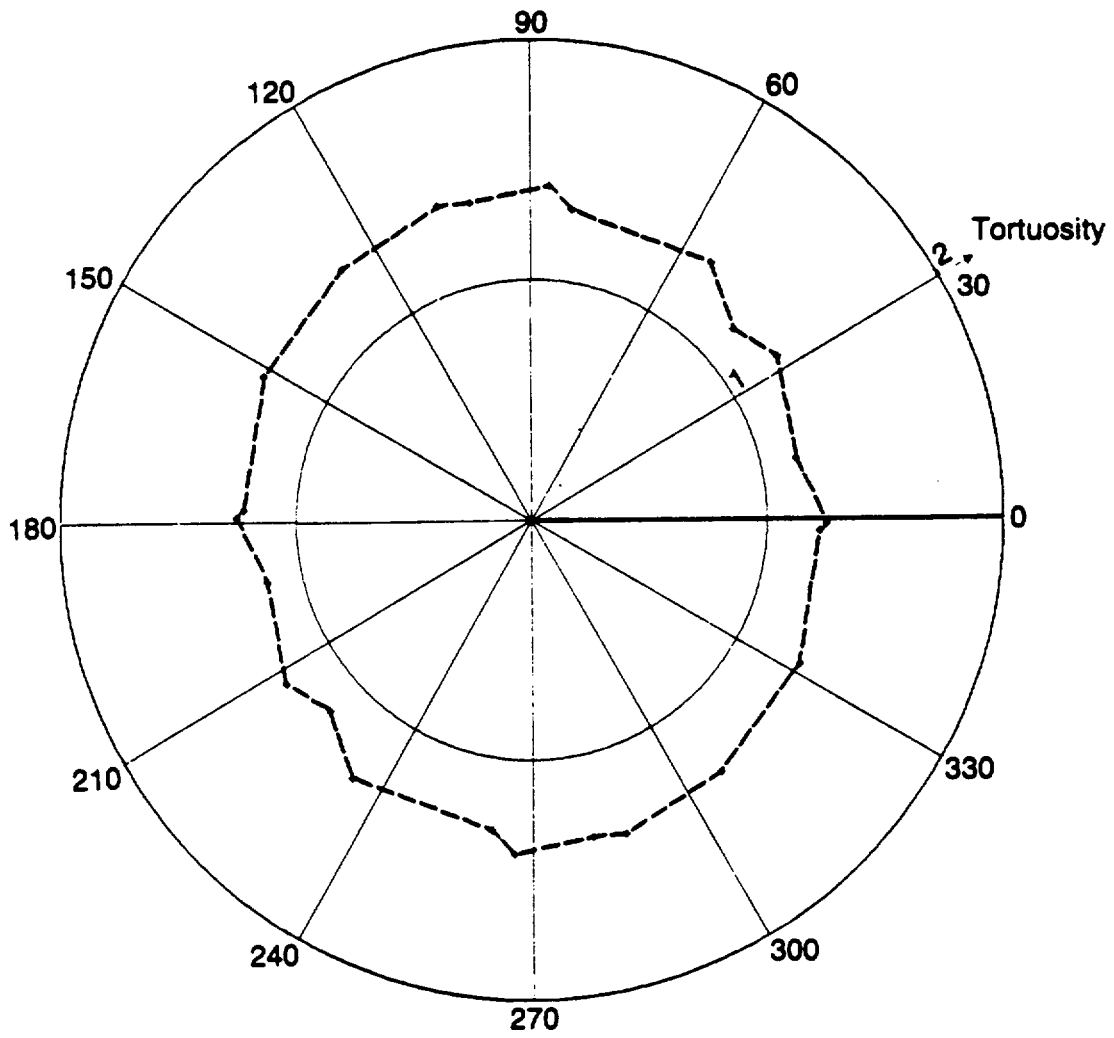
XBL 8312-7422

Figure 7-24 Breakthrough Curve in a Direction in Which Hydraulic Effective Porosity is Three Times Larger Than Rock Effective Porosity.



XBL 8401-6787

Figure 7-25 Mean DEVF and Mean DEVA Versus Direction of Flow for System With Mean Fracture Length of 50 m and Linearly Correlated Apertures.



XBL 8401-6794

Figure 7-26 Polar Plot of Mean Tortuosity for System With Mean Fracture Length of 50 m and Linearly Correlated Apertures.

because of the wide range of apertures. This large velocity variation caused fluid particles to spread out rapidly such that σ/\bar{v} exceeded unity. When σ/\bar{v} exceeds unity, the Peclet number and α_L approach infinity. Consequently, the rate of dispersion cannot be characterized by α_L using the classical approach. Transport is probably occurring in the initial non-Fickian period where dispersion occurs at a faster rate than in the later Fickian time domain.

7.3.1.2.2. System with Lognormally Distributed Apertures

Fractures were created in a generation region of 1000 by 1000 m by lognormally distributing apertures using a mean of 0.00005 m and a standard deviation of 0.00005 m. Twelve square flow regions of width 330 m were oriented at every 15° within the generation region. For each orientation, two realizations were run to study mechanical transport.

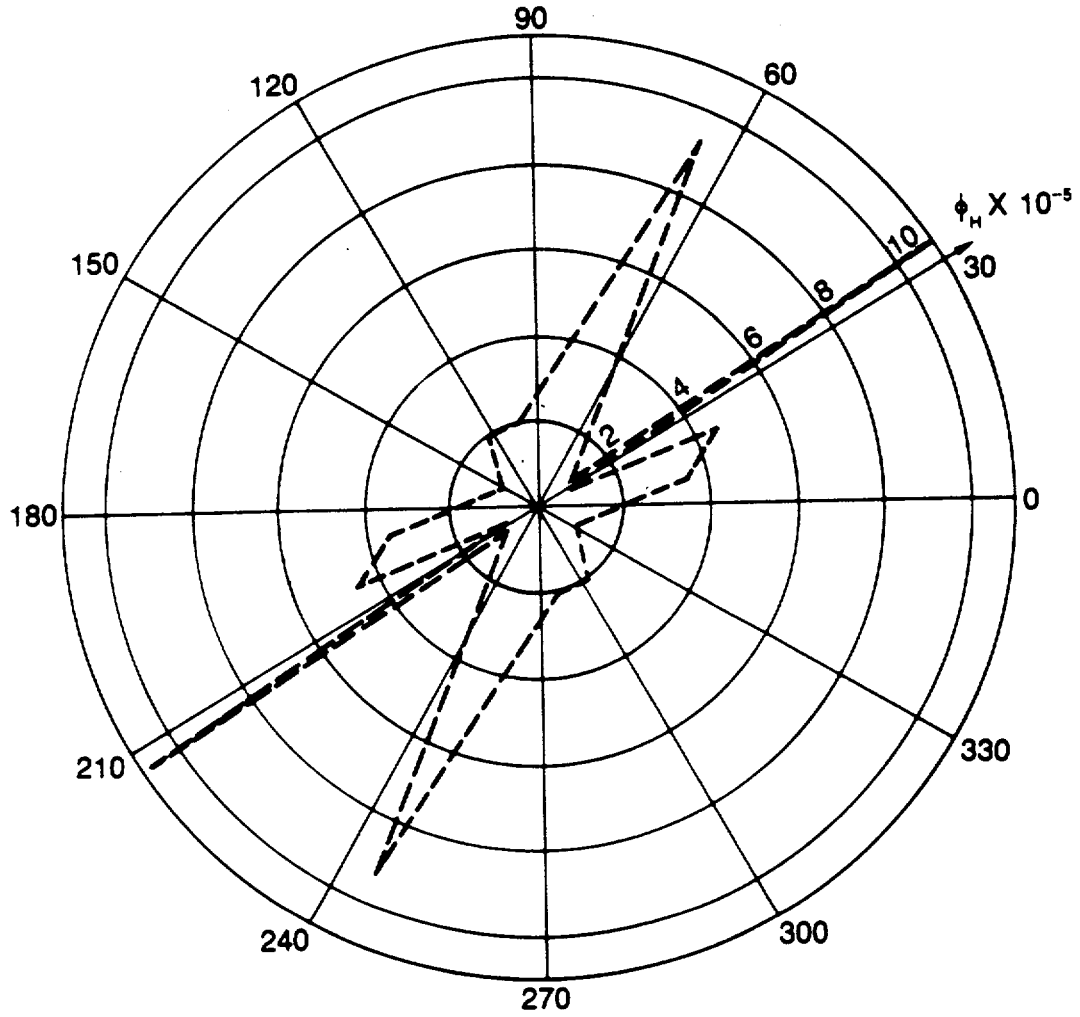
Figure 7-27 is the polar plot of mean hydraulic effective porosity. This system showed extreme directional variations in hydraulic effective porosity. Hydraulic effective porosity was much larger than rock effective porosity. Rock effective porosity and total porosity were both directionally stable at 0.0000072 and 0.0000098, respectively. The large directional variations in ϕ_H indicate that this fracture system cannot be treated like an equivalent porous medium for transport.

Figure 7-28 shows mean DEVA and mean DEVF plotted against the direction of flow. DEVA and DEVF are both very large in most directions. Consequently, this fracture system also does not behave like an equivalent porous medium for fluid flow. Of all the systems studied, this fracture system showed the greatest deviation from porous medium behavior.

7.3.2. Distributed Aperture Length-Density Study with Standard

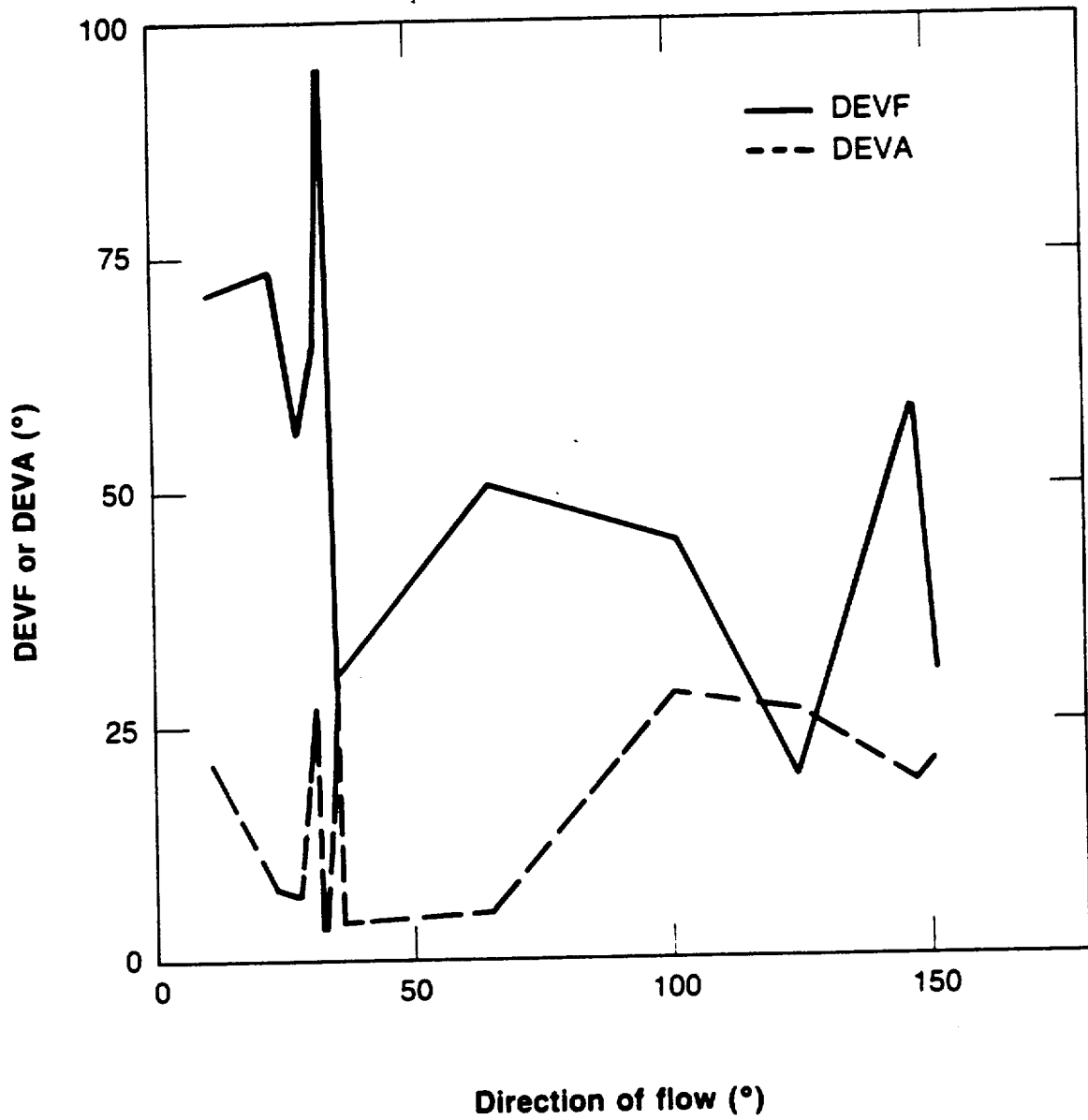
Deviation of Aperture Equal to 0.3 of Mean Aperture

The directional behavior of hydraulic effective porosity was different in the constant aperture and in the first distributed aperture length-density studies. Hydraulic effective porosity was directionally stable in the constant aperture study, such that the fracture systems behaved like equivalent porous media. Large directional variations in hydraulic effective porosity in the



XBL 8401-6792

Figure 7-27 Polar Plot of Mean Hydraulic Effective Porosity for System With Mean Fracture Length of 50 m in the First Distributed Aperture Study.



XBL 8401-6790

Figure 7-28 Mean DEVF and Mean DEVA Versus Direction of Flow for System With Mean Fracture Length of 50 m in the First Distributed Aperture Study.

first distributed aperture study showed that the fracture systems exhibited no porous media equivalence. A third length-density study was conducted for fracture systems in which the standard deviation of aperture was 0.3 of the mean aperture. Thus, this length-density study bridged together the two previous studies.

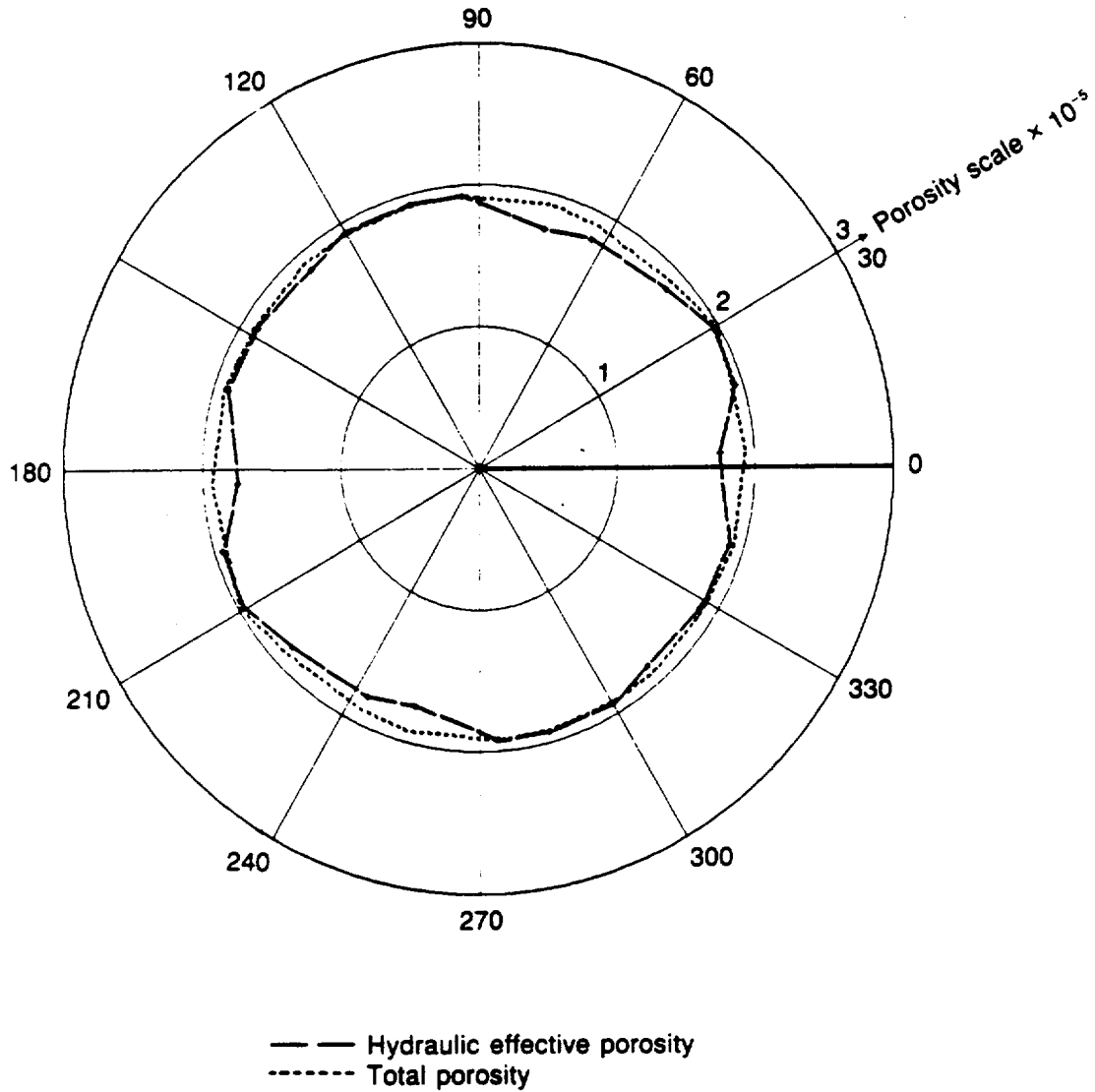
The two fracture systems used in this study were the continuous fracture system and the discontinuous system with μ_1 of 50 m. Each system was created in the same way as described in the distributed aperture study, except that apertures were lognormally distributed using a mean of 0.0000917 m and a standard deviation of 0.0000275 m. The mean and standard deviation were determined so that the mean b^3 was constant in all three length-density studies. For each fracture system, five realizations were run for each orientation of the flow region to study mechanical transport.

7.3.2.1. Continuous Fracture System

The polar plots of hydraulic effective porosity and total porosity are shown in Figure 7-29. Hydraulic effective porosity is nearly equal to total porosity in all directions. Thus, this fracture system behaves like an equivalent porous medium for transport. We have found that continuous systems with σ_b/μ_b less than 0.3 behaved like equivalent porous medium for transport when flow regions of size 250 by 250 m were used.

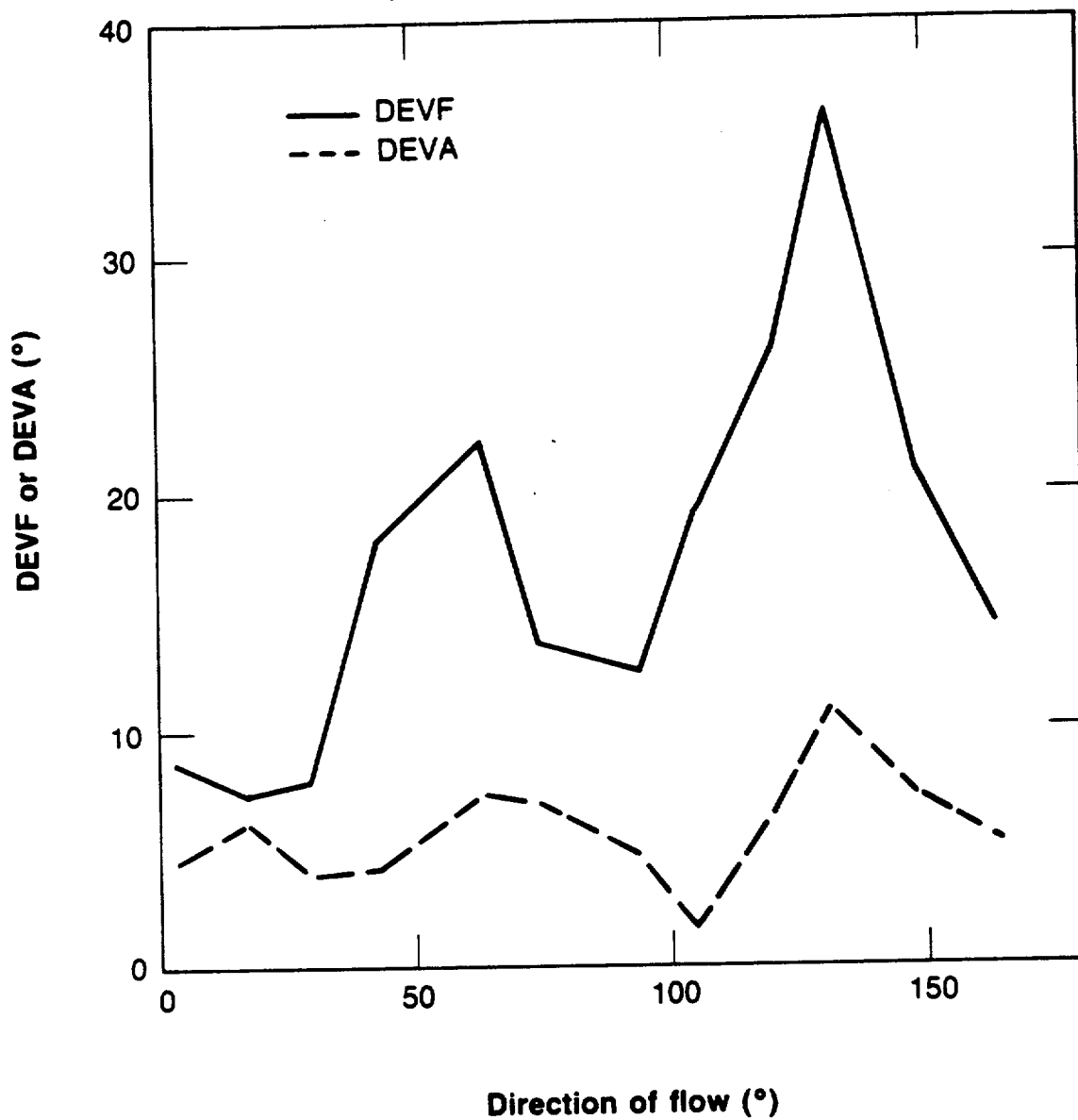
Mean DEVA and mean DEVF are plotted against direction of flow in Figure 7-30. DEVF is two times smaller in most directions for this system than for the continuous system with σ_b/μ_b of 1. The mean directional DEVF and DEVA were 9.35 and 2.12°, respectively, for the continuous system with constant aperture ($\sigma_b/\mu_b = 0$). Consequently, porous medium flow behavior is more likely to occur in continuous systems where the ratio of σ_b to μ_b is small.

Figure 7-31 shows the polar plot of tortuosity. In the three length-density studies, the same directional behavior in tortuosity was found. The polar plots of tortuosity were nearly circular, indicating that each system was fairly isotropic. Tortuosity decreased slightly as the ratio of σ_b to μ_b increased. Tortuosities were 1.261, 1.253, and 1.167 for the continuous systems with σ_b/μ_b of 0, 0.3, and 1, respectively.



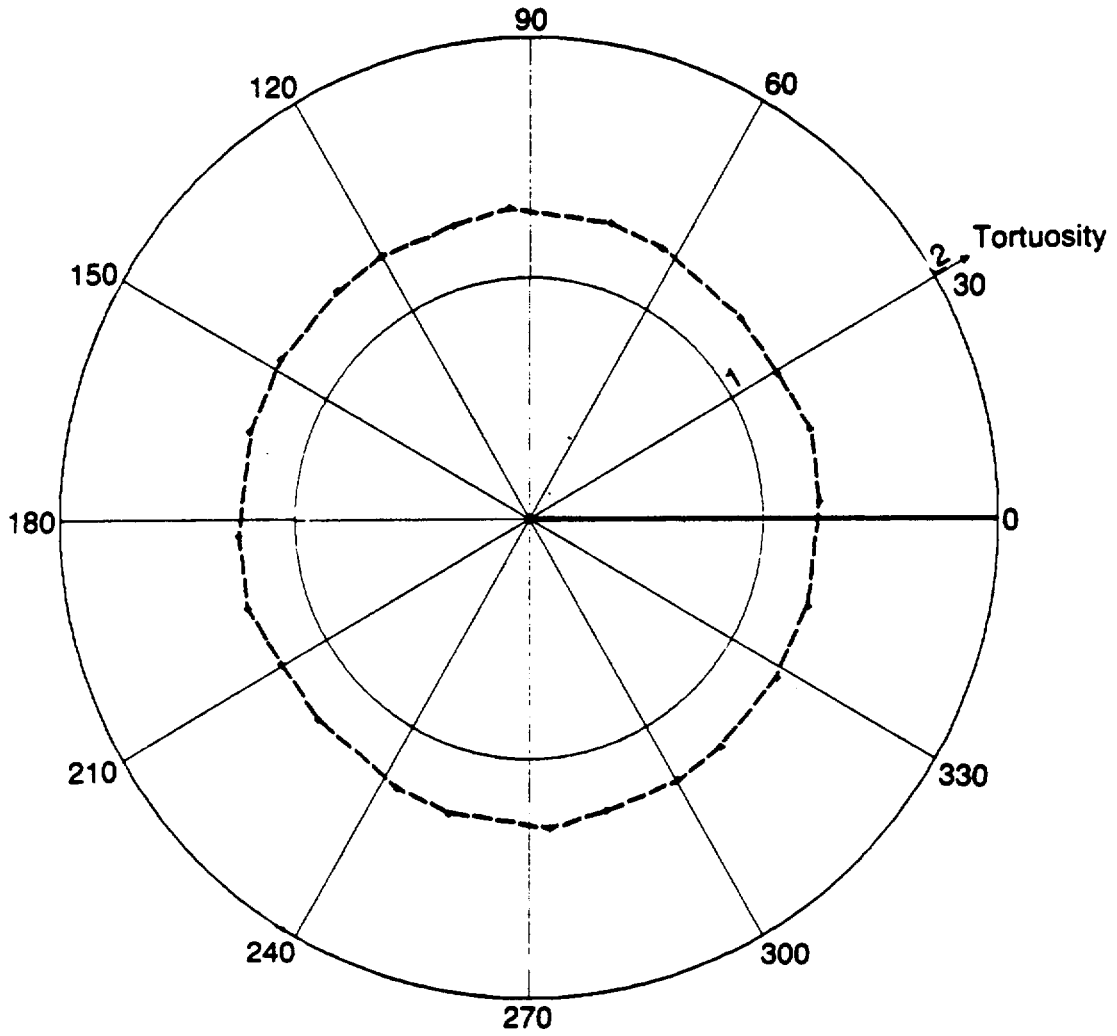
XBL 8312-7424

Figure 7-29 Polar Plots of Total Porosity and Hydraulic Effective Porosity for Continuous System With σ_b/μ_b of 0.3.



XBL 8401-6789

Figure 7-30 Mean DEVF and Mean DEVA Versus Direction of Flow for Continuous System With σ_b/μ_b of 0.3.



XBL 8401-6797

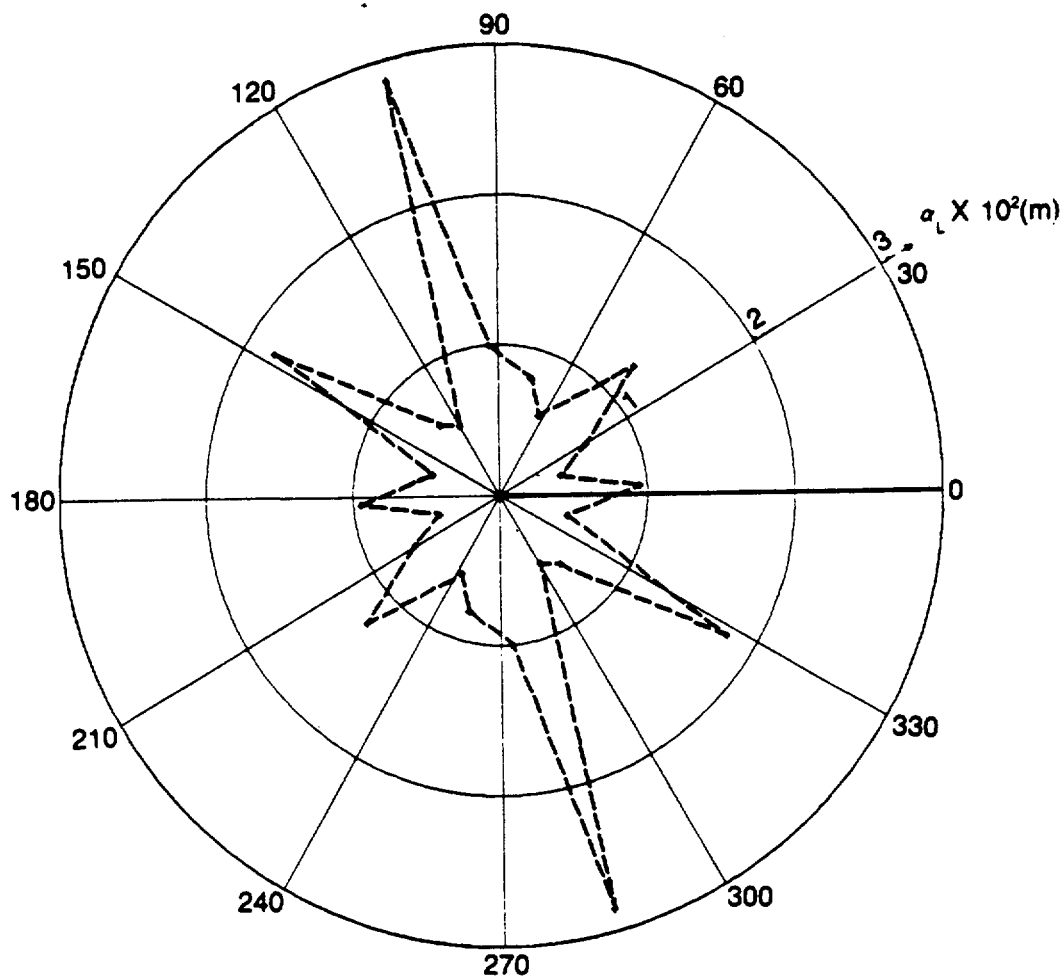
Figure 7-31 Polar Plot of Tortuosity for Continuous System With σ_b/μ_b of 0.3.

Figure 7-32 shows that polar plot of longitudinal geometric dispersivity. The maximum α_L occurred at 105° . This direction was near the direction of maximum α_L for the continuous system in the constant aperture study. However, the maximum α_L was three times larger for this system than for the system with σ_b/μ_b of 0. For the continuous system with σ_b/μ_b of 1, the Peclet number approached infinity, such that α_L could not be computed. Thus, the three length-density studies showed that α_L increased as σ_b/μ_b increased.

7.3.2.2. Discontinuous System with Mean Fracture Length of 50 m

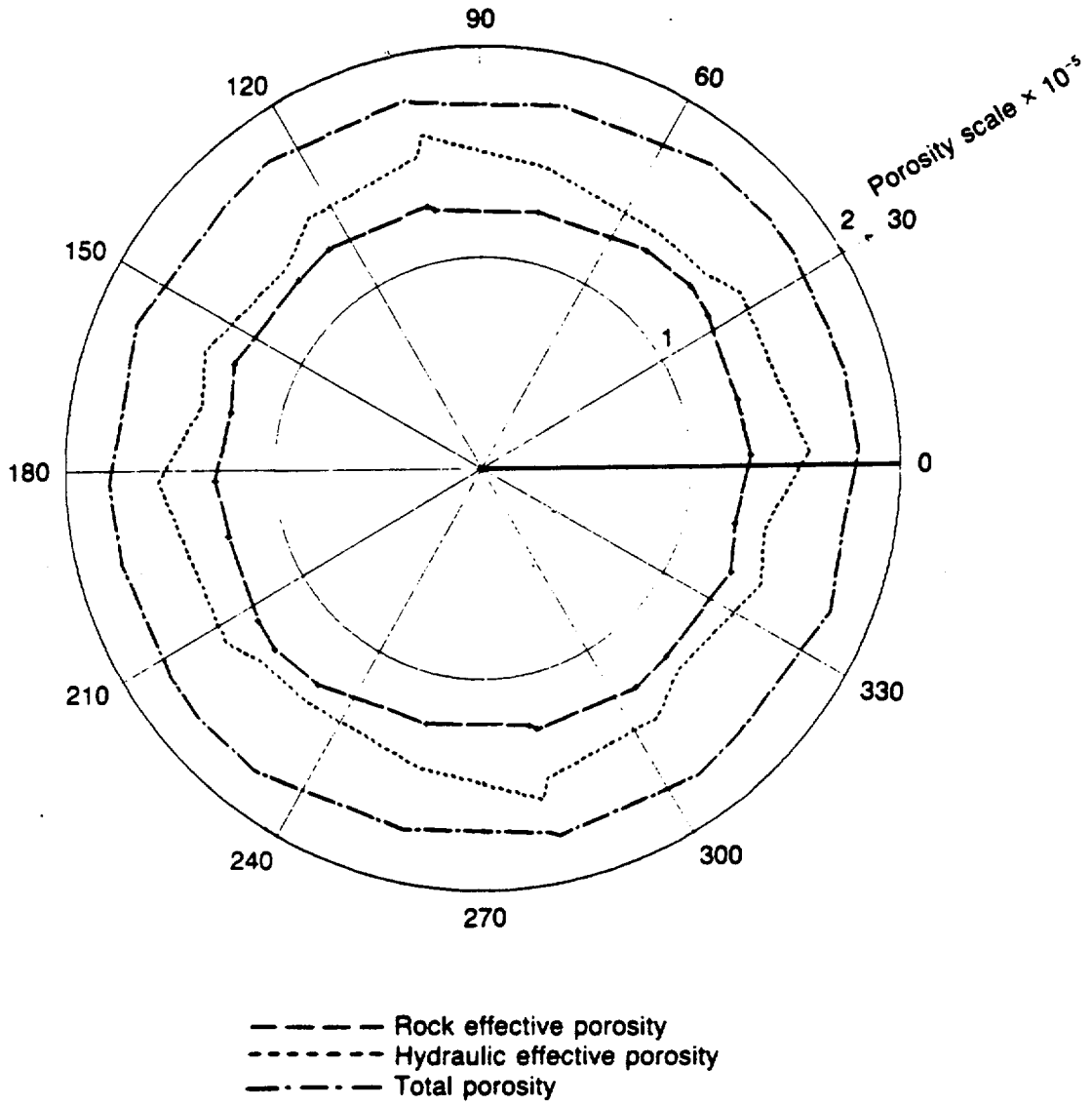
The polar plots of total porosity, hydraulic effective porosity, and rock effective porosity are shown in Figure 7-33. All three porosities are directionally stable, and this fracture system behaves like an equivalent porous medium for transport. The mean directional hydraulic effective porosity of 0.0000146 is larger than the rock effective porosity. The three length-density studies showed that hydraulic effective porosity deviated more from rock effective porosity as σ_b/μ_b increased. The ratios of hydraulic effective porosity to rock effective porosity were 1.10, 1.18 for the systems with σ_b/μ_b of 0 and 0.3, respectively. The ratio of ϕ_H to ϕ_R was much larger than 2 in most directions for the system with correlated apertures and σ_b/μ_b of 1.

Hydraulic effective porosity was greater than rock effective porosity for this discontinuous system, and ϕ_H was nearly equal to ϕ_R for the previous continuous system. In a discontinuous system, the flow rate in a series of elements is governed by the element with the smallest aperture, such that the large flow capacity of large aperture elements are often negated by small aperture elements. In a continuous fracture system, the flow rate in a fracture is theoretically independent of the flow rates in the fractures intersecting it. Consequently, two different effects of large aperture fracture on mean travel time (flow rate) occur in continuous and discontinuous fracture systems. Continuous fracture systems have, on a relative basis, smaller mean travel times than discontinuous systems because the flow rates in large aperture fractures are not controlled by small aperture fractures. One should keep in mind that travel time in an element is inversely proportional to the flow rate in the element. Since hydraulic effective porosity is equal to $q\bar{T}/L$, hydraulic effective porosity deviated less from rock effective porosity for



XBL 841-529

Figure 7-32 Polar Plot of Longitudinal Geometric Dispersivity for Continuous System With σ_b/μ_b of 0.3.



XBL 8312-7421

Figure 7-33 Polar Plots of Total Porosity, Rock Effective Porosity, and Hydraulic Effective Porosity for Discontinuous System With μ_1 of 50 m and σ_b/μ_b of 0.3.

the continuous fracture system.

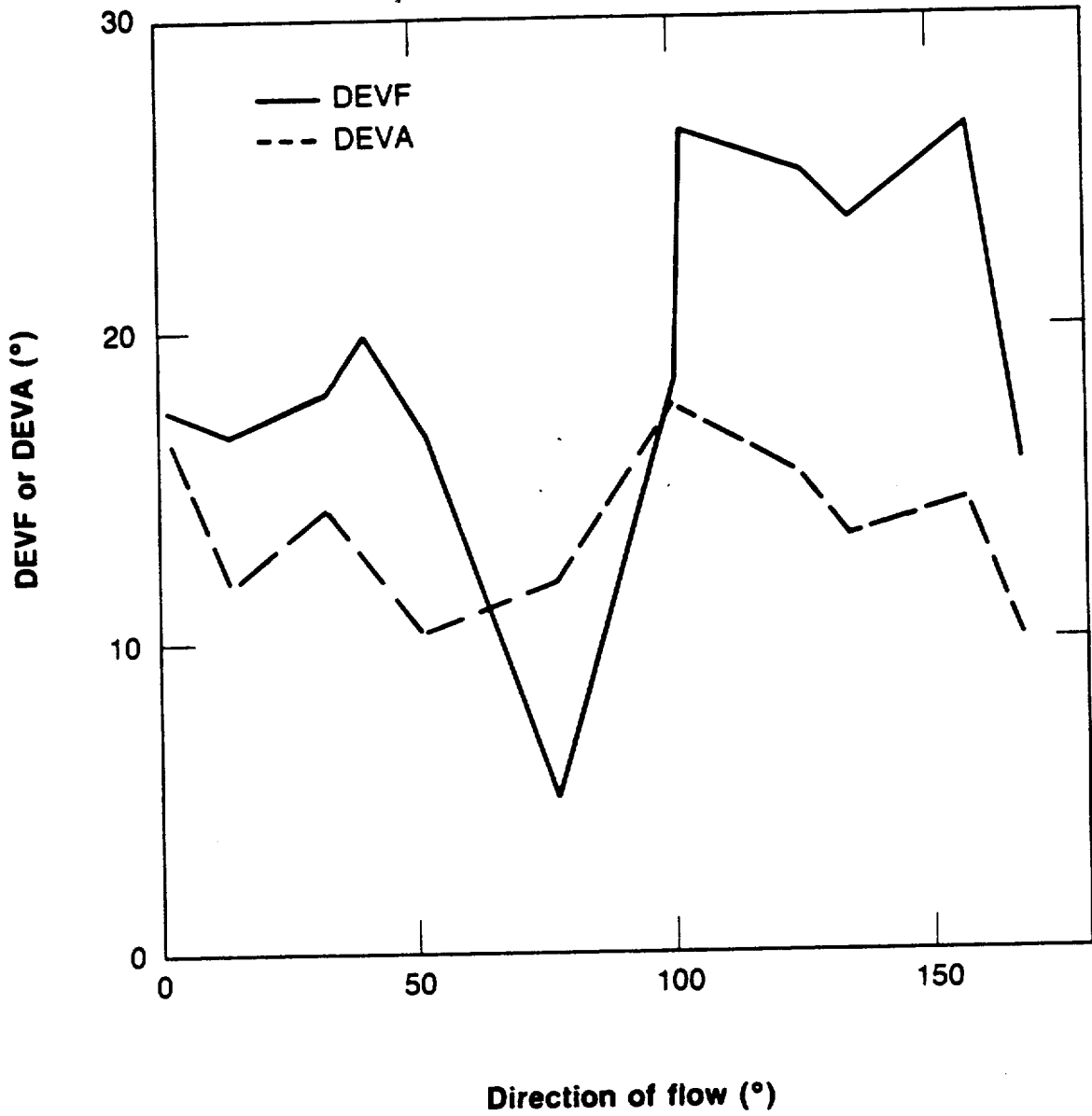
Figure 7-34 is a plot of mean DEVF and mean DEVA versus direction of flow. DEVF was two times smaller for this system than for the discontinuous system with σ_b/μ_b of 1, and about two times larger than DEVF for the discontinuous system with μ_1 of 50 m in the constant aperture study. Thus, equivalent porous medium flow behavior is more likely to occur for fracture systems with small σ_b/μ_b .

The polar plot of longitudinal geometric dispersivity in Figure 7-35 shows that α_L is relatively constant in most directions. The mean directional α_L is 96.6 m. The mean directional α_L was 66 m for the discontinuous system with μ_1 of 50 m in the constant aperture study. The results showed again that α_L increased as σ_b/μ_b increased. Tortuosity was directionally stable, with a mean of 1.365 (Figure 7-36).

7.4. SUMMARY OF LENGTH-DENSITY ANALYSIS

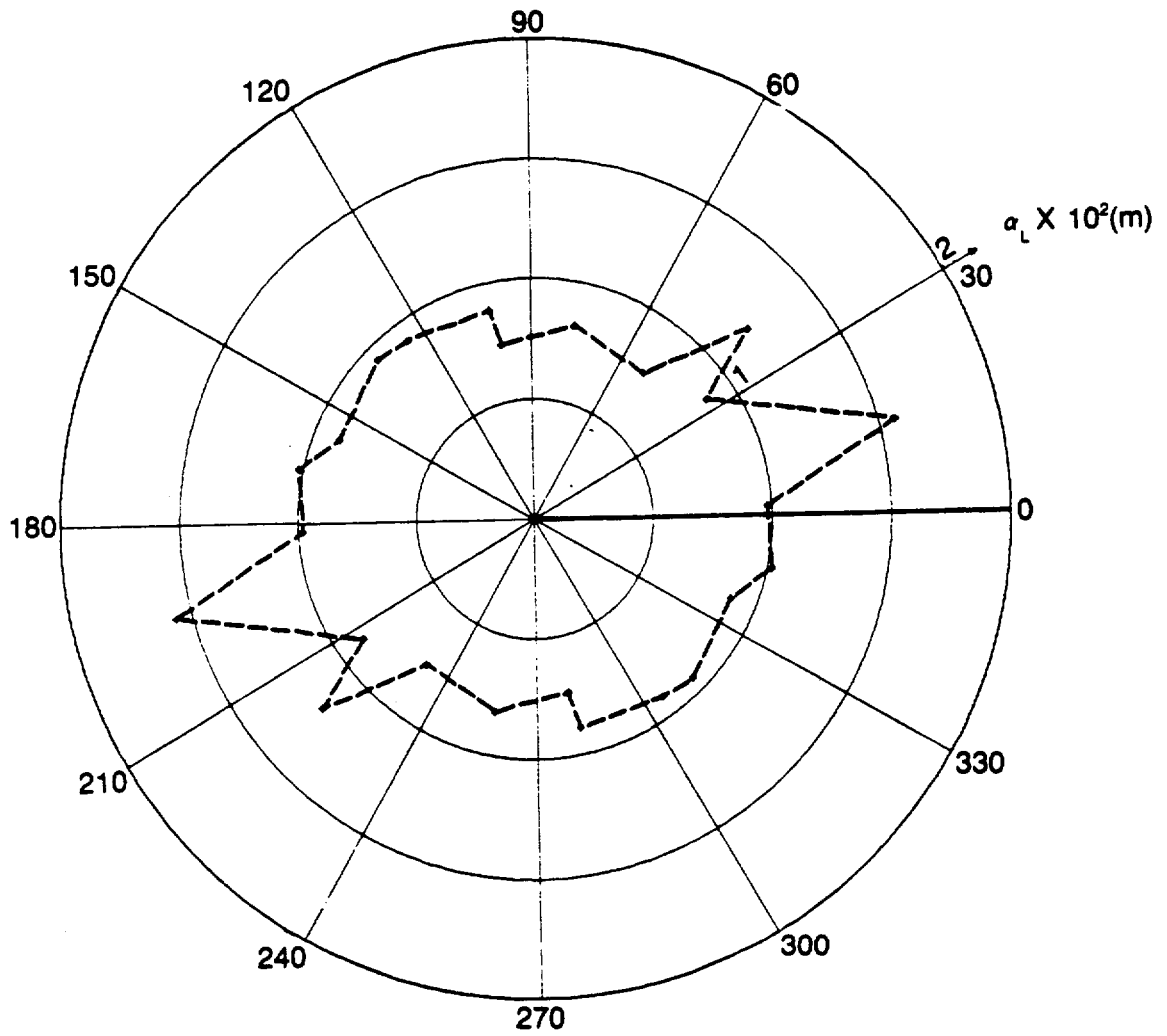
The fracture information needed to run the computer program was determined from hydrogeologic data collected at the research site. The geometric parameters of mean fracture length, standard deviation of fracture length, and set areal density could not be determined from the field data. Consequently, a length-density analysis was conducted to investigate the influence of length and density on mechanical transport. Since the aperture distribution of a fracture system has a major influence on mechanical transport, three length-density studies were conducted using different aperture distributions: 1) σ_b/μ_b equal to 0 (S1), 2) σ_b/μ_b equal to 0.3 (S2), and 3) σ_b/μ_b equal to 1 (S3).

The fracture systems in S1 and S2 behaved like equivalent porous media for transport. Hydraulic effective porosity was nearly equal to rock effective porosity for the continuous systems in S1 and S2. For the discontinuous systems in S1 and S2, hydraulic effective porosity was larger than rock effective porosity, and the deviation between hydraulic effective porosity and rock effective porosity increased as the ratio of σ_b/μ_b increased. Hydraulic effective porosity did not equal rock effective porosity in the discontinuous systems, because large aperture fractures have a different influence on mechanical transport in discontinuous and continuous



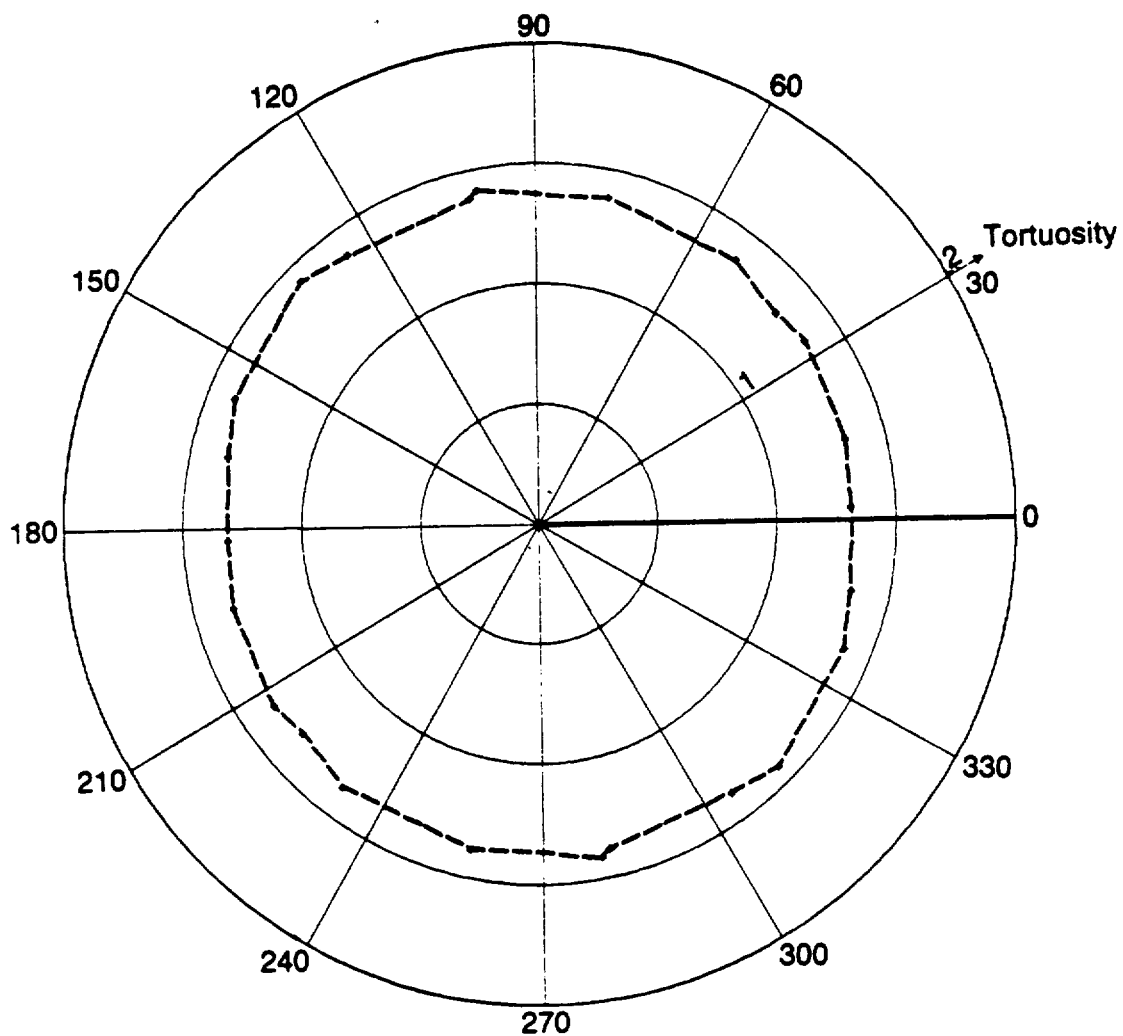
XBL 8401-6791

Figure 7-34 Mean DEVF and Mean DEVA Versus Direction of Flow for Discontinuous System With μ_1 of 50 m and σ_b/μ_b of 0.3.



XBL 8401-6798

Figure 7-35 Polar Plot of Longitudinal Geometric Dispersivity for Discontinuous System with μ_1 of 50 m and σ_b/μ_b of 0.3.



XBL 8401-6796

Figure 7-36 Polar Plot of Tortuosity for Discontinuous System With μ_1 of 50 m and σ_b/μ_b of 0.3.

systems.

The fracture systems in S3 did not behave like equivalent porous media for transport. The polar plots of hydraulic effective porosity were jagged because ϕ_H was directionally dependent. The direction of maximum ϕ_H was near 120° for each system in S3. Hydraulic effective porosity was greater than rock effective porosity for both the continuous and discontinuous systems in S3. The deviations between ϕ_H and ϕ_R were much larger for the fracture systems in S3 than for the discontinuous systems in S1 and S2. Also in S3, the deviations between ϕ_H and ϕ_R were larger for the discontinuous system than for the continuous system.

DEVF and DEVA are measures of equivalent porous medium flow behavior in a direction of flow. DEVA and DEVF both increased as σ_b/μ_b increased. Consequently, a fracture system with a narrow aperture distribution (small σ_b/μ_b) behaved more like an equivalent porous medium than a fracture system with a wide aperture distribution.

Tortuosity was directionally stable in all studies. A directionally stable tortuosity indicated that the fracture systems were fairly isotropic. Tortuosity was slightly less in the continuous systems than in the discontinuous systems. Fluid flows in a more direct path across the flow region in a continuous system than in a discontinuous system because the fractures in a continuous system span across the entire flow region. Consequently, tortuosity was smaller for the continuous systems.

The longitudinal geometric dispersivity is theoretically constant in all directions for an equivalent isotropic porous medium. However, the longitudinal geometric dispersivities were directionally dependent for the fracture systems in S1 and S2, and no general directional relationship for α_L was found. Each fracture system had a unique polar plot for α_L . However, we found that mean directional α_L was independent of mean fracture length for the discontinuous system in S1, even though the polar plots of α_L were different. These systems were not the only nearly isotropic systems which showed directionally dependent longitudinal geometric dispersivities in this research. The equivalent isotropic continuous system of two orthogonal sets of fractures in section 5.3 also had a directionally varying α_L . The aperture distribution greatly

influenced longitudinal geometric dispersivity as α_L could not be computed for the fracture systems in S3 because the Peclet number approached infinity. The three length-density studies showed that α_L increased as σ_b/μ_b increased.

CHAPTER 8

CONCLUSIONS AND RECOMMENDATIONS

8.1. CONCLUSIONS

The primary objectives of this research were to investigate directional mechanical transport parameters for anisotropic fracture systems, and to determine when a fracture system can be treated like an equivalent porous medium for mechanical transport. The two essential conditions necessary for measuring directional mechanical transport for an equivalent porous medium are a uniform flow field, and a test section where linear length is constant. When these two conditions are satisfied, mechanical transport parameters can be measured from the breakthrough curve for the fluid that flows within the test section.

Parameters were defined to evaluate directional mechanical transport. The mean rate of advection in a particular direction was characterized by the hydraulic effective porosity. The hydraulic effective porosity was defined as the ratio of specific discharge to average linear velocity. In porous media transport studies, hydraulic effective porosity is assumed to be directionally stable. Thus, the shape of the polar plot of hydraulic effective porosity was used to test whether a fracture system behaved like an equivalent porous medium for mechanical transport.

The mechanical dispersive flux in a particular direction was characterized by the longitudinal geometric dispersivity. The longitudinal geometric dispersivity is a function of several components of the geometric dispersivity tensor. The derivation of the relationship between longitudinal geometric dispersivity and this tensor showed that it is not necessary to determine all the components of this fourth-ranked tensor to evaluate longitudinal mechanical transport. In porous media transport studies, an anisotropic medium is treated as an equivalent isotropic medium. When this simplification is made, the longitudinal geometric dispersivity becomes directionally stable. We have found that the directional variation of the longitudinal geometric dispersivity can be significant for anisotropic fracture systems. Furthermore, a fracture system which behaved like an equivalent isotropic porous medium for fluid flow did not have a

directionally-stable longitudinal geometric dispersivity.

Another important mechanical transport parameter we studied was the tortuosity. Tortuosity was first used to predict permeability. Tortuosity can also be used to predict the effective diffusion coefficient and to estimate the mean pore velocity. Little work has been carried out on the directional characteristics of tortuosity.

The fact that fluid flow and mechanical transport are coupled made it necessary to investigate equivalent porous medium behavior for fluid flow. When a fracture system, under a constant hydraulic gradient, behaves like an equivalent porous medium, the specific discharge will be uniform in any direction of flow. The uniformity of the specific discharge in a direction was evaluated using the continuity test and the angle of flow test. Darcy's law also specifies that the flow field in any direction of flow can be predicted by a unique permeability tensor. If such a tensor exists, the square root of permeability in the direction of flow plots as an ellipse. Thus, the shape of the square root of permeability was used to test whether directional flow for the system behaved like an equivalent porous medium.

A numerical model was developed to simulate mechanical transport under steady laminar flow in a network of fractures. The model incorporated the principles of laminar flow to calculate the paths of streamtubes for fluid traveling from one side of a flow region to another. We assumed that fluid flow was restricted to planar fractures within an impermeable rock matrix, and that mechanical transport was the only transport process. Of course, other transport processes occur, but focusing on mechanical transport led to the evaluation of the directional transport properties for anisotropic systems.

Mechanical transport was first investigated for regular, anisotropic systems of continuous fractures. These fracture systems were first studied because they behaved like equivalent porous media for fluid flow, with flow parameters that could be analytically computed. The results showed that a fracture system which behaved as a continuum for fluid flow did not behave as a continuum for mechanical transport. This was demonstrated by a hydraulic effective porosity which was directionally dependent and that decreased well below the porosity in

certain directions. In these directions, part of the fracture voids became nonconductive because the direction of the hydraulic gradient was perpendicular to the orientation of a fracture set.

The size of the mechanical transport continuum was found to be directly related to tortuosity. As tortuosity increased, travel paths became more irregular and deviated more from the mean direction of flow. Consequently, larger flow regions were needed before representative mechanical transport behavior occurred when tortuosity was large.

Tortuosity did not behave as one would expect for an equivalent porous medium for these continuous fracture systems. Tortuosity decreased to a minimum of 1.0 in a direction where one fracture set became nonconductive. This direction was not necessarily in the direction of maximum permeability, where one would expect tortuosity to be a minimum for an equivalent porous medium. Thus, porous medium equivalence can be found for certain parameters, while the directional properties of other parameters show that porous medium equivalence is not possible.

The longitudinal geometric dispersivity showed large and abrupt directional variations for the continuous systems. The magnitude of the maximum longitudinal geometric dispersivity increased with the degree of anisotropy, and no general relationship was found between the principal directions of longitudinal dispersivity and the principal directions of permeability. Thus, both longitudinal geometric dispersivity and hydraulic effective porosity were highly directionally dependent. The use of a directionally stable longitudinal geometric dispersivity cannot be justified for these systems. Serious errors in transport prediction would result if one were to treat these anisotropic systems as equivalent isotropic systems.

The first two discontinuous fracture systems studied (section 6.2 and 6.3) behaved like equivalent porous media for fluid flow. Hydraulic effective porosity for both systems showed a slight directional dependence, with the minimum hydraulic effective porosity occurring near the direction of maximum permeability. The polar plots of hydraulic effective porosity, however, were nearly circular and we concluded that each fracture system behaved like an equivalent porous medium for transport. The mean directional hydraulic effective porosity for each sys-

tem was greater than the rock effective porosity so the average linear velocity was less than the usual porous medium estimate of specific discharge divided by rock effective porosity. Hydraulic effective porosity was larger than the rock effective porosity because zones of slow movement existed in the flow region which caused mean travel time to be large in relation to linear travel length and specific discharge. For these two discontinuous systems, tortuosity increased from the direction of maximum permeability to the direction of minimum permeability, as one would expect for equivalent porous media.

Tortuosities as high as 3.8 were measured for the discontinuous system of two sets oriented at 0° and 30°. In the literature, tortuosity is reported to normally range between 1 and 2. The large measured values of tortuosities were caused by the high anisotropy of the system, as the ratio of maximum permeability to minimum permeability was ten. The size of the fluid flow continuum was found to be related to tortuosity. As tortuosity increased, both DEVA and DEVF, measures of equivalent porous medium flow behavior, increased. Thus, the continuum size for both fluid flow and mechanical transport was found to be inversely related to tortuosity. VPORE computed as the product of tortuosity and average linear velocity was shown to be a good estimate of the mean pore velocity. The actual mean pore velocity is normally extremely difficult to determine so an estimate like VPORE is used.

Each discontinuous system showed a unique directional dependence for the longitudinal geometric dispersivity. The ratio of maximum to minimum longitudinal geometric dispersivity was directly related to the degree of anisotropy. The directional variations in longitudinal geometric dispersivity for the discontinuous systems were not as severe as those in the continuous fracture systems. However, the two discontinuous fracture systems showed again that the determination of the directional transport properties for an anisotropic medium is essential to predicting transport.

The large differences in longitudinal geometric dispersivity measured from laboratory and field data could be due to the directional nature of α_L . Longitudinal geometric dispersivity is properly measured in the laboratory when the procedure described in sections 3.5 and 3.6 is

used. We are unaware of any laboratory experiments which has used this procedure. In a groundwater aquifer, the natural direction of flow may vary spatially such that, to model transport in the aquifer, a directional α_L must be used. In most transport studies, a constant α_L is used to model transport in the aquifer. Consequently, the dispersivities measured from laboratory and field data may not properly characterize transport in the aquifer.

The connectivity sensitivity studies for mean fracture length, set areal density, and mean fracture orientation showed that mechanical transport parameters were generally much more sensitive to the three connectivity parameters than either specific discharge or rock effective porosity. For example, both mean travel time and the variance of the breakthrough curve were highly sensitive to each connectivity parameter, and no relationship was found between either mechanical transport parameter and any connectivity parameter. However, specific discharge and rock effective porosity both increased with connectivity. Tortuosity was the only mechanical transport parameter that showed no sensitivity to connectivity. The least sensitive connectivity parameter was the mean orientation of the fracture set, with the mean fracture length and the set areal density having about equal sensitivity. In the mean aperture sensitivity study, the variance of the breakthrough curve was the most sensitive mechanical transport parameter, followed by mean travel time. The longitudinal geometric dispersivity and tortuosity were both insensitive to mean aperture.

Connectivity increased when fracture orientations became distributed, while connectivity decreased when fracture lengths became distributed. The increased connectivity created a more random fracture system, and the following parameters increased because of this: rock effective porosity, specific discharge, tortuosity, mean travel time, and the variance of the breakthrough curve. Heterogeneity increased when fracture apertures became distributed. This increased heterogeneity caused a reduction in the specific discharge. The specific discharge decreased because the flow rate in a series of fractures is governed by the fracture with the smallest aperture. The smaller flow rate meant that fluid particles took a longer time to travel through the flow region, and thus, mean travel time increased. The variance in the breakthrough curve

increased because the increased heterogeneity caused a greater variation in pore velocities.

A length-density analysis was conducted using fracture data collected at a research site in Manitoba, Canada. Since the aperture distribution of a fracture system has a major influence on mechanical transport, three length-density studies were conducted using different aperture distributions. The studies showed that porous media equivalence for fluid flow and transport is likely to occur for fracture systems in which the ratio of σ_b to μ_b is small. For the continuous systems which showed porous media equivalence, hydraulic effective porosity was nearly equal to rock effective porosity. However, hydraulic effective porosity was larger than rock effective porosity for the discontinuous systems which exhibited porous media equivalence. The larger deviation between hydraulic effective porosity and rock effective porosity in the discontinuous systems was caused by the different effects of large aperture fractures on travel time in continuous and in discontinuous systems. Tortuosity was directionally stable for all systems which indicated that each fracture system was fairly isotropic.

Theoretically, the longitudinal geometric dispersivity is directionally stable for an equivalent isotropic medium. However, the longitudinal geometric dispersivities were directionally dependent for the fracture systems which otherwise exhibited porous media equivalence. We found that the mean directional α_L was independent of mean fracture length for the discontinuous systems in the constant aperture length-density study, even though the polar plots of α_L were different. These systems were not the only nearly isotropic systems which showed directionally varying longitudinal geometric dispersivities in this research. The equivalent isotropic system of two orthogonal sets of continuous fractures in section 5.3 also had a directionally dependent α_L . The aperture distribution greatly influenced longitudinal geometric dispersivity, as α_L could not be computed for the fracture systems in which the mean aperture equaled the standard deviation of aperture. The Peclet number approached infinity for these fracture systems. The three length-density studies showed that α_L increased as σ_b/μ_b increased.

8.2. RECOMMENDATIONS

The purpose of this research was to investigate the directional measurement of mechanical transport for anisotropic fracture systems. No extensive study of directional mechanical transport in groundwater systems has been reported in the literature. Consequently, in this research a set of experiments was developed to measure directional mechanical transport, and then it was shown how directional mechanical transport can be interpreted from these experiments. The primary mechanical transport parameters investigated were hydraulic effective porosity, tortuosity, and longitudinal geometric dispersivity.

This study has uncovered a number of significant findings on directional transport properties. For example, tortuosities much larger than three were measured in this study. In most transport studies, tortuosity is rarely determined, and is normally assigned a value about 1.4. Further research is needed to understand how travel paths influence fluid flow and transport. Tortuosity was used in this work to characterize the mean path length. Research is needed to determine how the distribution of paths lengths can be used in evaluating transport. Another area that can be investigated is the use of the Kozeny equation for anisotropic media. The computer program can be modified so that the shape factor and the hydraulic radius in the Kozeny equation can also be computed for different directions of flow.

The longitudinal geometric dispersivity was shown to be highly directionally dependent. Yet, in most transport studies, a constant longitudinal geometric dispersivity is assumed in all directions, as the anisotropic medium is treated as an equivalent isotropic medium. Future research can investigate the error that is made when this assumption is used. The error associated with this assumption can be determined by conducting tracer experiments for anisotropic media using the hydraulic boundary conditions for isotropic media described in section 2.2.2.

Directional mechanical transport is measured in this study using a numerical model. An alternative method would be to conduct laboratory experiments. The conventional laboratory tracer experiment consists of applying no-flow boundary conditions along the sides of the test sample, and constant-head boundary conditions across the inlet and the outlet to the sample.

Tracer is next injected across the inlet, and then the breakthrough curve is constructed to measure transport. The conventional tracer experiment can be used to measure mechanical transport in the two principal directions. Between the two principal directions, the tracer experiments described in Chapter 3 must be used to measure mechanical transport. The crucial step in designing this laboratory experiment is the application of the constant hydraulic gradient boundary conditions along the sides of the test sample. An innovative design is needed to implement such hydraulic boundary conditions. Once the hydraulic boundary conditions have been applied, the experiment can proceed in the manner described in section 3.6.

The computer program in Chapter 4 was written using single precision. Certain parts of the computer program require computational accuracy. For example, the flow rate in each streamtube must be accurately computed to ensure that the total flow rate into a node is equal to the total flow rate out of a node. Better accuracy can be gained by writing the computer program using double precision. However, the dimensions of variable arrays are reduced when double precision is used and this will result in an analysis of smaller sized problems unless a computer with a larger storage capacity becomes available. To increase accuracy without decreasing the size of the arrays used in the present computer program, one should switch from the VAX machine (Class IV) to a Class VI machine such as the Cray.

The accuracy of the modeling results also depends on the availability of detailed and reliable fracture data. We have shown that the statistical parameters of the aperture distribution are essential for modeling fluid flow and mechanical transport. To obtain a representative sample of the aperture distribution, a well planned set of packer tests would have to be conducted in the fractured rock mass. Thus, a dynamic interaction between theoretical (modeling) and experimental (field data) groundwater research activities is essential to significant advancements in this field.

A useful addition to the computer program would be to eliminate all dead-end loops in the fracture network formed by nonconductive fracture segments before the mechanical transport simulation stage. The program would not have to search for dead-end loops in the pro-

cess of locating streamtubes, and thus, computer time would decrease for this stage. The algorithm for eliminating dead-end loops should follow the fracture system generation stage. The elimination of dead-end loops would then decrease the number of elements and nodes in the flow region, and the bandwidth in the conductance matrix would probably decrease. Thus, computer time would also decrease in the hydraulic head calculation stage.

The next step in the theoretical development would be to determine if directional hydrodynamic dispersion can be analyzed. The investigation of directional hydrodynamic dispersion would require the understanding of another transport process, molecular diffusion. The two key steps that must be considered in developing the theory to measure directional hydrodynamic dispersion are: 1) finding the appropriate test section in which to measure hydrodynamic dispersion, and 2) determining how hydrodynamic dispersion parameters can be evaluated from measurements made within this test section. The concepts of directional mechanical transport in Chapter 3 will provide a good starting point for developing the necessary theory.

The present computer program would have to be modified to model hydrodynamic dispersion. Numerical methods that are commonly used to model hydrodynamic dispersion in porous media are the finite difference method (FDM), the finite element method (FEM), and the method of characteristics (MOC). If the present computer program were to be modified to include hydrodynamic dispersion, the MOC would be the best method to use. The MOC would be able to use some of the streamtubing principles developed in Chapter 4. Also, the MOC requires less computer time than either the FEM or the FDM. Both the FDM and the FEM require the solution of a larger matrix than the conductance matrix for fluid flow. Furthermore, this matrix would have to be solved for each time step since transport is a transient phenomenon.

The computer program as developed in this work for hydrodynamic dispersion should be used in two parts. First, the computer program should be used to evaluate directional mechanical transport and evaluate porous medium equivalence. Mechanical transport must be

evaluated first because the direction of flow, average linear velocity, and tortuosity are needed to model hydrodynamic dispersion. Then the computer program should be used to evaluate hydrodynamic dispersion. In this manner, the program can be used to evaluate both mechanical transport and hydrodynamic dispersion.

REFERENCES

- Anderson, M.P. (1979) Using models to simulate the movement of contaminants through groundwater flow systems. *Critical Reviews in Environmental Resour. Res.*, 17(4), 1075-1081.
- Baird, D. C. (1962) *Experimentation: an introduction to measurement theory and experiment design*, Prentice-Hall, New Jersey, 198.
- Biggar, J. W., and D. R. Nielsen (1960) Diffusion effects in miscible displacements occurring in saturated and unsaturated porous materials, *J. Geophys. Res.*, 65(9), 2887-1895.
- Carman, P. C. (1956) *Flow of gases through porous media*, Academic Press, New York, 182.
- Castillo, E., R. J. Krizek, and G. M. Karadi (1972) Comparison of dispersion characteristics in fissured rocks, *IAHR Proc. Second Symposium on Fundamentals of Transport Phenomena in Porous Media*, 778-797.
- Cherry, J. A., R. W. Gilham, and J. F. Pickens (1975) Contaminant hydrogeology, part 1 physical processes, *Geoscience Canada*, 2(2), 76-84.
- Childs, K. E., S. B. Upchurch, B. Ellis (1981) Sampling of variable, waste- migration patterns in groundwater, *Groundwater*, 12(6), 369-377.
- Collins, R. E. (1961) *Flow of fluids through porous materials*, The Petroleum Publishing Company, Tulsa, 270.
- Dieulin, A., G. Matheron, and G. de Marsily (1981) Growth of the dispersion coefficient with the mean traveled distance in porous media, *The Science of the Total Environment*, 21, 319-328.
- Dullien, F. (1979) *Porous media, fluid transport and pore structure*, Academic Press, New York, 306.
- Ellis, W. R., L. Kevi, and W. A. Wiebenga (1968) The investigation of water flow through porous mediums by means of radiotracers, *Water Resour. Res.*, 4(2), 413-416.
- Freeze, R. A., and J. A. Cherry (1979) *Groundwater*, Prentice-Hall, New York, 604.
- Fried, J. J., (1975) *Groundwater Pollution*, Elsevier Scientific, Amsterdam, 930.
- Gelhar, L. W., A. L. Gutjahr, and R. L. Naff (1979) Stochastic analysis of macrodispersion in a stratified aquifer, *Water Resour. Res.*, 15(6), 1387-1397.
- Gillham, R. W., and J. A. Cherry (1982) Contaminant migration in saturated unconsolidated geologic deposits, *Recent Trends in Hydrogeology*, Geological Society of America Special Paper 189, 31-63.
- Gill, W. N., V. Guceri, and R. J. Nunge (1969) Laminar dispersion in diverging channels in concentric annuli, Office of Saline Water, Research and Development Report No. 443.
- Grove, D. B., and W. A. Beetem (1971) Porosity and dispersion constant calculations for a fractured carbonate aquifer using the two well tracer method, *Water Resour. Res.*, 7(1), 128-134.
- Haring, R. E., and R. A. Greenkorn (1970) A statistical model of a porous medium with nonuniform pores, *A.I.Ch.E.*, 16(3), 477-482.

- Hazzaa, I. B., K. F. Saad, R. K. Girgis, A. A. Bakr, and F. M. Swailem (1964) Determination of porosity of groundwater aquifers by the radioactive tracer technique, *Int. J. Appl. Radiat. Isotopes*, 16, 261-165.
- Hazzaa, I. B., R. K. Girgis, K. F. Saad, F. M. Swailem, and A. A. Bakr (1966) Study of the applicability of different radioisotopes for determination of the porosity of ground-water aquifers, *Int. J. Appl. Radiat. Isotopes*, 17, 621-628.
- Hoehn, E., and P. V. Roberts (1982) Advection-dispersion interpretation of tracer observations in an aquifer, *Groundwater*, 20(4), 457-465.
- Karadi, G. M., R. J. Krizek, and E. Castillo (1972) Hydrodynamic dispersion in a single rock joint, *J. Appl. Phys.*, 43(12), 5013-5021.
- Krizek, R. J., G. M. Karadi, and E. Socias (1972) Mathematical model for two-dimensional percolation through fissured rock, *Proc. Int. Soc. Rock Mech. Symp. on Percolation Through Fissured Rock*, Stuttgart, TC1-TC15.
- Levenspiel, O. (1972) *Chemical reaction engineering*, John Wiley, New York, 578.
- Long, J. C. S. (1982) Verification and characterization of continuum behavior of fractured rock at AECL underground research laboratory, task 1: investigation of equivalent porous media behavior for networks of discontinuous fractures, report on activities for FY 1982, LBL-14975, Lawrence Berkeley Laboratory.
- Long, J. C. S. (1984) Permeability and porosity in three vertical planes near the URL shaft site, Letter Report in preparation.
- Long, J. C. S., J. S. Remer, C. R. Wilson, and P. A. Witherspoon (1982) Porous media equivalents for network of discontinuous fractures, *Water Resour. Res.*, 18(3), 645-658.
- Marcus, H., and D. E. Evenson (1956) Directional permeability in anisotropic porous media, *Water Resour. Center Contrib. No. 31*, University of California, Berkeley, 105.
- Matheron, G., and G. de Marsily (1980) Is transport in porous media always diffusive? a counter example, *Water Resour. Res.*, 16(5), 801-817.
- Neretnieks, I. (1980) Some difficulties in interpreting in-situ tracer tests, *Symp. on the Scientific Basis for Nuclear Waste Management*, Boston, 10.
- Ogata, A. (1970) Theory of dispersion in a granular medium, *U. S. Geol. Surv. Prof. Paper 411-I*, 34.
- Parsons, R. W. (1966) Permeability of idealized fractured rock, *Soc. Pet. Eng. Jour.*, 6(2), 126-136.
- Perkins, T. K., and O. C. Johnston (1963) A review of diffusion and dispersion in porous media, *Soc. Pet. Eng. Jour.*, 70-84.
- Pickens, J. F., and G. E. Grisak (1981a) Modeling scale-dependent dispersion in hydrogeologic systems, *Water Resour. Res.*, 17(6), 1701-1711.
- Pickens, J. F., and G. E. Grisak (1981b) Scale-dependent dispersion in a stratified granular aquifer, *Water Resour. Res.*, 17, 1191-1211.
- Rice, D. A., D. J. Fontugne, R. G. Lattini, and A. J. Barduhn (1969) Anisotropic permeability in porous media, *Proc. Sixth State-of-the-Art Symp. sponsored by Industrial and Engineering Chemistry of American Chemistry Society*, 48-56.

- Scheidegger, A. E. (1960) *The physics of flow through porous media*, MacMillan Company, New York, 313.
- Scheidegger, A. E. (1961) General theory of dispersion in porous media, *Jour. Geophys. Res.*, 66(10), 3273-3277.
- Scheidegger, A. E. (1964) Statistical hydrodynamics in porous media, *Advan. Hydrosci.*, 1, 161-181.
- Schwartz, F. W. (1977) Macroscopic dispersion in porous media: the controlling factors, *Water Resour. Res.*, 13(4), 743-752.
- Schwartz, F. W., L. Smith, and A. S. Crowe (1981) Stochastic analysis of groundwater flow and contaminant transport in a fractured rock system, *Proc. Material Research Society, Symposium on the Scientific Basis of Nuclear Waste Management*, Boston.
- Smith, L., and F. W. Schwartz (1980) Mass transport, 1, a stochastic analysis of macroscopic dispersion, *Water Resour. Res.*, 16(2), 303-313.
- Smith, L., and F. W. Schwartz (1981a) Mass transport, 2, analysis of uncertainty in prediction, *Water Resour. Res.*, 17(2), 351-369.
- Smith, L., and F. W. Schwartz (1981b) Mass transport, 3, role of hydraulic conductivity data in prediction, *Water Resour. Res.*, 17(5), 1463-1479.
- Snow, D. T. (1969) Anisotropic permeability of fractured media, *Water Resour. Res.*, 17(3), 555-564.
- Sudicky, E. A., and J. A. Cherry (1979) Field observations of tracer dispersion under natural flow conditions in an unconfined sandy aquifer, *Water Pollut. Res. Can.*, 14, 1-17.
- Taylor, G. I. (1953) Dispersion of soluble matter in solvent flowing slowly through a tube, *Proc. R. Soc. London Ser. A*, 219, 186-203.
- Topping, J. (1955) *Errors of observation and their treatment*, Reinhold Publishing Corp., New York, 119.
- Van der Laan, E. (1958) Notes on the diffusion-type model for the longitudinal mixing in flow, *Chem. Eng. Sci.*, 7, 187-191.
- Von Rosenberg, D. U. (1956) Mechanics of steady state single-phase fluid displacement from porous media, *A.I.Ch.E. Journal*, 2(1), 55-58.
- Walters, G. R., H. W. Bentley, and J. J. Ward (1983) Continuum and non-continuum aspects of groundwater movement at the waste isolation pilot plant, Southeastern New Mexico, *EOS Trans. Amer. Geophys. Union*, 64(45), 713.
- Warren, J. E. and F. F. Skiba (1964) Macroscopic dispersion, *Soc. Pet. Eng. Jour.*, 215-230.
- Wilson, C. R. (1970) *An investigation of laminar flow in fractured porous rocks*, Ph.D. thesis, University of California, Berkeley, 178.
- Wyllie, M. R. J., and M. B. Spangler (1952) Application of electrical resistivity measurements to problem of fluid flow in porous media, *Bulletin of the American Association of Petroleum Geologists*, 36(2), 359-403.